NASA TECHNICAL MEMORANDUM

NASA TM X-3458

NASA TM X-3458

SPACE PROCESSING APPLICATIONS ROCKET PROJECT

SPAR I Final Report

George C. Marshall Space Flight Center
Marshall Space Flight Center, Ala. 35812

NATIONAL AERONAUTICS AND SPACE ADMINISTRATION • WASHINGTON, D. C. • DECEMBER 1976

SPACE PROCESSING APPLICATIONS

ROCKET PROJECT

SPAR I

FINAL REPORT

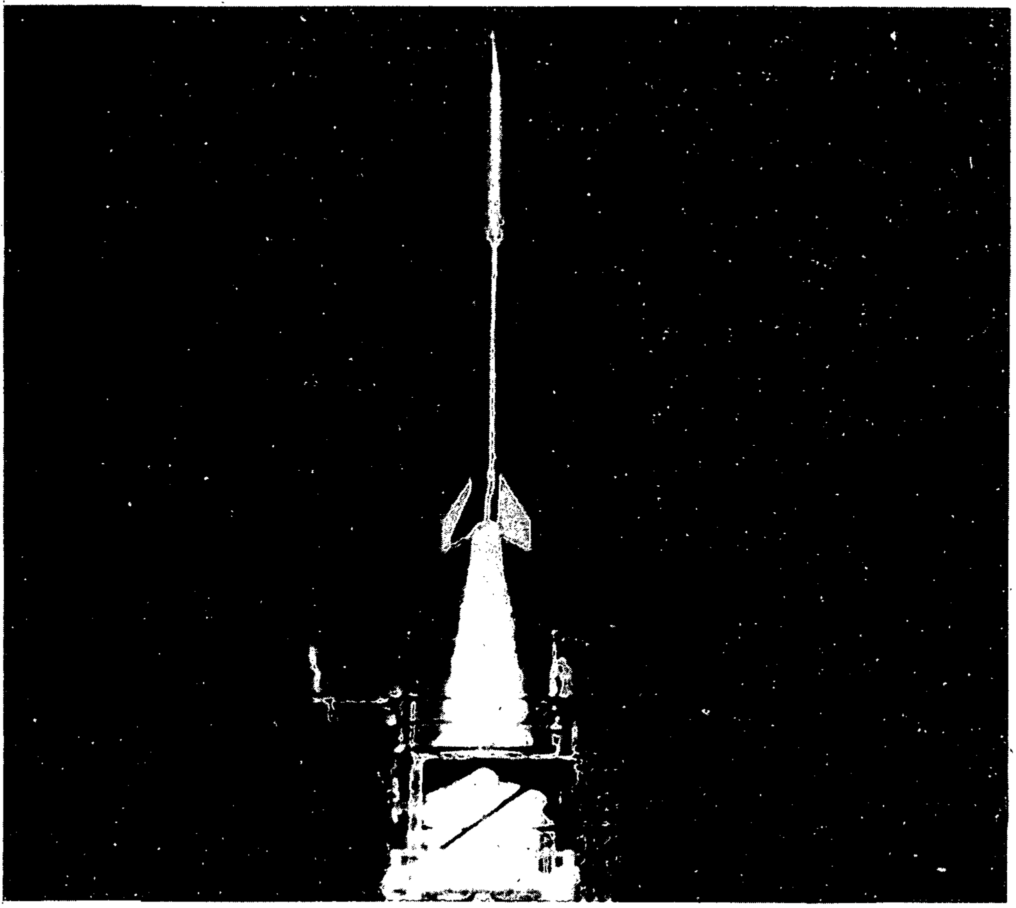

TECHNICAL REPORT STANDARD TITLE PAGE

1. REPORT NO. NASA TM X-3458	2. GOVERNMENT ACCESSION NO.	3. RECIPIENT'S CATALOG NO.

4. TITLE AND SUBTITLE

Space Processing Applications Rocket Project
SPAR I Final Report

5. REPORT DATE
December 1976

6. PERFORMING ORGANIZATION CODE

7. AUTHOR(S)

8. PERFORMING ORGANIZATION REPORT #
M-196

9. PERFORMING ORGANIZATION NAME AND ADDRESS

George C. Marshall Space Flight Center
Marshall Space Flight Center, Alabama 35812

10. WORK UNIT NO.

11. CONTRACT OR GRANT NO.

13. TYPE OF REPORT & PERIOD COVERED
Technical Memorandum

12. SPONSORING AGENCY NAME AND ADDRESS

National Aeronautics and Space Administration
Washington, D.C. 20546

14. SPONSORING AGENCY CODE

15. SUPPLEMENTARY NOTES

This report was compiled by Fred Reeves and Roger Chassay of the Space Processing Applications Rocket Project Office, Special Projects, George C. Marshall Space Flight Center.

16. ABSTRACT

This document summarizes the experiment objectives, design/operational concepts, and final results of each of nine scientific experiments conducted during the first Space Processing Applications Rocket (SPAR) flight flown by NASA in December 1975. The nine individual SPAR experiments, covering a wide and varied range of scientific materials processing objectives, were entitled: Solidification of Pb-Sb Eutectic, Feasibility of Producing Closed-Cell Metal Foams, Characterization of Rocket Vibration Environment by Measurement of Mixing of Two Liquids, Uniform Dispersions of Crystallization Processing, Direct Observation of Solidification as a Function of Gravity Levels, Casting Thoria Dispersion-Strengthened Interfaces, Contained Polycrystalline Solidification, and Preparation of a Special Alloy for Manufacturing of Magnetic Hard Superconductor Under Zero-g Environment.

17. KEY WORDS

18. DISTRIBUTION STATEMENT

STAR Category 15

19. SECURITY CLASSIF. (of this report) Unclassified	20. SECURITY CLASSIF. (of this page) Unclassified	21. NO. OF PAGES 301	22 PRICE $9.25

MSI

*For sale by the National Technical Information Service, Springfield, Virginia 22161

CONTENTS

Chapter Page

SPACE PROCESSING APPLICATIONS ROCKET PROJECT

SPAR I

FINAL REPORT

INTRODUCTION

NASA has recognized a clear need for continuing flight research to bring to fruition the new era in materials signaled by the Skylab and Apollo-Soyuz experiments and other related ground-based and flight research.

The Space Processing Applications Rocket (SPAR) project has been initiated to capitalize on this new technology which has generated widespread interest in the international scientific community. A broad spectrum of space processing flight experiments is being conducted aboard available and economical research rockets. The project will concentrate on solidification kinetics, improvement in homogeneity and defect density of various materials, and similar improvements in composite materials, glasses and ceramics, and biological preparations which Skylab and Apollo-Soyuz have shown are possible.

These rocket experiments, which continue until the Space Shuttle becomes available in the 1980's, will provide much needed scientific data on materials and may lead to work of considerable sophistication on the early Shuttle missions. It is believed that experiments within the capabilities of SPAR flights can also provide experience with new modes of experiment operation analogous to those expected for the Shuttle and Spacelab. For example, each principal investigator will conduct a project that includes experiments on up to three rocket flights, and the average cost of flying experiments will be minimized by maximizing the number carried on each flight.

The initial launch was successfully accomplished on December 11, 1975, with the flight of nine experiments on SPAR I. Performance of all payload and rocket systems was excellent, with the exception of one camera anomaly (Ref. Chapter VIII). The subsequent launches are planned at approximately 4 month intervals. The Black Brant VC sounding rockets, which can carry approximately

400 pounds of science payload weight for 5 minutes of low-g, were selected for the first flights of this project. The SPAR project will continue after the initial missions using a Nike boost if required to supplement the Black Brant VC payload weight capability. Other rocket configurations such as Aries will be considered for later flights. The baseline plan is to fly approximately three missions per year through 1980.

CHAPTER I

SPACE SOLIDIFICATION OF Pb-Sb EUTECTIC

Experiment 74-5

By

Robert B. Pond, Sr., John W. Winter, Jr.,
Stephen L. Van Doren, and David A. Shifler

Marvalaud, Inc.

Page Intentionally Left Blank

SUMMARY

A three-part experiment to attempt to produce a complete eutectic structure in Pb-Sb has been undertaken using microgravity to eliminate the gravitational segregation problems. The first of three alloys was flown on SPAR I. The returned specimen has undergone extensive comparisons with ground-based specimens with respect to mechanical properties and microstructural characteristics. Several tentative conclusions have been reached pending the results of the other two parts of the experiment to be flown on SPAR II. It has been found that the eutectic composition for both flight and ground-based specimens has apparently been shifted because of supercooling at the solidification rates involved, but this shift is not well defined because of the unexpected presence of dual primary crystallization products. The occurrence of the latter is not possible according to the equilibrium diagram. It has also been found that an increase in solidification rate in ground-based specimens can cause primary lead dendrites to be replaced by primary antimony dendrites without a change in composition. Finally, it has been determined that there is no discernible difference between the flight specimen and ground-based specimens based on the mechanical properties studied and the microstructural observations that were made.

STATEMENT OF THE PROBLEM

Background Information

There has been a great interest in superplasticity during the past 15 years. A search for materials that behave superplastically was instituted for two reasons. The first of these reasons was to allow a deeper understanding of this phenomenon whereby metallic materials can undergo enormous tensile strains (of the order of 1000%) before rupturing. The second of these was to allow operations and manufacturing procedures that heretofore had not been possible. One of these operations that was heralded is the deep drawing of cases and containers. A second area that has been little publicized is the use of superplastic material in shaped charge liners to enhance the penetrating power of the jet formed when the shaped charge is properly detonated. Besides having use as devices for tapping furnaces and opening up oil sands, the liners are used in warfare.

One of the materials the U.S. Army has been interested in is the eutectic of Pb-Sb. This material in the eutectic structure should be superplastic and should possess the proper average density to be an effective liner. One of the principal problems with the material is that its eutectic composition is not precise. The alloy composition for this structure should be 88.8 Pb and, although portions of a heat will solidify into a lamellar or Chinese script structure of this composition, there always seems to be some segregation of the primary crystallization type. Blumenthal [1] concludes that it is because of the tendency of the eutectic to supercool that this imprecision occurs.

It should be noted that the density of Pb is 11.34 and the density of Sb is 6.62 [2]. If during the solidification process nucleation of either of these phases occurs homogeneously (or unattached to a wall or substrate), the density difference will cause an immediate tendency to separate because of gravity. If this solidification experiment was carried out at near zero gravity, then the material should not have a tendency to segregate and the imprecision problem should disappear, thereby allowing a true measurement of the superplastic properties of this material.

Objective of the Experiment

The prime purpose of this investigation is to ascertain whether it is possible to get a faithful and complete eutectic structure in 88.8 Pb-11.2 Sb in microgravity. With relatively high solidification rates, it is recognized that the material does supercool [1] and that because of this nonequilibrium condition, the eutectic composition will shift. It would be difficult to predict which way the eutectic point would shift, but it is certainly possible to start with the accepted eutectic composition (88.8 Pb-11.2 Sb) and get an off-eutectic structure because of the high rate.

It is interesting to note from the work of Varich and Yakunin [3], Borromee-Gautier, et al. [4], and Ramachandrarao et al. [5] that if the solidification rate of Pb-Sb alloys is maximized, the solid solubility of Pb in Sb and Sb in Pb is extended or increased, new metastable crystalline solids can be developed, and amorphous solid constituents can be identified. Certainly the solidification rate is not maximized in the rocket experiments, but because the rate is increased, it is necessary to establish the extent to which these identified shifts occur.

Approach

The experiment is being carried out using three different alloys: (1) a hypoeutectic alloy (7.0 wt.% Sb), (2) a eutectic alloy (11.2 wt.% Sb), and (3) a hypereutectic alloy (18.0 wt.% Sb). As can be seen from the binary phase diagram, if supercooling to the 200°C level is experienced, it is expected that either the 7.0% Sb or the 18.0% Sb alloy may become the eutectic composition. Supercooling to the 117°C level has been reported for pure Sb [6]. The extent to which these alloys will supercool as a function of quench rate is not known; however, such hypoeutectic and hypereutectic alloys will allow an evaluation of the shift in the eutectic composition as a function of solidification rate.

In the rocket experiments the abbreviated time during which microgravity is effective necessitated the use of every precaution to make sure the melt was devoid of any segregation and was absolutely homogeneous. This condition was met by mechanically mixing small particles of wrought eutectic and then consolidating the mass and not remelting it again until microgravity was achieved. The abbreviated time has also necessitated the rapid solidification of the alloy, which in turn required prior knowledge of the effect of such rapid solidification on the microstructure at 1 g. Such a requirement demanded a ground-based study of structure as a function of solidification rate.

SCHEDULE

Only one of the three alloys was carried in SPAR I. The cartridge carrying the eutectic composition is the only one that has undergone heating and cooling in microgravity. The other two alloys will be carried in cartridges on SPAR II.

The three alloys were prepared using the same technique, and each of the alloys was sealed in stainless steel cartridges. A decision had to be made as to the integrity of the Pb-Sb in the 321 stainless cartridge when operating at the anticipated temperatures during flight. A series of experiments was therefore scheduled to investigate the corrosion of the cartridge by the alloy as a function of temperature. After it was ascertained that the welded cartridge was satisfactory, 17 loaded cartridges were delivered to Marshall Space Flight Center where I. C. Yates and W. Aldrich used several of them in evaluating the flight furnaces; the balance were either flight specimens, or backup specimens.

The eutectic alloy was melted and solidified at varying rates at Marvalaud to determine the effect of the quench rate on the microstructure as well as on the mechanical properties of the alloy.

After the SPAR I flight, the recovered sample was examined to determine its solidification rate (by comparison with the ground-based rate studies) as well as its microstructure and its mechanical properties.

PROCEDURE DURING PHASE I (SPAR I FLIGHT)

Cartridge Compatibility

An initial survey of the literature including appropriate binary phase diagrams raised some doubt as to the compatibility between the 321 stainless furnace cartridge and the Pb-Sb alloys. The use of a graphite liner, although considered, has the disadvantage that for a reasonable design, the flight sample would be considerably smaller (40% of the volume without a liner). Direct experiment showed that a TIG welded cartridge would contain the eutectic alloy satisfactorily at temperatures as high as 1000°C, as long as the supply of air to the surface of the melt was restricted. The latter was accomplished experimentally by covering the top of the open cartridge with a plate of graphite. The flight specimens are sealed into the stainless furnace cartridge under vacuum to guarantee this condition is met.

Alloy Preparation

Both the antimony and lead used were Asarco Grade B-58 (99.99+%) from lots A-75 and 2-73 respectively. The major impurities in the Sb are 50 ppm of As and 10 ppm of both Pb and Bi. The major impurities in the Pb are 7 ppm of Bi and 3 ppm of Cu. In preparing the alloys, our weighing accuracy is more than adequate to ensure the given composition will be achieved within the implied accuracy. Melts were prepared by first melting the Pb in a stainless steel crucible at about 400°C, deoxidizing it thoroughly, adding the Sb and immersing it to coat it with Pb, and covering the crucible with graphite and rapidly heating it to approximately 600°C. At this point the balance of the Sb can be quickly dissolved by stirring with a stainless steel rod, and the resulting alloy is quickly quenched by casting it into appropriate molds. This casting is then remelted and recast as required, but these operations can now be conducted at low temperatures, since the alloy melts at 252°C.

Flight Sample Preparation

The flight samples were prepared by remelting at approximately 260°C and recasting the alloy into a bar approximately 1 inch wide by 0.375 inch thick and 6 inches long. This bar was then rolled to achieve an approximately 90% reduction in thickness. In the process, the alloy becomes extremely ductile. The resulting strip is cut into small pieces, and these are hydrostatically compressed to form a cylindrical briquette. This in turn was extruded with a 4.5 to 1.0 extrusion ratio to form a cylinder (with a 0.471 inch diameter) which was approximately 1 foot long. Segments were then sawed from the cylinder to become specimens after the ends were machined with a lathe. Lengths ranged from 0.825 inch to 0.830 inch. Weights and densities were measured and recorded. The specimens were then inserted into the stainless cartridges, the lids were TIG welded into place, the cartridges were evacuated to approximately 1×10^{-4} torr, and the cartridges were sealed off. Upon receipt of the flight specimen from SPAR I, the cartridge was carefully sawed open, and the specimen was weighed and its density was measured.

Ground-Based Sample Preparation

Ground-based samples were prepared using a number of different quench methods on specimens of the same size and shape as the flight specimens, except these specimens were instrumented with thermocouples. The methods are listed and described as follows:

Quench Method 1 — The melt is contained in a stainless furnace cartridge and is allowed to solidify while totally surrounded with insulating refractory brick.

Quench Method 2 — The melt is contained in a stainless furnace cartridge and is allowed to solidify while resting in quiescent air on top of a refractory brick.

Quench Method 3 — The melt is contained in a small graphite crucible and is allowed to solidify as water is poured into a bowl containing the crucible.

Quench Methods 4 and 5 — The melt is contained in a small graphite crucible and is allowed to solidify as high pressure air is blown around the crucible.

Two additional quench methods were employed to prepare ground-based specimens that were not instrumented with thermocouples and not used in mechanical testing, but were used as a source of microstructures for comparison. These final two are listed as follows:

Quench Method 6 — The melt is contained in a very thin walled graphite crucible and is allowed to solidify as the crucible is quickly thrust into a bowl of water.

Quench Method 7 — The melt is not contained in a crucible, but droplets of alloy are permitted to fall into a bowl of water.

Each of the quench methods which employed a thermocouple can be characterized by some quench rate information as follows:

Quench Method 1 — 220 sec thermal arrest, approximately 0.5°C/sec drop before and after arrest.

Quench Method 2 — 150 sec thermal arrest, approximately 1.0°C/sec drop before and after arrest.

Quench Method 3 — No discernible arrest, average rate of approximately 20°C/sec.

Quench Methods 4 and 5 — No discernible arrest, average rate of approximately 3°C/sec.

Finally, it can be assumed that the quench rates corresponding to quench methods 6 and 7 are much higher.

Specimen Sectioning and Metallography

After removing the stainless steel can, a longitudinal plank to be used in the resistivity measurements was sliced off the Pb-Sb cylinder with a thin (0.018 inch) slotting saw. The cut was defined by a chord 0.100 inch from the cylinder exterior, resulting in a 0.080 inch maximum thickness plank (Fig. 1). To define the tensile specimen gage section, two longitudinal slots, 180° apart, were machined with a 0.1875 inch diameter end mill that had rounded corners. The result is shown in Figure 2. Transverse slices with the thin slotting saw

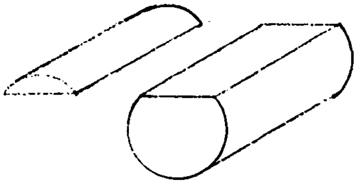

Figure 1. Resistivity slice.

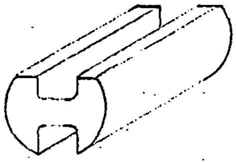

Figure 2. Machining gage section.

then produced the tensile specimen wafers, approximately 0.070 inch thick. The final test specimen is shown in Figure 3. The gage length of the wafer specimens, as defined by the straight portion of the machined opening, was 0.120 inch. The gage width varied from 0.115 inch to 0.143 inch among all the test specimens.

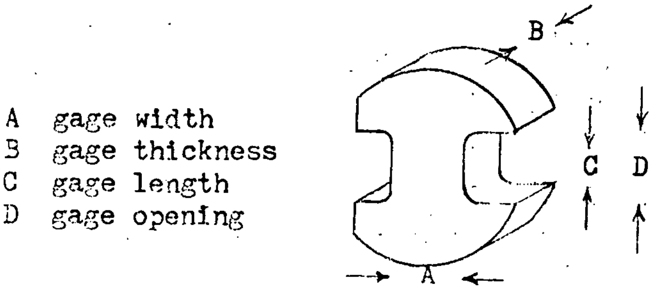

Figure 3. Final test specimen.

The machining procedure for the ground-based specimens was the same as for the flight specimens. All but one of the ground-based specimens (F2) were different in that the upper half of each cylinder (containing thermocouple wires) was cut off as the first step. Identification of the wafers from each cylinder was achieved using a numbering system as shown in Figure 4. The wafers were numbered consecutively, beginning with 1, from the uppermost (relative to gravity) slice from the ground-based cylinders and from an assigned end of the flight cylinders. It should be noted that at the ends of each cylinder, typically a very thin wafer is cut to provide an initial parallel surface. Hence, for example, wafer 2 is the first flight tensile wafer.

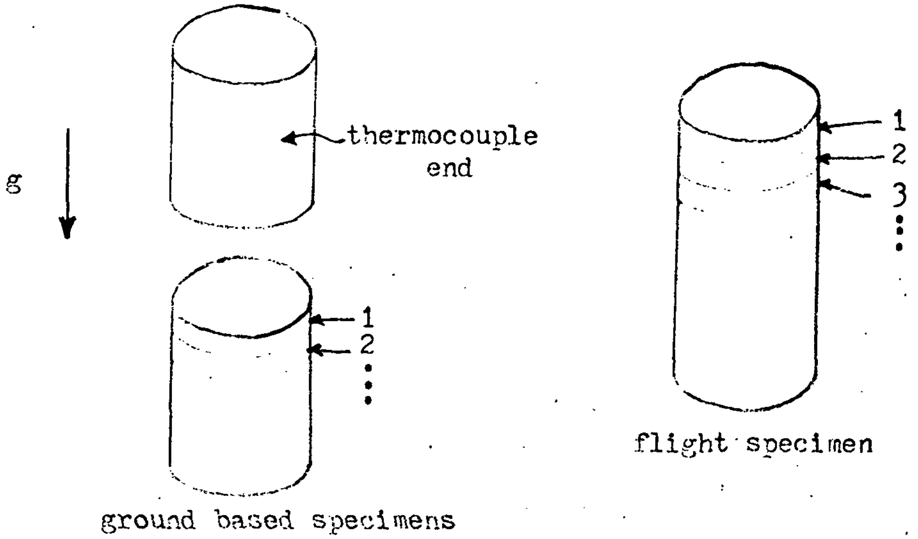

Figure 4. Identification of tensile wafers.

The faces of each wafer were then ground by hand on silicon carbide papers, finishing with a 600 grit paper. One face of each specimen was then polished for metallographic inspection. A coarse polish was achieved on wet Buehler microcloth which was covered with a thick paste of levigated (15 micron) alumina and water. Using one fingertip to hold the specimen with moderate pressure on the stationary polishing cloth, the specimen was rotated in 2 inch circles for approximately 3 to 5 minutes. Following a water rinse, the specimen was ready for final polishing on wet microcloth on top of flat glass with a thick paste of Linde B alumina (0.5 micron) and water. Approximately 5 milliliters of fresh etchant (1 part ammonium hydroxide, 2 parts 3% hydrogen peroxide, and 3 parts water) were added to the paste before the actual polishing of each specimen. Polishing was achieved as with the coarse polishing for approximately 2 to 5 minutes. Immediately after rinsing the specimen with water, the specimen was dried with a blast of nitrogen gas.

Mechanical Testing

To justify the assertion that tensile tests of specimens with these unorthodox dimensions would produce meaningful data, preliminary testing was made of lead-tin eutectic alloy. Two mechanical states of Pb-Sb were tested: 40% rolled reduction in thickness, and greater than 88% reduction in thickness by rolling. The latter material exhibits superplasticity at crosshead rates of near 0.01 cm/min. The tensile specimens were approximately the same size and shape as those later tested in the lead-antimony study, and the specimen grips, testing machine, and crosshead rate were also the same. In the lead-tin tests, the greater than 88% rolled material produced elongations from 1200% to 1800%, while the 40% rolled material elongated no more than 500%. This demonstrates the sensitivity of the mechanical test to material properties.

The tensile tests were performed on a two screw testing machine with a constant crosshead rate. All tests were completed at a crosshead rate of 0.009 cm/min. A total of 50 specimens were tested. The testing temperature was room temperature.

The specimen grips utilized sliding, tapered clamps producing a wedge effect to hold the thin, soft specimens (Fig. 5). Loads were determined by a bending beam load cell connected in series with the grip system. Output of the beam strain gages was monitored at timed intervals on a Vishay/Ellis 10 Portable Strain Indicator. Dead weight loading was used to calibrate the system to within 0.25 pound. In addition to load-time information, a specimen total elongation was measured after rupture. The two pieces were fitted back together and the gage opening, previously defined by the milling operation, was measured at both sides with a vernier caliper while viewing at 7X through a stereo microscope. Elongation values could not be taken from crosshead displacements because the wedge grips operate with varying amounts of movement before positively gripping each specimen.

Resistivity

Resistivity measurements will be postponed until the specimens from SPAR II are available for measurement.

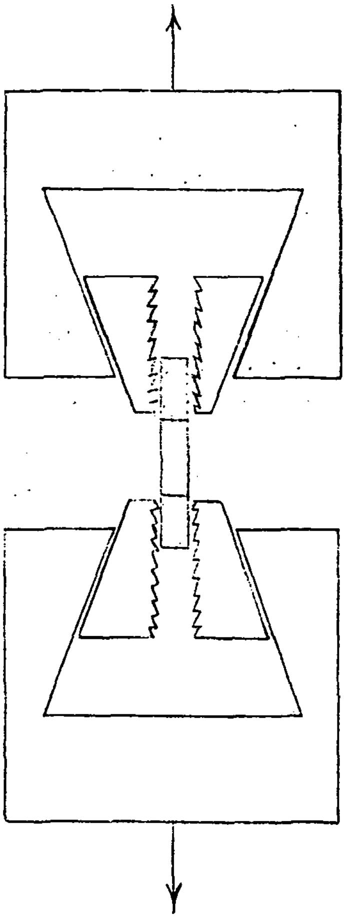

Figure 5. Specimen wedge grips.

OBSERVATIONS AND DATA

Mechanical Testing Data

A total of 50 tensile tests were conducted, 9 of which were specimens from the flight sample. Some of the resulting data for each test is listed in the appendix. Figure 6 shows peak stress versus strain at fracture for all the tests. It is to be noted that the peak stress is essentially constant regardless of the elongation (or strain) exhibited at fracture. This means the modulus of toughness (or the area under an individual stress-strain curve) is essentially directly and linearly proportional to the ductility for all tests. It is also true

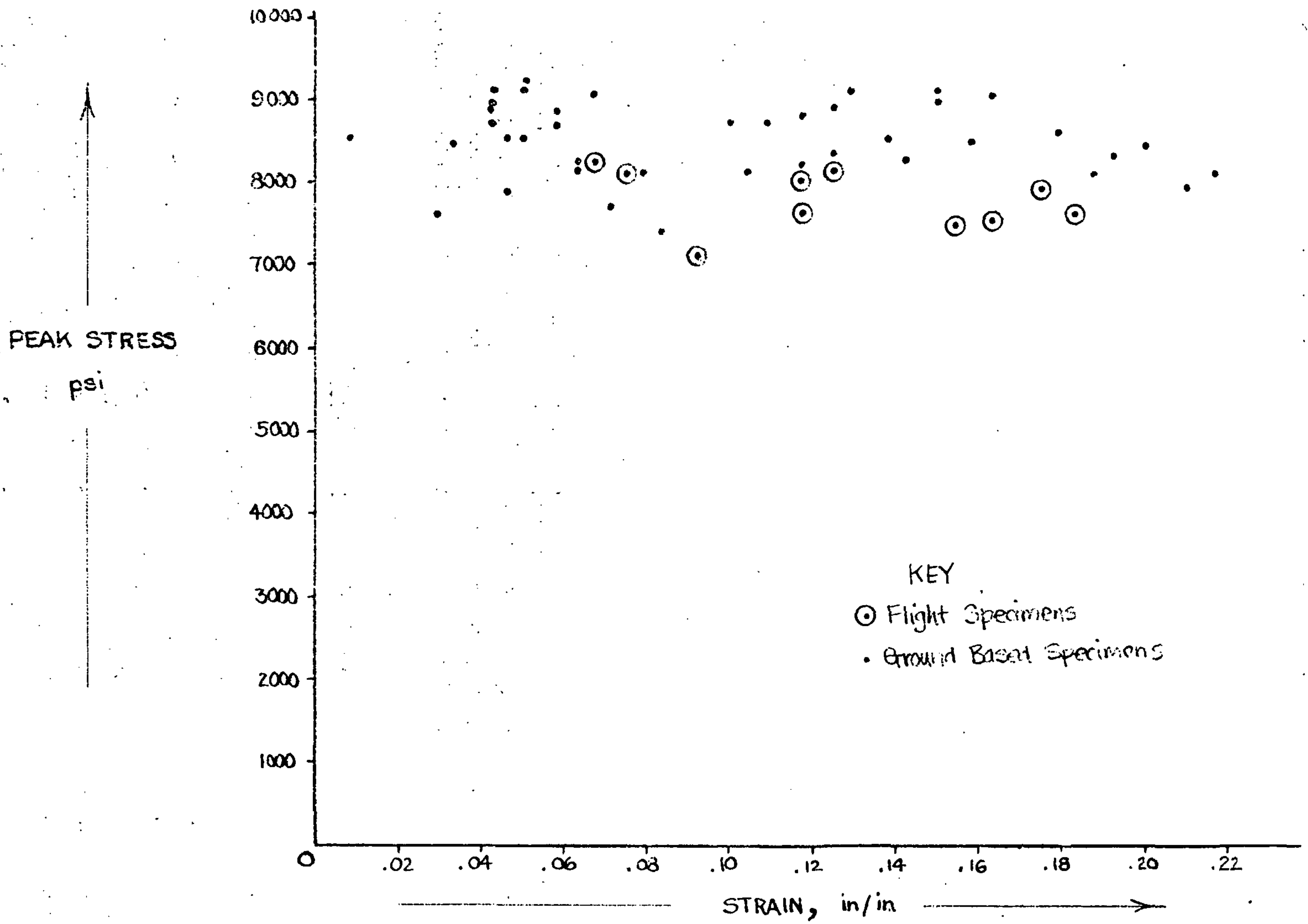

Figure 6. Peak stress versus strain at fracture.

that almost all the ground-based specimens from quench methods 3, 4, and 5 are more ductile than ground-based specimens from quench methods 1 and 2. This can be seen from the data in the appendix. It should also be noted that the mechanical properties of the flight specimens are well bracketed by the ground-based specimens.

Microstructural Observations

Approximately 450 photomicrographs were taken of ground-based and flight specimens. In these photomicrographs, the lead phases are dark and the antimony phases are light, as a result of the etching procedure used. The following paragraph contains several pertinent observations.

In general, the microstructures could be placed into three categories: (1) those with coarse eutectic structures and wide primary lead dendrites, (2) those with fine eutectic structures and wide primary lead dendrites, and (3) those with fine eutectic structures and very fine slender primary lead dendrites. The terms "wide" and "fine," although subjective, refer to the dendrite appearance at 255X. The flight specimens and a few ground-based specimens tended to fit in category (2), although such a classification is subjective and not in keeping with the principles of good quantitative metallography. Ten of the remaining specimens tended to fit into category (3), and these are indicated in the appendix. The balance belong to category (1).

Figures 7 through 10 show a comparison of the effects of quench method on microstructure. The photomicrographs are all taken at 255X.

Figures 11 through 14 show lower magnification composites of nearly the entire gage section of specimens for each quench method. The magnification is 64X.

Figures 15 and 16 show 64X and 255X photomicrographs, respectively, of one of the flight specimens (U7).

Figures 17, 18, and 19 show blocky primary antimony crystallization products either alongside or within the midst of primary lead dendrites. (The antimony is the white phase, and the lead is the dark phase.) The magnification is 255X.

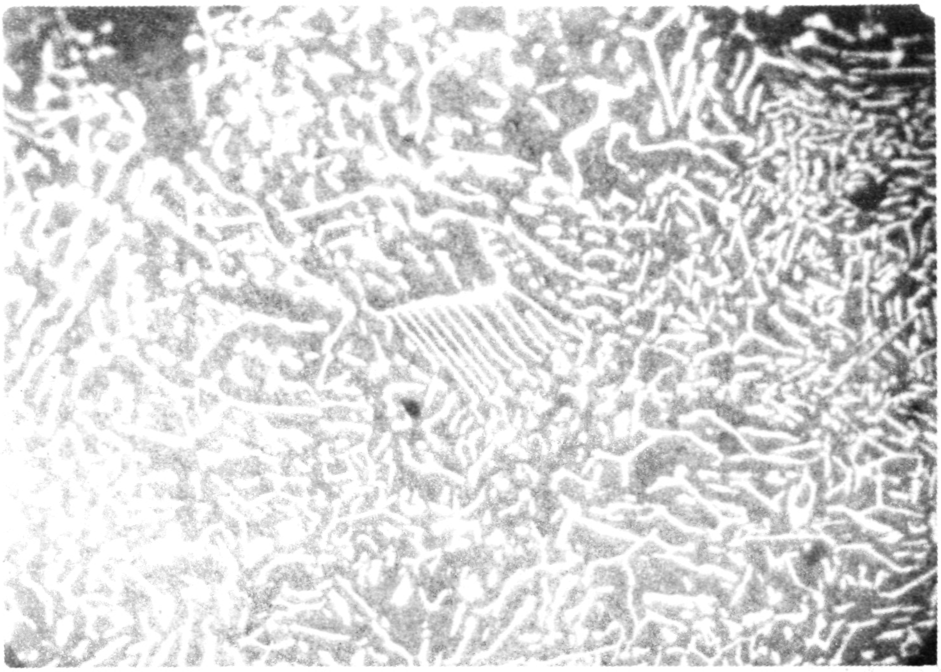

Figure 7. Specimen A15, quench method 1, 0.5°C/sec quench rate.

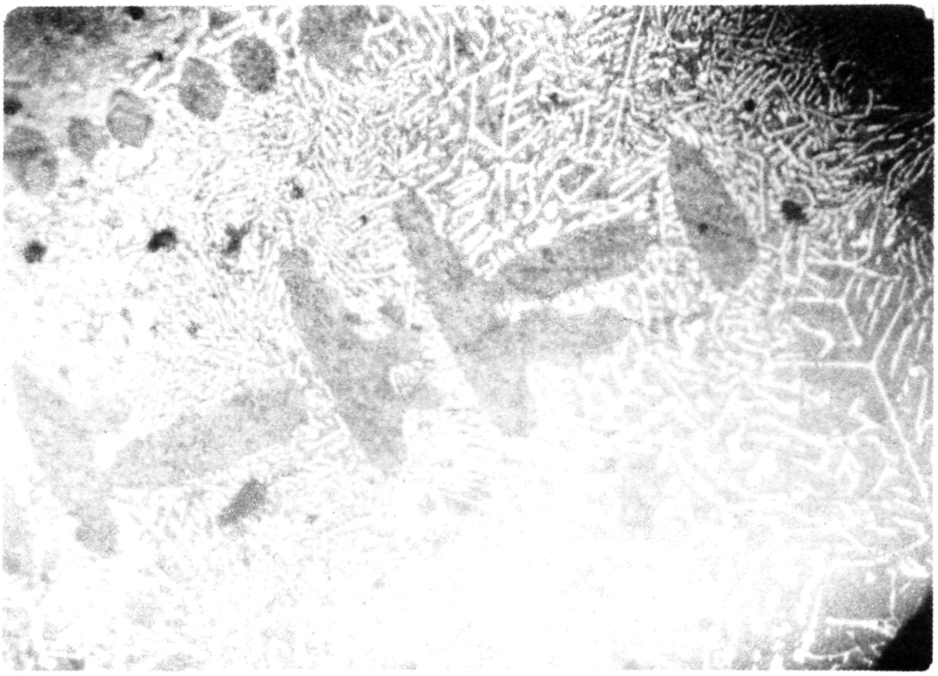

Figure 8. Specimen C22, quench method 2, 1°C/sec quench rate.

Figure 9. Specimen C45, quench method 4, 3°C/ sec quench rate.

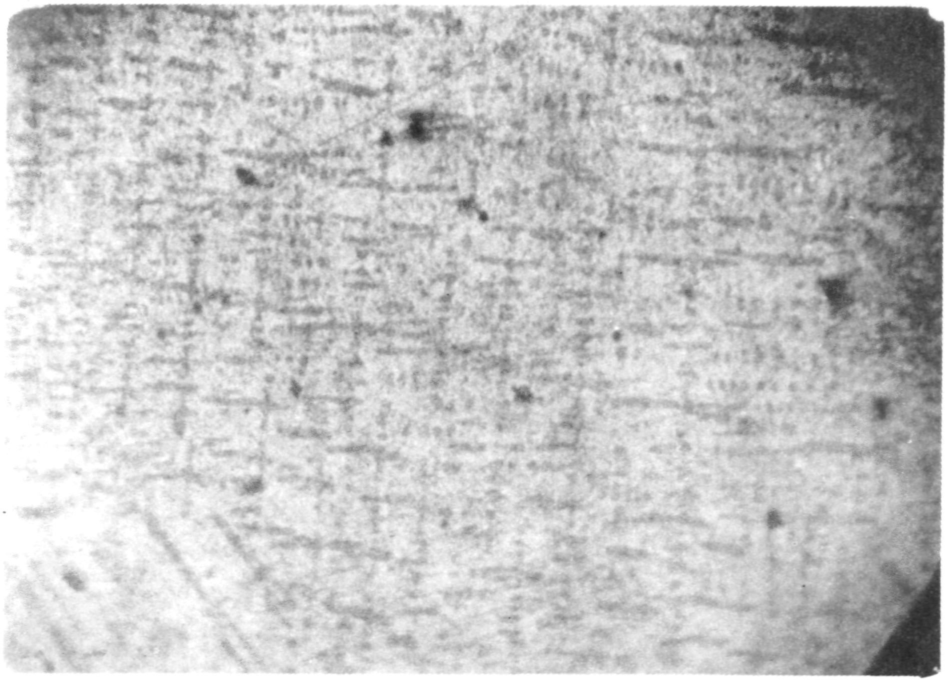

Figure 10. Specimen C35, quench method 3, 20°C/ sec quench rate.

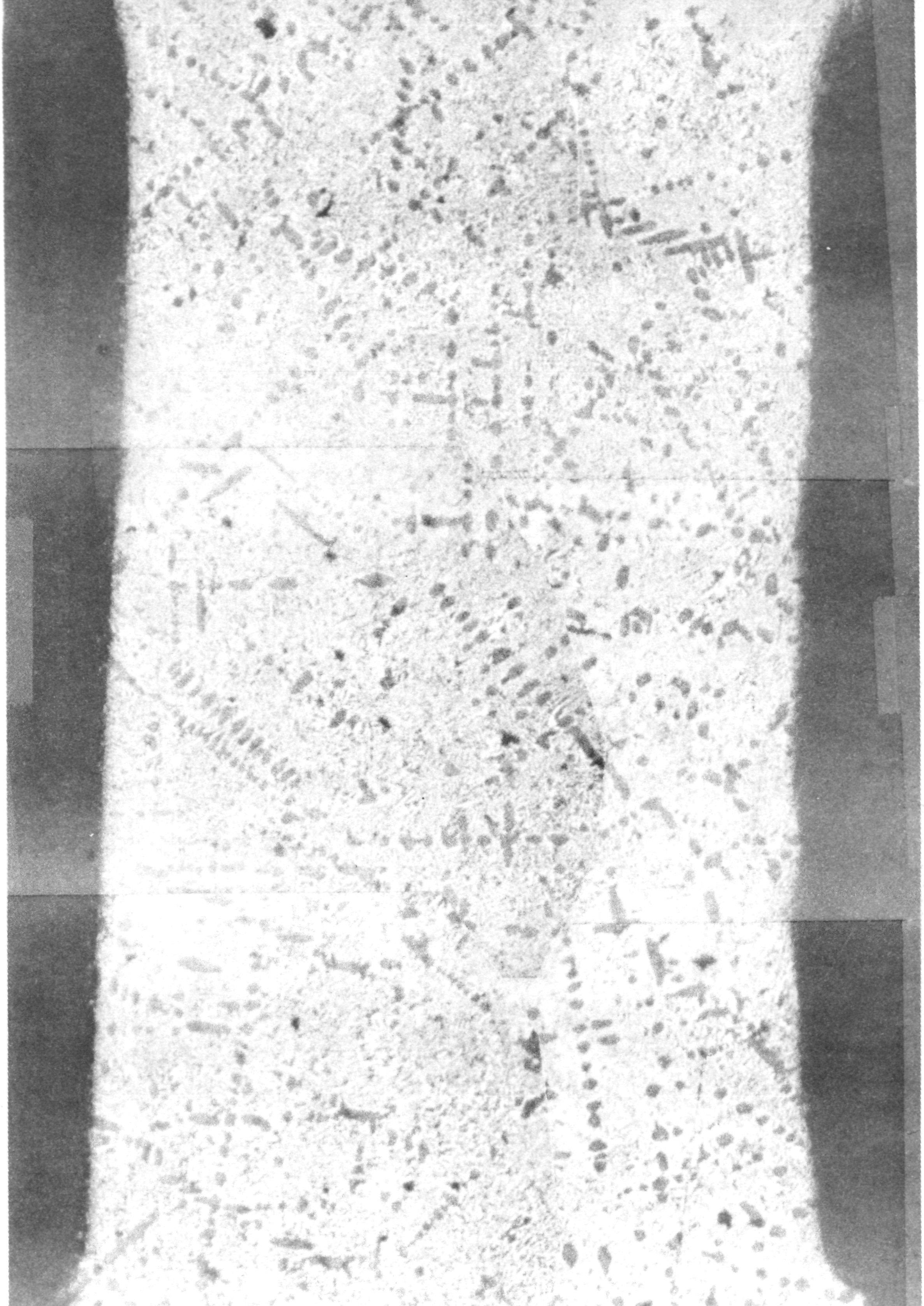

Figure 11. Specimen C15, quench method 1, 0.5°C/sec quench rate.

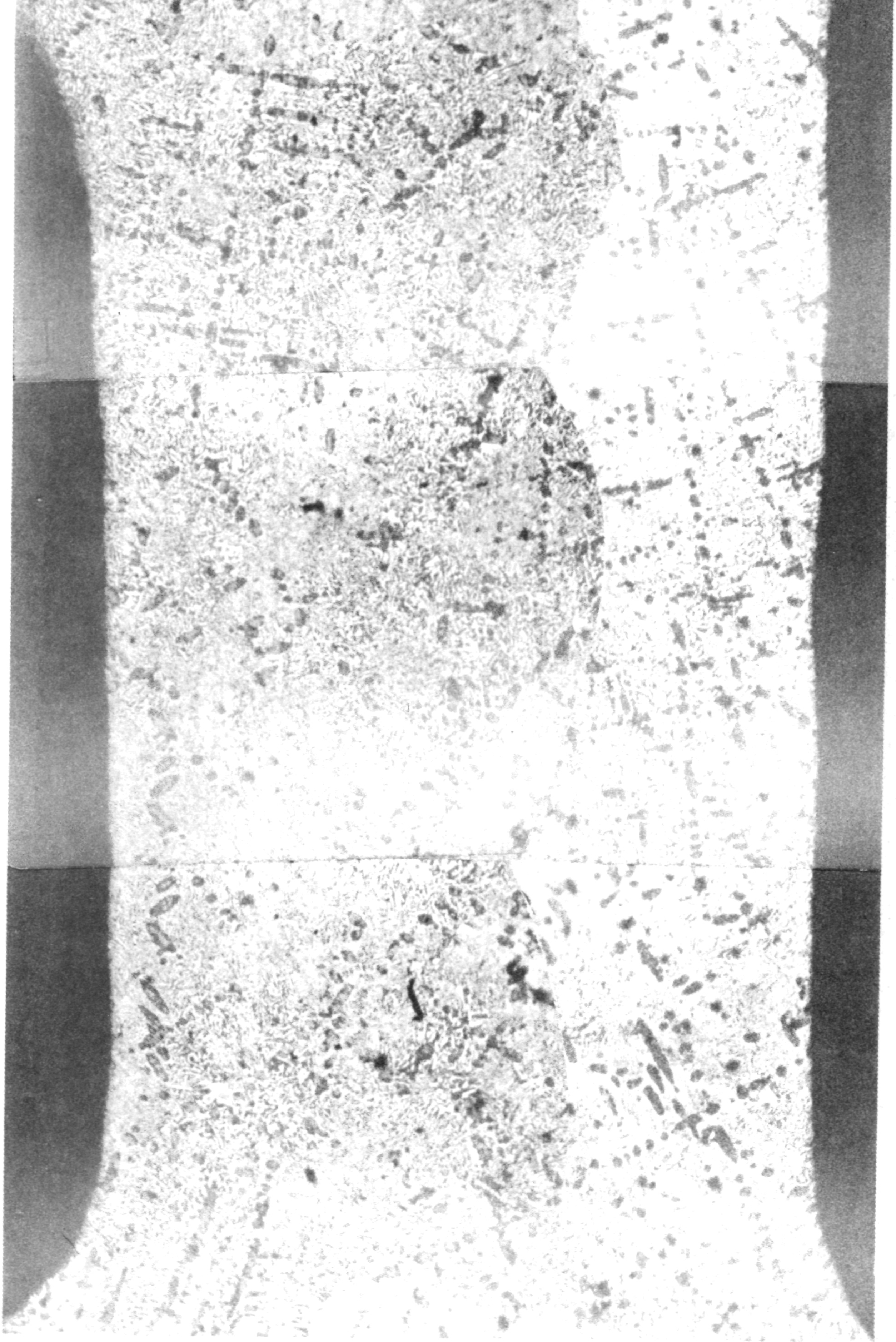

Figure 12. Specimen C23, quench method 2, 1°C/sec quench rate.

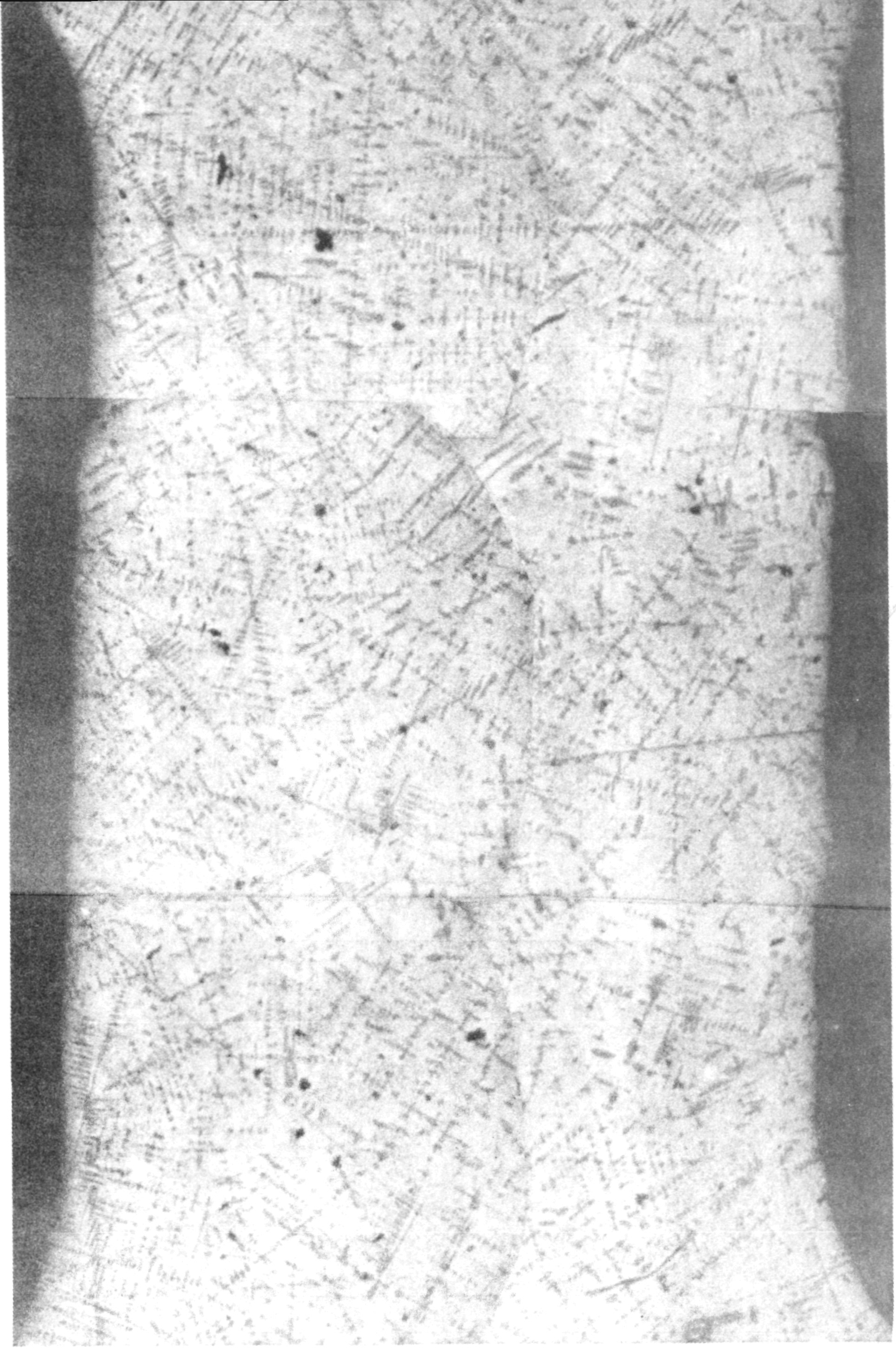

Figure 13. Specimen C45, quench method 4, 3°C/sec quench rate.

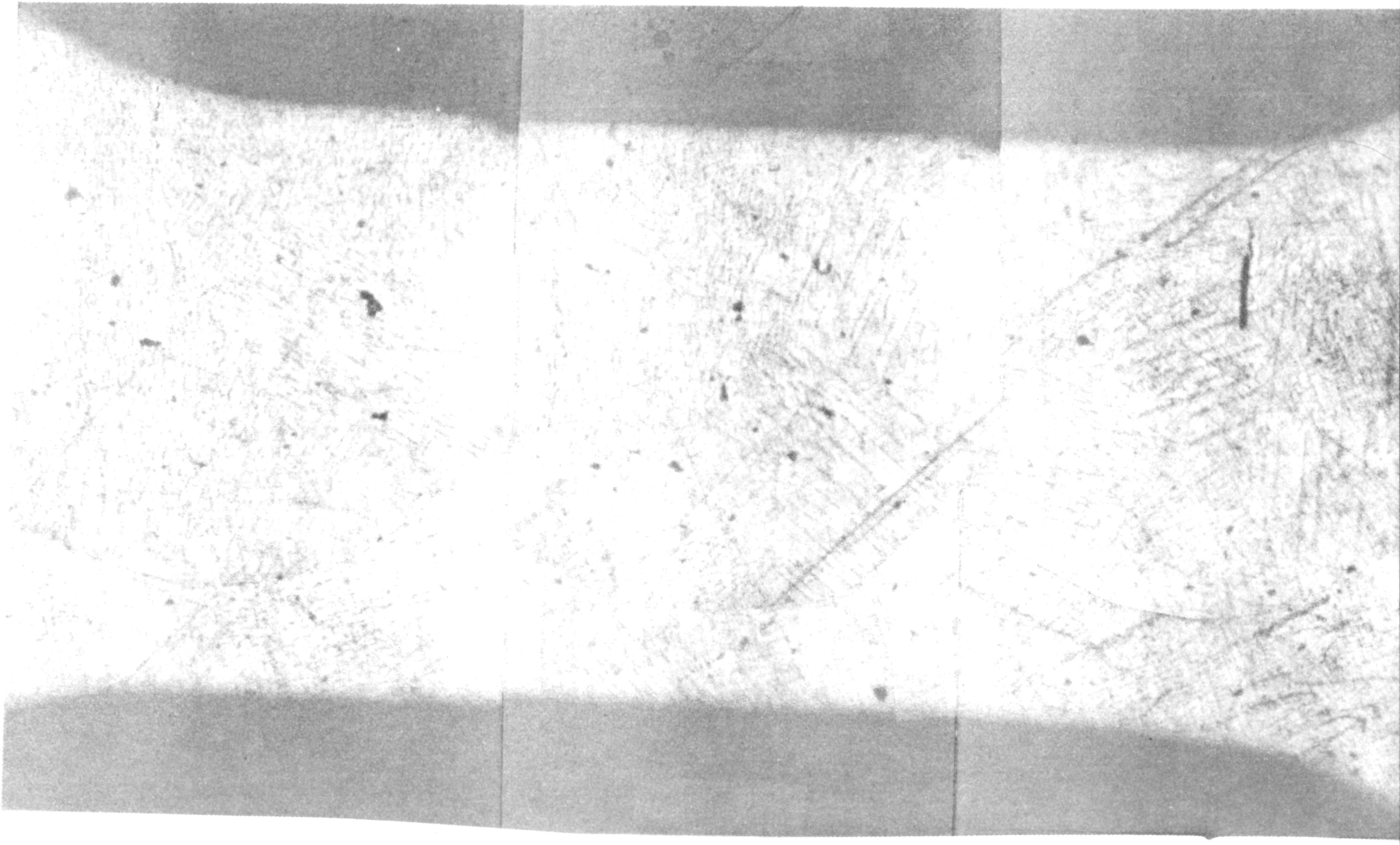

Figure 14. Specimen C35, quench method 3, 20°C/ sec quench rate.

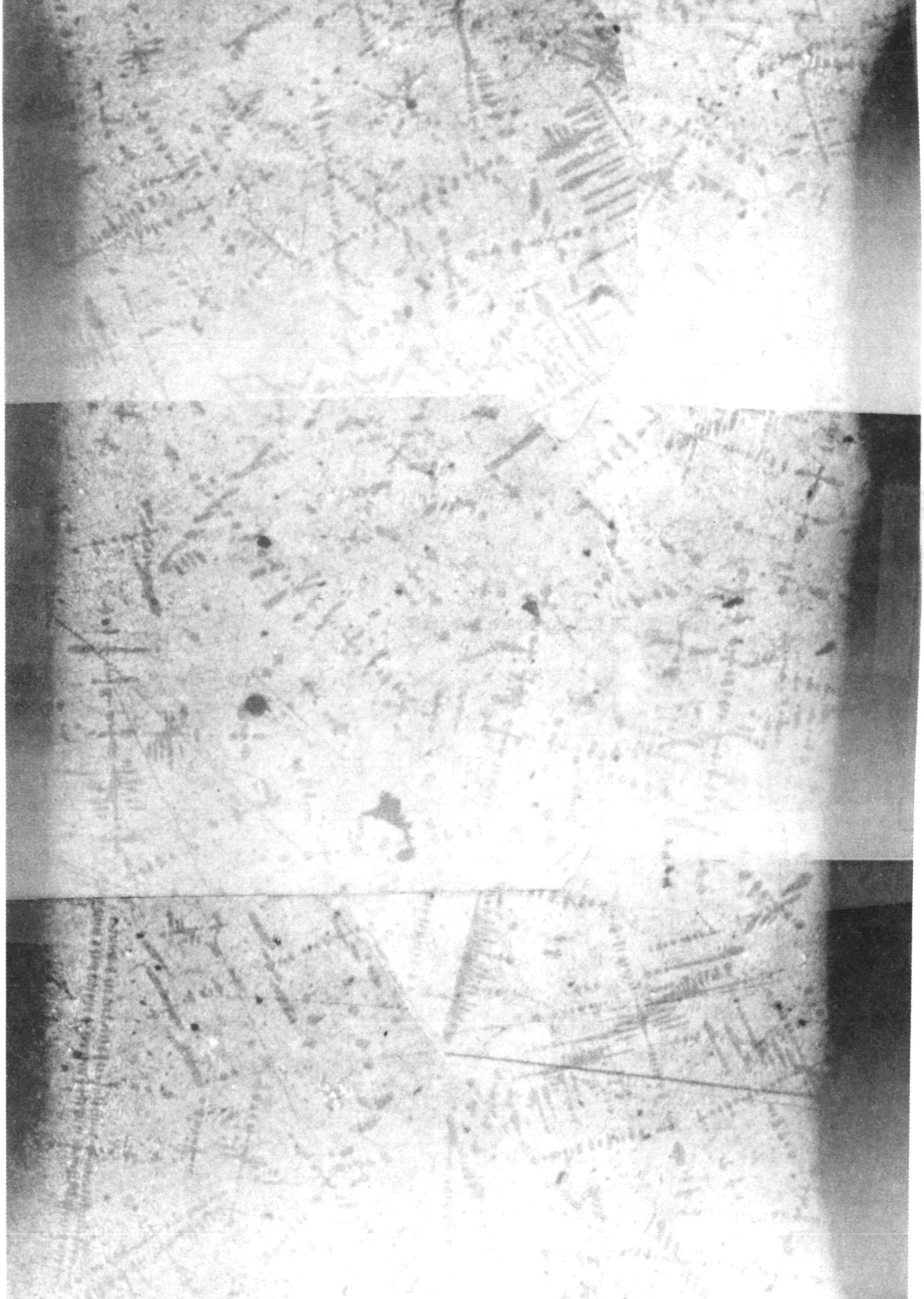

Figure 15. Flight specimen U7.

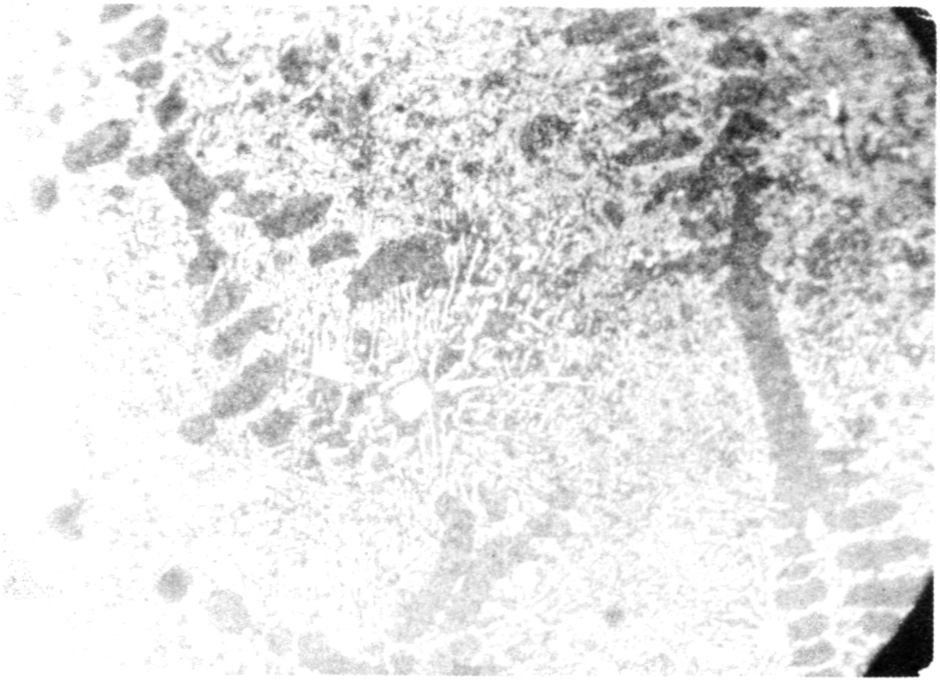

Figure 16. Flight specimen U7.

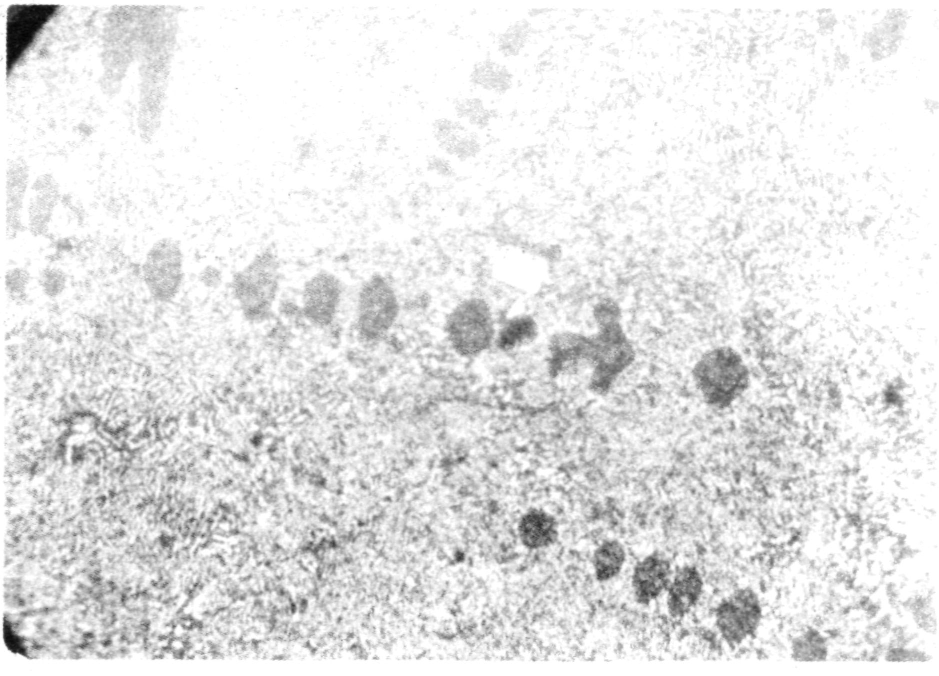

Figure 17. Flight specimen U7, dual primary crystallization products.

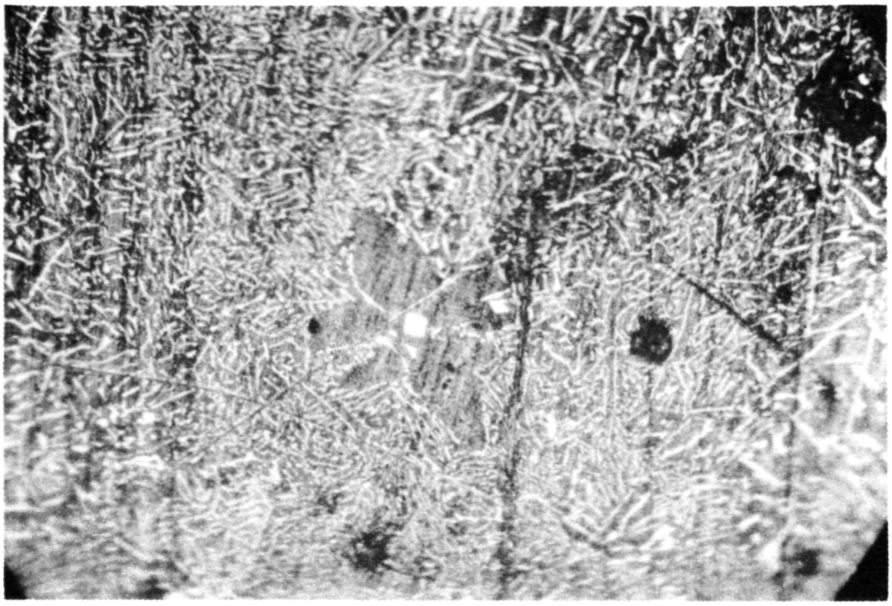

Figure 18. Specimen A12, dual primary crystallization products.

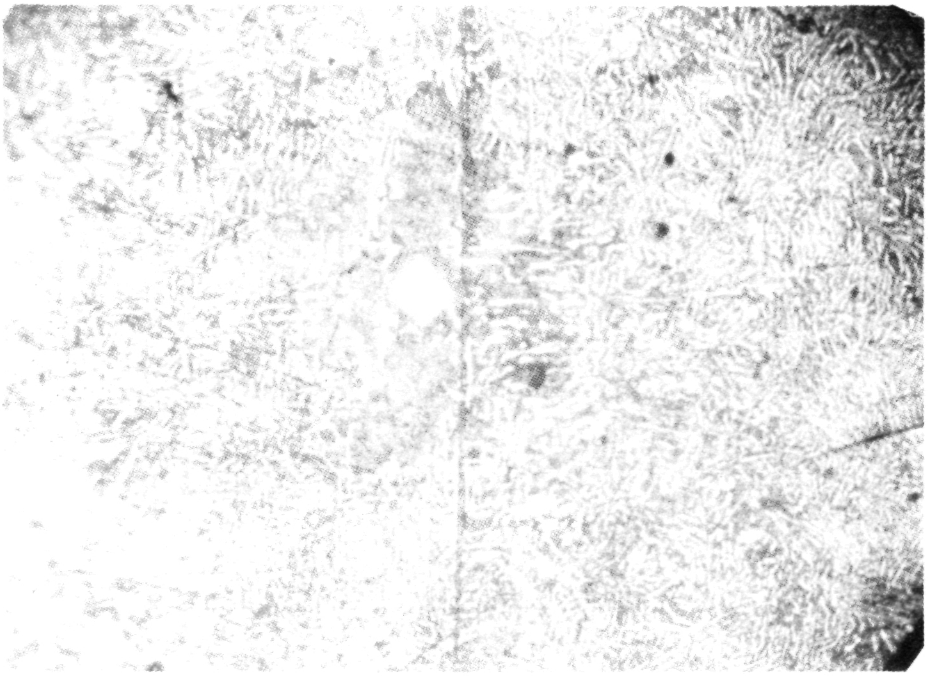

Figure 19. Specimen A12, dual primary crystallization products.

Figure 20 shows a 300X photomicrograph of the specimen prepared by quench method 6. The specimen was prepared with the same metallographic procedure as all the other specimens. The white phase is again antimony, except this time the antimony appears as dendrites, and no lead dendrites are present.

Figure 20. Specimen C6, quench method 6.

Finally, no microstructures could be resolved in the specimen prepared by quench method 7. They are too fine for our techniques to resolve.

DISCUSSION OF OBSERVATIONS

Mechanical Properties Versus Microstructure

Approximately 425 of the photomicrographs of the tensile specimens were closely examined using standard methods of quantitative metallography (both 255X and 64X). The average dendritic arm spacing was determined for the lead dendrites in each specimen. The results are listed in the appendix and are shown in Figure 21 in which the arm spacing is plotted versus ductility. There is a correlation between the two, although there is much scatter in the data. It is to be noted that the flight specimens do not stand apart in the plot.

Additionally, a characteristic eutectic lamellar spacing was determined for a number of specimens (but not all) using statistically valid methods of quantitative metallography. The results are listed in the appendix and are shown in Figure 22 as a plot of lamellar spacing versus ductility. Here again a correlation exists although the data show scatter, and the flight specimens do not stand apart from the ground-based specimens.

It should be pointed out that both Figures 21 and 22 show parameters proportional to solidification rate plotted versus ductility.

Figures 17, 18, and 19 (and even 16) showed blocky white antimony primary crystallization products either adjacent to or within primary lead crystallization product. This is not possible if one is to believe that the solidification process is governed by the equilibrium diagram for Pb-Sb. It is to be noted that the phenomenon occurs in both flight and ground-based specimens.

Finally, the fact that Figure 20 shows primary antimony dendrites occurring at very high quench rates shows that as quench rate is increased, the microstructure changes from one with primary lead dendrites to primary antimony dendrites. It must be emphasized this is accomplished with material from the same melt.

TENTATIVE CONCLUSIONS

These conclusions must be tentative since they depend upon the results of the off-eutectic alloys study to be conducted in SPAR II.

First, it has been found that the ground-based specimens have bracketed the SPAR I flight specimen with respect to mechanical and microstructural properties and that there is no classification with respect to these properties that sets the SPAR I flight specimen apart from the ground-based ones. There is no discernible difference between them.

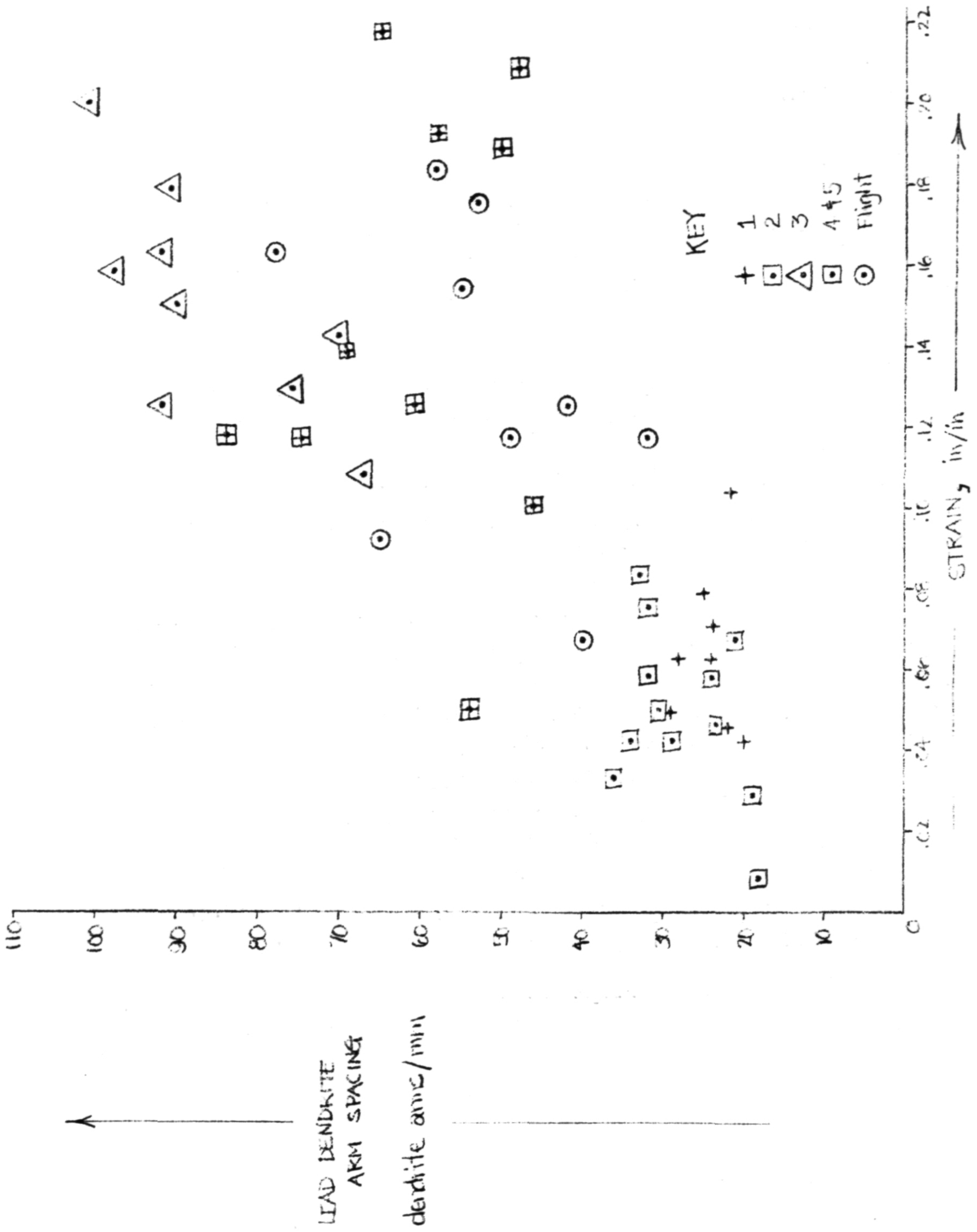

Figure 21. Lead dendrite arm spacing versus ductility.

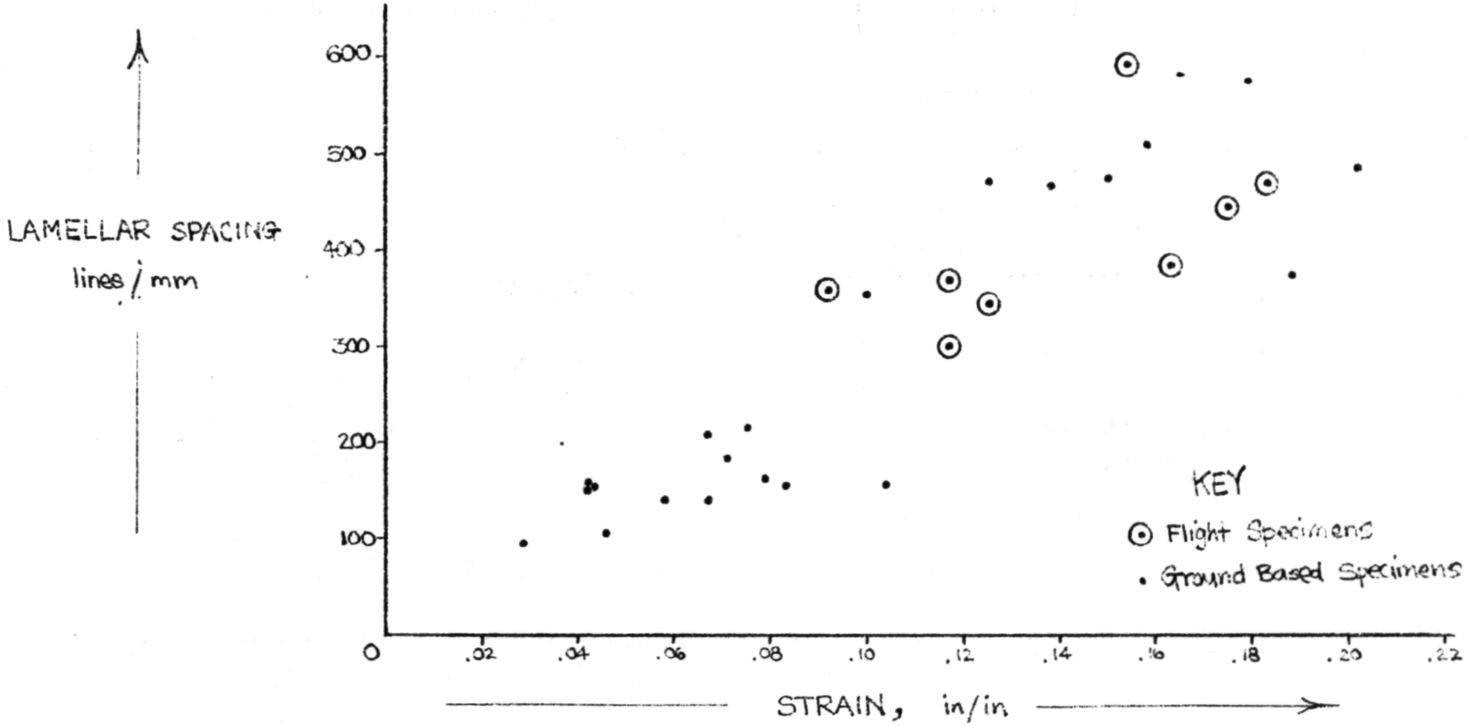

Figure 22. Eutectic lamellar spacing versus ductility.

Secondly, the eutectic composition in both the flight specimen and ground-based specimens has apparently been shifted because of supercooling at the solidification rates involved, but this shift is not clearly defined because of the presence of dual primary crystallization products. The occurrence of the latter is not possible according to the equilibrium diagram.

Thirdly, it has been observed that an increase in solidification rate in ground-based specimens can cause primary lead dendrites to be replaced by primary antimony dendrites without a change in composition.

APPENDIX

MECHANICAL AND MICROSTRUCTURAL DATA

Specimen No. Code: XYZ X = melt, Y = quench method, Z = wafer number (Fig. 4).

Melts A, C, and F all ground-based; U, flight samples

Specimen Number	Peak Stress, psi	Elongation (Δl), in.	Strain, in./in.	Dendrite, Arms/mm	Lamellar Spacing, Lines/mm
C23	8560	0.001	0.008	18	
C22	7610	0.0035	0.029	19	98
A24	8470	0.004	0.033	36	
C15	8970	0.005	0.042	20	152
A25	9130	0.005	0.042	29	154
F29	8730	0.005	0.042	34	153
F27	8930	0.005	0.042		
A15	8540	0.0055	0.046	22	106
F28	7920	0.0055	0.046	23	
A53	9120	0.006	0.050	54	
A13	8540	0.006	0.050	29	
F23	9240	0.006	0.050	30	
C24	8880	0.007	0.058	24	
A23	8710	0.007	0.058	32	140
A14	8270	0.0075	0.063	28	
C14	8160	0.0075	0.063	24	
C25	9070	0.008	0.067	21	140
U8	8270	0.008	0.067	40	209
C12	7720	0.0085	0.071	24	183
F24	8130	0.009	0.075	32	215
A12	8120	0.0095	0.079	25	162
F22	7420	0.010	0.083	33	155
U3	7130	0.011	0.092	65	360
A52[a]	8750	0.012	0.100	46	356
C13	8150	0.0125	0.104	22	158
A33	8760	0.013	0.108	67	
A54[a]	8830	0.014	0.117	75	

Specimen Number	Peak Stress, psi	Elongation (Δl), in.	Strain, in./in.	Dendrite, Arms/mm	Lamellar Spacing, Lines/mm
A44	8240	0.014	0.117	84	
U10	8050	0.014	0.117	32	300
U4	7650	0.014	0.117	49	370
C31[a]	8920	0.015	0.125	92	471
A43	8360	0.015	0.125	61	
U9	8160	0.015	0.125	42	346
A32[a]	9140	0.0155	0.129	76	?
A55[a]	8560	0.0165	0.138	69	468
C34[a]	8310	0.017	0.142	70	
C32	9150	0.018	0.150		
A34[a]	9020	0.018	0.150	90	475
U5	7510	0.0185	0.154	55	593
C35[a]	8530	0.019	0.158	98	510
C33	9080	0.0195	0.163	92	
U2	7590	0.0195	0.163	78	384

Specimen Number	Peak Stress, psi	Ductility, (Δl), in.	Strain, in./in.	Dendrite, Arms/mm	Lamellar Spacing, Lines/mm
U7	7960	0.021	0.175	53	443
A36[a]	8630	0.0215	0.179	91	575
U6	7660	0.022	0.183	58	470
C42	8130	0.0225	0.188	50	376
C43	8360	0.023	0.192	58	
A35[a]	8500	0.024	0.200	101	
C45	7960	0.025	0.208	48	485
C44	8130	0.026	0.217	65	

a. "Fine" dendrites, category (3); see "Microstructural Observations."

REFERENCES

1. Blumenthal, B.: Trans. AIME, vol. 156, 240, 1944.

2. Metals Handbook. 8th Ed., vol. 1, 53, Am. Soc. for Metals, Metals Park, Ohio, 1961.

3. Varich, N. I. and Yakunin, A. A.: The Solubility of Cd, Mg, Sb, and Sn in Pb on Quenching the Alloys from the Liquid State. Russian J. Phys. Chem., vol. 41, 437, 1967 (From Zhur. Fiz. Khim. vol. 41, 844, 1967.

4. Borromeé-Gautier, C.; Giessen, B. C.; and Grant, N. J.: Metastable Phases in the Pb-Sb and Pb-Bi Systems. J. Chem. Phys., vol. 48, 1905, 1968.

5. Ramachandrarao, P.; Garg, P. K.,; and Anantharaman, T. R.: Rapid Quenching of Liquid Pb-Sb Alloys. Indian J. Technol., vol. 8, 263, 1970.

6. Hollomon, J. H. and Turnbull, D.: Progress in Metal Physics. Vol. 4, 356, Bruce Chalmers, ed., Pergamon Press, London, 1953.

CHAPTER II

FEASIBILITY OF PRODUCING CLOSED-CELL METAL FOAMS IN A ZERO-GRAVITY ENVIRONMENT FROM SPUTTER-DEPOSITED INERT GAS-BEARING METALS AND ALLOYS

Experiment 74-10

By

J. W. Patten and E. N. Greenwell

Battelle-Northwest Laboratories

ABSTRACT

This report describes work on SPAR Flight No. 1 directed towards demonstrating the feasibility of producing closed-cell metal foam in a zero-gravity environment from sputter-deposited inert gas-bearing metals and alloys. A new furnace design was developed and used for this program, along with an associated fully automatic electronic control package. Metal foams were successfully produced in this furnace both on the ground and in SPAR Flight No. 1 (zero-gravity). These samples were evaluated by quantitative metallographic techniques. The resulting data together with time-temperature data acquired during the furnace experiments and data acquired from SPAR Flight No. 2 are expected to reveal some of the effects of gravity on formation of metal foams and the potential for variation in foam structure.

SUMMARY AND CONCLUSIONS

This report describes technical results obtained on the first SPAR flight (December 1975) from experiment 74-10, "Feasibility of Producing Closed-Cell Metal Foams in a Zero-Gravity Environment from Sputter-Deposited Inert Gas-Bearing Metals and Alloys."

The long-range objective of this program is to produce metal foam materials from sputtered metal deposits. It is anticipated that these foams will be produced with a wide range of preselected and reproducible densities and uniform, isolated, evacuated cells. It is further anticipated that the foams will be produced from a wide range of metallic materials and in complex shapes usable in engineering applications.

The work required to achieve this objective was divided into feasibility, experimental scale-up, and fabrication of application prototype phases. The current program is concerned with the feasibility phase.

A new furnace design was developed along with an associated fully automatic electronic control package. Operation during ground-based testing and SPAR Flight No. 1 was fully satisfactory.

All of the minimum success criteria for SPAR Flight No. 1 were met and metal foam materials have now been produced both on Earth and in a zero-gravity environment. Data were produced which, in combination with data from SPAR Flight No. 2, are expected to reveal some of the effects of gravity on formation of metal foams. The data also indicate, in a preliminary way, the potential for variation in foam structure.

INTRODUCTION

This report describes technical results obtained on the first SPAR flight (December 1975) from experiment 74-10, "Feasibility of Producing Closed-Cell Metal Foams in a Zero-Gravity Environment from Sputter-Deposited Inert Gas-Bearing Metals and Alloys." This experiment is one of three to be conducted in a 1 year Phase I Feasibility study. It was a very critical experiment since development and operation of a new furnace design with an associated fully automatic electronic control package was required in addition to demonstration of the metal foam formation concept.

Related ground-based experiments are discussed briefly. These will be discussed in more detail in a later report summarizing all results obtained in the Phase I Feasibility Study.

OBJECTIVE

The long-range objective of this program is to produce metal foam materials from sputtered metal deposits. It is anticipated that these foams will be produced with a wide range of preselected and reproducible densities and uniform, isolated, evacuated cells. It is further anticipated that the foams will be produced from a wide range of metallic materials and in complex shapes usable in engineering applications.

The work required to achieve this long-range objective was divided into the three phases listed below. As originally proposed, Phase I was to be completed in the first 2 years. However, at the present time Phase I is scheduled to be completed in the first year in order to aid NASA/MSFC in attaining their flight scheduling objectives. The results of the Phase I experiments will be used to direct the experiments in Phases II and III.

Phase I — Feasibility

A. Produce inert gas-bearing metal sputtered deposits and melt small samples of these deposits in a zero-g environment to produce a foam. Evaluate the effects of gas concentration, melt temperature, and time at melt temperature on foam structure and foaming kinetics. Correlate results with data from similar experiments conducted in a 1-g environment. Formulate a model describing the effects of gravitational fields on the behavior of gases in molten metals. Measure basic physical and mechanical properties of foam samples to predict suitability for engineering applications.

B. Produce hollow right-circular cylinders of inert gas-bearing metal by sputter deposition and melt samples of these deposits in a zero-g environment to produce foamed shapes. Evaluate the feasibility of accurately predicting the shape and dimensions of complex parts formed in this manner.

Phase II — Experimental Scale-Up

A. Investigate zero-g production of more massive foam products from large sections of thick sputtered deposits.

B. Investigate additional metal (or alloy) inert-gas systems.

C. Investigate reproducible production of more complex shapes, including complex curvatures.

D. Investigate forming, cutting, welding, and brazing of metal foams.

Phase III — Fabrication of Prototypic Configurations for a Specific Application

APPROACH

Phase I — Feasibility

A. The first experiments in Phase I were to be conducted in a 1-g environment with the objective of identifying a suitable pure metal and gas combination for further examination. Suitable sputtered deposits from this pure metal and gas system (Al and Ar) were then to be produced for the first series of tests conducted in space. Six of the 1 cm × 0.10 cm × 0.05 cm samples were to be mounted in a quartz fixture with spot-welded thermocouple leads. This fixture was to be mounted in a TCU (Temperature Control Unit) furnace, as provided by NASA/MSFC and modified by BNW, and flown in Flight No. 1. In flight, the samples were to be radiantly heated to a temperature above their melting point, held at this temperature for a time less than 2 minutes, and water quenched. Time and temperature were to be recorded for each sample. The metal foam samples were to be recovered for metallographic examination and measurements of density, cell size and distribution, cell wall thickness, electrical and thermal conductivity, compressive strength, and other properties. It was anticipated that only one metal-gas combination would be used for this first phase. Three gas concentrations were to be investigated. Since duplicate samples were to be exposed to each test condition, a total of 6 samples would be foamed in the zero-g environment and examined for each furnace run.

B. The second series of tests (Flight No. 2) to be conducted in space will use two TCU furnaces similar to the one used in Flight No. 1. These furnaces will contain both flat specimens (as in Flight No. 1) and specimens sectioned from sputter-deposited hollow cylinders. Foam density will be varied by the amount of gas trapped during sputter deposition and the length of time above the sample melting point. The two furnaces in this flight will provide different times above the melting point to supplement data obtained in Flight No. 1. Evaluation will be similar to that conducted on samples from the first flight. The three different times above the melting point will allow an approximate Arrhenius determination of activation energies involved in the foaming process and, perhaps, speculation on the mechanism(s) involved. In addition, changes in sample dimensions and shape will be recorded. Concurrent experiments on similar samples will be conducted in a 1-g environment and results will be compared with results of the zero-g experiments. A model describing the behavior of these metal foams during formation will be formulated. The Phase I experiments will be considered successful if uniform closed-cell metal foams with predictable densities are produced.

Phase II and Phase III — Experimental Scale-Up and Fabrication of Prototypic Configurations for a Specific Application

If the results of Phase I are sufficiently encouraging, specific Phase II and Phase III experiments will be designed to achieve the results outlined in the Objectives section. Since the size and capabilities of the rockets available in 2 to 3 years are in question at this time, it is not possible to specify the extent of the experiments. It is hoped, however, that they will be considerably more ambitious in sample size and complexity than the Phase I experiments.

EXPECTED RESULTS

It is expected that a new class of engineering materials will be produced by these investigations. These materials will be pure metal or alloy closed-cell foams with uniform cell size and wall thickness, and evacuated cell or cells. Good control of foam density and cell size is expected. In addition, it is expected to be possible to accurately foam-produce complex engineering shapes to final dimensions. These foams are expected to be useful in a wide range of structural applications. Additional applications such as hydrogen storage batteries and reactor fuels are also possible.

MATERIALS AND PROCEDURES

Constraints on Experiment Design

Time constraints imposed by the NASA/MSFC request to fly on SPAR Flight No. 1 and the availability of the TCU equipment flown on previous space flights dictated that the initial metal foam experiment be based on the TCU design. This design had several drawbacks, however. It was not equipped to process more than one sample capsule, to measure sample temperature directly or to heat samples above approximately 300°C. It was determined that all of these limitations could be overcome by using only the TCU outer container and water quench apparatus and redesigning all heating elements, heat shields, sample capsules, sample geometry, temperature measurement provisions, and furnace controls. Preliminary calculations indicated that design would be much simplified if the maximum sample temperature sought was less than 1000°C.

Sample Preparation by Sputter Deposition

The pure metal-inert gas system chosen for initial experimentation was Al-Ar. This choice was based on the melting point of Al (660°C, well below the 1000°C equipment maximum temperature), the ready availability of pure Al target material, previously published data on Ar trapping in Al during sputtering [1,2], and the commercial importance of Al.

Four sputter-deposition experiments were conducted with each experiment producing a 12.7 cm (5 in.) diameter disc of sputtered Al. The nominal chemical composition of all deposits is indicated in Table 1. Sputter-deposition parameters, deposit thickness, and Ar content are indicated in Table 2. A schematic illustration of the demountable triode sputtering apparatus used is shown in Figure 1. In operation, the chamber was evacuated to 3×10^{-8} torr to test system integrity. High purity argon was then admitted to the chamber while continuously pumping to maintain a pressure of approximately 6.2×10^{-3} torr. Next a plasma was ignited, and the high purity aluminum substrate on which deposition was to take place was ion-bombardment etched at -100 volts substrate potential and 0.5 amp current for 5 minutes. Potential of the target was then adjusted to -2000 volts, the appropriate bias voltage was placed on the substrate, and the deposition experiment was thus initiated. Upon completing the deposition, the substrate (with deposit attached) was removed from the

TABLE 1. NOMINAL DEPOSIT COMPOSITION*

Element	Concentration (wt%)
Cr	0.01 to 0.1
Cu	0.01 to 0.1
Fe	0.1
Mg	0.001 to 0.01
Mn	0.001 to 0.01
Ni	0.01 to 0.1
Si	0.01 to 0.1
Ti	0.01 to 0.1
V	0.01 to 0.1
Ca	$<$ 0.001

Not Detected

B, Cd, Co, Pb, Mo, Sn, W, Zr, Nb, Ta and Zn

---

*Chemical composition of the deposits was determined by standard analytical techniques and by x-ray fluorescence.

TABLE 2. SPUTTER DEPOSITION PARAMETERS AND RESULTS

Experiment Number	Target Potential (volts)	Target Current (amps)	Substrate Bias (volts)	Substrate Current (amps)	Argon Pressure (x 10^{-3} torr)	Substrate Temperature (^{o}C)	Deposit Thickness (mm)	Argon Content* (ppm)
NASA #1	2000	1.5	Floating	0	6.2	21	0.2	30
NASA #2	2000	1.75	-100	1.9	6.2	21	0.9	231
NASA #3	2000	1.75	- 60	1.75	6.2	21	0.6	23
NASA #4	2000	1.75	-150	1.75	6.2	21	0.6	272

---

*Argon content was measured by vacuum fusion techniques with gas composition measured with a quadropole mass spectrometer.

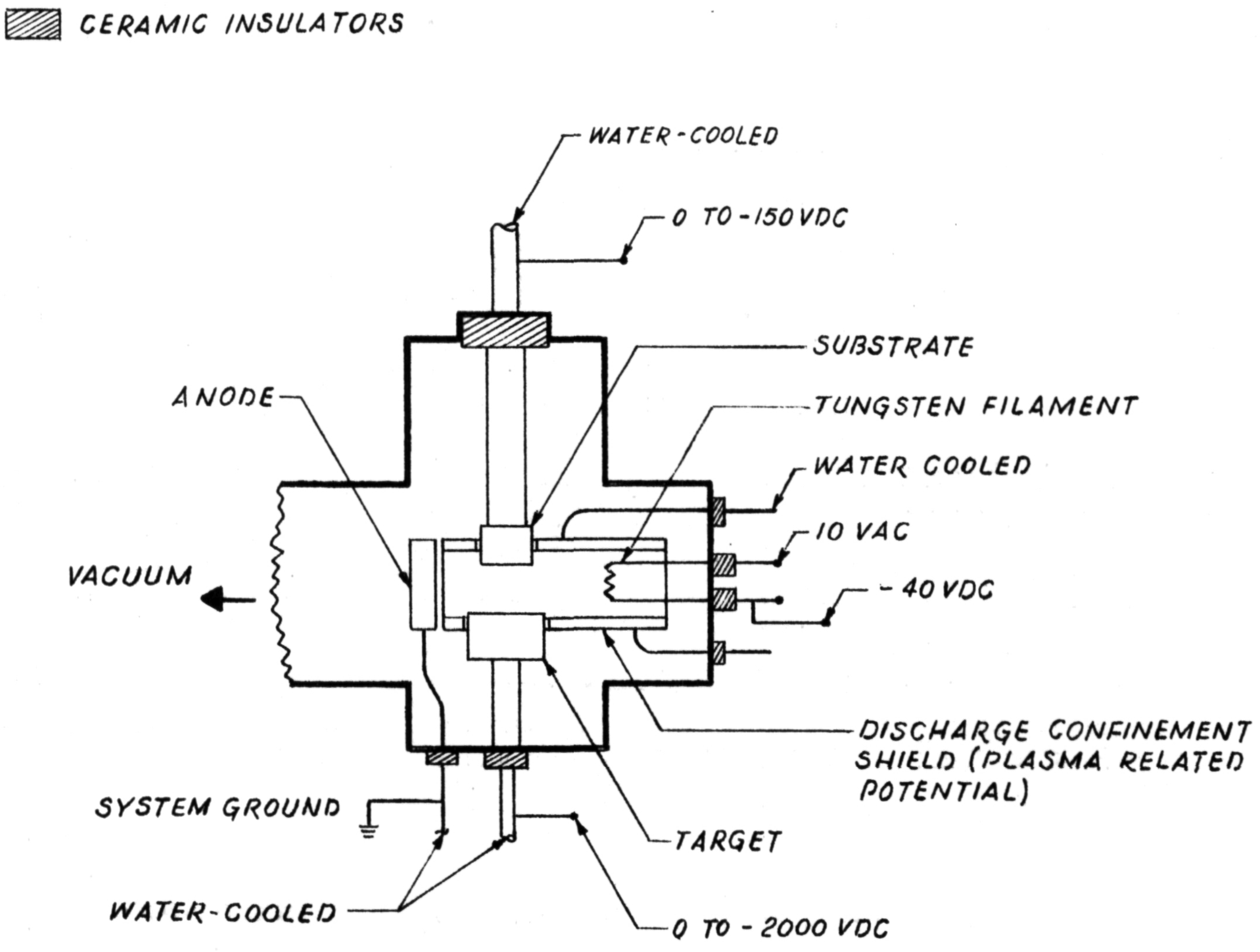

Figure 1. Schematic of sputtering apparatus.

sputtering chamber and machined away from the deposit. No machining lubricant or coolant was used, so that a clean free-standing sputtered disc of Al resulted from each of these four experiments.

Furnace Design

As mentioned earlier, the TCU furnace available was modified for this project. The modifications resulted from several iterations of building and testing, and included provisions to rapidly heat six individually thermocoupled samples to near 1000°C and cool them with a water quench. The resulting design proved to be very reliable. An assembly and testing procedure was developed and is included in its most recent form as Appendix A. Photographs taken at various stages during assembly are also included in Appendix A.

Details of the design modifications are included in Battelle Drawings R-2160, Sheet 1, Rev. 2 and Sheet 2, Rev. 0, Appendix B. Three features, however, do not appear in these drawings and are critical to performance of the design. First, all quartz-metal contact areas are coated with Dow-Corning RTV prior to vibration testing or flight use to reduce stress concentrations in the quartz. Second, the stainless steel radiant heat shields are sputter-coated with approximately 0.00025 cm (0.0001 in.) of Pt to retain reflectivity after several heating cycles. Third, the furnace design is critical to the atmosphere present during heat-up. That is, the gas present must have a particular combination of thermal conductivity and specific heat properties for satisfactory furnace operation. In early testing it was found that satisfactory (and comparable) performance was obtained with either an air or nitrogen environment. Good heating element life and good specimen heating rates were observed and the TCU outer wall remained at approximately 25°C throughout a simulated experiment cycle. Temperature at the outer radiant heat shield remained below 100°C during this same type of heating cycle. Helium was less satisfactory in that heater life was reduced (perhaps due to helium's much lower specific heat), the TCU outer wall heated up much more rapidly (due to helium's higher thermal conductivity), and sample heating rates were not changed significantly (because sample heating is largely radiant). Argon was not satisfactory, as heating elements melted before the test samples reached 700°C. This was attributed to argon's combination of lower thermal conductivity (not much different than air or nitrogen) and lower specific heat.

Furnace Control Electronics

Requirements

The control requirements for Flight 1 were:

1) Turn on furnace heating element 75 seconds after launch (about a 25 amp load).

2) Turn off heating element when the furnace temperature reached 700°C.

3) Immediately open the valve releasing the quench water.

4) Provide appropriately conditioned signals to the rocket telemetry system from the sample thermocouples, temperature reference, and input power voltage.

5) Physically, the control unit had to mount in a small space beside the TCU and withstand the 25-g vibration testing.

Circuit Description

The sample and furnace temperatures are monitored by chromel-alumel thermocouples. Seven amplifiers change these millivolt signals to the 0 to 5 volt signals required by the rocket telemetry system. As there is no cold-junction compensation for ambient temperature changes on these amplifiers, a compensated thermocouple amplifier is used to measure the cold-junction temperature and provide a telemetry signal. A regulated 25 volt supply powers all the amplifiers.

An Exar 2240 M IC timer provides the delay between launch and applying power to the furnace element. A "G" switch activated by the launch acceleration triggers the timer, which closes the N219 furnace power relay 75 seconds later. A single thermocouple in the furnace center monitors the overall furnace temperature. This amplified signal is combined with the temperature reference signal to produce a voltage proportional to the absolute furnace temperature. An LM311 voltage comparator detects the moment this signal is equal to a preset voltage equivalent to 700°C and triggers the quench solenoid SCR driver. The quench solenoid is opened releasing the water into the sample chamber and simultaneously the furnace power relay is turned off, preventing any further heating.

A regulated 5 volt output powers the timer and provides reference bias to the amplifier and comparator.

Design and construction details are included in Battelle Drawings R-2773, Sheet 1, Rev. 1 and Sheet 2, Rev. 0. Reproductions of these two drawings are included in Appendix C.

Ground-Based Testing

Ground-based testing at Battelle-Northwest (BNW) included sufficient furnace and electronics testing to assure satisfactory operation through at least five repeated heating cycles. The water quench was not operated, however, as MSFC personnel intended to replace the solenoid activating the water quench in our TCU because of a mechanical problem encountered in a similar solenoid at MSFC. In addition, sputtered aluminum samples from the same material to be flown in the zero-g experiments were heated above their melting point in the preliminary laboratory furnace models and in the flight furnace assembly. These samples were air cooled. The micrographs in Figure 2 indicated that the samples did foam and thus gave a preliminary indication that both the furnace design and the materials concepts were sound.

Modification of the TCU was completed, the associated control electronics were completed, dummy samples appropriate for the NASA testing plan were installed in the TCU, and the TCU with electronics was shipped via courier to NASA/MSFC on August 14, 1975 with delivery on August 15.

The following drawings were also completed and delivered to NASA/MSFC at this time:

Drawing Title	BNW Drawing Number
TCU Furnace Modification	R-2160 (2 sheets)
Specimen Metallic Foam Experiment	R-2170
Rocket Furnace Electronics	R-2173 (sheet 1 of 2)
Rocket Furnace Electronics Details	R-2173 (sheet 2 of 2)
Block Diagram Furnace Electronics	R-2183

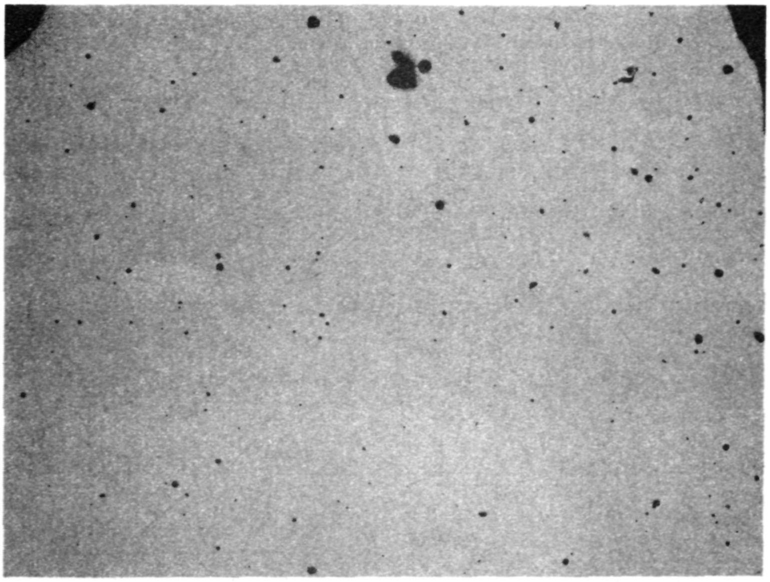

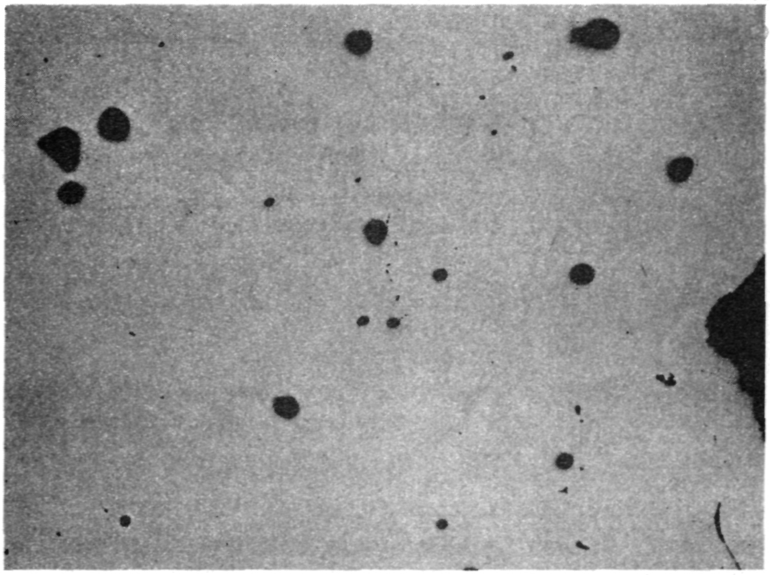

FIGURE 2. Samples Heated in Laboratory Furnace Model and Air Cooled. The top photo shows a sample heated to 680°C and the bottom photo shows a sample heated to 720°C. 100X magnification

In addition, the assembly procedure used to install samples in the TCU and prepare the TCU for testing was recorded and several photographs were taken during the assembly process (Appendix A).

The TCU was further modified at NASA (after delivery from BNW) in areas relating to gas purge fittings, water input lines, and provision for pressure equilization between the water reservoir and the furnace chamber. No drawings or written description of these modifications were prepared by NASA/MSFC.

The TCU and associated electronics withstood MSFC vibration testing the first time they were tested, in September 1975. One crack was observed in the quartz heater support, but this crack was not expected to affect the experiment in any way. Several assembly screws used in the heat shield assembly worked loose, none of which would affect the experiment. However, the assembly procedure was modified and now includes RTV coating of the screws to prevent loosening during future tests and experiments. Some failures in sample thermocouple solder joints (cold junction) were also encountered and procedures were modified to provide better joint reliability.

This and earlier similar work demonstrated that shipping time to BNW from MSFC or to MSFC from BNW can be a minimum of 1 day. For this reason it was indicated to MSFC that it is preferable to conduct any equipment alterations or refurbishment at BNW if at least 3 days are available in the MSFC schedule.

The MSFC-provided water quench solenoid valve leaked during vibration testing. MSFC indicated that they would change valves to prevent future problems in this area.

MSFC personnel indicated that ground-based tests would be conducted on or about October 10, and that presence of the Principal Investigator or his representative would be required for installation of test samples and for furnace refurbishment.

The TCU was partially disassembled at MSFC in early October 1975 and the water quench solenoid valve was replaced. After reassembly, a short was noted in the control thermocouple, so the TCU was immediately shipped back to Battelle. The control thermocouple was replaced with a design that is expected to be more resistant to damage. All solder joints to thermocouples were examined and some were resoldered. The TCU was shipped back to MSFC the same day it had been received.

MSFC tested the TCU through its complete temperature cycle more than one time, and after one of these cycles noted that the heating element was shorted to the TCU outer wall. The TCU was shipped back to BNW, where it was refurbished including installation of all new thermocouples, quartz sample tubes, quartz heater support, a heating element wound in such a way as to avoid the shorting problem, and new dummy test samples. The TCU was then shipped to MSFC where it again underwent testing through the complete temperature cycle with no difficulties being encountered.

On Monday, October 20, 1975, MSFC telephoned and requested the presence of the PI and Eric Greenwell at MSFC on Wednesday, October 22, for ground-based tests. On October 22 the TCU was completely refurbished as above but including new radiation shielding and ground-based test samples. Testing difficulties associated with NASA control functions and with other experiments produced delays in the test schedule such that the first ground-based test (GB 1) was conducted on October 28. A second set of ground-based test samples was then installed in the furnace and a second ground-based test (GB 2) was conducted. On October 30 the refurbished TCU, complete with a new set of dummy samples, was made available to MSFC for installation in the science payload and shipment to Goddard.

The ground-based tests described above provided 12 specimens for evaluation and use as a basis of comparison for the zero-gravity processed specimens. Four samples were much larger than originally planned in this group (four times as wide), see Table 3. External appearances seemed to indicate that foaming had occurred, and the effects of gravity were clearly evident in sample "sagging" or flowing, see Table 4. These samples were all evaluated metallographically. In addition, a computer program designed to analyze metallography of indicated reactor fuel cell materials was modified to suit the foam material and used to provide statistical analysis of the microstructure.

The ground-based testing was conducted without any difficulties related to the TCU or its associated electronics. Experiment performance was satisfactory as was the collection of in-test time and temperature data. To date only a pen trace of the time-temperature data from GB 1 has been made available to BNW and no data have been available from GB 2. MSFC personnel indicated that detailed data would be available later.

TABLE 3. QUANTITATIVE OBSERVATIONS ON FOAM SPECIMENS

Processing	Specimen Number	Mean Cell Size (μ)	Median Cell Size (μ) Volume	Cell Count/cm^3	Cell Volume Fraction (%)	Cell Specific Surface Area (cm^2/cm^3)	Argon Content (ppm)	Specimen Width* (mm)	Specimen Thickness* (mm)	Time Above Melting Point (sec)	Cooling Rate through Melting Point (^{o}C/sec)
Space	1-D-1	2.66	5.00x10^1	2.87x10^8	1.15	1.07x10^2	30	1.1	0.2	31.0	1310
	1-D-2	5.05	3.99x10^1	1.32x10^8	3.34	1.87x10^2					
	1-D-3	6.39	6.27x10^1	7.10x10^7	3.26	1.57x10^2					
Space	1-J-1	4.09	9.10	2.91x10^8	1.69	2.33x10^2	30	4.2	0.2	25.0	220
	1-J-2	4.90	2.84x10^1	1.35x10^8	3.80	1.97x10^2					
	1-J-3	4.49	2.53x10^1	2.02x10^8	4.00	2.54x10^2					
Space	2-C-1	7.61	4.46x10^1	1.61x10^7	2.10	7.34x10^1	231	1.2	0.9	31.0	170
	2-C-2	5.45		4.31x10^7	12.79	1.18x10^2					
	2-C-3	5.71	3.18x10^1	5.10x10^7	2.80	1.34x10^2					
Space	3-C-1	4.51	2.02x10^1	6.86x10^7	1.52	9.59x10^1	23	1.2	0.6	29.0	1370
	3-C-2	7.42		1.59x10^7	32.82	1.24x10^2					
	3-C-3	3.97	8.81x10^1	4.20x10^7	3.76	9.07x10^1					
Space	4-C-1	3.97	8.15	5.91x10^7	0.25	3.98x10^1	272	1.2	0.6	22.0	1310
	4-C-2	1.01x10^1	4.46x10^1	2.22x10^7	6.13	1.81x10^2					
	4-C-3	5.83	3.99x10^1	3.68x10^7	4.17	1.35x10^2					
Space	4-J-2	5.21	4.46x10^1	3.07x10^7	2.35	8.55x10^1	272	4.1	0.5	26.0	1250
	4-J-3	4.29	4.46x10^1	5.33x10^7	4.52	1.33x10^2					
GB 1	1-A-1	4.04	4.65	2.65x10^8	0.60	1.48x10^2	30	1.1	0.2	42	
	1-A-2	3.56	3.70	2.24x10^8	0.60	1.90x10^2					
	1-A-3	2.91	2.95	3.75x10^8	0.28	1.05x10^2					
GB 1	1-G-1	4.45	9.10	2.07x10^8	1.29	1.81x10^2	30	4.2	0.2	21	
	1-G-2	4.25	1.02x10^1	2.19x10^8	1.33	1.75x10^2					
	1-G-3	4.05	8.15	1.57x10^8	0.66	1.09x10^2					
GB 1	2-A-1	3.58	5.20	1.48x10^8	0.31	7.23x10^1	231	1.1	0.9	14	
	2-A-2	4.41	1.29x10^1	6.30x10^7	0.60	6.24x10^1					
	2-A-3	4.70	8.15	8.80x1o^7	0.51	8.01x10^1					

---

*All specimens were 1-cm long.

TABLE 3. (Concluded)

Processing	Specimen Number	Mean Cell Size (μ)	Median Cell Size (μ) Volume	Cell Count/cm^{3}	Cell Volume Fraction (%)	Cell Specific Surface Area (cm^{2}/cm^{3})	Argon Content (ppm)	Specimen Width* (mm)	Specimen Thickness* (mm)	Time Above Melting Point (sec)	Cooling Rate through Melting Point (^{o}C/sec)
GB 1	3-A-1	5.65	2.53x10^{1}	8.92x10^{7}	3.62	1.93x10^{2}	23	1.1	0.6	8	
	3-A-2	5.80	3.18x10^{1}	9.90x10^{7}	4.42	2.15x10^{2}					
	3-A-3	3.77	1.15x10^{1}	7.00x10^{7}	0.32	4.37x10^{1}					
GB 1	4-A-1	3.88	3.56x10^{1}	6.77x10^{8}	6.77	5.03x10^{2}	272	1.1	0.6	24	
	4-A-2	4.30	7.87x10^{1}	5.20x10^{8}	16.37	5.89x10^{2}					
	4-A-3	2.95	3.70	1.16x10^{8}	0.11	3.51x10^{1}					
GB 1	4-G-1	5.82	2.02x10^{1}	2.12x10^{8}	5.18	3.83x10^{2}	272	4.0	0.6	21	
	4-G-2	5.68	9.10	2.29x10^{8}	2.11	2.96x10^{2}					
	4-G-3	6.41	1.44x10^{1}	2.54x10^{8}	4.51	4.23x10^{2}					
GB 2	1-B-1	4.44	7.30	2.55x10^{8}	1.15	1.99x10^{2}	30	1.1	0.2		
	1-B-2	3.19	4.15	2.30x10^{8}	0.32	8.45x10^{1}					
	1-B-3	3.67	4.65	2.27x10^{8}	0.44	1.11x10^{2}					
GB 2	1-H-1	3.52	4.65	1.40x10^{8}	0.24	6.28x10^{1}	30	4.2	0.2		
	1-H-2	3.46	4.65	2.17x10^{8}	0.41	9.58x10^{1}					
	1-H-3	5.34	1.02x10^{1}	1.36x10^{8}	1.38	1.73x10^{2}					
GB 2	2-B-1	5.38	7.87x10^{1}	2.25x10^{8}	17.28	4.50x10^{2}	231	1.1	0.9		
	2-B-2	4.46	6.27x10^{1}	5.75x10^{8}	8.93	5.53x10^{2}					
	2-B-3	3.98	2.02x10^{1}	1.05x10^{9}	6.67	7.29x10^{2}					
GB 2	3-B-1	5.48	9.10	4.11x10^{8}	3.54	4.95x10^{2}	23	1.2	0.6		
	3-B-2	5.15	7.30	3.61x10^{8}	2.26	3.68x10^{2}					
	3-B-3	4.24	5.20	2.51x10^{8}	0.66	1.56x10^{2}					
GB 2	4-B-1	3.67	5.80	1.58x10^{8}	0.37	7.96x10^{1}	272	1.1	0.6		
	4-B-2	4.46	9.10	1.31x10^{8}	0.74	1.08x10^{2}					
	4-B-3	4.14	1.02x10^{1}	1.13x10^{8}	0.65	8.41x10^{1}					
GB 2	4-H-1	5.08	1.29x10^{1}	2.66x10^{8}	2.81	3.12x10^{2}	272	4.0	0.6		
	4-H-2	5.03	3.18x10^{1}	1.85x10^{8}	4.84	2.84x10^{2}					
	4-H-3	4.87	3.99x10^{1}	1.69x10^{8}	4.88	2.49x10^{2}					

*All specimens were 1-cm long.

TABLE 4. QUALITATIVE OBSERVATIONS ON FOAM SPECIMENS SPACE PROCESSED SPECIMENS

Specimen No.	Cell Volume	Deformation	TC Contact Maintained?
1-D	Sampling apparently very good except for 2 large coalescence areas.	Very little sample deformation observed.	No
1-J	Sampling did not count area with highest density of large cells (rt of 1-J-2) or large tear or coalescence areas (resulting from deformation?)	Sample elongation and resulting tearing, possibly due to mechanical recovery in the supporting TC wires.	Yes
2-C	Sampling did not count area with highest density of large cells (left of 2-C-2) or large coalescence areas. Overall sample cell volume fraction probably 20-25%.	Very little deformation. Sample bending possibly occurred during quench as sample was detached from support and TC wires.	No
3-C	Sampling did not count areas of highest cell density. Areas with about 5 times more porosity were present. Only 1 large coalescence area was present and it was counted.	Very little sample deformation evident.	Yes
4-C	All typical areas sampled well. Sample very uniform with no large coalescence areas.	Very little sample deformation evident.	No
4-J	Sampling fairly good but did not count large coalescence areas. Overall sample cell volume fraction probably 15-20%.	Sample elongation and thickening to one end, probably due to quench.	No

TABLE 4. (Continued)

GB 1 Specimens

Specimen No.	Cell Volume	Deformation	TC Contact Maintained?
1-A	Sampling apparently very good.	Extensive elongation apparent.	Yes
1-G	Sampling very good. No large coalescence areas were present.	Very extensive sample elongation, appearance of "running" or fluid flow.	No
2-A	Sampling good but one very large coalescence area (cell) formed as did several smaller ones. These were not counted. Overall sample cell volume fraction was probably 20-25%.	Very little plastic flow was evident but a very extensive oxide or corrosion product film was observed on the sample. This film probably limited fluid flow.	Yes
3-A	Sampling was good but did not count the many large coalescence areas. Sample cell volume fraction was probably 15-20%.	Very little sample elongation was observed.	Yes
4-A	Sampling was good but the sample had only melted on one end.	Sample flow was extensive on the end that melted. Breakup (mechanical) of the heavy corrosion product film was evident.	Yes
4-G	Sampling was very good with no large coalescence areas observed.	Flow was very extensive with nearly all of the sample material accumulating at the bottom support wire.	Yes

TABLE 4. (Concluded)

GB 2 Specimens

Specimen No.	Cell Volume	Deformation	TC Contact Maintained?
1-B	Sampling good but did not count large coalescence areas. Overall sample cell volume fraction probably 20-25%.	Extensive elongation apparent.	Yes
1-H	Sampling very good but one very large coalescence area (cell) formed so that overall sample cell volume was probably 60-70%.	Extensive fluid flow bordering on droplet formation.	No
2-B	Sampling was very good. No large coalescence areas were observed.	Very little plastic flow was evident, again probably a result of the very heavy corrosion product film.	Yes
3-B	Sampling was very good. No large coalescence areas were observed.	Sample bent and sagged severely.	Yes
4-B	Sampling was good except that a large coalescence area (cell) was not counted. This cell was 20-25% of the sample volume.	The center of the sample formed a droplet and fell off the support wires. The large cell was formed in this piece.	No
4-H	Sampling was very good with only one large coalescence area forming (not counted).	Flow was similar to that observed in 4-G. However, the sample separated in the middle (tearing) during the quench.	Yes

SPAR Flight No. 1

On December 2 the flight samples and flight furnace components were delivered to White Sands Missile Range, New Mexico. Due to delays in the White Sands testing schedule, the TCU was made available for refurbishment on December 5. At this time the furnace was refurbished and the flight samples were installed.

The flight experiment was flown on December 11. The TCU and electronics packages were shipped by MSFC personnel and arrived at BNW on December 16. The TCU was immediately disassembled and examined. The water quench had operated, heating element operation seemed to have been normal, all samples remained in their quartz capsules and appeared to have melted and foamed, and the thermocouples appeared to have remained intact throughout the experiment. It was tentatively concluded that the experiment was a success, provided that suitable time-temperature data had been transmitted to the ground facility and recorded.

The flight samples were analyzed in the same manner as the ground-based tested samples and preliminary results were presented during a review meeting at MSFC on January 5 and 6. Statistical and metallographic data were left with project personnel at MSFC to aid in demonstration of the success of the SPAR I experiment and to indicate feasibility of metal foam production.

An informal post-flight preliminary report in the form of a letter to Roger Chassay was written on January 21, 1976. This report briefly documented the results presented at the January 5-6 MSFC meeting and is reproduced in Appendix D.

Note that although the raw thermocouple voltage data from SPAR Flight No. 1 were available to examine at the January 5-6 MSFC meeting, detailed time-temperature and time-voltage data were not available for examination until February 20, 1976, 7 days before the scheduled Comprehensive Review Meeting at MSFC on March 5, 1976 and more than 2 months after the flight. Furthermore, this data revealed that drift had occurred in the thermocouple amplifiers before the flight so that a new zero-point had to be determined for each thermocouple system and all data received from MSFC had to be adjusted to compensate for these values. Corrections to the time-temperature data from the flight were completed on March 8, permitting final analysis of flight data to begin.

RESULTS AND DISCUSSION

Metallography from the six SPAR Flight No. 1 samples and the twelve ground-based tested samples is included in Figures 3 through 20. Table 3 summarizes sample sizes, processing methods, time above the melting point (if available), cooling rate through the melting point, trapped argon content, and cell size and distribution statistics. In the case of cell distribution statistics, much more extensive and detailed information was available due to the computer program used for quantitative metallographic analysis. Much of this data was not useful for the present analysis, however, and so was not included here.

Table 4 contains qualitative observations on the foamed specimens.

Note that times at which melting occurred on heating for space processed samples were taken as the beginning of thermal arrests observed in the time-temperature data. Each of these thermal arrests occurred within a few degrees of the published 660°C melting point of aluminum. Times at which solidification occurred were taken as the times when the samples cooled through 660°C. Cooling rates here were very rapid so very little time error was involved with this measurement. Cooling rates from each sample (temperature was measured each 0.1 sec) are listed in Table 3. Accuracy in the estimated times above the melting point (Table 3) for space-processed samples was judged to be ±1 sec. Heating rate was approximately 10°C/sec.

Approximate times above the melting point for GB 1 samples were estimated from recording pen traces and thermal arrests. No computer-processed data have yet been received from NASA/MSFC so the data have only been included as a very rough indication that ground-based heating approximated flight heating.

No times above the melting point for GB 2 samples were included in Table 4 because no data have been received from NASA/MSFC.

Detailed analysis of the scatter in cell size, number density, and related features will not be attempted since a sufficiently large number of samples was not available to allow reliable determination of trends. However, it seemed generally true that gas content variations up to 250 ppm were not as strongly influential on foaming behavior as expected. This may have been clouded by the difficulty in counting large pores in the quantitative analysis, by the very

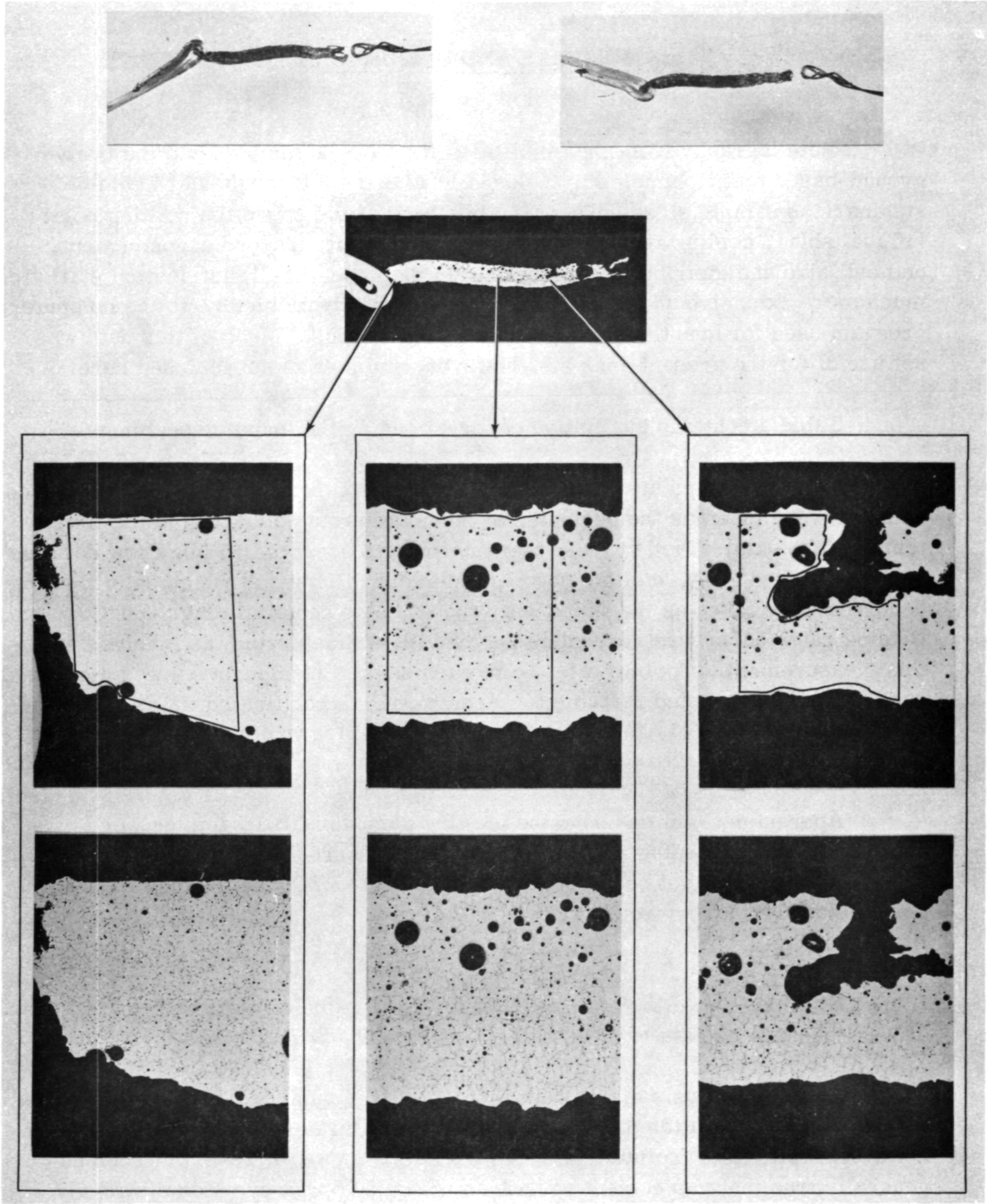

FIGURE 3. Specimen 1-D, Space Processed.
The top two photos are 3X magnification and show two views of the specimen with support wires at the left and thermocouple wires at the right. The next lower photo is 5X magnification and shows a cross-section of the specimen. The bottom six photos are 50X magnification and show as-polished (top 3) and etched (bottom 3) microstructures.

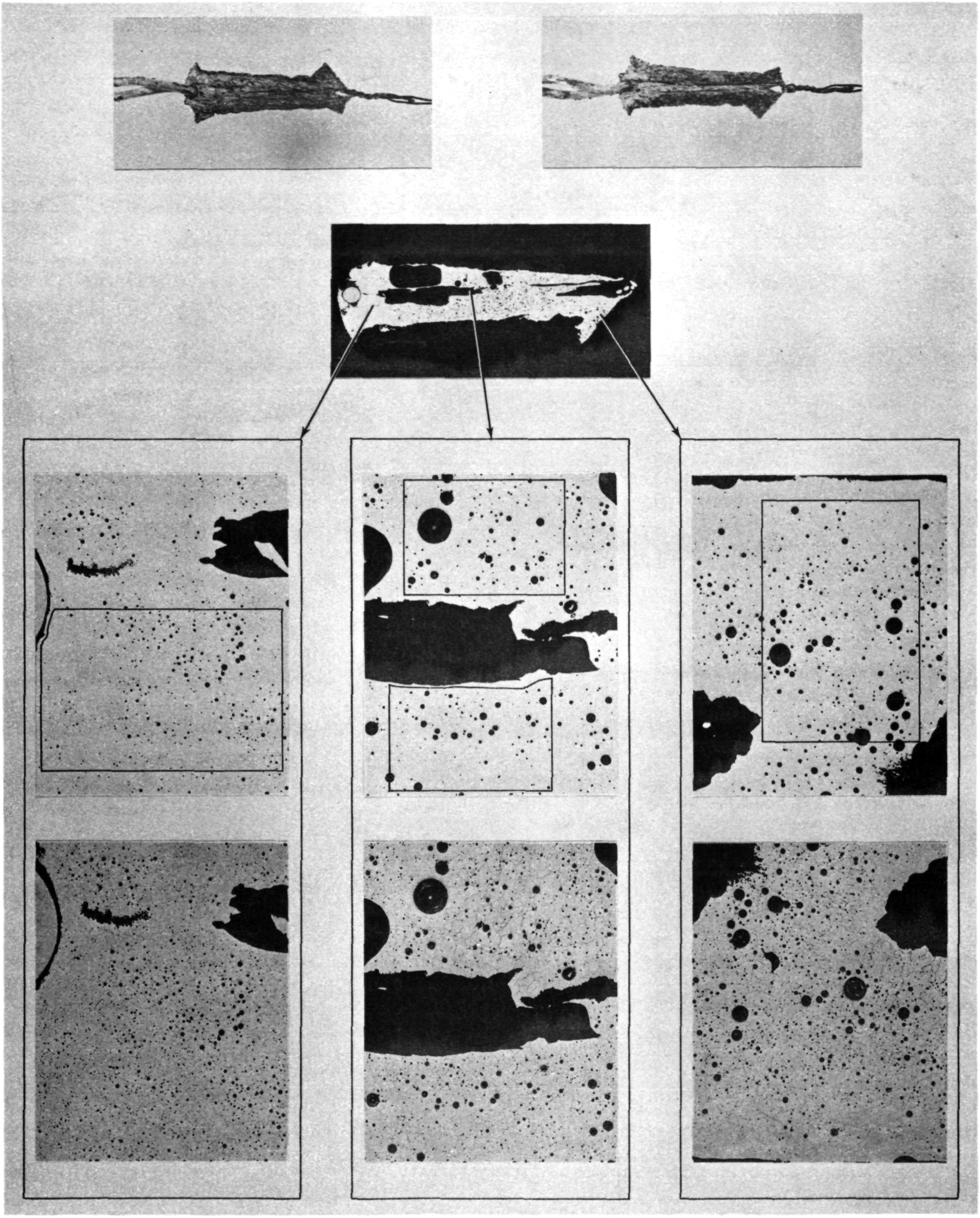

FIGURE 4. Specimen 1-J, Space Processed. The top two photos are 3X magnification and show two views of the specimen with support wires at the left and thermocouple wires at the right. The next lower photo is 5X magnification and shows a cross-section of the specimen. The bottom six photos are 50X magnification and show as-polished (top 3) and etched (bottom 3) microstructures.

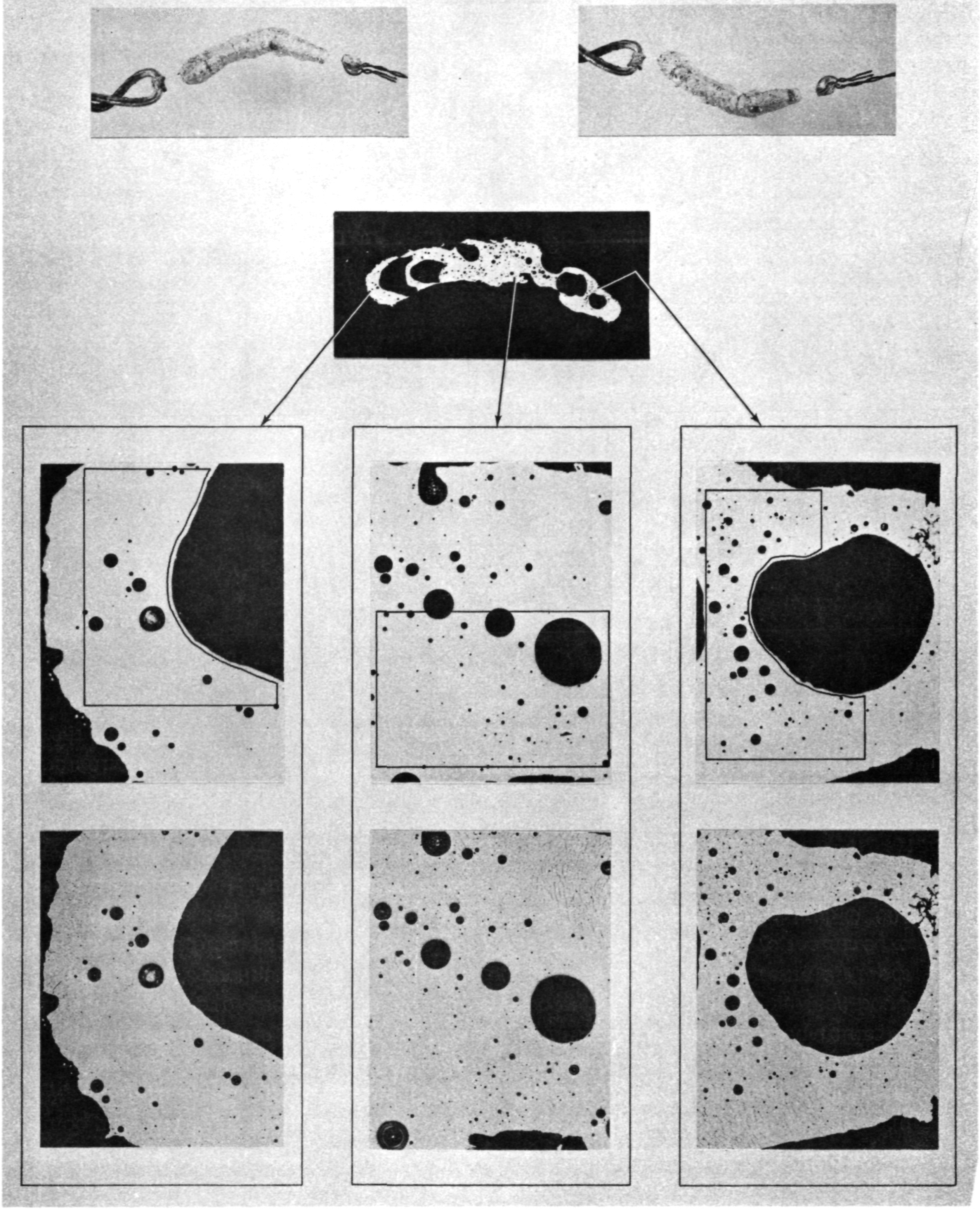

FIGURE 5. Specimen 2-C, Space Processed.
The top two photos are 3X magnification and show two views of the specimen with support wires at the left and thermocouple wires at the right. The next lower photo is 5X magnification and shows a cross-section of the specimen. The bottom six photos are 50X magnification and show as-polished (top 3) and etched (bottom 3) microstructures.

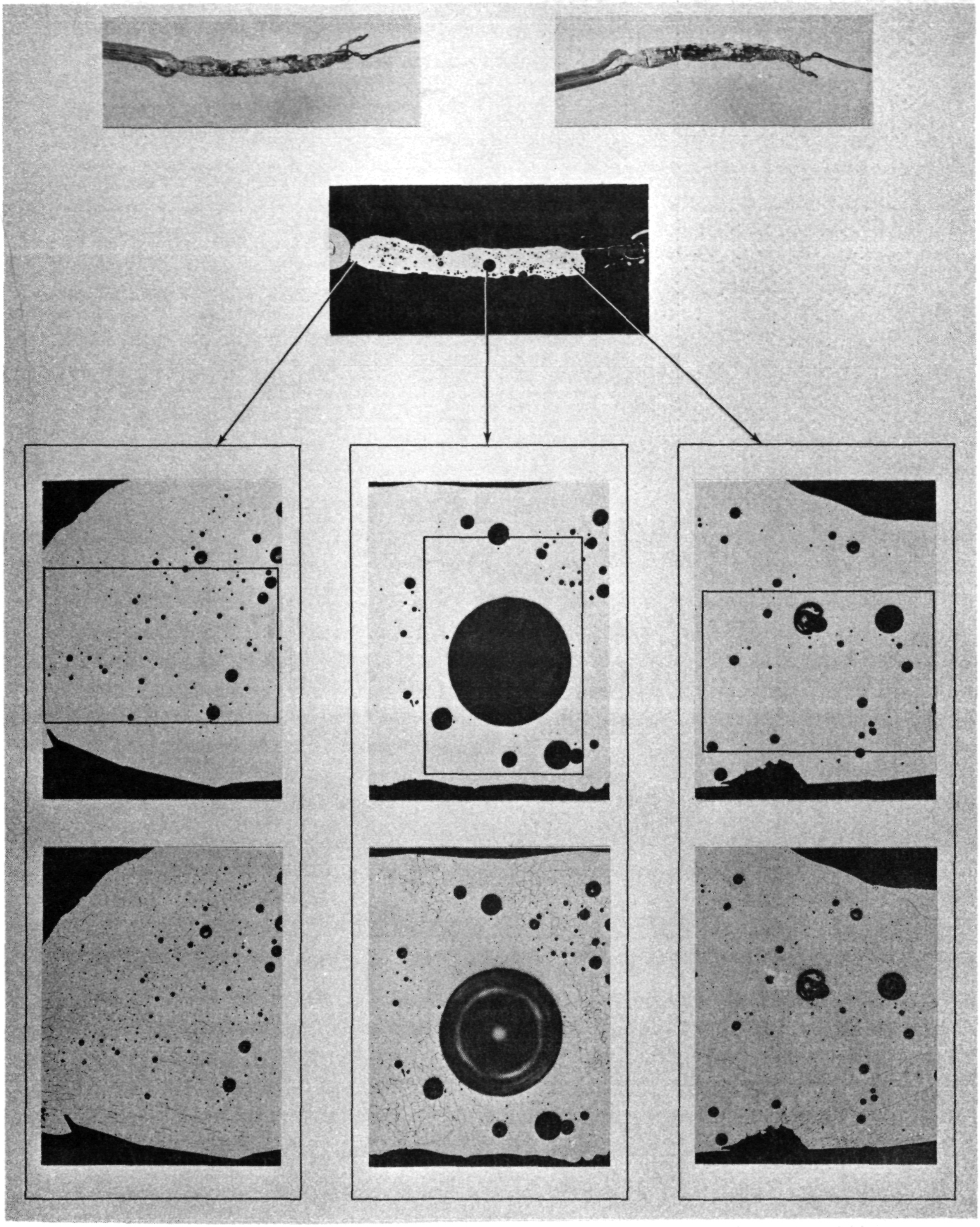

FIGURE 6. Specimen 3-C, Space Processed.
The top two photos are 3X magnification and show two views of the specimen with support wires at the left and thermocouple wires at the right. The next lower photo is 5X magnification and shows a cross-section of the specimen. The bottom six photos are 50X magnification and show as-polished (top 3) and etched (bottom 3) microstructures.

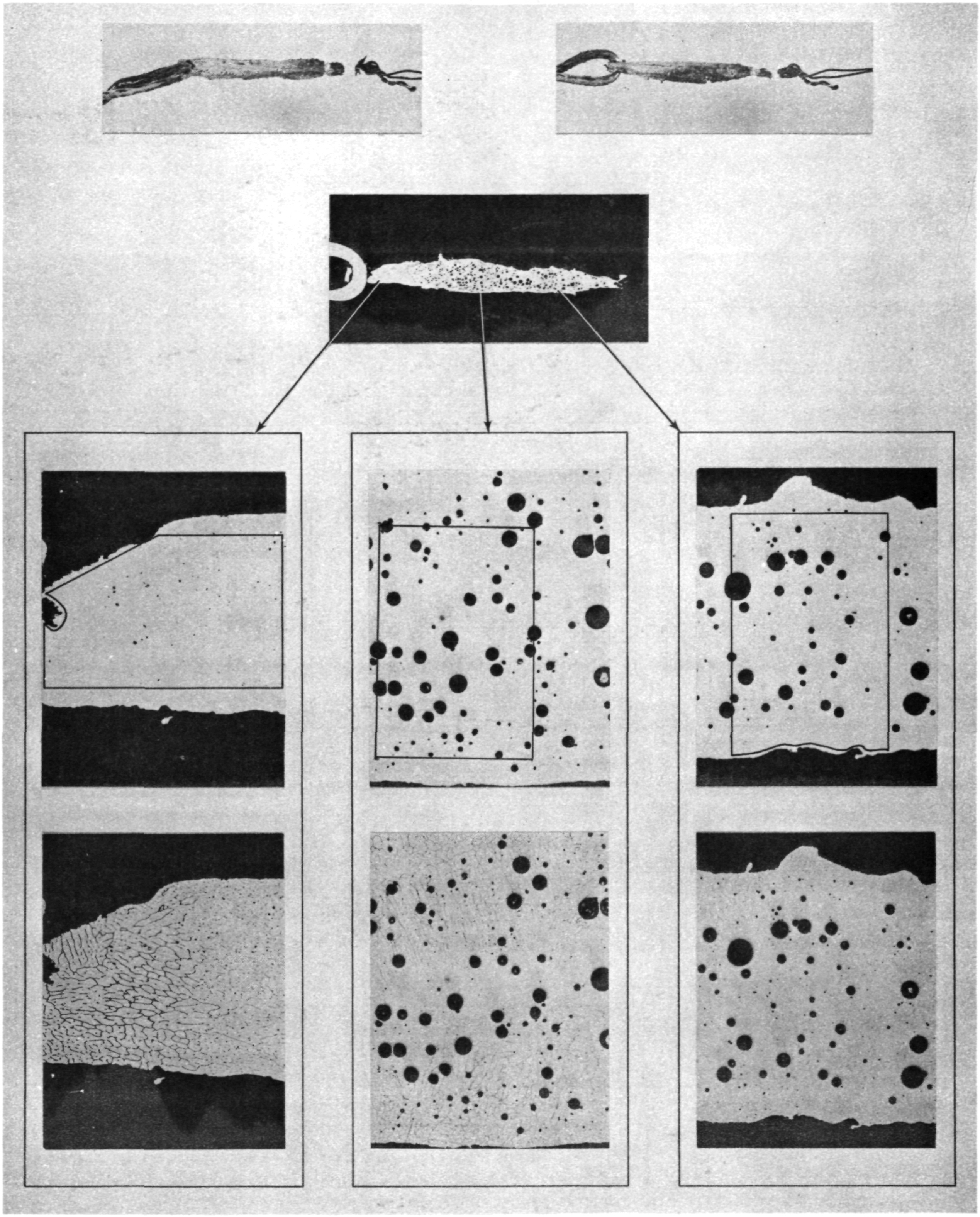

FIGURE 7. Specimen 4-C, Space Processed.
The top two photos are 3X magnification and show two views of the specimen with support wires at the left and thermocouple wires at the right. The next lower photo is 5X magnification and shows a cross-section of the specimen. The bottom six photos are 50X magnification and show as-polished (top 3) and etched (bottom 3) microstructures.

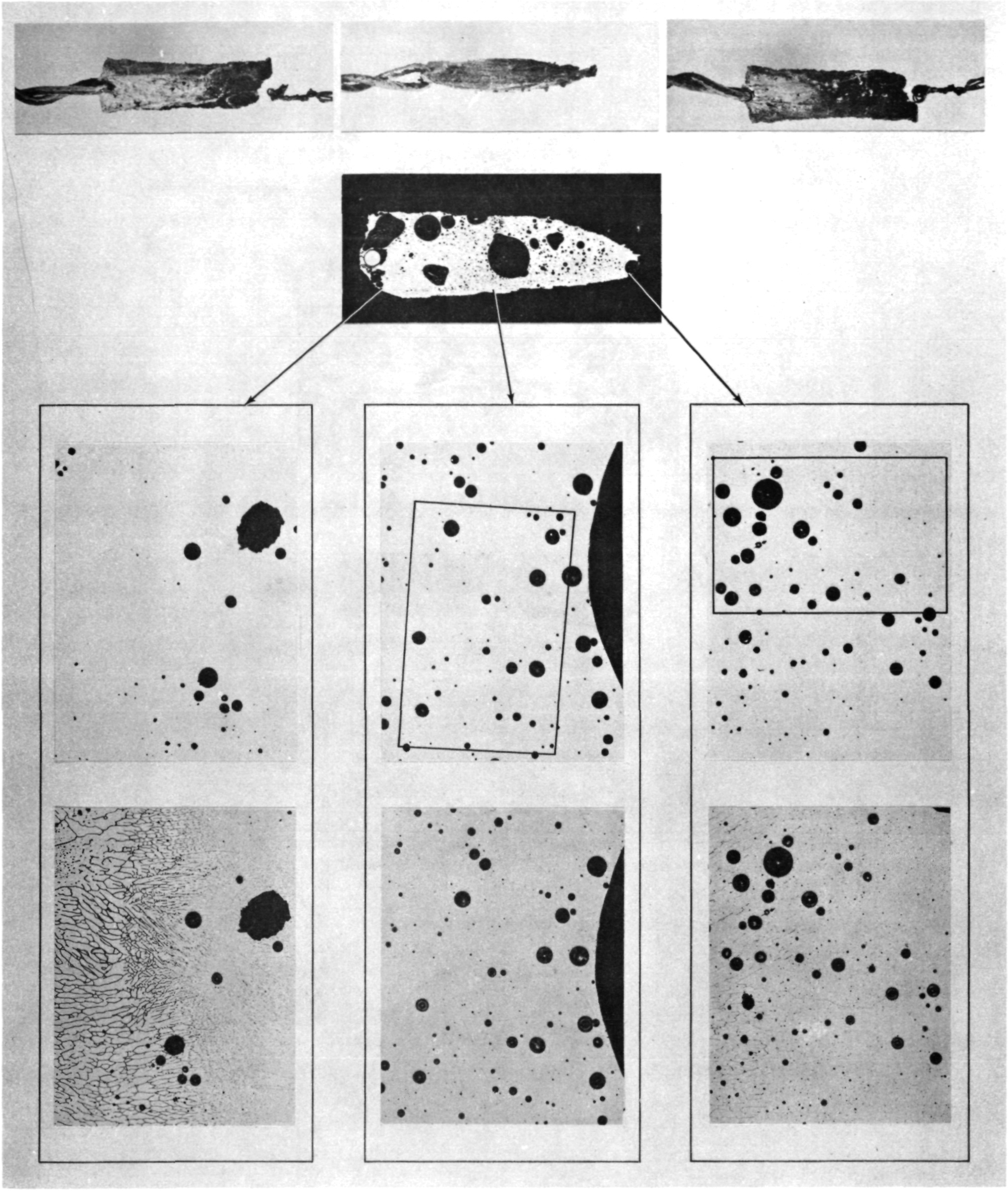

FIGURE 8. Specimen 4-J, Space Processed.
The top two photos are 3X magnification and show two views of the specimen with support wires at the left and thermocouple wires at the right. The next lower photo is 5X magnification and shows a cross-section of the specimen. The bottom six photos are 50X magnification and show as-polished (top 3) and etched (bottom 3) microstructures.

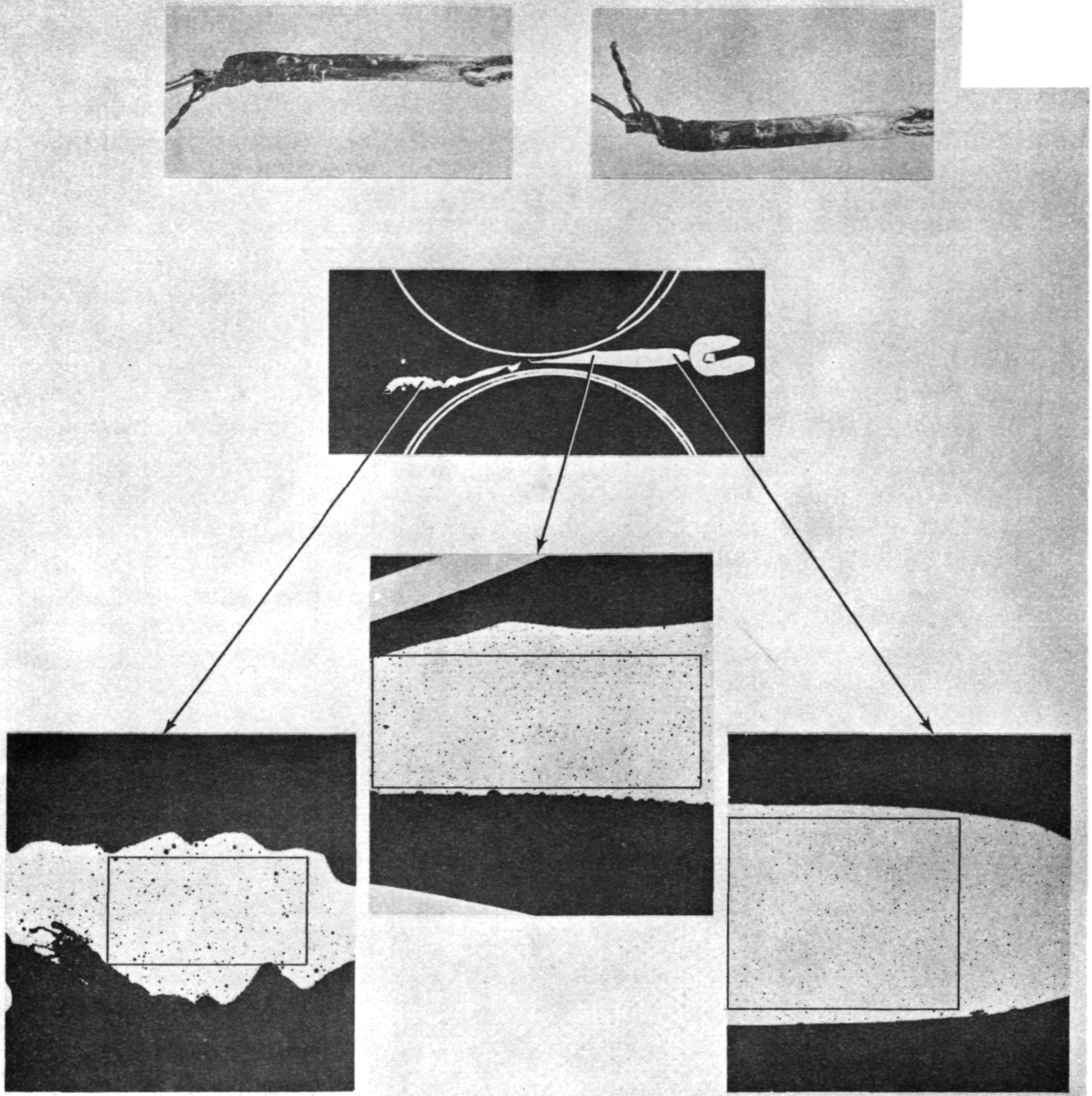

FIGURE 9. Specimen 1-A, GB 1.
The top two photos are 4.2X magnification and show two views of the specimen. The next lower photo is 4.8X and shows a cross-section of the specimen. The bottom three photos are 60X magnification and show as-polished microstructures.

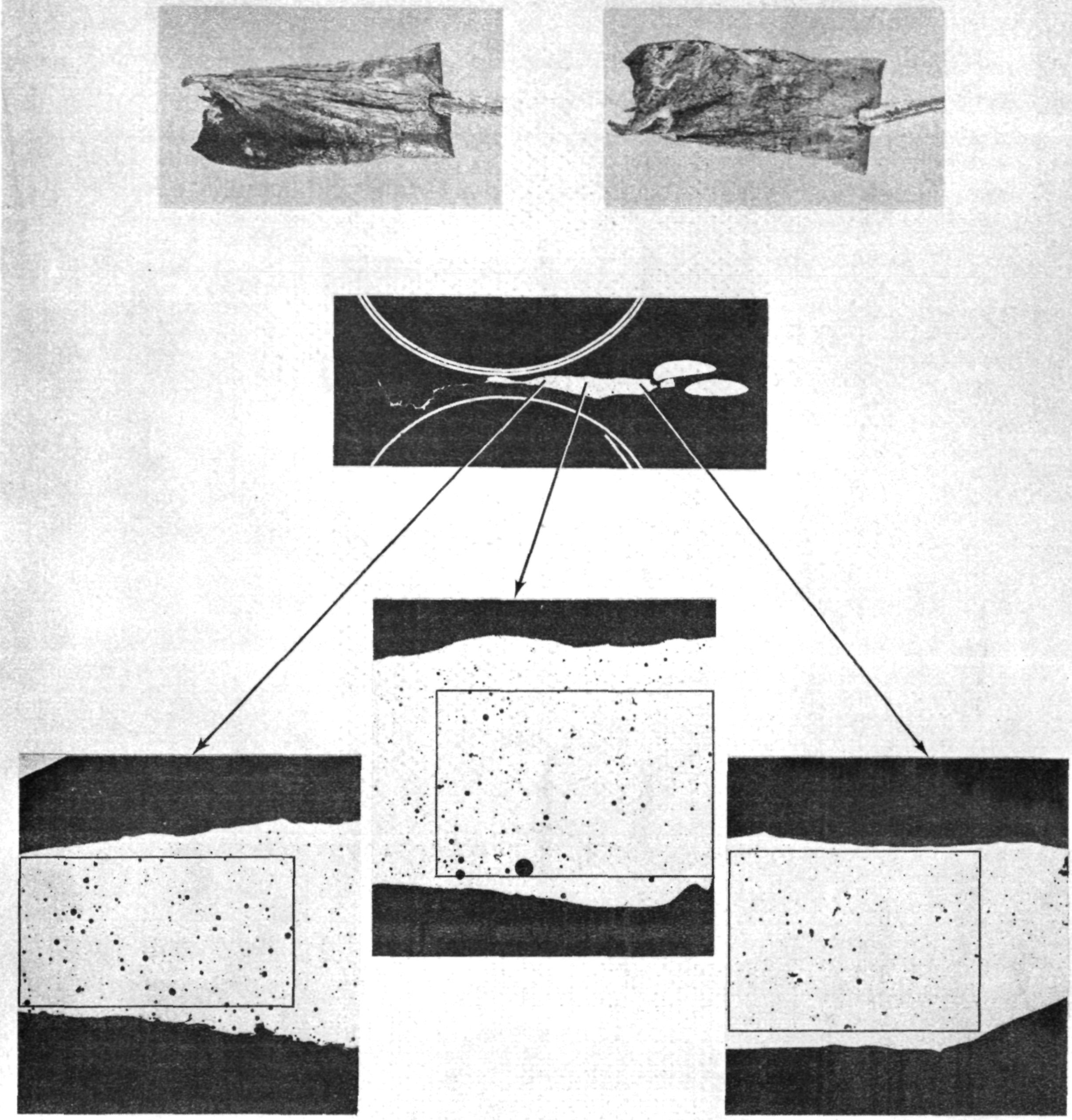

FIGURE 10. Specimen 1-G, GB 1.
The top two photos are 4.2X magnification and show two views of the specimen. The next lower photo is 4.8X and shows a cross-section of the specimen. The bottom three photos are 60X magnification and show as-polished microstructures.

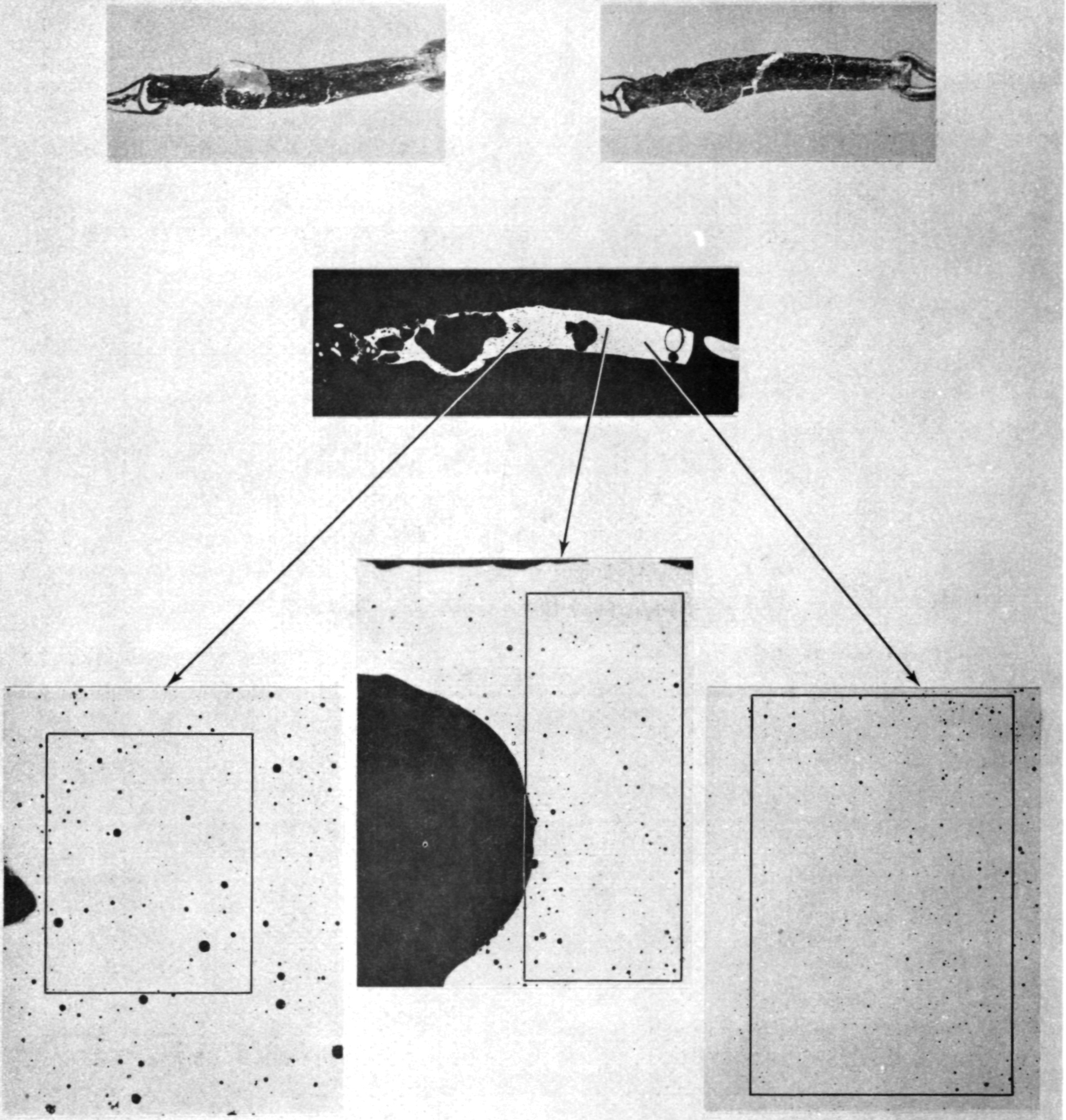

FIGURE 11. Specimen 2-A, GB 1.
The top two photos are 4.2X magnification and show two views of the specimen. The next lower photo is 4.8X and shows a cross-section of the specimen. The bottom three photos are 60X magnification and show as-polished microstructures.

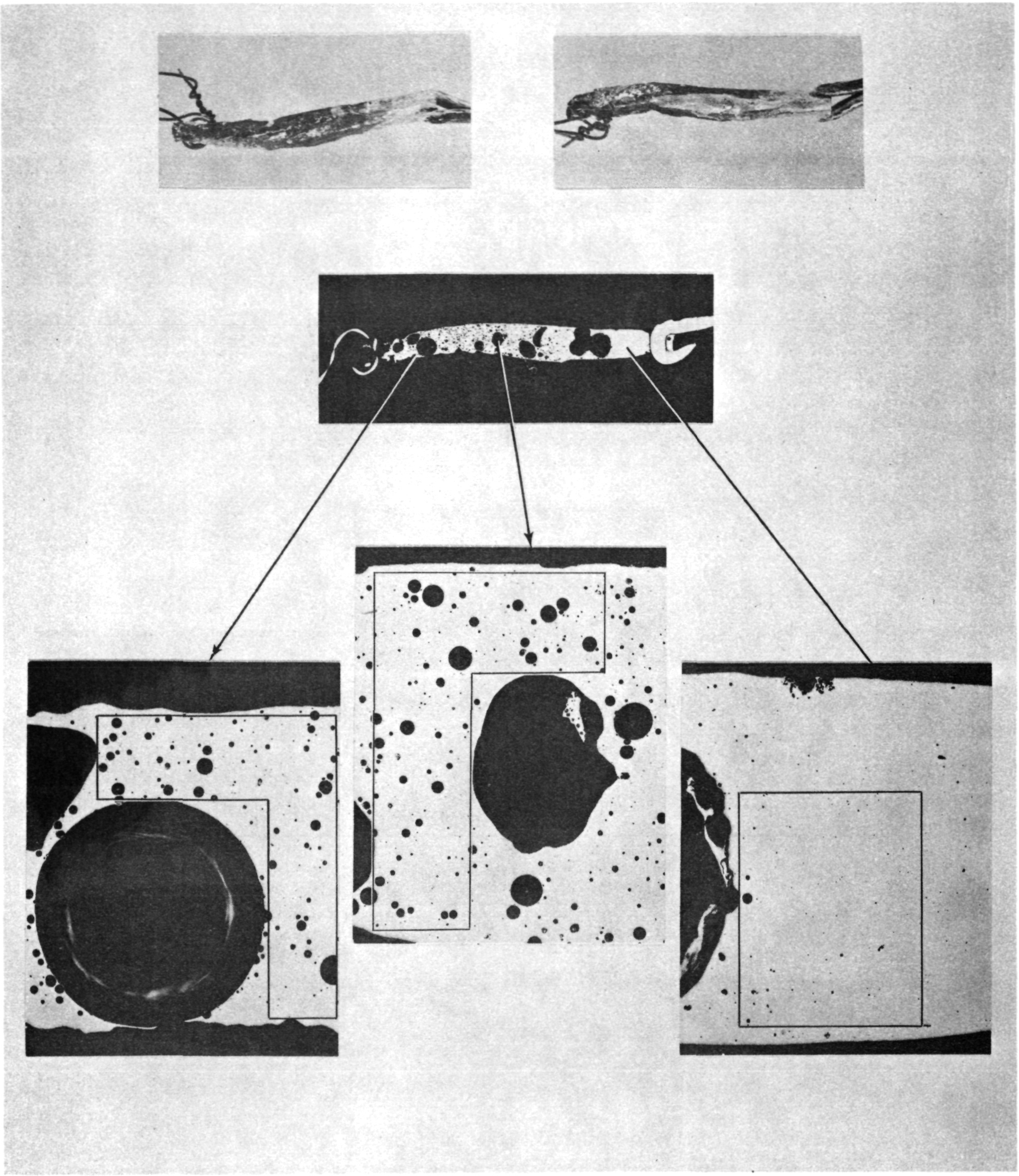

FIGURE 12. Specimen 3-A, GB 1.
The top two photos are 4.2X magnification and show two views of the specimen. The next lower photo is 4.8X and shows a cross-section of the specimen. The bottom three photos are 60X magnification and show as-polished microstructures.

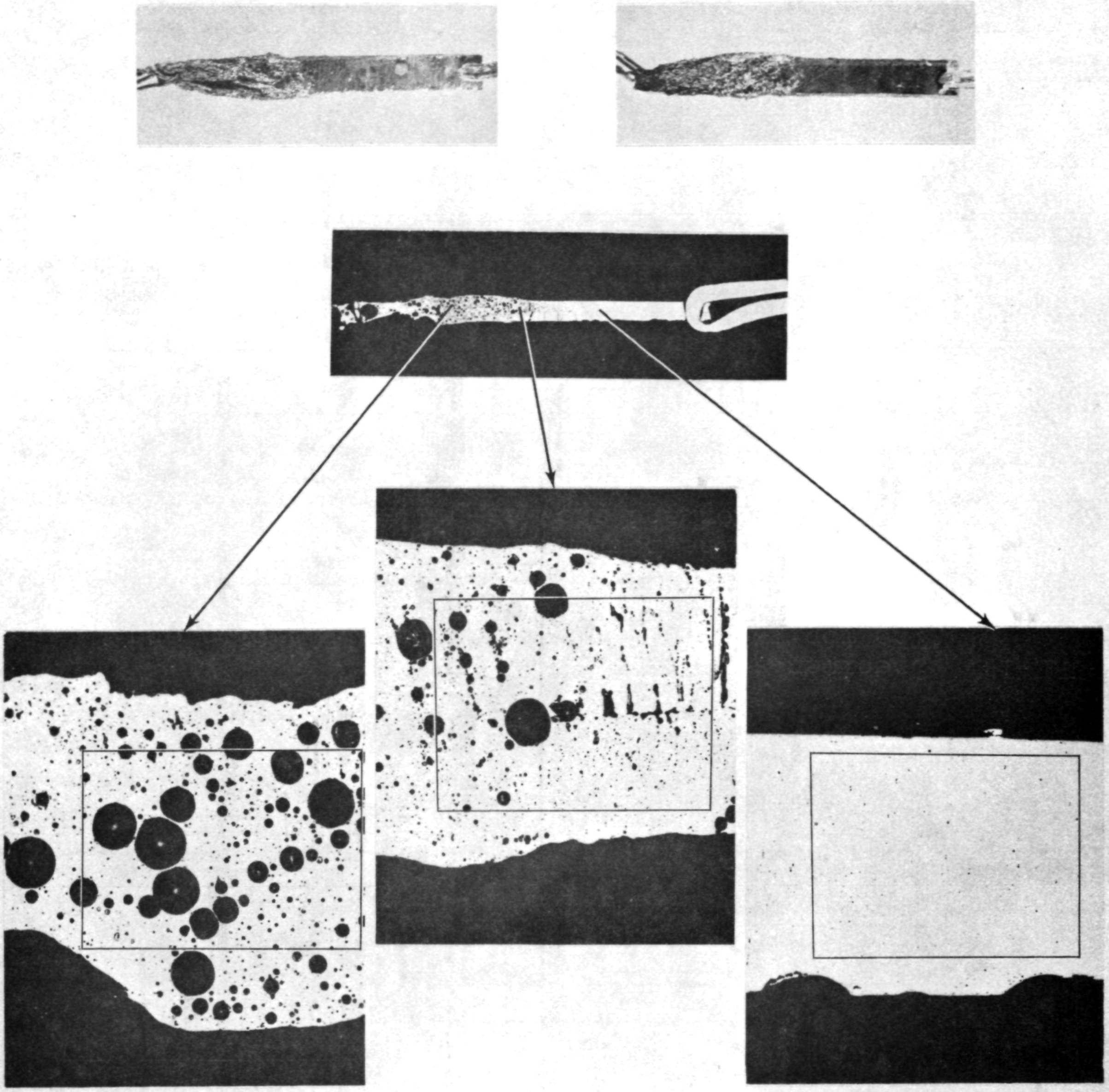

FIGURE 13. Specimen 4-A, GB 1.
The top two photos are 4.2X magnification and show two views of the specimen. The next lower photo is 4.8X and shows a cross-section of the specimen. The bottom three photos are 60X magnification and show as-polished microstructures.

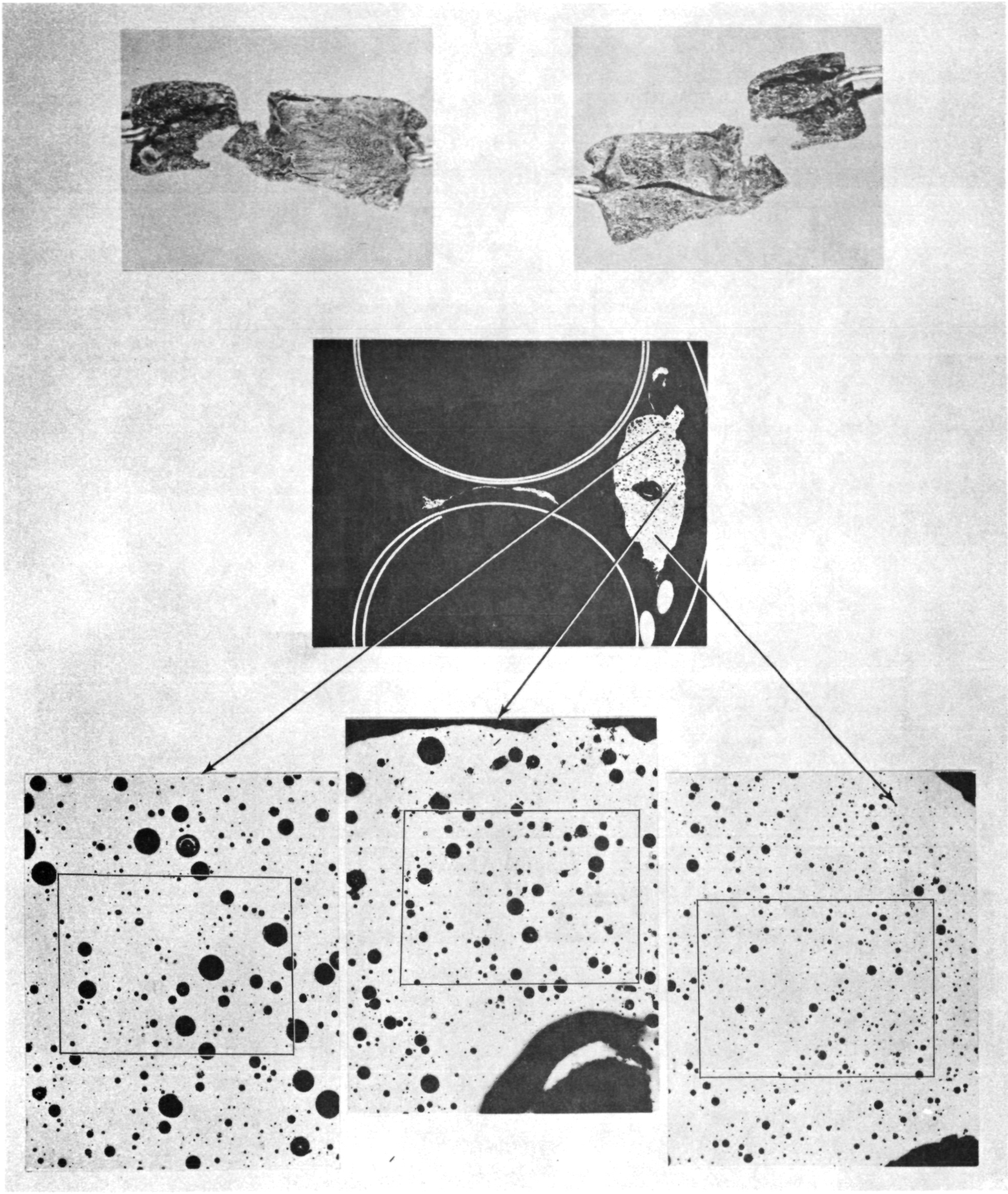

FIGURE 14. Specimen 4-G, GB 1.
The top two photos are 4.2X magnification and show two views of the specimen. The next lower photo is 4.8X and shows a cross-section of the specimen. The bottom three photos are 60X magnification and show as-polished microstructures.

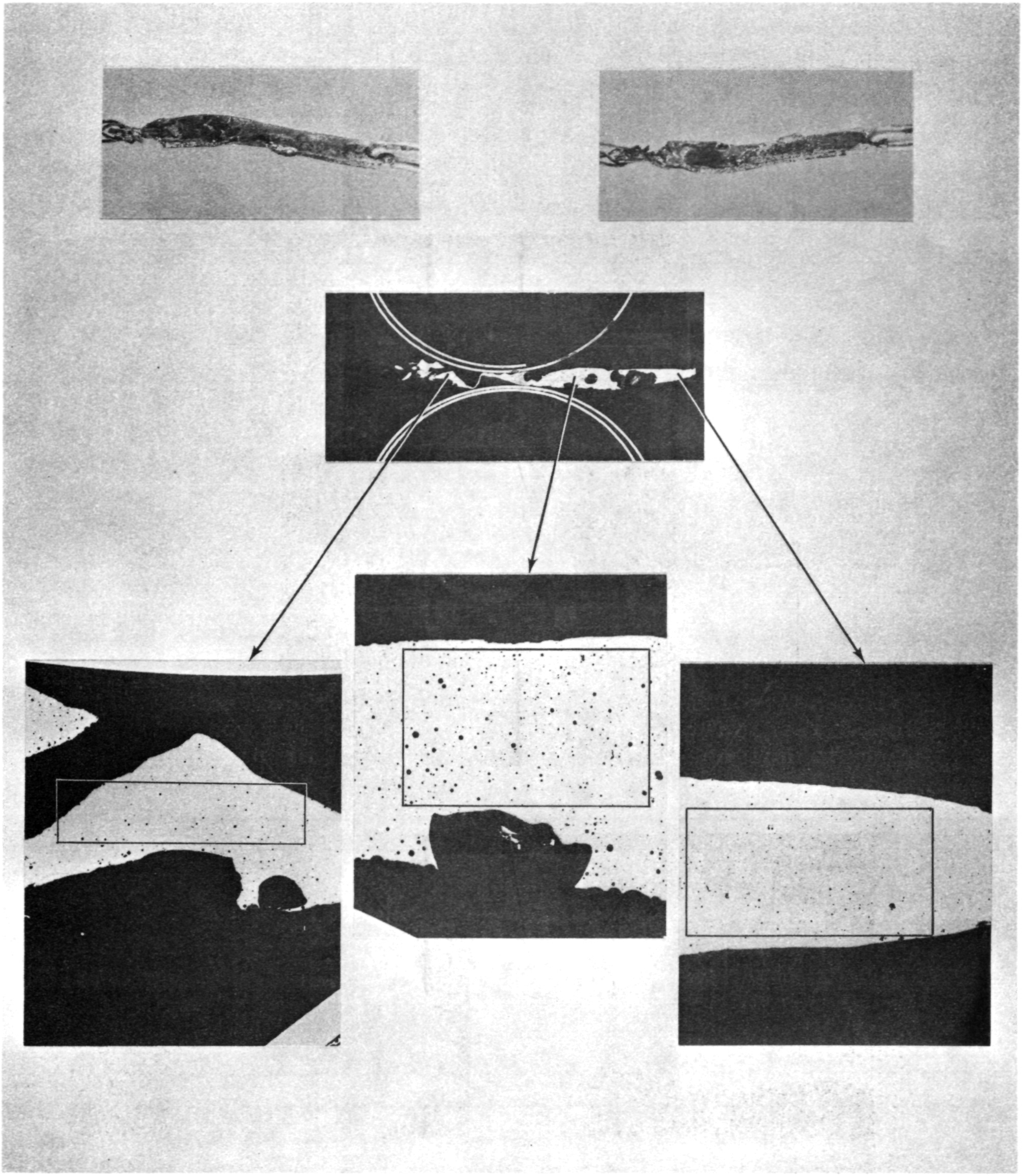

FIGURE 15. Specimen 1-B, GB 2.
The top two photos are 4.2X magnification and show two views of the specimen. The next lower photo is 4.8X and shows a cross-section of the specimen. The bottom three photos are 60X magnification and show as-polished microstructures.

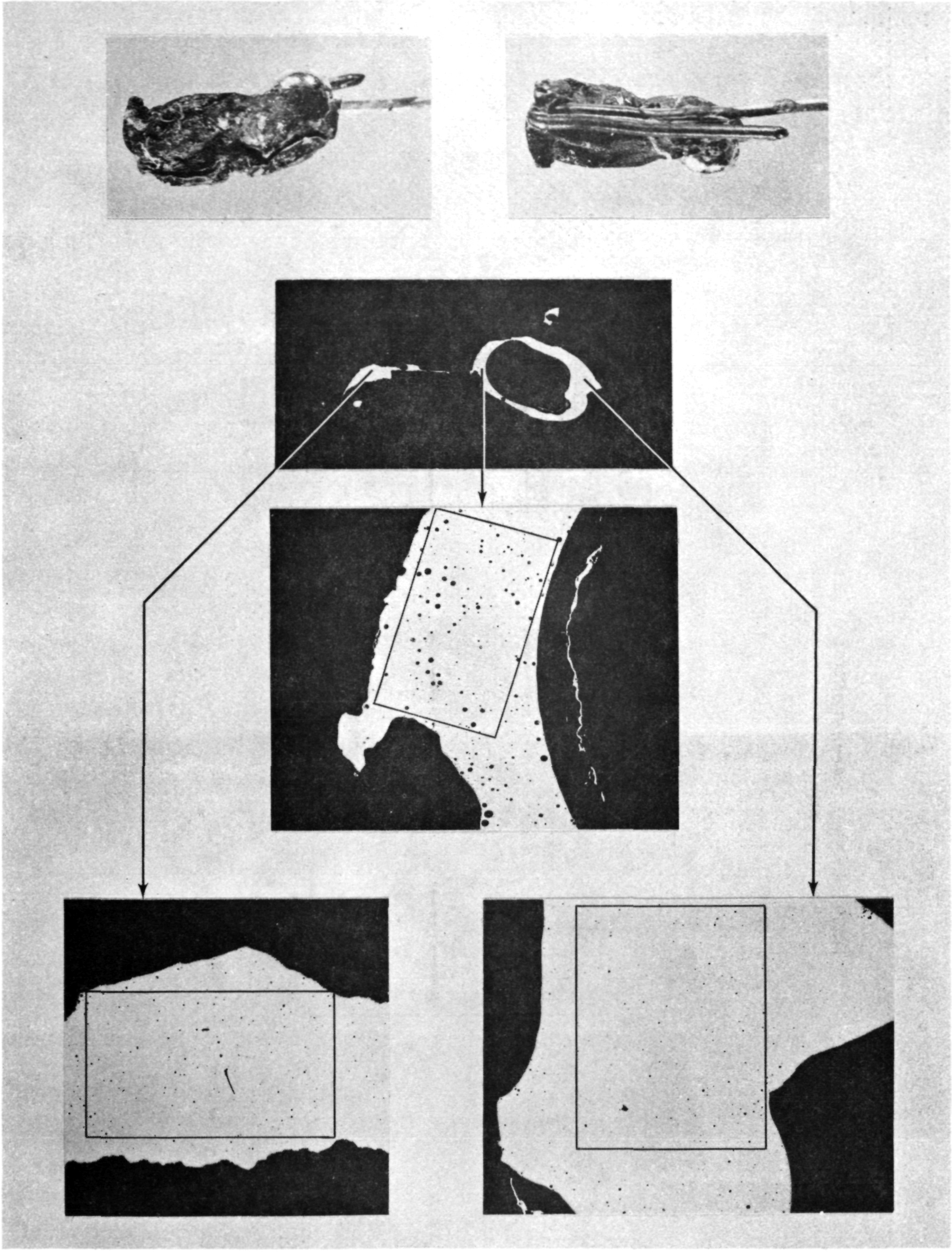

FIGURE 16. Specimen 1-H, GB 2.
The top two photos are 4.2X magnification and show two views of the specimen. The next lower photo is 4.8X and shows a cross-section of the specimen. The bottom three photos are 60X magnification and show as-polished microstructures.

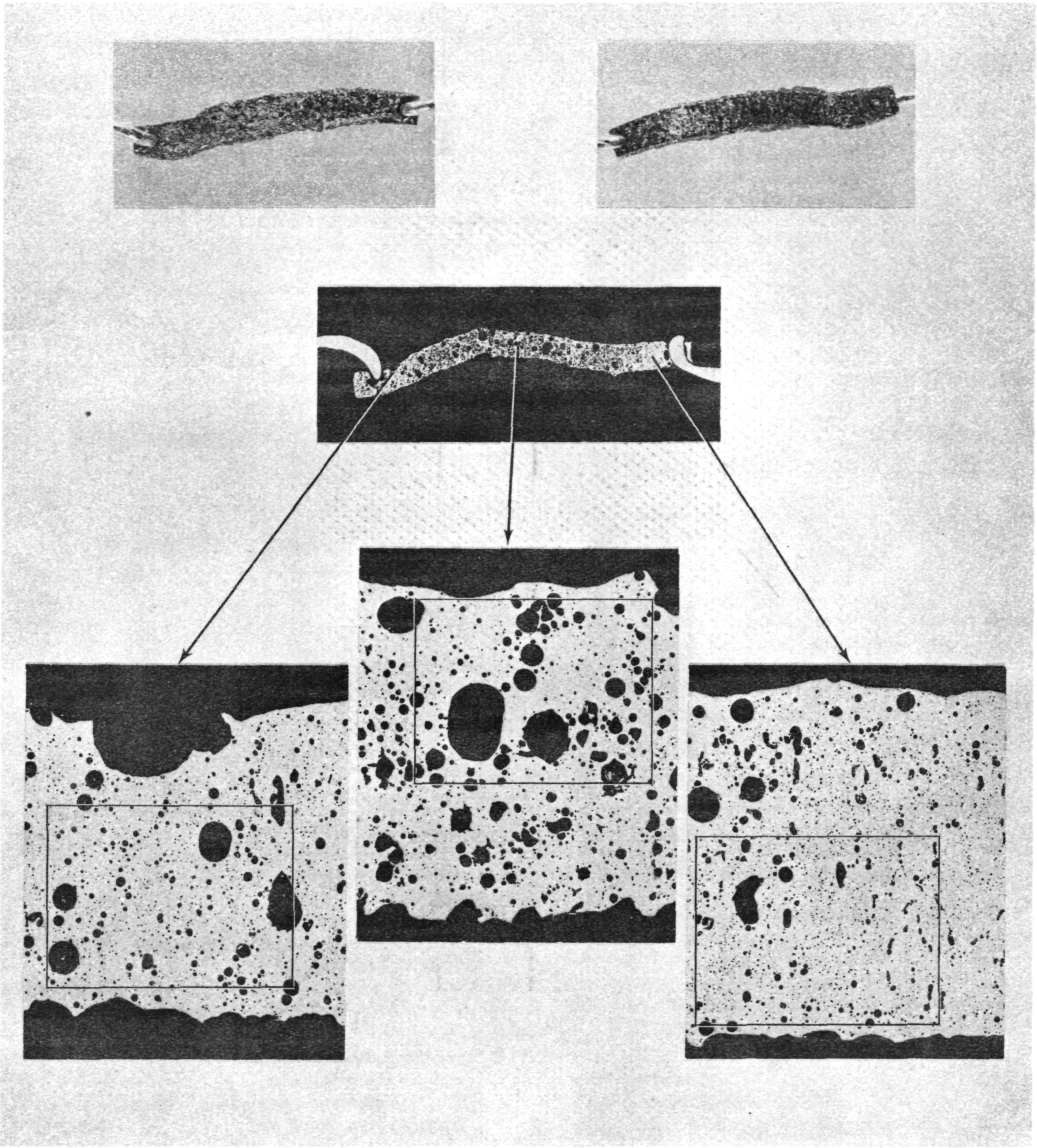

FIGURE 17. Specimen 2-B, GB 2.
The top two photos are 4.2X magnification and show two views of the specimen. The next lower photo is 4.8X and shows a cross-section of the specimen. The bottom three photos are 60X magnification and show as-polished microstructures.

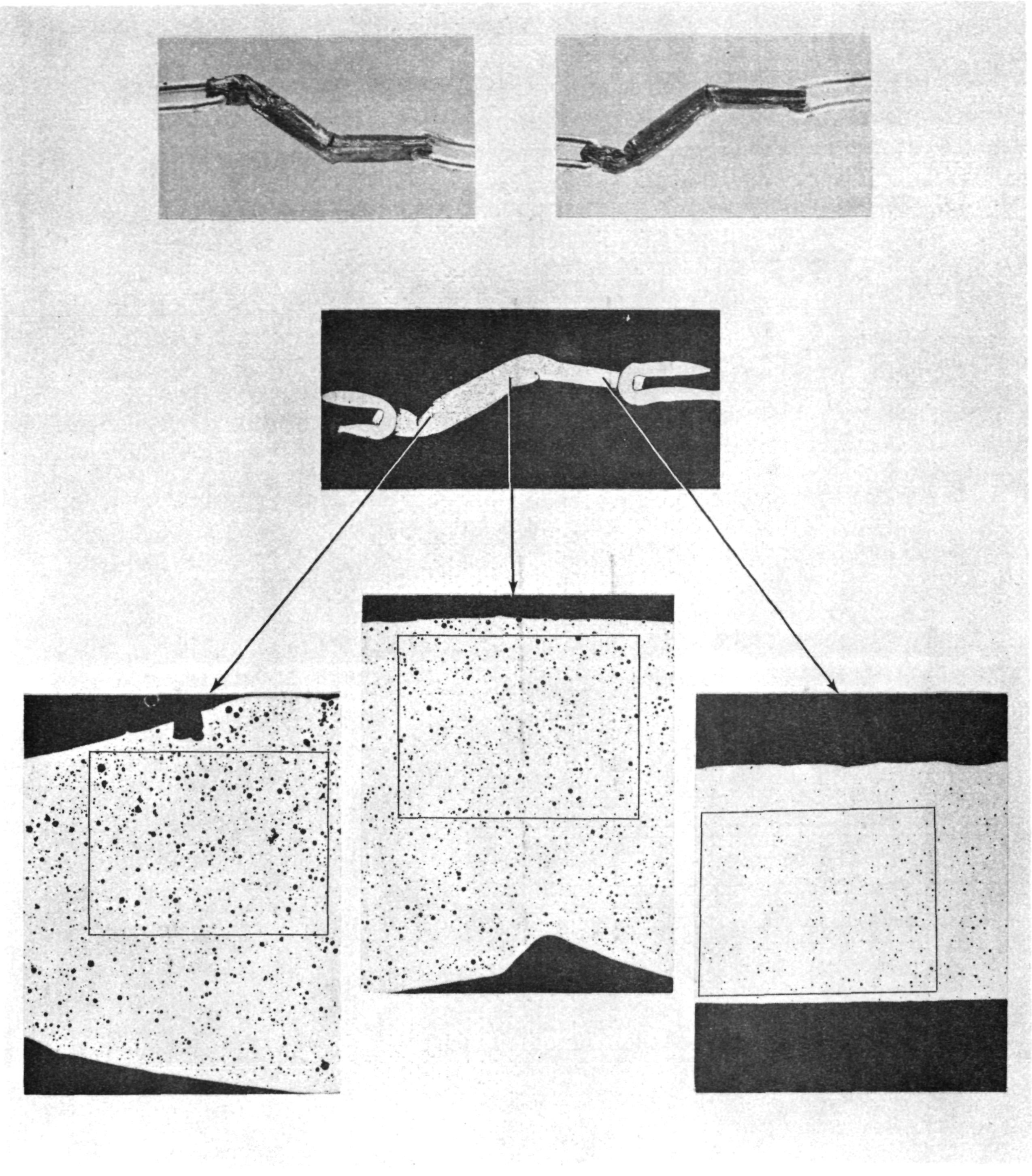

FIGURE 18. Specimen 3-B, GB 2.
The top two photos are 4.2X magnification and show two views of the specimen. The next lower photo is 4.8X and shows a cross-section of the specimen. The bottom three photos are 60X magnification and show as-polished microstructures.

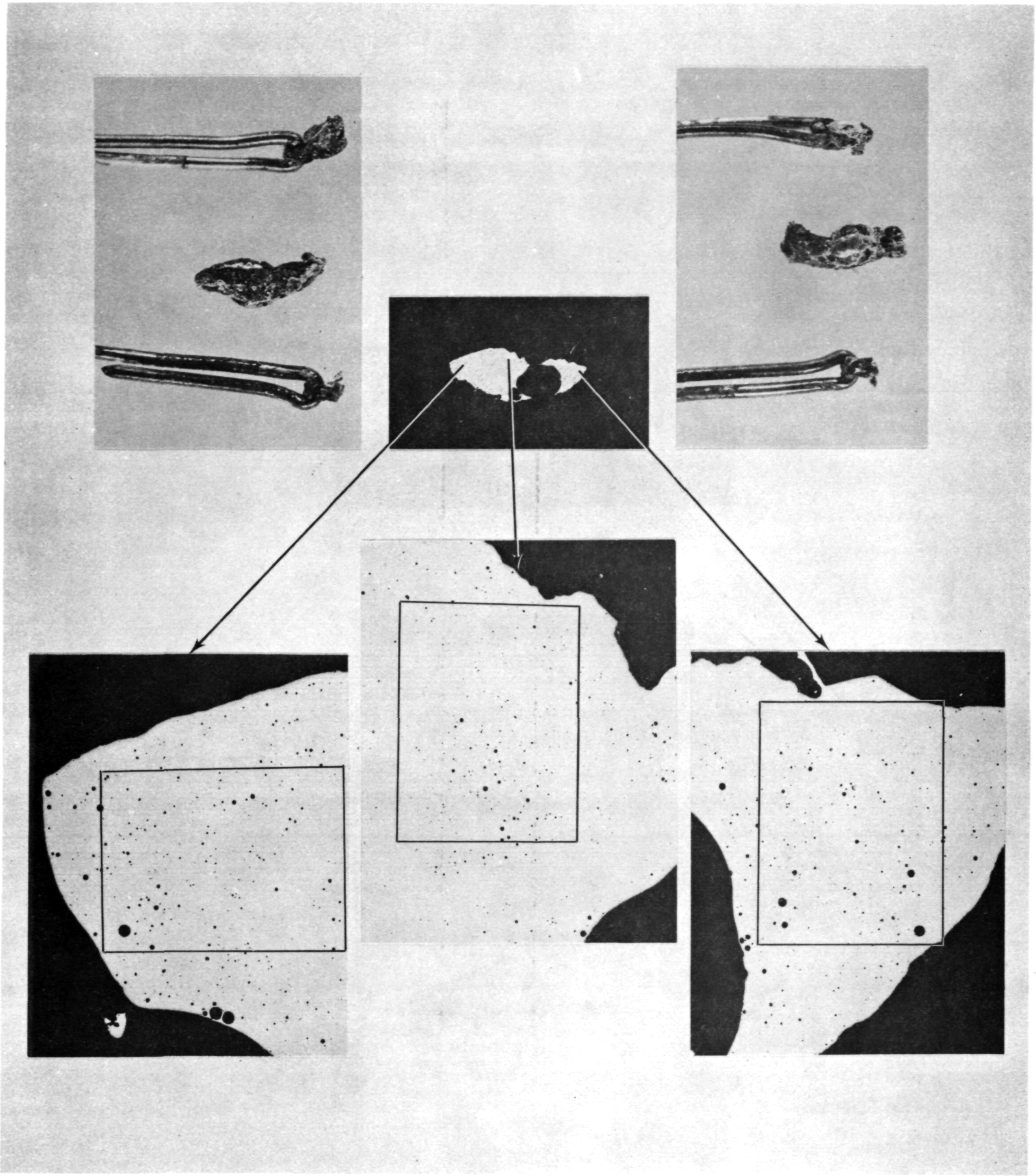

FIGURE 19. Specimen 4-B, GB 2.
The top two photos are 4.2X magnification and show two views of the specimen. The next lower photo is 4.8X and shows a cross-section of the specimen. The bottom three photos are 60X magnification and show as-polished microstructures.

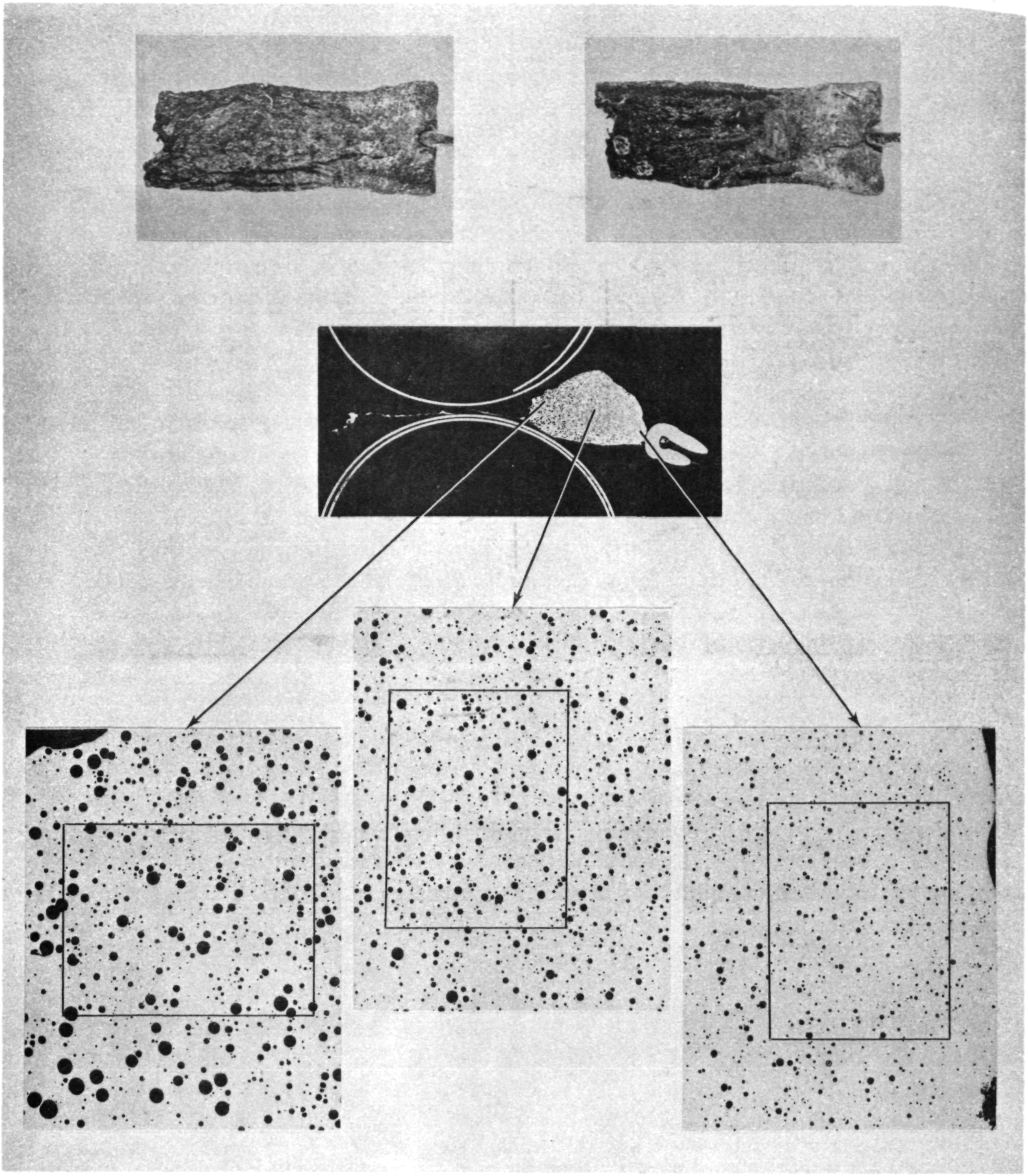

FIGURE 20. Specimen 4-H, GB 2.
The top two photos are 4.2X magnification and show two views of the specimen. The next lower photo is 4.8X and shows a cross-section of the specimen. The bottom three photos are 60X magnification and show as-polished microstructures.

strong (positive) influence on cell volume fraction of a few large cells, and by the weak (negative) influence on pore specific surface area of a few large cells. These effects could be more effectively treated in samples of much greater sample thickness. This will be done for experiments on SPAR Flight No. 2.

Trends were observed toward fewer cells/unit volume, less scatter in the number of cells/unit volume, and a larger median cell size in space processed samples than in ground-based samples. No trends were observed in mean cell size or scatter in mean cell size. More speculation concerning these data, however, must await availability of reliable time-temperature data for the ground-based tested samples.

The above information, particularly that included in Table 3, provides very good characterization of SPAR Flight No. 1 samples for comparison with SPAR Flight No. 2 samples (processed for two longer times above the melting point) to obtain kinetic data. This is quite significant since results of GB 1 and GB 2 testing showed gross sample flow and separation from thermocouples during testing due to the effects of gravity indicating that the ground-based tests associated with SPAR Flight No. 2 will probably not yield much useful data on foam growth. All kinetic information, then, will have to be provided by zero-gravity processed samples.

Formation of a corrosion product scale (in spite of a flushed nitrogen atmosphere) on the samples (Figs. 5 through 20) and the resulting nonuniform constraints on sample movement during foam development, combined with the small sample thickness (on the order of bubble dimensions) presented the most significant obstacles to analysis of results. Largely because of these effects, each sample was used completely for metallographic examinations and no mechanical testing was conducted.

APPENDIX A

ASSEMBLY PROCEDURE AND PHOTOGRAPHS

Assembly Procedure

1. Assemble support wires and thermocouples to samples.

2. Adjust heating element leads and ceramic insulators to mate with terminal bolts (in part 11, R-216) such that the insulators (part 32, R-2160) prevent the heating elements (part 10, R-2160) from shorting to the heat shields (parts 7, 8, and 9, R-2160).

3. Assemble sample support wires (assembly 1, R-2160, Sheet 1) to solenoid-end plate (part 2, R-2160).

4. Assemble water manifold (part 6, R-2160) and manifold plate (part 3, R-2160) to solenoid-end plate (part 2, R-2160).

5. Place water housing (part 19, R-2160) in a support with the solenoid up and with solenoid housing (part 15, R-2160) and heater housing (part 12, R-2160) assembled.

6. Place solenoid end plate (part 2, R-2160) with attached parts to solenoid housing (part 15, R-2160).

7. Place heat shields (parts 7, 8, and 9, R-2160) in grooves of solenoid-end plate (part 2, R-2160).

8. Install heater assembly (part 10, R-2160) in solenoid-end plate (part 2, R-2160) such that insulators fit in the slots in the three heat shields (parts 7, 8, and 9, R-2160).

9. Connect heating element leads to terminal block (part 11, R-2160) along with power leads such that power leads contact the micarta terminal block, the heating element leads cover the power leads, and washer covers each heating element lead between the lead and the head of the attaching bolt (part 45, R-2160).

10. Thread six quartz sample tubes (part 22, R-2160) over thermocouples, samples, and support wires, seating the quartz sample tubes in recesses in solenoid-end plate (part 2, R-2160).

11. Insert seventh quartz tube in center recess of solenoid-end plate (part 2, R-2160) to house control thermocouple (part 51, R-2160).

12. Thread sample thermocouples through base plate (part 4, R-2160) and assemble base plate to heat shields (parts 7, 8 and 9, R-2160) such that quartz tubes (part 22, R-2160) and quartz heater support (part 10, R-2160) align with the recess in the base plate.

13. If all parts fit well through step 12 above, disassemble to step 7 and reassemble with RTV compound on all quartz-metal surfaces.

14. Hot-glue sample thermocouple leads to base plate (part 4, R-2160).

15. Insert control thermocouple (part 51, R-2160) through base plate (part 4, R-2160) and hot-glue lead to base plate.

16. Glue all seven thermocouple lead sets to base plate with RTV.

17. Mount base support plate (part 5, R-2160) to base plate (part 4, R-2160).

18. Solder thermocouple leads to thermocouple cables (chromel to chromel, alumel to alumel) in connector (part 35, R-2160) making sure gasket (part 20, R-2160) is assembled to connector before beginning.

19. Record correlation between sample numbers and thermocouple connections.

20. Verify thermocouple electrical continuity with ohmeter.

21. Assemble furnace base plate (part 14, R-2160) and O-ring (part 38, R-2160) to heater housing (part 12, R-2160) adding washer shims such that base support plate (part 5, R-2160) is held with moderate pressure.

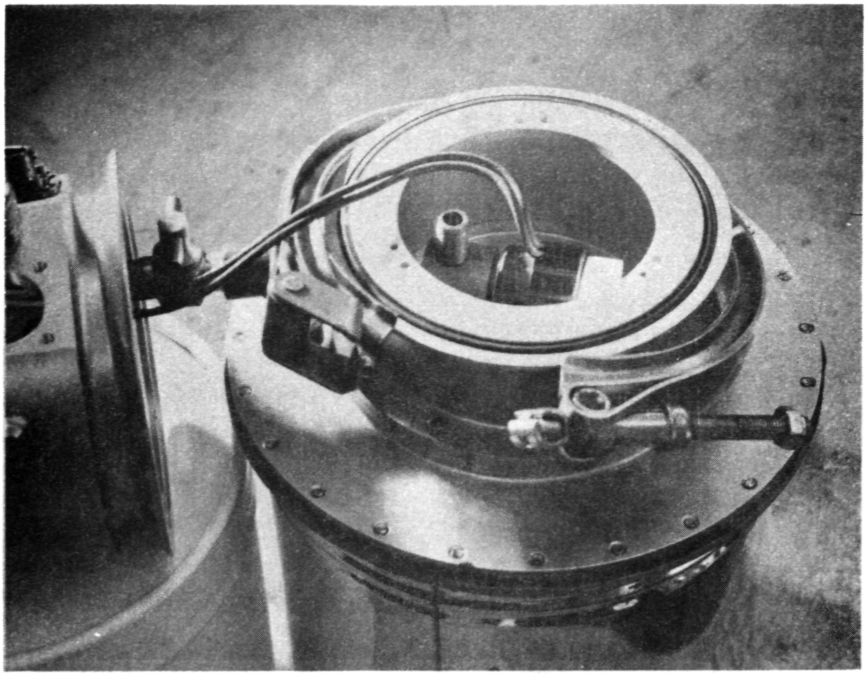

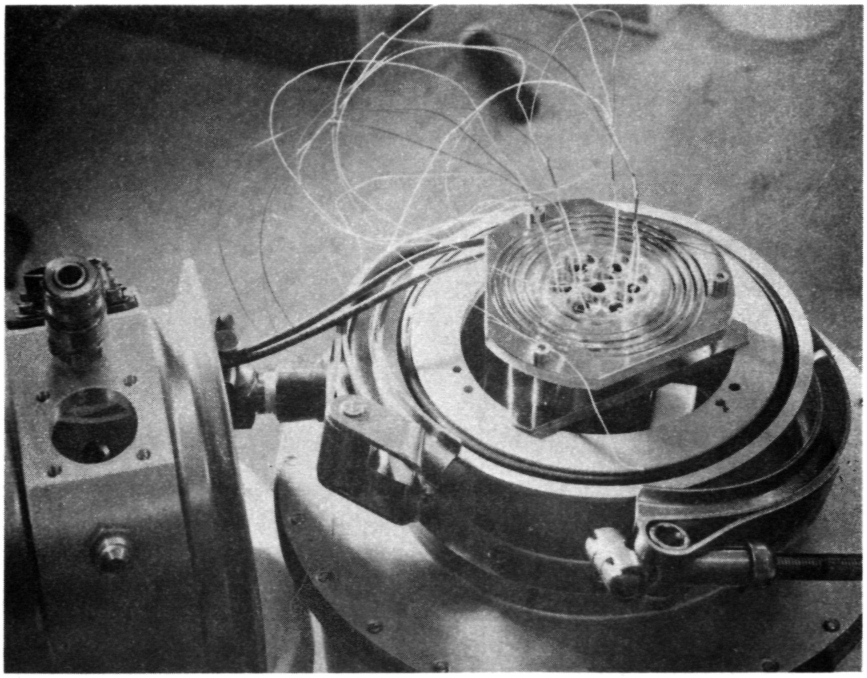

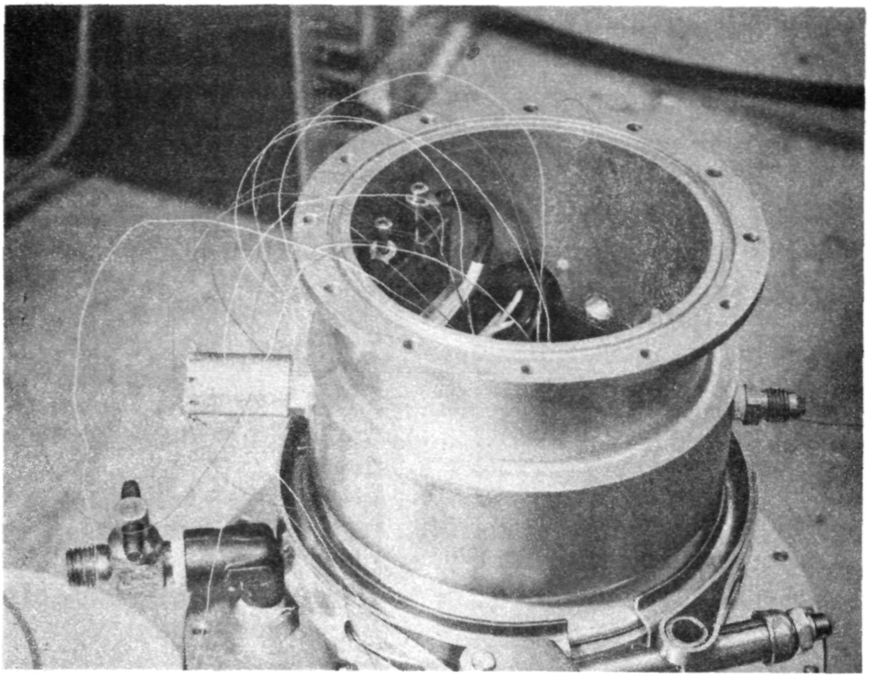

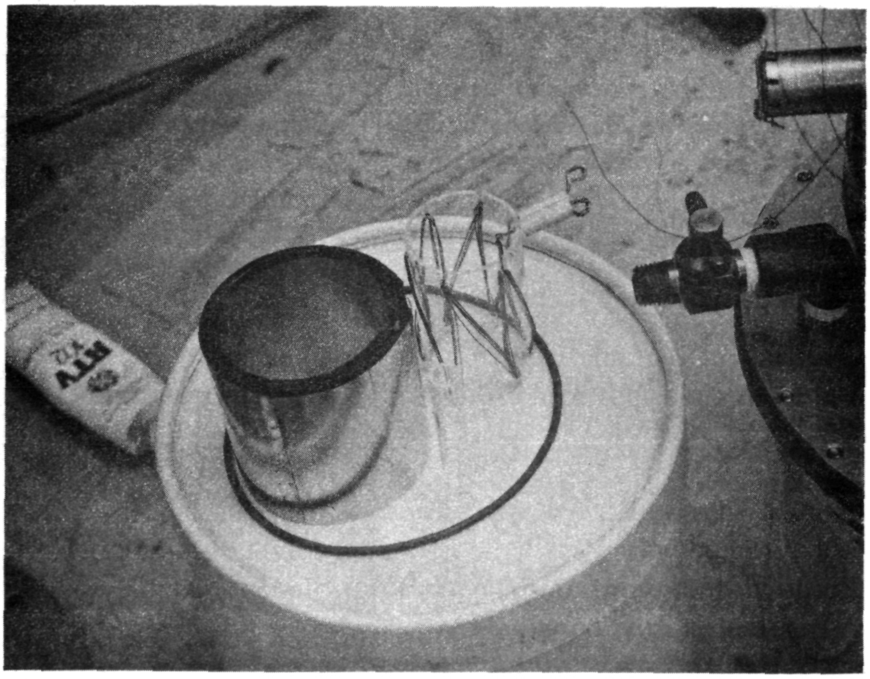
RTV 102

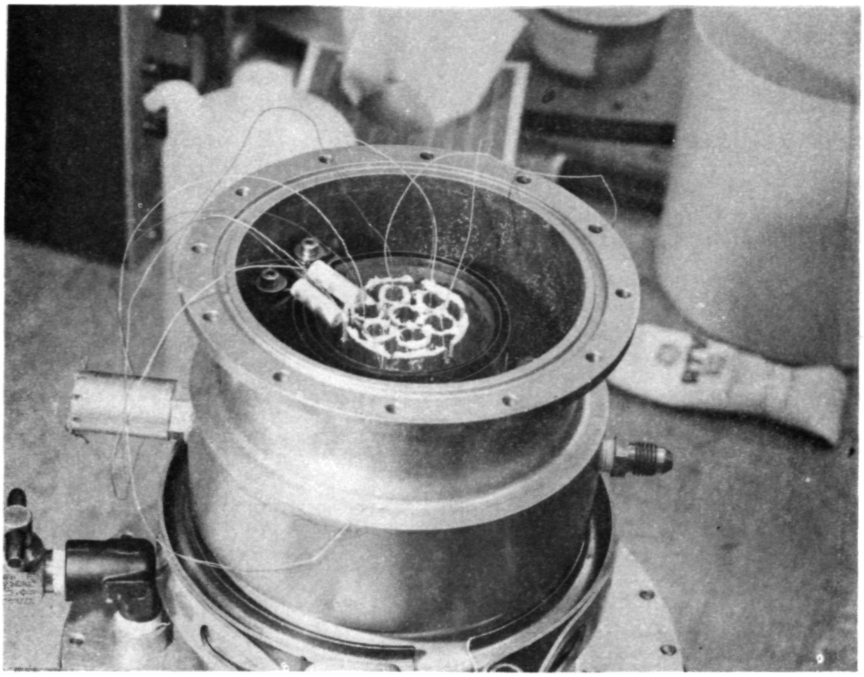

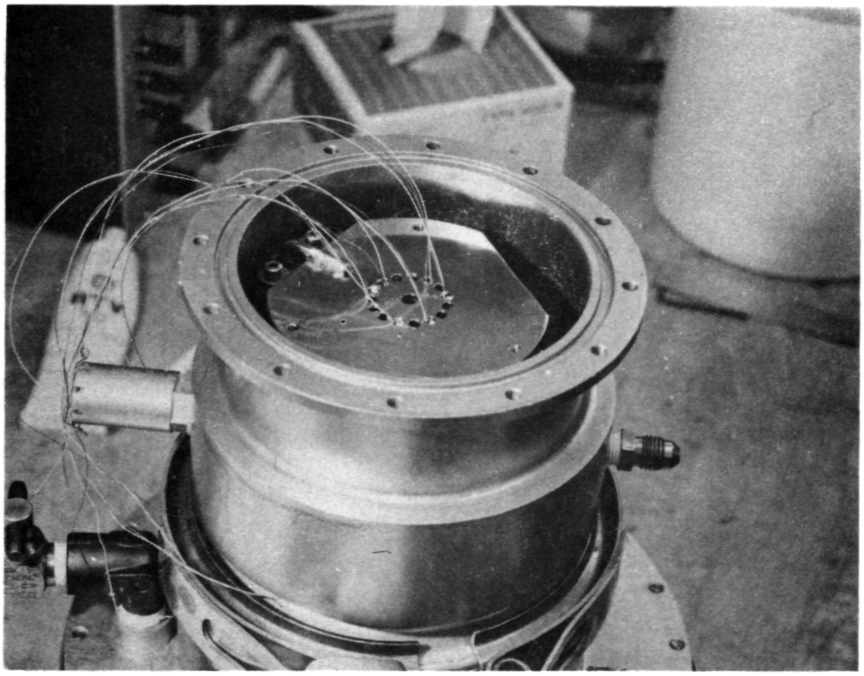

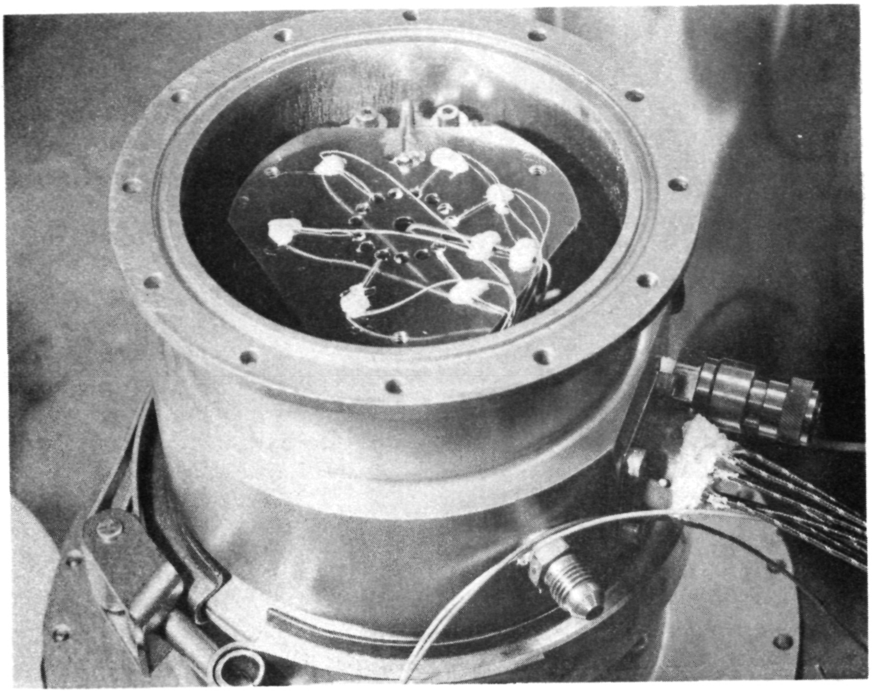

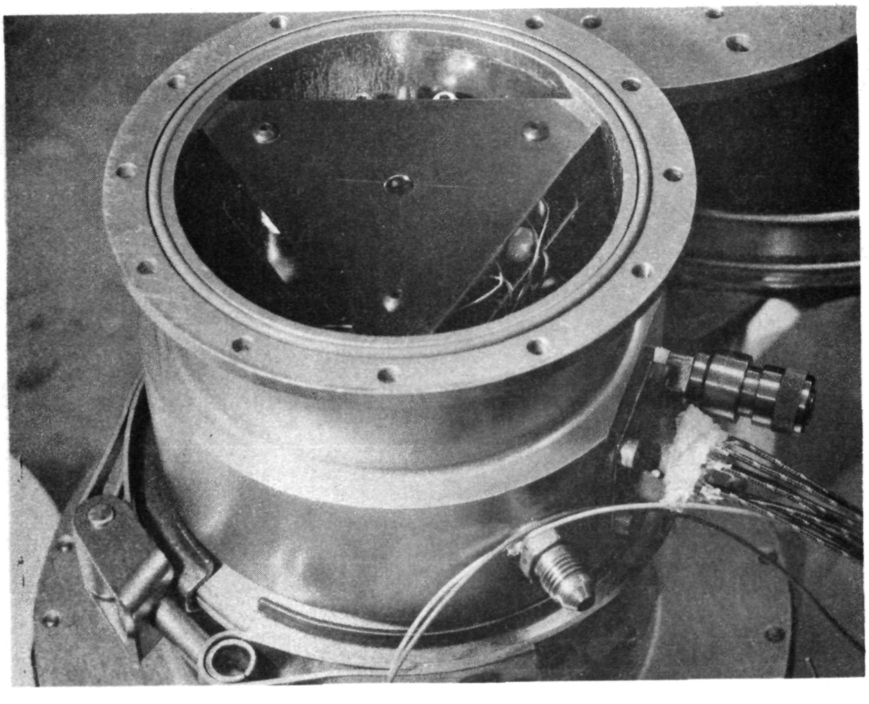

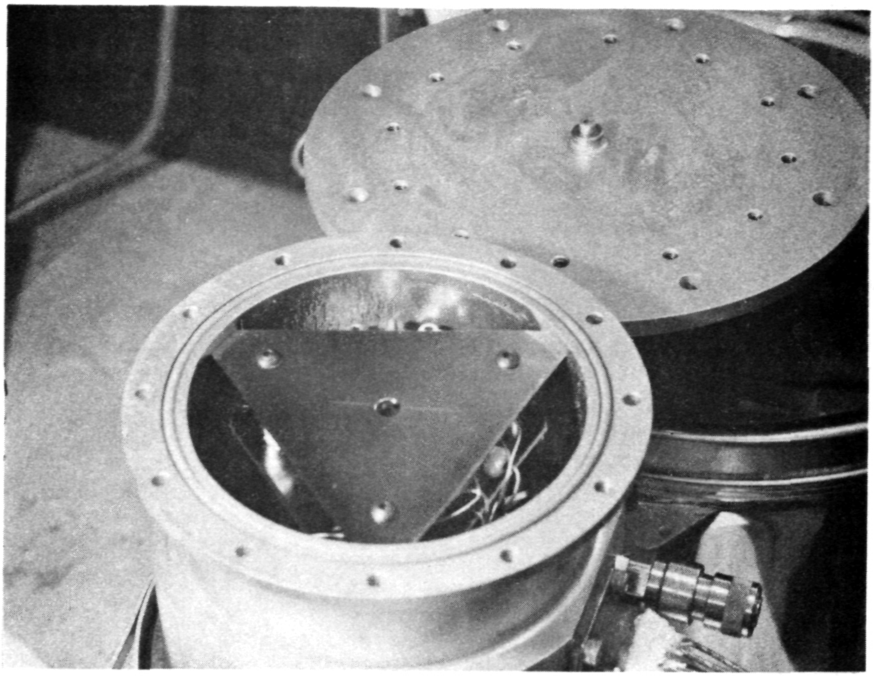

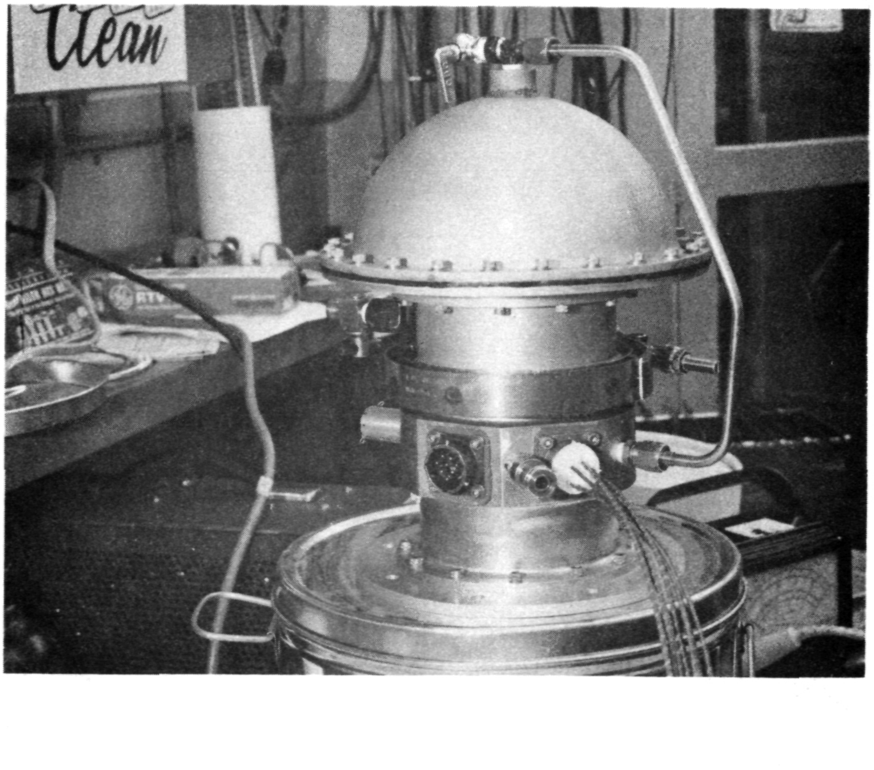
Clean

APPENDIX B

FURNACE DRAWINGS

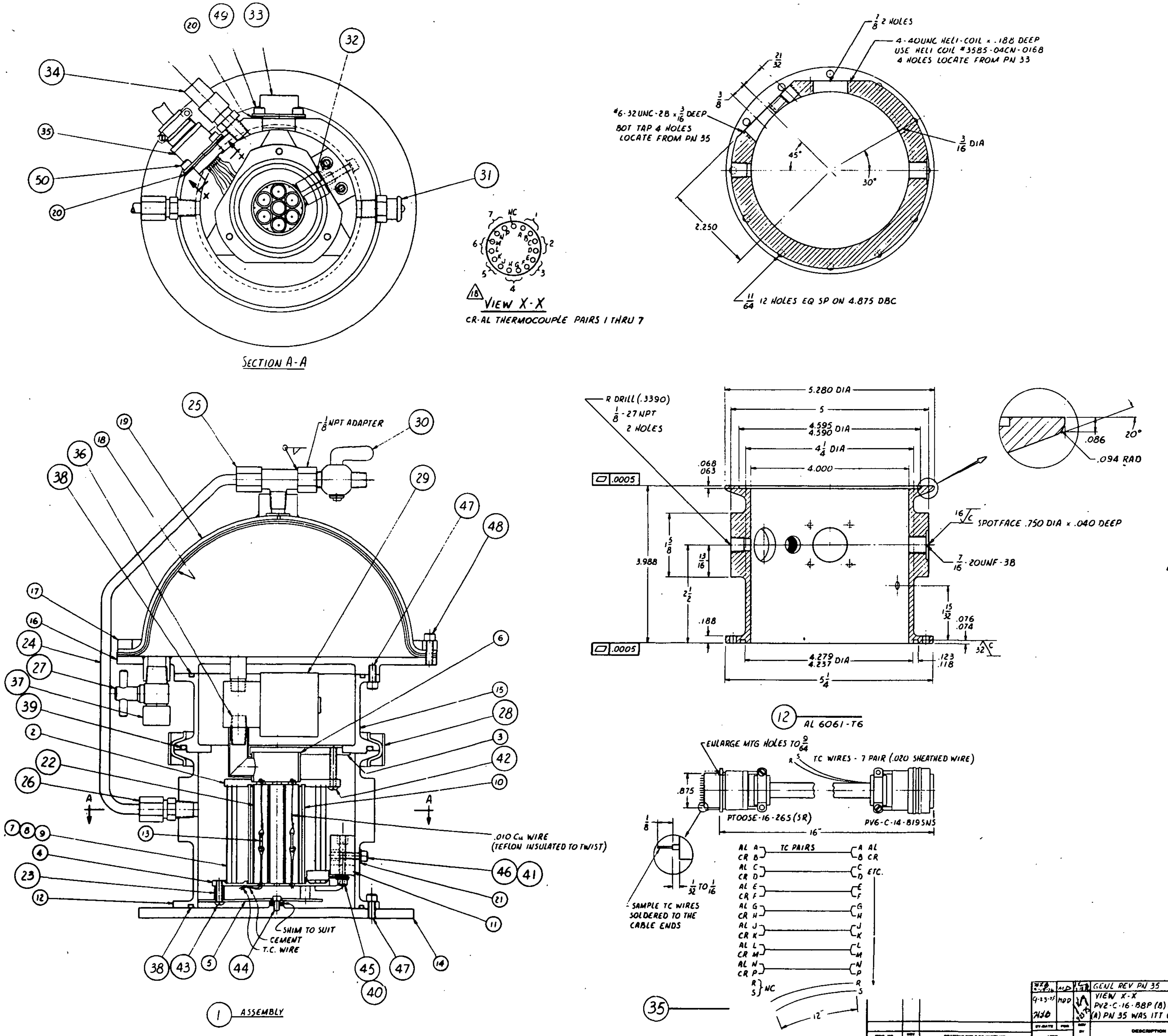

QTY	PN	
	1	ASSY
1	2	PLATE SHEET 2
1	3	↓ ↓
1	4	↓ ↓
1	5	↓ ↓
1	6	MANIFOLD ↓
1	7	SHIELD ↓
1	8	↓ ↓
1	9	↓ ↓
1	10	HTR ↓
1	11	BLOCK ↓
1	12	HSG
6	13	SAMPLE R-2170
1	14	PL G.C. MARSHAL (NASA) MIT-15473-25
1	15	HSG -52
1	16	PL -13
1	17	RING -35
2	18	DIAPHRAM -15
1	19	HSG -14
2	20	GASKET ↓ ↓ -26
1	21	↓ $\frac{3}{8}$OD x $\frac{3}{16}$ID x $\frac{1}{32}$ THK TEFLON
7	22	TUBE 10 MM OD x 1MM WALL x 2.500"L QUARTZ
3	23	SPACER $\frac{1}{4}$OD x .035 WALL x .320L SST
1	24	TUBE $\frac{1}{4}$OD x .035 WALL x 18L CRES
1	25	TEE PARKER NO 4SBTX-SS MODIFY AS SHOWN
1	26	MALE CONN PARKER NO 4FBTX-SS
1	27	SHUT OFF VALVE. CIRCLE SEAL PRECISION NO 9559B-2MM
1	28	V-BAND COUPLING AEROQUIP NO 4565-450
1	29	SOLENOID VALVE. ASCO RED HAT NO 8262C2 24V DC
1	30	SHUT OFF COCK IMPERIAL NO 108EF
1	31	RELIEF VALVE. CIRCLE SEAL NO D559T-1M
2	32	T.C. INSULATOR, OMEGA NO TRA 56414 x $\frac{5}{8}$L
1	33	CONN ITT CANNON PV6-L-16-88SNS
1	34	QUICK-CONNECT BODY ASSY SWAGELOK NO $\frac{1}{4}$QC-100-2-316
1	35	CONN USED AS FEED THRU BENDIX PT02-16-26P WITH PINS REMOVED
1	36	CLOSE NIPPLE $\frac{1}{8}$-27NPT BRASS
1	37	PIPE CAP $\frac{1}{8}$-27NPT BRASS
2	38	O-RING -156 (NOM $4\frac{1}{4}$ID x $\frac{3}{32}$W) PARKER COMPOUND S604-7
1	39	↓ -247 (NOM $4\frac{5}{8}$ID x $\frac{1}{8}$W) ↓
2	40	ALLENUT #6-32UNC-3B SST
1	41	↓ #8-32UNC-3B ↓
3	42	CAP SCR #6-32UNC-3A x 1"L RDH SLTD
3	43	↓ x$\frac{1}{2}$L ↓ ↓
1	44	#5-40UNC-3A x$\frac{3}{8}$L SCH
2	45	#6-32UNC-3A x $1\frac{1}{8}$L
1	46	#8-32UNC-3A x $\frac{3}{4}$L ↓
24	47	x$\frac{7}{16}$L CRES
24	48	↓ x$\frac{5}{8}$L
4	49	#4-40UNC-3A x$\frac{1}{4}$L
4	50	↓ #6-32UNC-3A x$\frac{1}{4}$L ↓ ↓

△2 △1A (PN 35)

NOTE · ALL MATL TO BE AS SPECIFIED OR APPROVED EQL QUALITY

REFERENCE DRAWINGS

DWG. NO.	REV NO	DRAWING TITLE OR INDEX NO.

REVISIONS

BY-DATE	APPD	REV BY DATE	DESCRIPTION	REV NO.
MZB 9-13-76	MD		GENL REV PN 35	2
9-23-75 HJB	MDD		VIEW X-X PV2-C-16-88P (B) ADDED (A) PN 35 WAS ITT CANNON	1

Battelle
Pacific Northwest Laboratories
Richland, Washington 99352

TCU FURNACE
MODIFICATION

J W Patten
MDD 9-4-75
9-4-75
J.W. PATTEN
H. King 9/2/75
SCALE NONE
R-2160
1 2 2

Preceding Page Blank

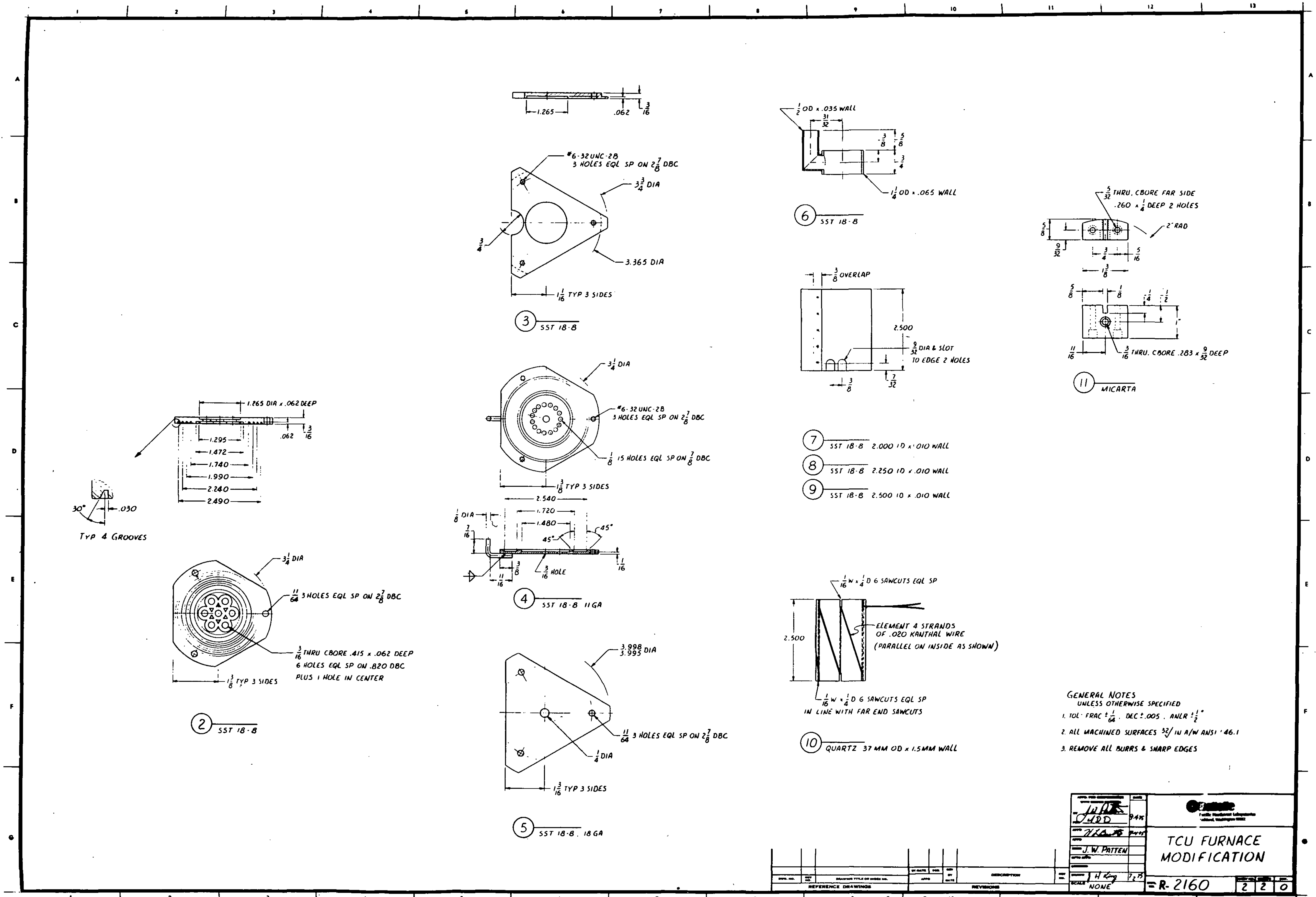

GENERAL NOTES
UNLESS OTHERWISE SPECIFIED

1. TOL: FRAC ± 1/64, DEC ± .005, ANLR ± 1/2°
2. ALL MACHINED SURFACES 32/ IN A/W ANSI '46.1
3. REMOVE ALL BURRS & SHARP EDGES

ODD 9-4-75
J. W. PATTEN
H King 7-2-75
SCALE NONE

TCU FURNACE
MODIFICATION

R-2160

2 2 0

APPENDIX C

ELECTRONICS DRAWINGS

POWER REGULATORS

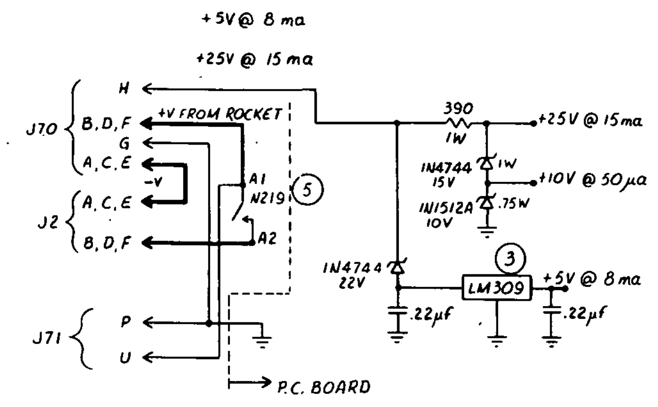

⑦— J70 POWER FROM ROCKET
— J2 POWER TO TCU
⑧— J71 TELEMETRY FROM ROCKET
— J4 THERMOCOUPLES FROM TCU
—— CARRIES 30 AMPS FOR 2 MINUTES

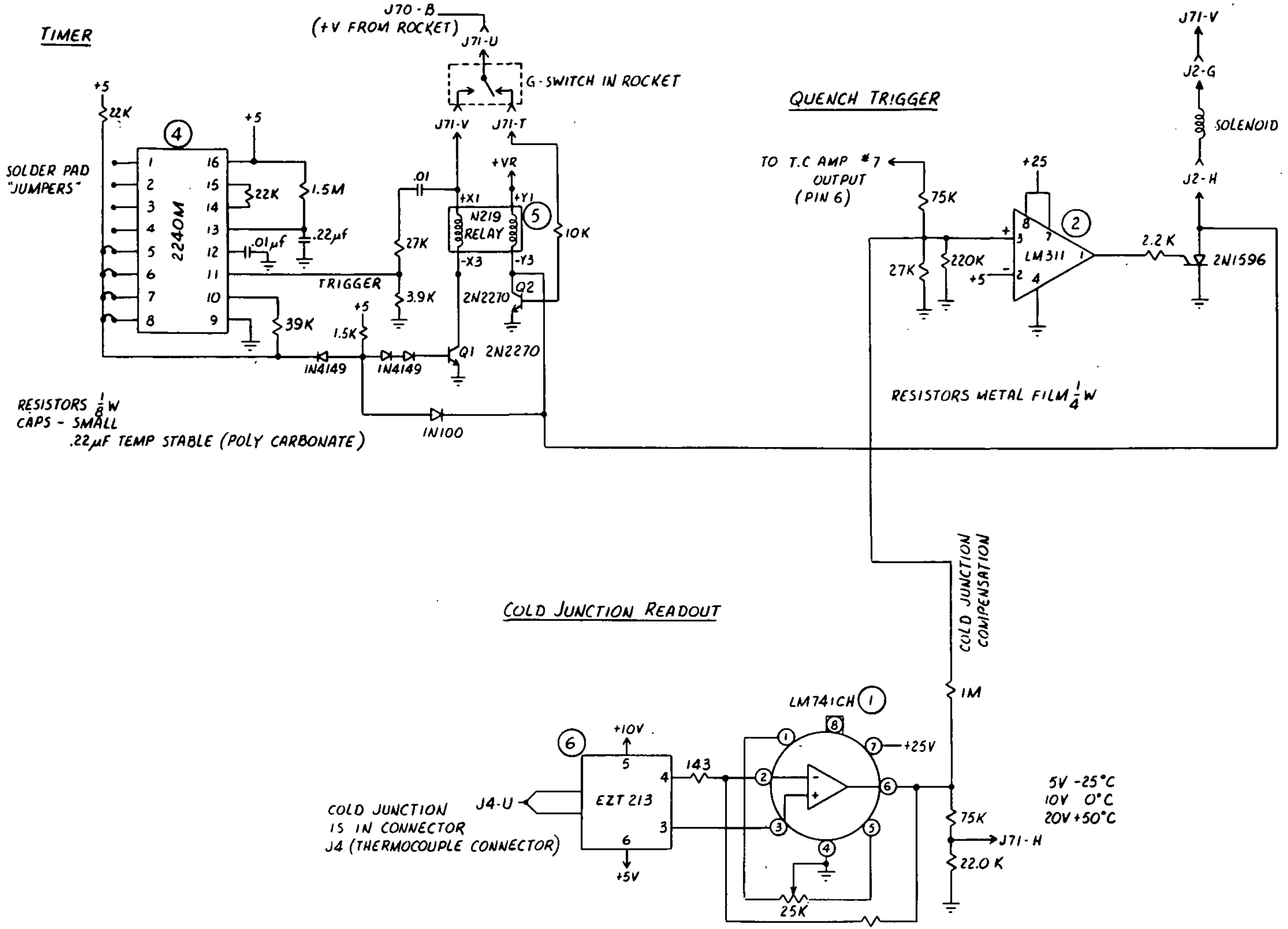

METAL FILM RESISTORS 1/4 W
CERMET POT
EZT 213 - COLD JUNCTION COMPENSATOR 0°C REF

7 T.C. AMPS

ALUMEL-CHROMEL THERMOCOUPLE (AL-CR)

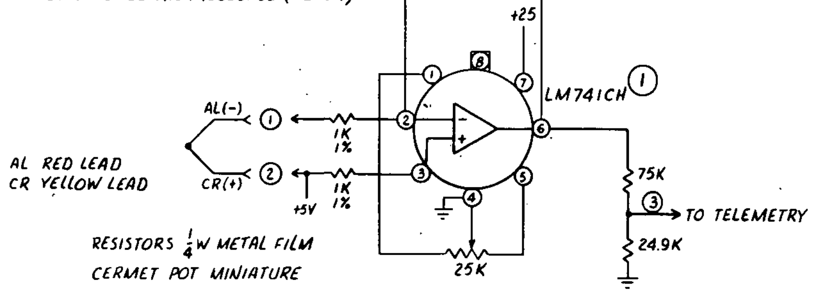

CONNECTOR PIN TABLE

	TC #	AL(-) ①	CR(+) ②	③
SAMPLES	1	J4-A	J4-B	J71-A
	2	C	D	B
	3	E	F	C
	4	G	H	D
	5	J	K	E
	6	L	M	F
FURNACE CENTER	7	N	P	G

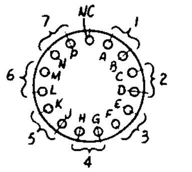

TCU THERMOCOUPLE FEEDTHRU
(VIEW FROM INSIDE TCU)

QTY	PN	
2	8	↑ PV7-C-14-B19P
2	7	ITT CANNON PV7-C-16-B8P
1	6	CONSOLIDATED OMIC DEVICES
1	5	HARTMAN ELEC MFG
1	4	EXAR INTEGRATED SYSTEMS
1	3	↑ ↑
1	2	
8	1	NATIONAL SEMICONDUCTOR

DWG. NO.	REV NO.	DRAWING TITLE OR INDEX NO.

REFERENCE DRAWINGS

BY-DATE	FOR	REV BY DATE	DESCRIPTION	REV NO.
			GENERAL REVISION	1

APPD REVISIONS

APPD. FOR CONFORMANCE WITH DESIGN CRITERIA — DATE
BY — 9-3-75
FOR MDD
APPD — 9-3-75
APPD
ENGR E. GREENWELL
DPTG APPD
CHECKED
DRAWN J. H. King 7-29-75
SCALE

Battelle
Pacific Northwest Laboratories
Richland, Washington 99352

ROCKET FURNACE ELECTRONICS

DWG. NO. R-2173 SHEET NO. 1 SHEETS 2 REV. 1

Preceding Page Blank

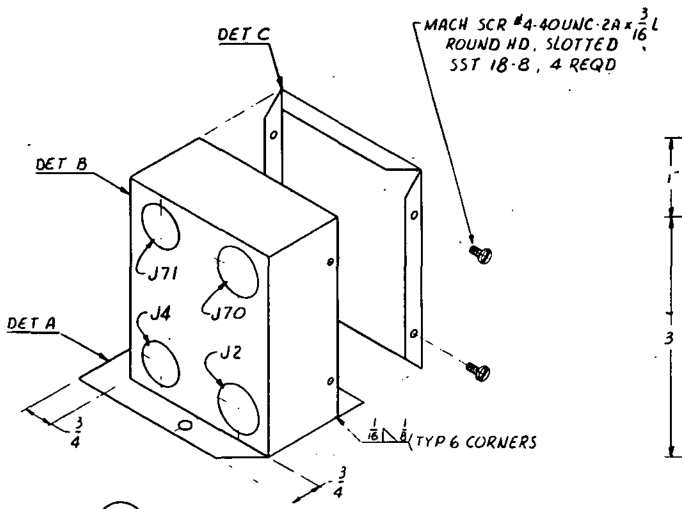

① ELECTRONICS BOX

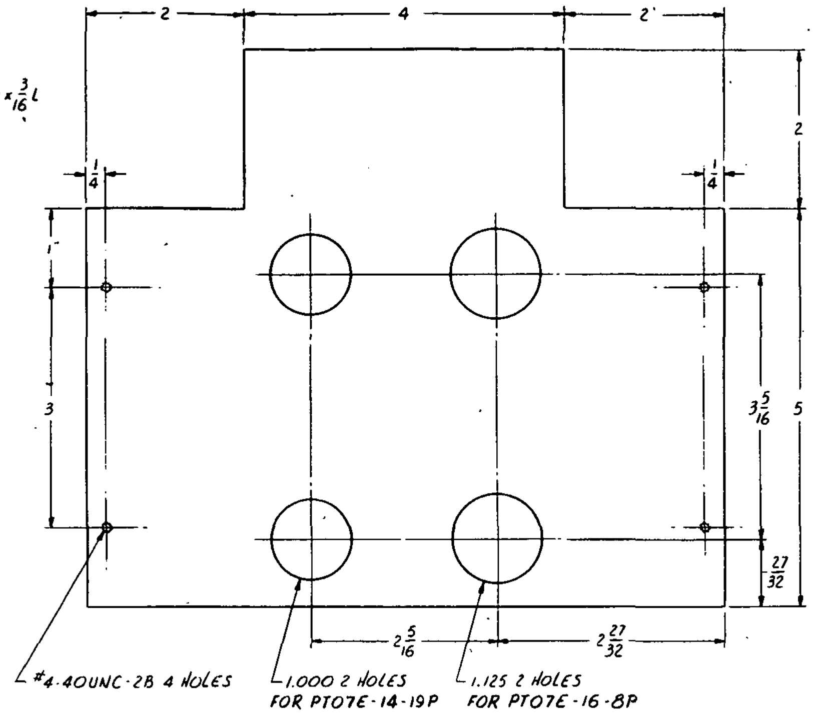

DET B
16 GA SST 304-L

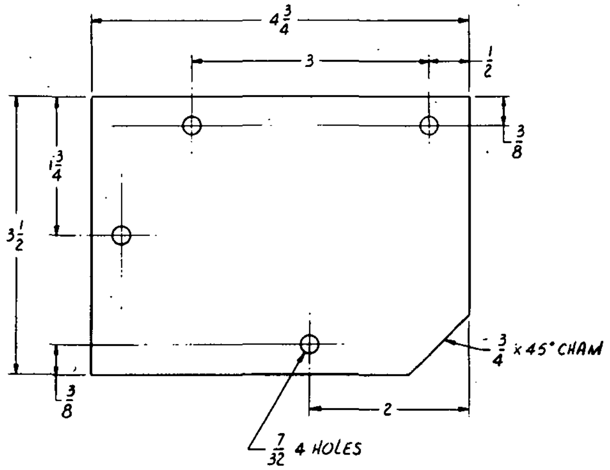

DET A
16 GA SST 304-L

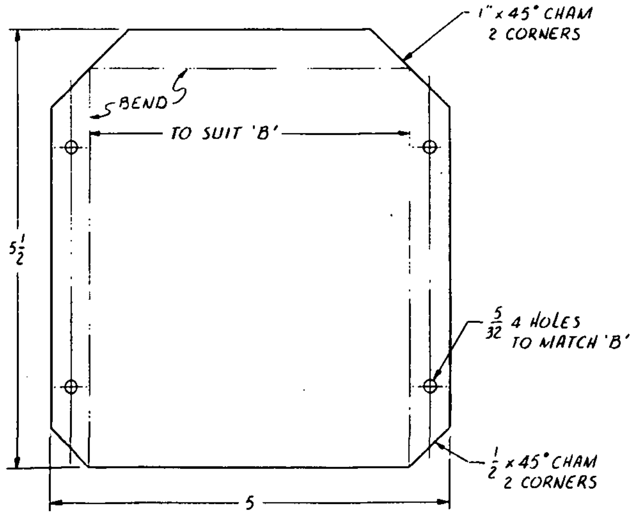

DET C
16 GA SST 304-L

GENERAL NOTES
UNLESS OTHERWISE SPECIFIED
1. TOL: FRAC ± 1/32 DEC ± .005 ANLR ± 1/2°
2. REMOVE ALL BURRS & SHARP EDGES

DWG. NO.	REV NO.	DRAWING TITLE OR INDEX NO.	BY-DATE	FOR	REV BY DATE	DESCRIPTION	REV NO.
REFERENCE DRAWINGS			APPD			REVISIONS	

APPD. FOR CONFORMANCE WITH DESIGN CRITERIA	DATE
BY E. Greenwell	9-3-75
FOR MDD	
APPD H L Butts	9-3-75
APPD	
ENGR E. GREENWELL	
DFTG APPD	
CHECKED	
DRAWN J. H. King	8 22 75
SCALE NONE	

Battelle
Pacific Northwest Laboratories
Richland, Washington 99352

ROCKET FURNACE
ELECTRONICS
DETAILS

DWG. NO. R-2173

SHEET NO.	SHEETS	REV.
2	2	0

Preceding Page Blank

APPENDIX D

POST-FLIGHT PRELIMINARY REPORT

Battelle
Pacific Northwest Laboratories
Battelle Boulevard
Richland, Washington 99352
Telephone (509) 942-2603
Telex 32-6345 FTS 444-2603

January 21, 1976

Roger Chassay
Code PF01S
George C. Marshall Space Flight Center
Marshall Space Flight Center, Alabama 35812

Dear Mr. Chassay:

This letter is intended to fulfill your requirements for an informal Post-Flight Preliminary Report describing results of Flight Number 1. These same results were presented at the Review Meeting at MSFC on January 5, 1976.

The TCU furnace, electronics package, and flight samples were received from White Sands on December 16. It appeared as if the heating elements had been activated, the quench had operated, thermocouples seemed to have remained intact, no quartz was broken, all samples remained in their capsules, and all samples appeared to have melted and foamed.

The first information concerning performance of the thermocouples and electronics was received on January 5 during the Review Meeting at MSFC. The raw thermocouple voltage traces were available to examine at that time. A quick look at these traces led to the preliminary conclusion that all systems functioned satisfactorily.

Preliminary metallographic examination indicates that all samples did melt and foam. No boiling (bubble segregation) was observed in these samples. However, none was observed in ground-based samples either. This may be because bubble diameter is often not greatly different from sample thickness with the current sample design. It may prove true that boiling effects are only evident in much thicker samples.

The zero-gravity samples did not sag, flow, or drop free of their support wires as the ground-based samples did. Aside from distortions caused during the quench and by shifting support wires, the zero-gravity samples seemed to maintain the original configurations quite well during melting and foaming, which could be important to the practical manufacture of metal foam products.

In summary, all of the minimum success criteria for this experiment were met. In addition, metal foam materials have now been produced both on earth and in a zero-gravity environment. Data are available which are expected to reveal some of the effects of gravity on formation of metal foams and indicate, in a preliminary way, the potential variations in foam structure.

Very truly yours,

J. W. Patten

J. W. Patten
Mat'ls & Process Engr. Section
231-Z Bldg., 200-W Area

JWP:amd

REFERENCES

1. Blachman, A. G.: IBM Research Report RC 3952, IBM Thomas J. Watson Research Center, P.O. Box 218, Yorktown Heights, NY, 1972.

2. Lee, William W. Y. and Oblas, Daniel: J. Appl. Phys., vol. 46, 1728, 1975.

CHAPTER III

UNIFORM DISPERSIONS OF CRYSTALLIZATION PROCESSING

Experiment 74-15

By

Donald R. Uhlman

Massachusetts Institute of Technology

INTRODUCTION

This report describes the preparation and characterization of the sample which was flown in the Grumman (74-36) apparatus on the SPAR 1 flight on December 11, 1975. It also describes the ground-based tests which were carried out in support of this flight experiment. It discusses as well the conclusions which were drawn from this first flight experiment and suggestions for the follow-on experiments.

The experiment which was flown (74-36/15) represented an initial part of a study of the interaction of second-phase particles with a solidification front. The experiment consisted of a single sample tube which was melted and solidified in the apparatus provided by the Grumman Aerospace Corp. Workers at Grumman utilized the other three sample tubes of the apparatus for their own experiments.

Because of the constraints imposed by the apparatus and the solidification conditions which it employed, the 74-36/15 experiment on the SPAR 1 flight was not intended to provide a critical or definitive evaluation of the physical phenomena. Rather, it represented a piggyback experiment which was intended primarily to provide insight into the characteristics of the research rocket flights and experimental variables which will be critical in future, definitive flights. Beyond this, it was intended to demonstrate within the time limitations of research rocket flight some important features of the interaction between second-phase particles and a solidification front.

Among the questions to be answered by the 74-36/15 experiment on the SPAR 1 flight were the following: (1) If a sample having the dimensions of the Grumman sample tubes is partially melted prior to launch, are the liquid motions associated with blast-off and despin sufficient to achieve a uniform distribution of particles in the liquid? (2) If the sample is partially molten prior to launch, does significant melting back of the solid occur after blast-off? (3) Can the interaction between particles and interface be elucidated from *ex post facto* observations and from low magnification photographic recording taken during flight? (4) How critical is close control of the thermal regime during solidification? and (5) Can particle rejection and entrapment be documented for a microgravity environment, and does the elimination of gravitational effects substantially modify the characteristics of the solidification behavior? Useful insight into each of these areas was provided by the results of the single sample on the SPAR 1 flight.

Preceding Page Blank

Our interest in the behavior of second-phase particles at a solidification front and in studying this behavior in a microgravity environment has been motivated by two principal considerations. First, such behavior seems certain to be important for the fabrication in space of many composite materials having unique microstructures. It already seems clear that uniform and unique dispersions of solid or liquid phases in matrix liquids can be obtained in the space environment. Interest in this area is illustrated by Prof. Dr. Heye's experiment on the SPAR 1 flight (74-63), which was concerned with the hardening of metallic superconductors using second-phase ceramic particles. In this work, as in nearly all other attempts to achieve uniform dispersions by crystallization processing, the crystallization of the matrix liquid upon cooling can substantially change the initially uniform distribution of second-phase material due to rejection of the second-phase materials at the solidification front.

Second, and perhaps more important for the overall program of space applications, the understanding and insight gained in the study of particles-at-interfaces in space can be used to provide improved understanding and control of many processes and phenomena on Earth. Among the applications areas of the present investigation are the behavior of inclusions in metal castings, the phenomenon of frost heave in soils, the agglomeration of small (micron and submicron size) powders of ceramic materials, the development of dust-repellent coatings for glasses, and even the interaction between blood cells and other materials.

In previous work [1-5] it was found that at sufficiently small growth rates, particles of nearly all materials are rejected by a moving crystal-liquid interface; i.e., they are pushed ahead into the liquid, traveling along with the interface as it advances. Particles can thus be pushed for long distances, thousands of times the particle diameters.

Particles at, and moving along with, the interface can be observed to impinge upon other particles in the liquid. These are, in turn, pushed by the particles at the interface and move along as the interface advances. These may impinge upon still other particles, and in this way large pile-ups of particles can be pushed by the advancing interface. Such pile-ups, extending dozens of particles in the direction normal to the interface, have been observed.

As the growth rate is increased, a speed is reached at which a particle or pile-up of particles ceases to be pushed by the interface, but is trapped or incorporated in the solid. This speed represents a "critical velocity" for particle rejection by the interface. The critical velocity is in general different for different types of particles in a given matrix, as well as for different matrix materials with a given type of particle.

It is apparent that the pushing of a particle or pile-up of particles by an interface demands both a force preventing incorporation of the particle in the crystal and a feeding of fresh material to the region of the interface immediately behind the center of the particle. The interaction of the particles with the interface, which is responsible for their rejection from the growing solid, can be represented in terms of a short-range repulsion which exists between the particle and the solid. The particle is pushed ahead of the advancing interface and becomes incorporated into the solid when liquid cannot diffuse sufficiently rapidly to the growing solid behind the particle.

The present investigation is concerned broadly with developing improved understanding of the interaction between second-phase particles and an advancing solidification front, and with developing criteria for the solidification processing of many two-phase composite materials in space. The elimination in space of the effects of density differences between particles and matrix offers the opportunity for systematically determining the factors which are important to the phenomenon of particle rejection and incorporation.

In addition to obtaining appropriate experimental data, the investigation will also be concerned with developing a satisfactory theoretical description of the behavior of second-phase particles at a solidification front. In this work, the forces of interaction between particles and interfaces will be computed from the refractive indices, characteristic absorption frequencies, and static dielectric constants following the approach suggested by Lifshitz [6]. Also to be explored is the intriguing approach suggested by Neumann [7], in which the interaction is evaluated from measurements of contact angles. Both descriptions of the interaction will be combined with a description of the relevant transport phenomena to obtain theoretical descriptions of the expected critical velocities.

With this background, let us consider the results obtained from the sample capsule on the SPAR 1 flight, as well as the results of companion ground-based studies.

GROUND-BASED STUDIES, CRITICAL VELOCITY

The single most important parameter used to evaluate the interaction of second-phase particles with a solidification front is the so-called critical velocity. As indicated above, the critical velocity is the solidification rate below which the particles are rejected by the advancing interface and above which they are incorporated into the growing crystal. The critical velocity can conveniently be measured on Earth — subject to the reservations discussed below — by carrying out solidification in either of two geometries: (1) a horizontal geometry in which the sample is contained within a thin chamber, with the particles resting (because of gravity) on the bottom support of the chamber, and the solidification behavior observed through a microscope as the interface advances horizontally; and (2) a vertical geometry in which the particles rest on the interface (because of gravity) as the interface advances vertically upward. In this case, the behavior has usually been characterized by measuring the distribution of particles after solidification rather than by direct observation during the solidification. In both cases, the effects of gravity introduce a significant complication into the measurement.

In work carried out to date in our laboratory, the horizontal solidification geometry has been employed. Selected particles are mixed into a molten sample contained between a glass support and a cover glass, and the sample is cooled and crystallized rapidly. The resulting sample is typically in the range of 50 to 200 microns in thickness, and is confined between two glass plates. The sample is then located in a controlled temperature gradient in the apparatus shown schematically in Figure 1. This apparatus represents a modification of that described originally by Hunt and Jackson [8]. The sample is traversed through the temperature gradient by a motor-driven screw to provide the desired rate of solidification. When viewed through a microscope at magnifications in the range of 100X, particles as small as 2 to 5 microns in diameter can easily be seen, and their behavior can be followed individually as solidification proceeds. By varying the solidification rate, the critical velocity for each type (and size) of particle can be measured.

While this geometry has the disadvantage that the particles rest on the bottom supporting glass plate and are subjected to unknown frictional forces, the thin horizontal geometry has the advantage of simplicity and ease of viewing the sample at high magnification over a range of readily controlled growth rates. A version of this apparatus appropriate for solidification in a vertical geometry is presently being developed.

Previous measurements of critical velocities have been carried out for a number of particle-matrix combinations. In all cases, the matrix materials have been characterized by large entropies of fusion in Jackson's sense [9]. Since the entropy of fusion has been demonstrated to have a significant effect on the crystal-liquid interface morphology as well as upon many characteristics of the crystallization process, it has seemed highly desirable to explore the behavior of second-phase particles in matrix materials characterized by low entropies of fusion. In addition to the intrinsic interest in such behavior, our

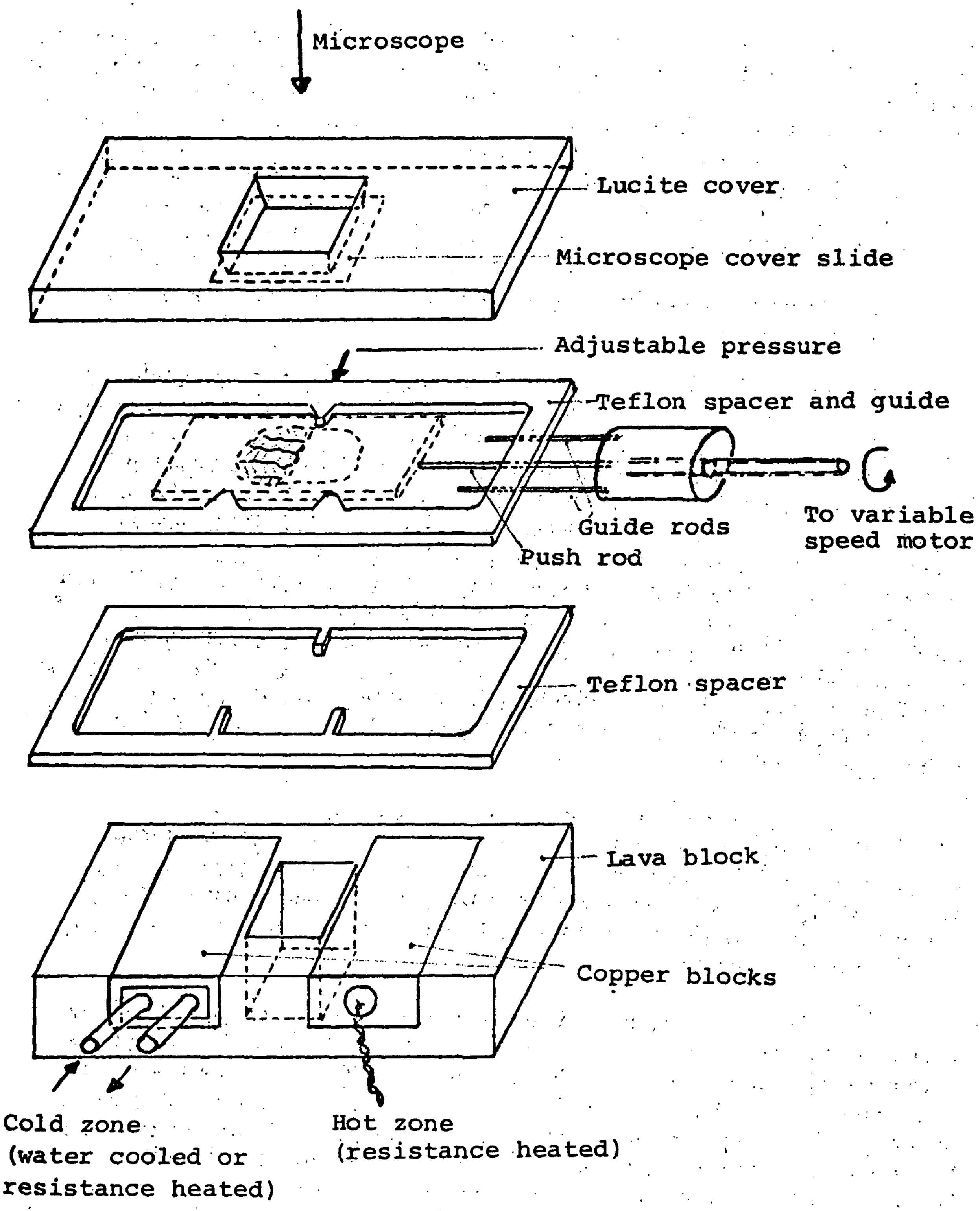

Figure 1. Controlled gradient microscope stage used in measuring rejection-incorporation of second-phase particles at solidification fronts. (The sample was translated through the temperature gradient by the drive screw.)

concern in this regard has been prompted by the fact that many technologically important materials such as metals are characterized by small entropies of fusion. For this reason, carbon tetrabromide (CBr_4), which was originally identified by Jackson and Hunt [10] as having a small entropy of fusion, was chosen as the first matrix material for the SPAR 1 flight. Ground-based measurements of the critical velocity for various particles in CBr_4 were carried out using the apparatus shown in Figure 1. The particles which were investigated included zinc, tungsten, oxide glasses of two compositions, aluminum oxide, ferric oxide, and zinc sulfide. In all cases, the critical velocities were determined to be less than 1 micron sec^{-1}.

These results posed significant problems for use of CBr_4 as the matrix material in the SPAR 1 experimental capsule, since it was desired to demonstrate particle rejection in the microgravity environment. The problems were associated with the fact that the solidification rate which was expected to be provided by the Grumman apparatus was in the range of 10 microns sec^{-1}. Hence it would be expected that all the particles would be incorporated in the crystal during solidification of the sample in the apparatus. For this reason, it was decided to seek a matrix liquid having a melting point in the range of 75 to 100°C (to be consistent with the Grumman experiments), in which rejection of particles at the solidification front might be observed at the rates imposed by the apparatus.

In surveying a number of organic matrix materials, the results shown in Table 1 were obtained. Of the materials investigated, naphthalene was selected as having appropriately large critical velocities (in excess of 10 microns sec^{-1} for zinc) coupled with a melting point in the desired range (about 80°C). More detailed measurements were therefore carried out on the critical velocities of a variety of particles in naphthalene. The resulting data are shown in Table 2.

One particular interesting feature of the interaction between second-phase particles and a solidification front was uncovered during the course of this characterization. In particular, while theoretical attention has principally been directed to the behavior of an isolated particle at a crystal-liquid interface, in practice sizable pile-ups of particles are often observed to be pushed along by the advancing interface (see "Introduction"). In characterizing particle-matrix systems for possible inclusion in the SPAR 1 sample, attention was directed to the behavior of systems containing particles with a range of chemistries and sizes. It was found that for growth rates exceeding the critical velocity for large particles, a sizable pile-up of large particles can be pushed by the interface provided that the large particles are separated from the interface by smaller particles whose critical velocities are not exceeded by the imposed growth rate.

TABLE 1. PRELIMINARY SCREENING OF ORGANIC MATRIX MATERIALS

Low Entropy of Fusion Organics	Molecular Weight	Density, g cm^{-3}	Melting Point, °C	Critical Velocity, µm sec^{-1}
Camphene $C_{10}H_{16}$	136.24	0.84	51	Zn Vc<1 dendritic growth
Succinonitrile $NC\ CH_2\ CH_2\ CN$	80.09	0.99	55	Vc<0.5
Carbon Tetrabromide CBr_4	331.65	3.0	91	$V_c<0.3$
d-Camphor $C_{10}H_{16}O$	152.24	0.99	175	Zn $V_c \sim$ 1-10
High Entropy of Fusion Organics				
Thymol $5CH_3\ C_6H_3-2-CH(CH_3)_2$ $-1-OH$	150.22	0.92	52	Zn $V_c \sim 5$ glass $V_c \sim 1.5$
O-Terphenyl $C_6H_5C_6H_4C_6H_5$	230.31		58	Zn $V_c \sim 2.5$
3-4 Dimethyl phenol $(CH_3)_2\ C_6H_3OH$	122.17	0.98	68	Zn $V_c \sim 5$
3-5 Dimethyl phenol $(CH_3)_2\ C_6H_3OH$	122.17	0.97	68	Zn $V_c \sim 1$ needle growth
Durene $1,2,4,5-(CH_3)_4$ C_6H_2	134.22	0.83	79	Zn $V_c \sim 7$
Biphenyl $C_6H_5C_6H_5$	154.21		70	Zn $V_c \lesssim 1$
Naphthalene $C_{10}H_8$	128.17	1.02	81	Zn $V_c > 35$
Vanilin $4HO\ C_6H_3-3-OCH_3$ $-1-CHO$	152.15		83	No pushing

TABLE 1. (Concluded)

Low Entropy of Fusion Organics	Molecular Weight	Density, g cm^{-3}	Melting Point, °C	Critical Velocity, μm sec^{-1}
α-phenyl o-cresol	184.24		84	Zn $V_c \lesssim 1.5$
p. tert. Pentyl Phenol $C_2H_5(CH_3)_2\ CC_6H_4OH$	164.25		94	$V_c < 1$
3'-Hydroxyacetophenone $HOC_6H_4COCH_3$	136.15		95	Zn $V_c \sim 1$-2 needle growth
Acenaphtene $C_{12}H_{10}$	154.21	1.02	96	Zn attracted to interface, $V_c \sim 1$
Phenanthrene $C_{14}H_2O$	178.23	0.98	101	Zn $V_c \lesssim 1$
2 Naphthyl Benzoate $C_{10}H_5COOC_{10}H_7$	248.28		108	No pushing
Resorcinol C_6H_{14}-1,3-$(OH)_2$	110.11	1.27	111	$V_c \lesssim 1$
Idoform CHI_3	393.73	4.0	123	No pushing

TABLE 2. CRITICAL VELOCITIES OF VARIOUS PARTICLES IN NAPHTHALENE

Particle	Diameter, μm	Critical Velocity, μm sec^{-1}
Zinc	2-7	> 35
Iron Oxide	3	> 35
Calcium Sulfate	1*	> 35
Magnesium Oxide	1*	> 35
Tungsten	2-10	20
Copper	5	< 2
Glass spheres	7	11
	16	3
	50-80	< 0.3

---

*Small particles in large aggregates

This phenomenon presumably reflects the greater ease of liquid transport behind the smaller particles (in the region between the smaller particles and the crystal). It has also been observed for systems in which different types of particles, characterized by different critical velocities, are employed. The behavior is illustrated schematically in Figure 2 and was commonly observed during the solidification of naphthalene with various combinations of second-phase particles.

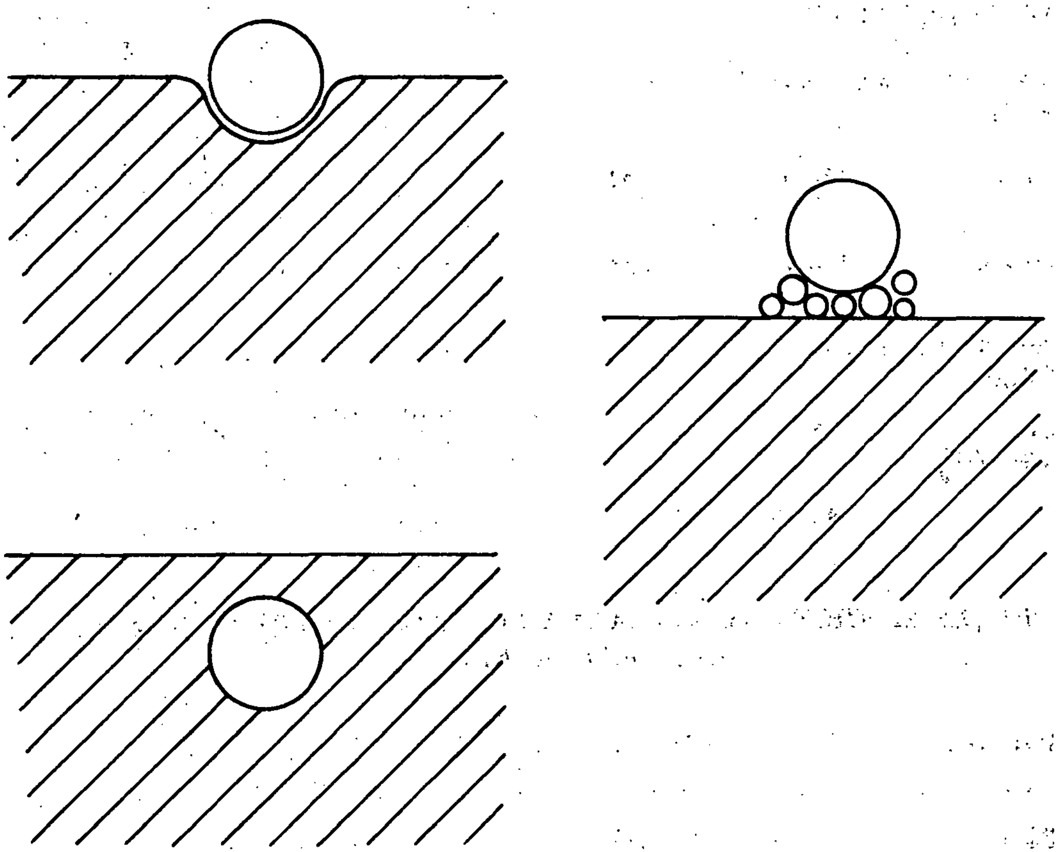

Figure 2. An individual large glass sphere is trapped by the growing crystal (left); small spheres are rejected by the crystal and prevent the large sphere from being trapped (right).

The determinations of the critical velocities in this phase of this investigation were used to select the particle-matrix system which was flown in the SPAR 1 experiment. In particular, it was decided to use a sample consisting of naphthalene with glass beads of two compositions as well as with zinc particles (see the discussion in the following section).

GROUND-BASED STUDIES, FLIGHT APPARATUS

As indicated above, the experiment run on the SPAR 1 flight was carried out in a sample tube of the 74-36 apparatus. This apparatus was designed and built by the Grumman Aerospace Corp. and was used principally for the experiments of Drs. G. Papazian and W. Wilcox. In particular, it was designed to provide a controlled solidification rate in the range of 10 microns sec^{-1} for carbon tetrabromide for investigating phenomena such as the nucleation and growth of bubbles at the solidification front.

As indicated previously, our original plans for the SPAR 1 flight were based on an intended use of carbon tetrabromide as the matrix material. This in turn was based on the expectation that the solidification rate of 10 micron sec^{-1} provided by the Grumman apparatus would be appropriate for our experiment. As described above, however, it was found that all second-phase particles investigated in CBr_4 were incorporated into the advancing solid at solidification rates greater than 1 micron sec^{-1}. It seemed likely, therefore, that no particles would be rejected in the rocket experiment at the imposed growth rate of 10 microns sec^{-1}, and hence, the objective of obtaining insight into the ease or difficulty of determining rejection-incorporation would not be realized.

For this reason, it seemed desirable to select a suitable replacement material for carbon tetrabromide which could be used in the flight apparatus without disturbing the experiments of Papazian and Wilcox. Among several considerations, the melting point of the replacement material had to be close to that of CBr_4. Since there are no known organic materials characterized by small entropies of fusion which have melting points within 20°C of that of carbon tetrabromide, it was decided to postpone space experiments using low entropy of fusion organic materials until an apparatus is available for carrying out solidification at controlled low rates.

After surveying some dozen organic materials using the microscopic technique described in the previous section, it was decided to use naphthalene as the basic material with the most desirable combination of characteristics for the SPAR 1 flight. At slow growth rates, naphthalene grows smooth, faceted interface and does not break down into dendritic or needle-like crystallization morphologies. Further, the critical velocities for several types of particles in naphthalene exceed 10 microns sec^{-1}; still further, certain aspects of the behavior of second-phase particles in this material have recently been explored by Wilcox and Neumann and their collaborators.

Table 3 shows a comparison of some of the important material characteristics of carbon tetrabromide and naphthalene. As noted earlier, the most significant difference between the two materials lies in their entropy of fusion. The entropy of fusion of CBr_4 is only about 0.8 R, while that of naphthalene is about 6.4 R. This difference in the heat of fusion between the two materials has a profound effect upon the interface morphologies and details of the crystallization process in the two materials.

TABLE 3. COMPARISON OF PROPERTIES OF NAPHTHALENE AND CARBON TETRABROMIDE

	Naphthalene	Carbon Tetrabromide
Molecular Weight	128.18	331.65
Melting Point	80.2°C	91°C
Boiling Point	210.8°C	189°C
Density	1.145 g cm^{-3} @ 24°C	2.96 g cm^{-3} @ 100°C
Viscosity	80°C 0.967 cp	100°C 2.44 cp
	100°C 0.776 cp	139°C 1.48 cp
Heat of Fusion	4494 cal $mole^{-1}$	570 cal $mole^{-1}$
Entropy of Fusion	6.4 R	0.8 R

The Grumman apparatus is shown schematically in cross section in Figure 3. The basic apparatus consists of an aluminum block with cartridge heaters in both ends. The sample is contained in a glass test tube (8 mm i.d. × 10.6 cm long) which is placed in the aluminum block. A viewing port is provided on one side of the aluminum block, and a light source is located above the sample to provide illumination for photography. The sample was photographed at 1 second intervals using a Nikon F2 camera with a 55 mm "micro" lens. The photographic system provided a magnification of 1/2 X.

The cartridge heaters were used to establish the temperatures of the ends of the aluminum block at 115°C and 65°C, respectively, with a temperature gradient of approximately 7.8°C cm^{-1} between two ends. At the beginning of the

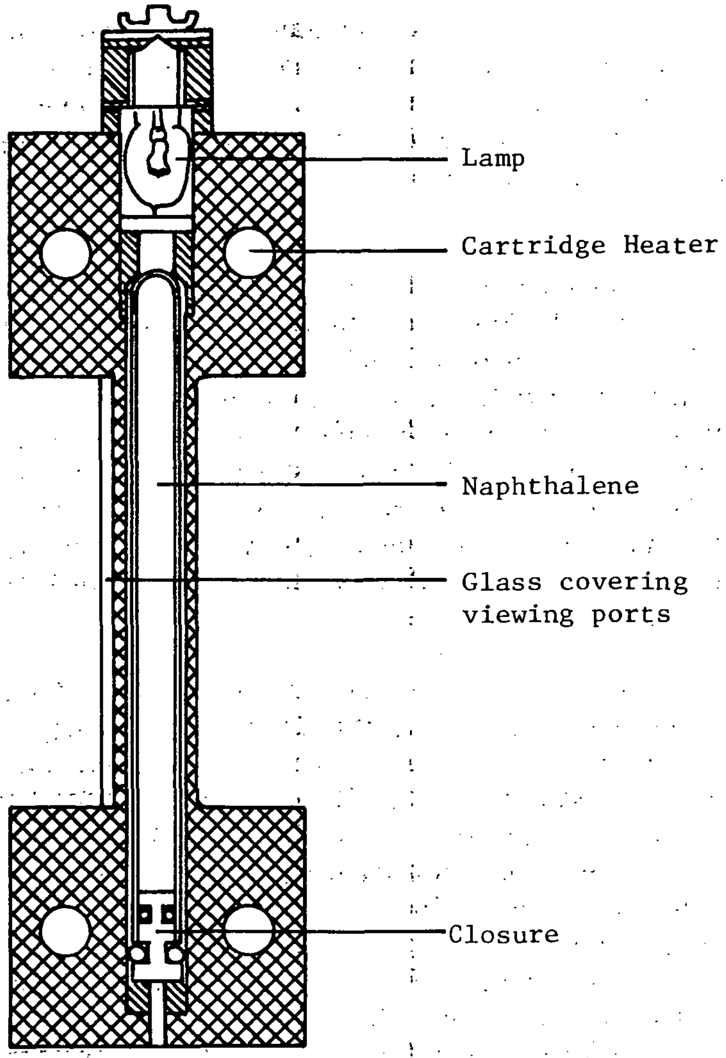

Figure 3. Simplified cross-section view of the aluminum furnace assembly of the Grumman (74-36) apparatus.

experiments (upon launch in the case of the rocket experiments), the heaters were turned off and the aluminum block was allowed to cool at a rate determined by connection in the ambient air and conduction through a thermal path from the low temperature end of the block to a heat sink.

The glass sample tube in the Grumman apparatus is separated from the aluminum block. Hence, in a good vacuum, the thermal coupling between the sample and the aluminum block (the furnace) is quite poor. The solidification rate then depends importantly upon the conduction of heat — specifically, the heat of fusion — through the sample and the glass walls of the sample tube. For this reason, the temperature of the sample may deviate significantly from the temperature of the supporting aluminum block. This deviation should be more pronounced in a material such as naphthalene which is characterized by a high entropy of fusion than for a material such as carbon tetrabromide which has a low entropy of fusion.

Based on the experiments carried out using the microscope with a gradient hot stage, it was decided to use a combination of zinc particles and two types of glass beads in a matrix of naphthalene for the SPAR 1 flight. The concentration of each type of particle was approximately 1/3000 by volume. The zinc particles were 2 to 7 microns in diameter. One type of glass was a soda-line-silicate glass with a range of diameters between 2 and 80 microns; the second type of glass was a lead-alkali-silicate glass with a mean particle diameter of about 80 microns. A molten slurry of particles in matrix liquid was prepared, the sample tubes were filled, and rapid crystallization was induced by immersing the tubes in water.

The ground-based experiments were carried out at the Grumman Aerospace Corp. using the 74-36 apparatus. Provided that the sample tube was centered properly in its cavity in the aluminum block, the form of the melting interface upon applying heat to the system through the cartridge heaters followed the course shown schematically in Figure 4. The sample material melted first near the walls of the sample tube. Subsequently, the interface flattened out as the temperature gradient was maintained for longer times. As melting took place during the initial period after application of the heat, the particles in the just-melted liquid were observed to roll and bounce down the central dome of the interface such that a large fraction of the particles rested in a narrow, deep pile along the periphery of the sample tube. Even after the interface flattened, a large fraction of the particle was located in a narrow band around the periphery of the sample tube. In addition, there was a thin layer of particles covering the central region of the interface.

In the ground-based tests, the initial melting was carried out at atmospheric pressure to simulate the melting of the sample on the ground prior to launch. With the imposed temperature gradient, the interface was located well within the central region of the sample length. After a stable interface position was obtained in the ground-based tests, the heater was turned off and a vacuum system containing the apparatus was pumped out with a roughing pump. The form of the interface observed during growth after turning off the heaters in the ground-based tests is shown schematically in Figure 5. Growth takes place more rapidly in the center of the sample tube than in the peripheral regions,

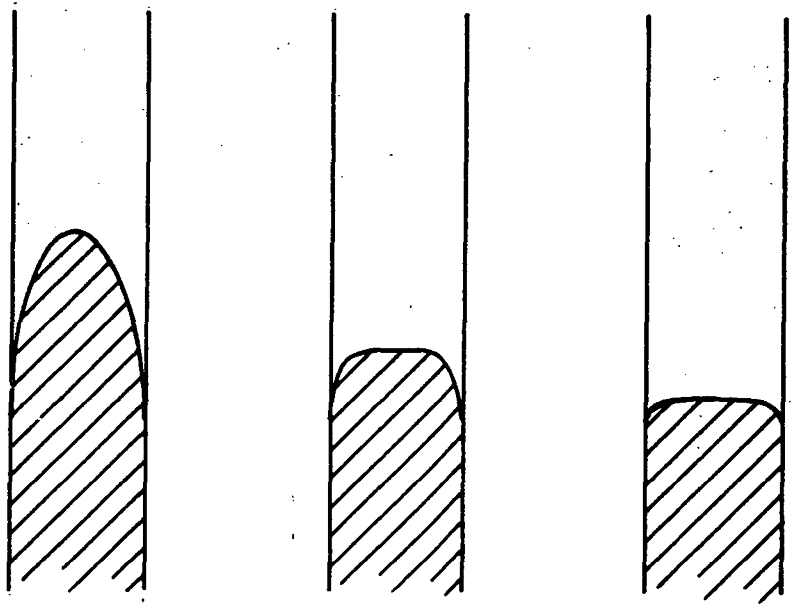

Figure 4. Form of interface during melt-back. (As the sample is melted, the interface becomes progressively flatter.)

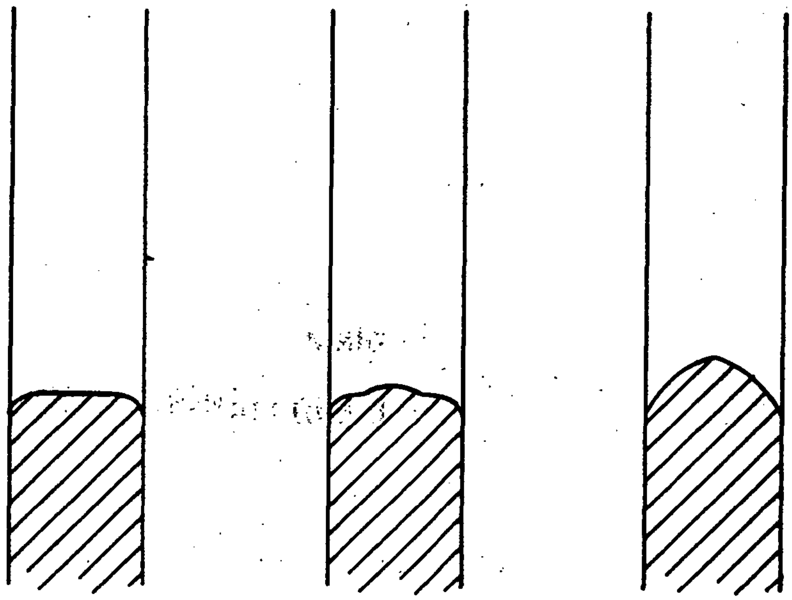

Figure 5. Form of interface during growth. (The crystal grows most rapidly in the central region of the sample tube, producing a dome structure.)

thus producing a dome-like or cap-like appearance of the interface. The observed shape of the interface can be explained in terms of the primary path for conduction of the heat of fusion being through the sample when the system is evacuated. This interface shape as well as the thermal and material parameters which can produce various interface shapes have been discussed previously by Chang and his associates.

At the termination of the simulated flight in the ground-based tests in the Grumman apparatus (after a desired period of solidification corresponding to the time of the rocket flight), air was admitted into the vacuum chamber. Increased thermal coupling was thereby provided between the sample tube and the somewhat cooler aluminum block, and the aluminum block itself cooled more rapidly. Both of these effects led to a more rapid solidification of the sample. The ground-based samples then consisted of three regions: (1) a virgin region formed during the initial preparation of the sample; (2) a region of relatively slow growth which simulates the solidification during the microgravity period of the rocket flight; and (3) a region of relatively rapid growth in which growth in from the walls of the tube is a significant factor.

In contrast to the microscopic observations of the behavior of particles at crystal-liquid interfaces described in the previous section (in which the particle density was usually sufficiently low that the solidification front can interact with individual particles or with small groups of particles), the solidification front in the vertically-oriented tests in the Grumman apparatus was characterized by sizable pile-ups of particles and by a highly preuniform distribution of particles across the interface. As discussed in the previous section and illustrated in Figure 2, a single large glass sphere which would be incorporated by the solidification front at a given growth rate can instead be rejected by the front when zinc particles or smaller glass particles are located between the solidification front and the large glass sphere. Hence, instead of incorporating the large glass particles and rejecting the smaller ones, the whole mass of particles can be rejected at the interface and pushed along by the solidification front.

As shown schematically in Figure 5, the sample grows primarily in the central region of the sample tube during the relatively short, slow growth regime used to simulate the flight experiment. The particles were pushed by the solidification front as it advanced. Little or no growth occurred in the peripheral region of the sample tube, and the particles delineate the dome structure of the interface during the region of the slow growth.

This is illustrated in some detail in Figure 6. The schematic drawing and the adjacent photograph indicate how the sample was cut relative to the dome structure. The sample was sectioned perpendicular to the direction of growth, and the photograph was taken looking upward in the direction of interface motion. Since the region of slow growth produced the dome structure, with progressively less growth taking place toward the peripheral region of the sample, particles in the peripheral region were not pushed along within the interface. Hence, there are no particles seen in the photograph in the peripheral region of the sample close to the walls of the sample tube.

Experimentally, the problem of sectioning the naphthalene to reveal the distribution of particles in the solidified sample was considerably more difficult than originally anticipated. Several techniques were utilized on the ground-based samples in an attempt to obtain the desired information.

It was originally hoped that a microtome could be used to produce thin transparent sections in which the particles in each layer would be easily visible. Due to the large (80 micron diameter) glass spheres, the thin sections would need to be at least 150 to 200 microns thick to include the large spheres. Unfortunately, naphthalene proved to be much too brittle to permit cutting such thick sections. It might be possible to impregnate the naphthalene with a soft mounting medium to hold the naphthalene together during sectioning, but an appropriate mounting medium which would not dissolve the naphthalene was not found.

In view of the relatively thick sections desired, effort was then devoted to developing procedures using a string saw to cut sections which could subsequently be polished. The brittleness of the naphthalene forced mounting the samples in a potting compound to avoid breaking the sample during handling. Here, "Clear Cast" resins were found to be acceptable. Difficulties were encountered, however, in washing off the cutting compound. More importantly, substantial difficulties were encountered in polishing the sections for optical examination. To assist in this work, the services of a firm specializing in preparing thin sections (mostly of geological materials) were employed — without notable success. Because of problems in making useful thin sections which were associated with evaporation of the sample (the relatively high vapor pressure of the naphthalene necessitated its storage at subambient temperature), as well as the rather large kerf losses associated with cutting the slices and preparing the thin sections, a more direct but inherently destructive technique was adopted to determine the distribution of particles in the solidified sample.

This technique included the following steps. A fresh sample was sectioned parallel to its long dimension and along a diameter such that it was divided into a front half and back half (corresponding to the front and back of the photographs).

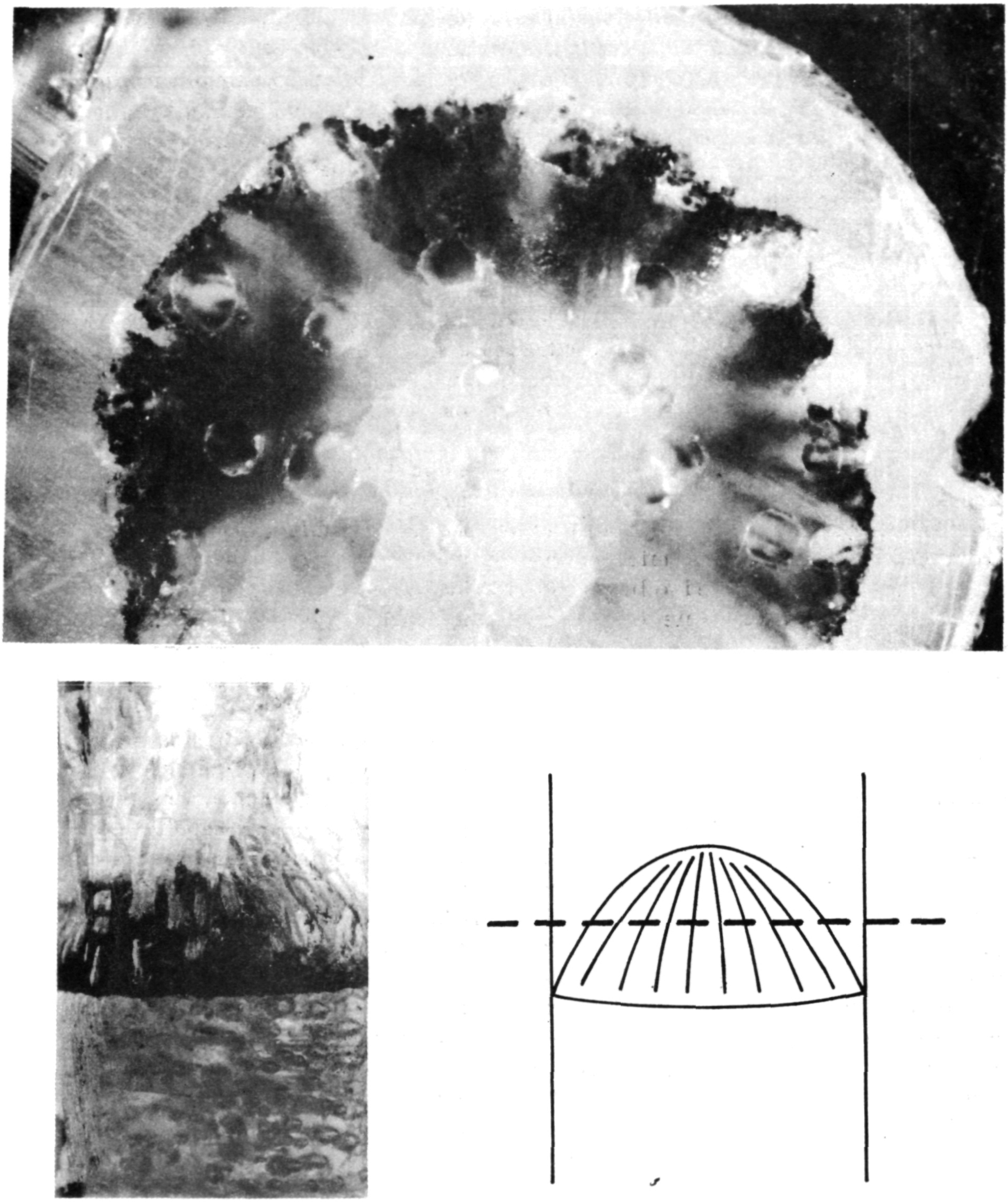

Figure 6. Photographs of a ground-based sample. (The lower left photograph was taken from outside the sample tube and shows the dome structure. The line drawing illustrates where the sample was cut for the upper photograph which was photographed in the direction of crystal growth.)

Each half was embedded in Clear Cast resin. Then using 600 grit grinding paper followed by 0.3 micron Al_2O_3 polishing compound, the sample was alternately polished and photographed in increments of about 0.3 mm. Each half of the sample was studied in a series of planes parallel to the cylindrical axis from the outside of the sample inward toward the center. The use of a longitudinal section and polishing procedure was chosen to emphasize the relative position of the particles to the region of the crystal grown during the experiments.

From data obtained in this way, it was determined that rejection of the particles (pile-ups of particles) took place during the period of solidification. It was also determined that the relative positions of the particles were not altered during the rapid cooling of the sample at the termination of the experiment, because the rapid growth predominantly proceeds inward from the walls of the glass tube and because the particles are trapped in the solid at the higher growth rates.

The solidification behavior will be discussed further in the following section when the results of the SPAR 1 flight experiment are considered.

SPAR 1 FLIGHT EXPERIMENT

A sample of naphthalene containing particles of zinc and two types of glass beads (soda-lime-silicate and lead-alkali-silicate) was prepared following procedures identical to those used in preparing the sample for the ground-based tests described in the preceding section. This sample, containing 1/3000 by volume of each type of particle, was flown in the 74-36 apparatus on the SPAR 1 rocket.

Photographs taken prior to launch indicate that the flight sample melted back in a manner similar to that illustrated in Figure 4, with a slightly rounded interface, approximately flat on top, and a band of particles around the periphery of the glass tube. During launch, the various forces due to thrust, vibration, and the vehicle spinning severely agitated the molten naphthalene, causing considerable mixing of the particles and liquid. Because of the temperature gradient along the sample length, the average temperature of the molten naphthalene was well above the melting point. Hence, the agitation and mixing of the liquid caused melting back of the solid (caused the interface to move toward the cold end of the tube). The extent of this melt-back on launch has been estimated as about 4 mm (by a comparison of pre-launch and post-launch photographs).

Figure 7 shows a sequence of photographs taken during the low-gravity portion of the flight as crystallization was taking place. One of the most striking features of the photographs is the appearance of a vortex-like spiral in the molten naphthalene above the crystal-liquid interface. The spiral is apparently delineated by particles in the melt and very likely reflects the effects of fluid motion during the launch and despin phases of the flight. Any such vortex which existed during the despin phase apparently was damped out rather rapidly in the low-gravity period of the flight, leaving only an array of particles to mark its existence. Measurements from the photographs on several specific features of the spiral indicate that over the period covered by the photographs, the spiral is no longer spinning or otherwise changing shape. This observation provides striking evidence for the absence of significant fluid motion during the low-gravity portion of the flight.

The solidification rate during the low-gravity period was determined from the photographs by measuring the distance from a fixed point at the top of the viewing port to center and edge locations on the interface. The results for the central region of the interface are shown in Figure 8. As indicated there, at the beginning of the data recording (75 sec after launch), growth proceeded at a relatively low rate (about 2 microns sec^{-1}) for the first 60 sec. This was followed by a period of more rapid growth in which the growth rate was about 6 microns sec^{-1}. The origin of the rather abrupt change in growth rate has not been established, but seems likely to reflect a thermal lag in the system.

In contrast to this growth in the central region, the peripheral region shown in the photographs exhibited no significant growth during the period of low-gravity solidification. The difference between the growth characteristics of the two regions presumably reflects thermal diffusion through the solidified sample as the principal path for the heat of fusion.

It is interesting to compare the observed growth behavior with measured temperature at various locations along the aluminum block. Curve 1-2 in Figure 9 shows the variation with time of the temperature at the center of the sample height; curves 1-1 and 1-3 show the temperature at locations 1.9 cm above and below the center, respectively. The data shown in Figure 9 indicate an initial temperature gradient along the aluminum block of about 6.3°C cm^{-1}. At the beginning of data recording 75 sec after launch, this gradient had decreased to about 5.9°C cm^{-1}, and 375 sec after launch, it had decreased to about 3.4°C cm^{-1}.

At the beginning of the data recording, the interface was located about 9 mm below the center of the height of the sample. If the sample was coupled sufficiently well to the aluminum block so that the interface was at the same

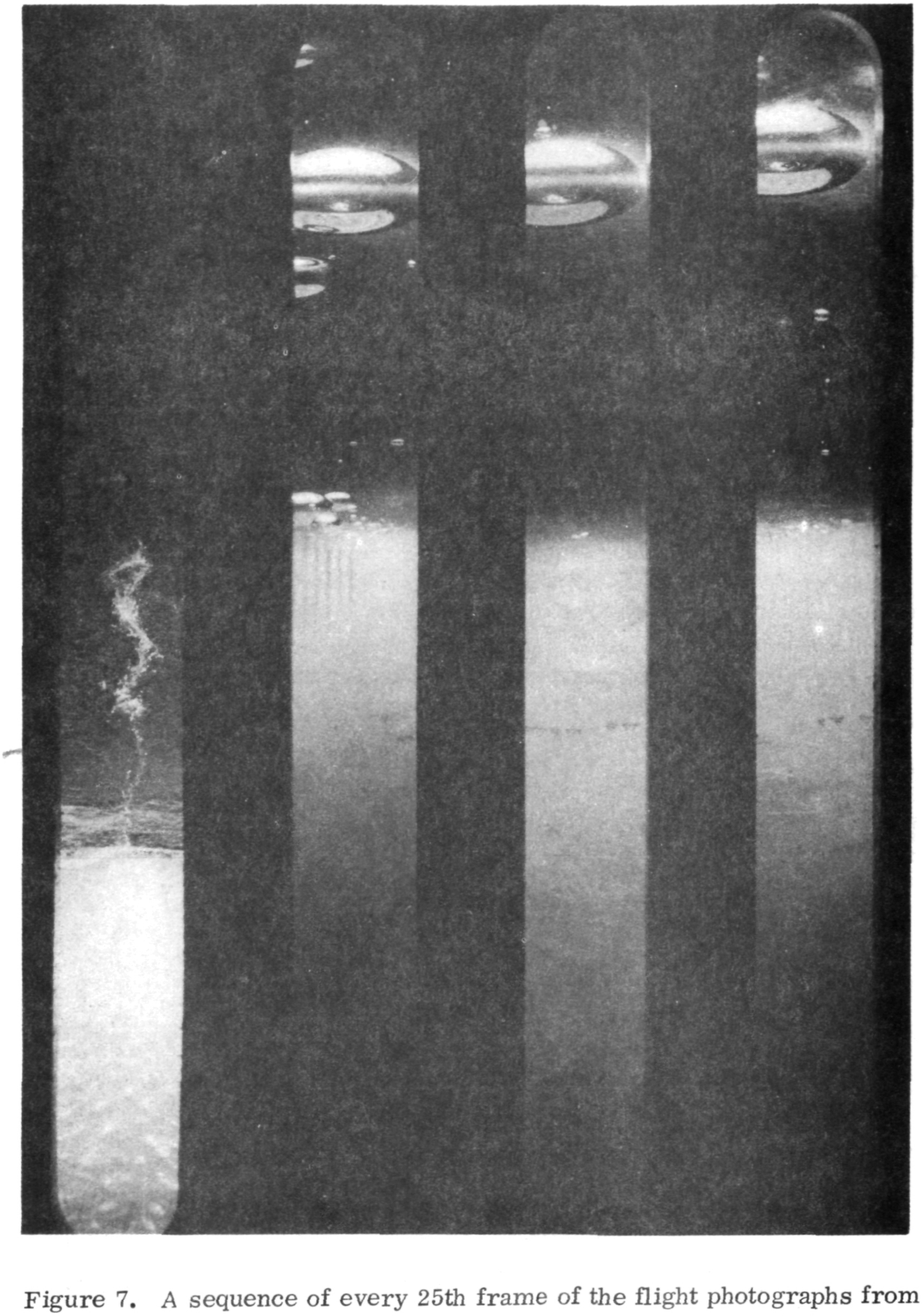

Figure 7. A sequence of every 25th frame of the flight photographs from experiment 74-36/15. (The left tube contains the naphthalene sample studied in the present work.)

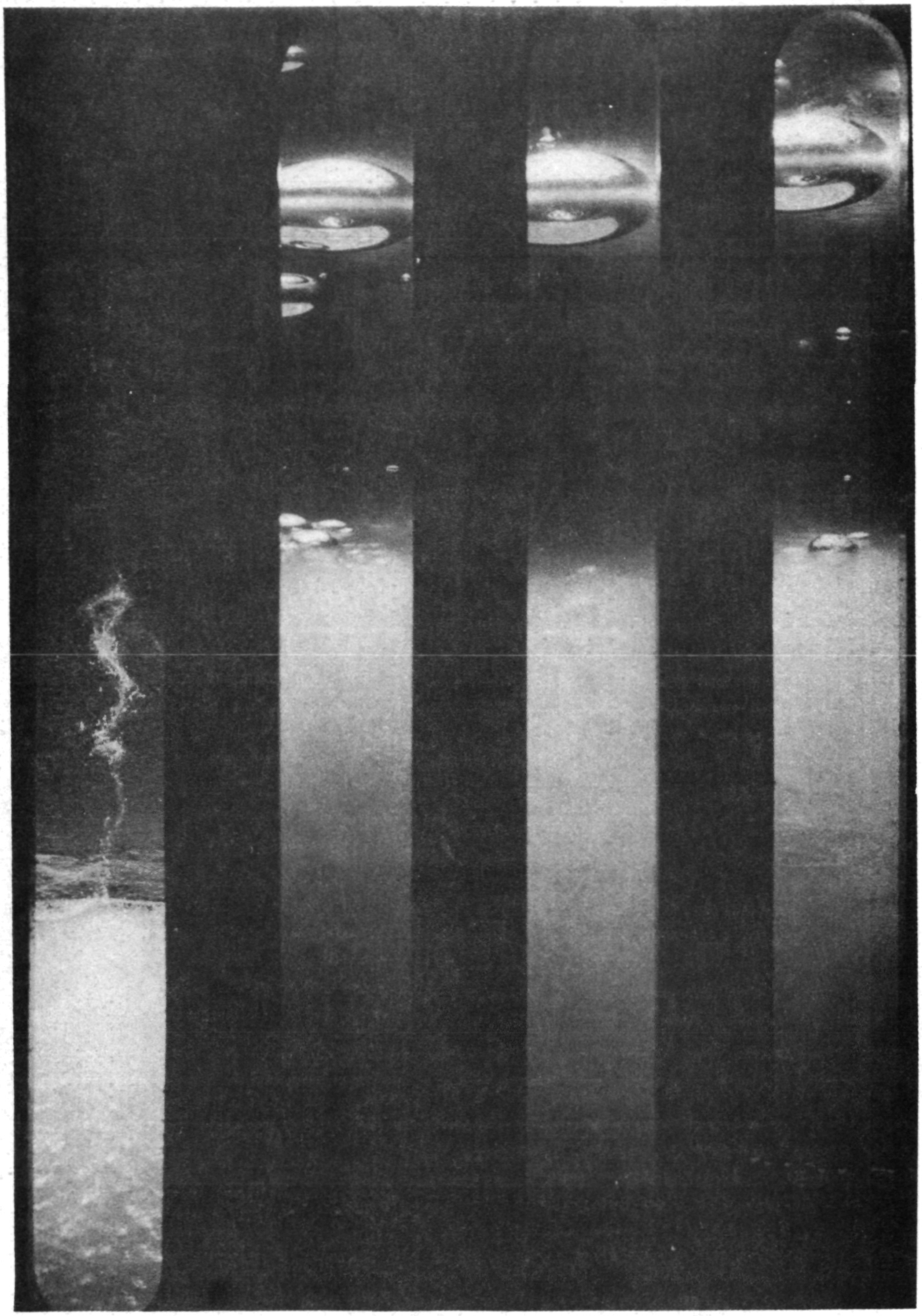

Figure 7. (Continued)

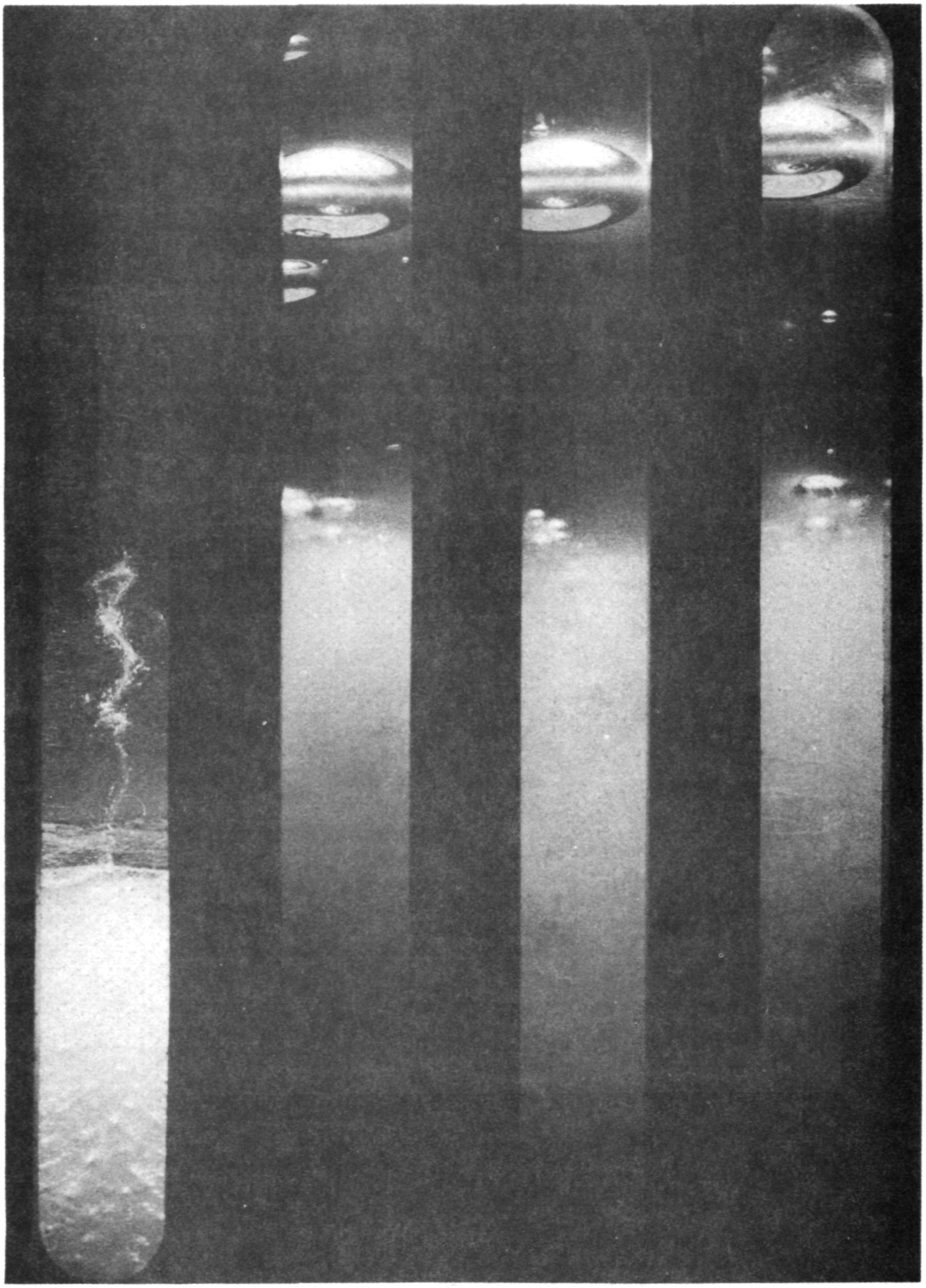

Figure 7. (Continued)

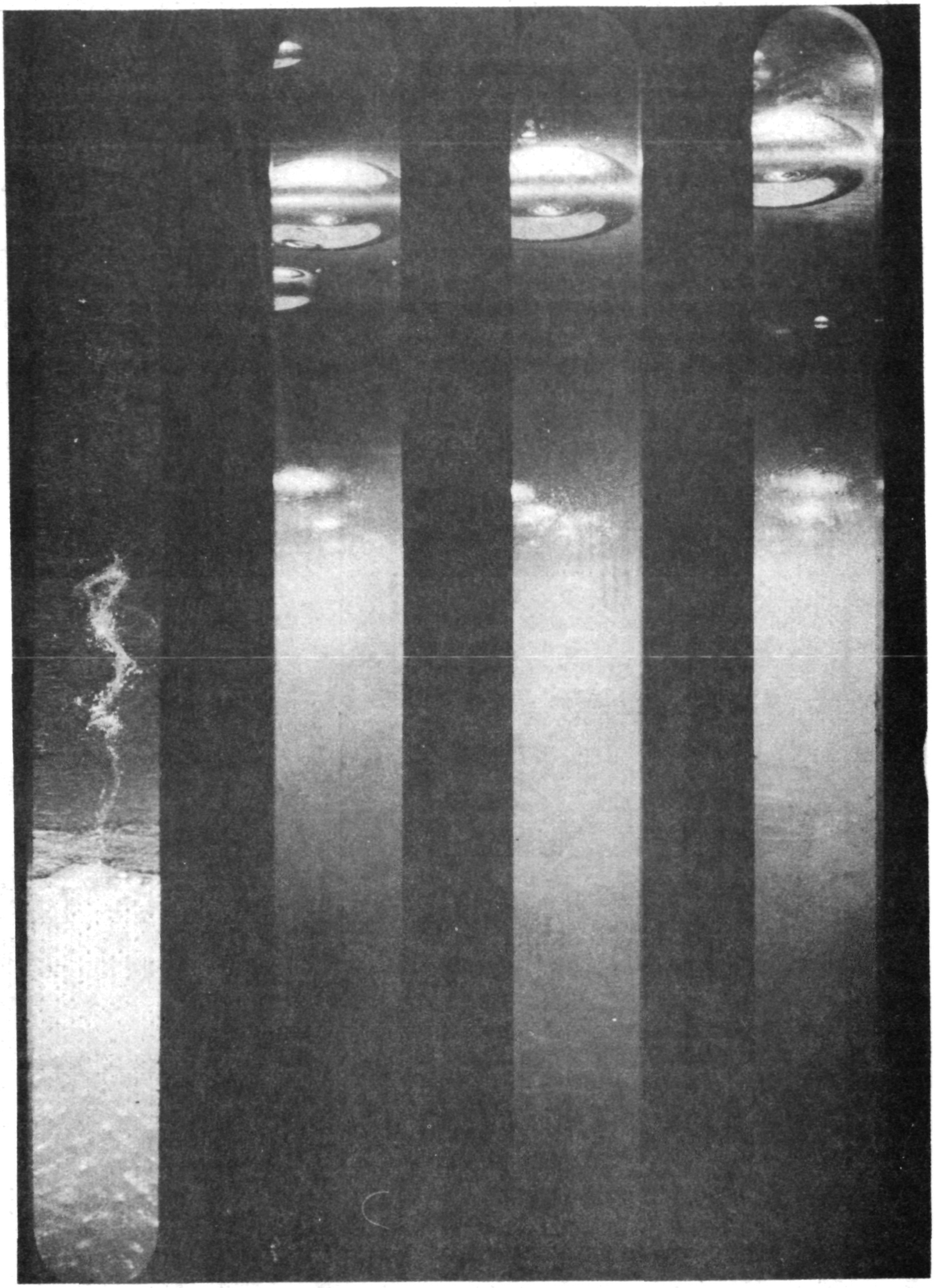

Figure 7. (Continued)

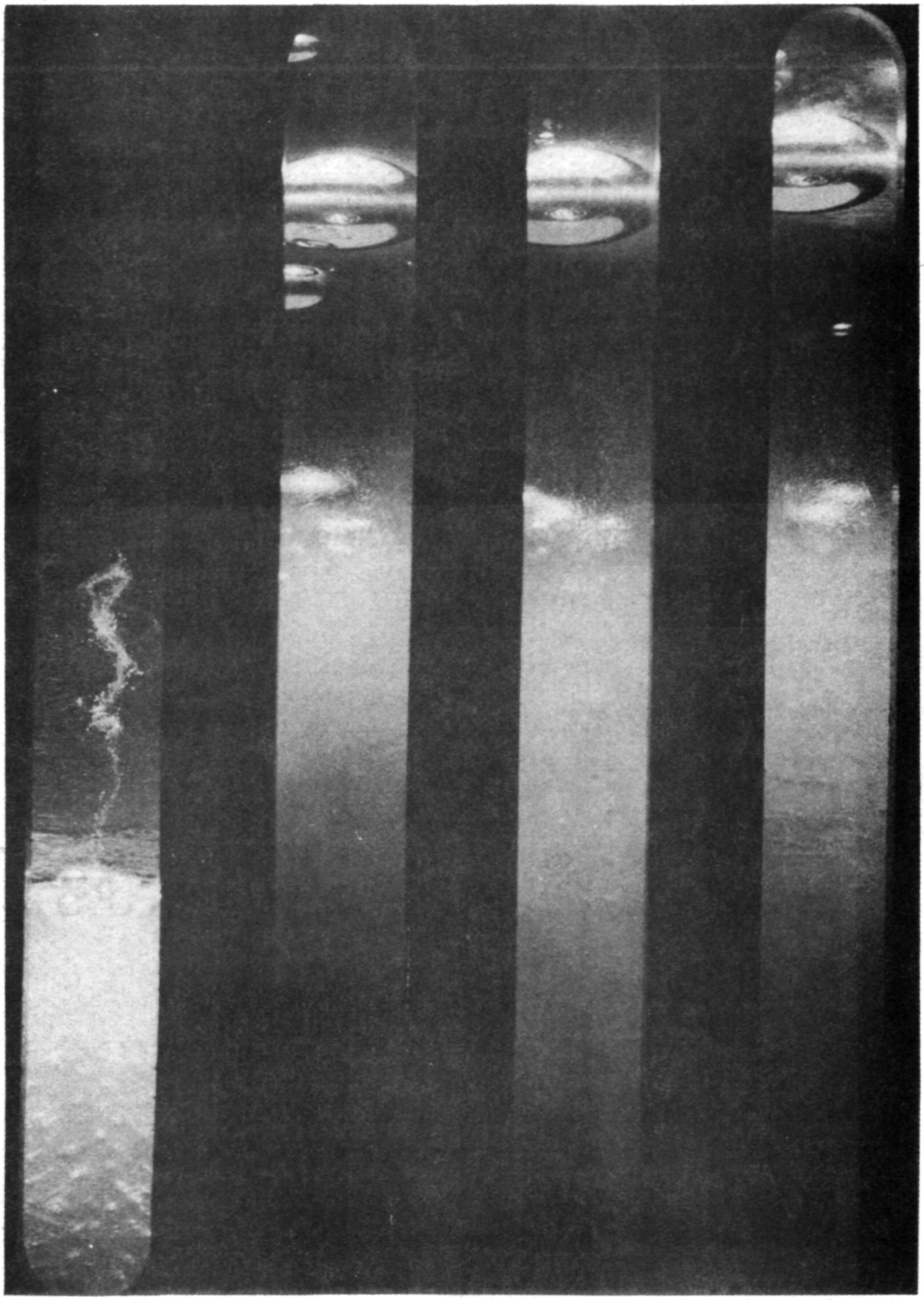

Figure 7. (Continued)

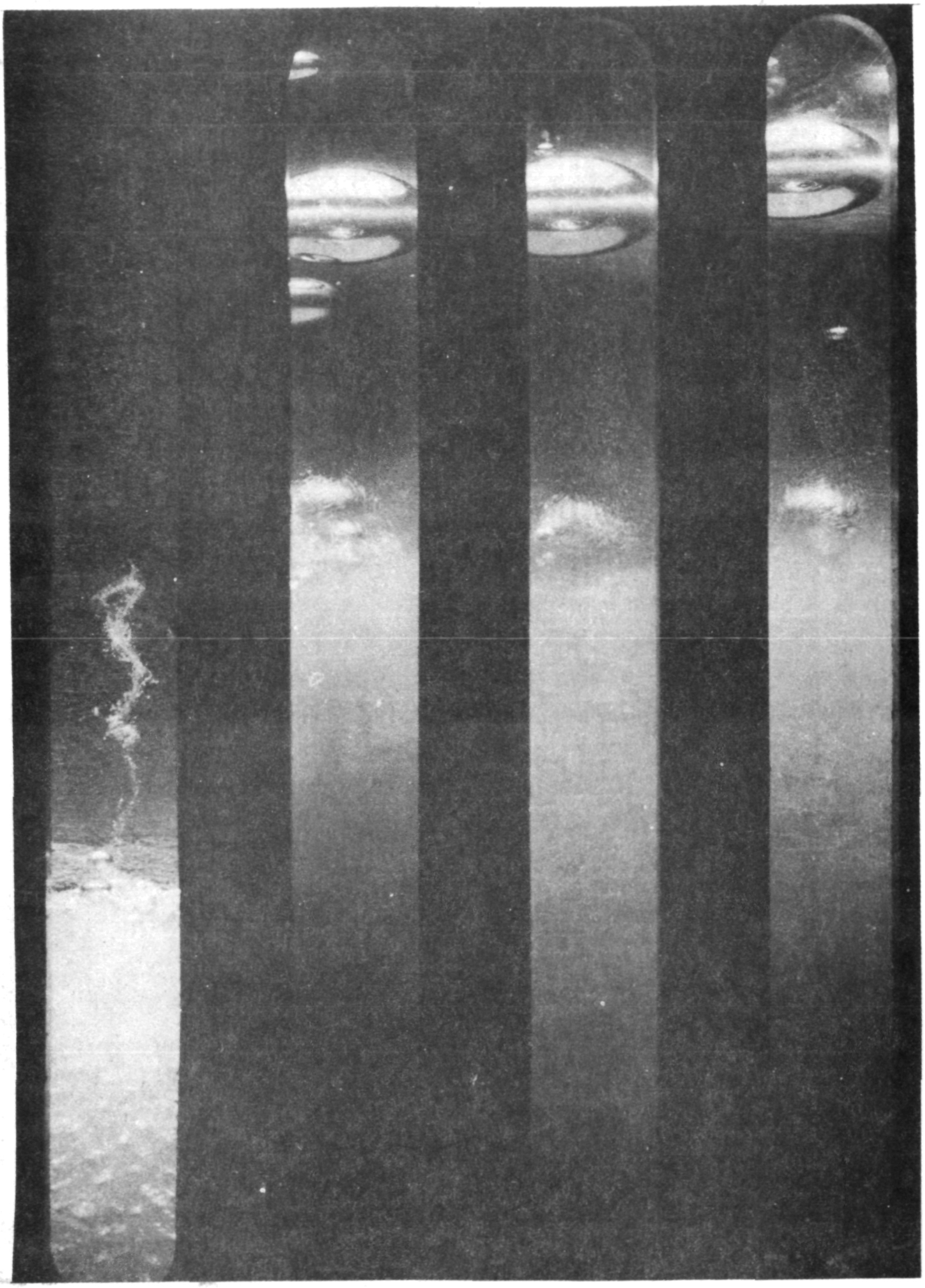

Figure 7. (Continued)

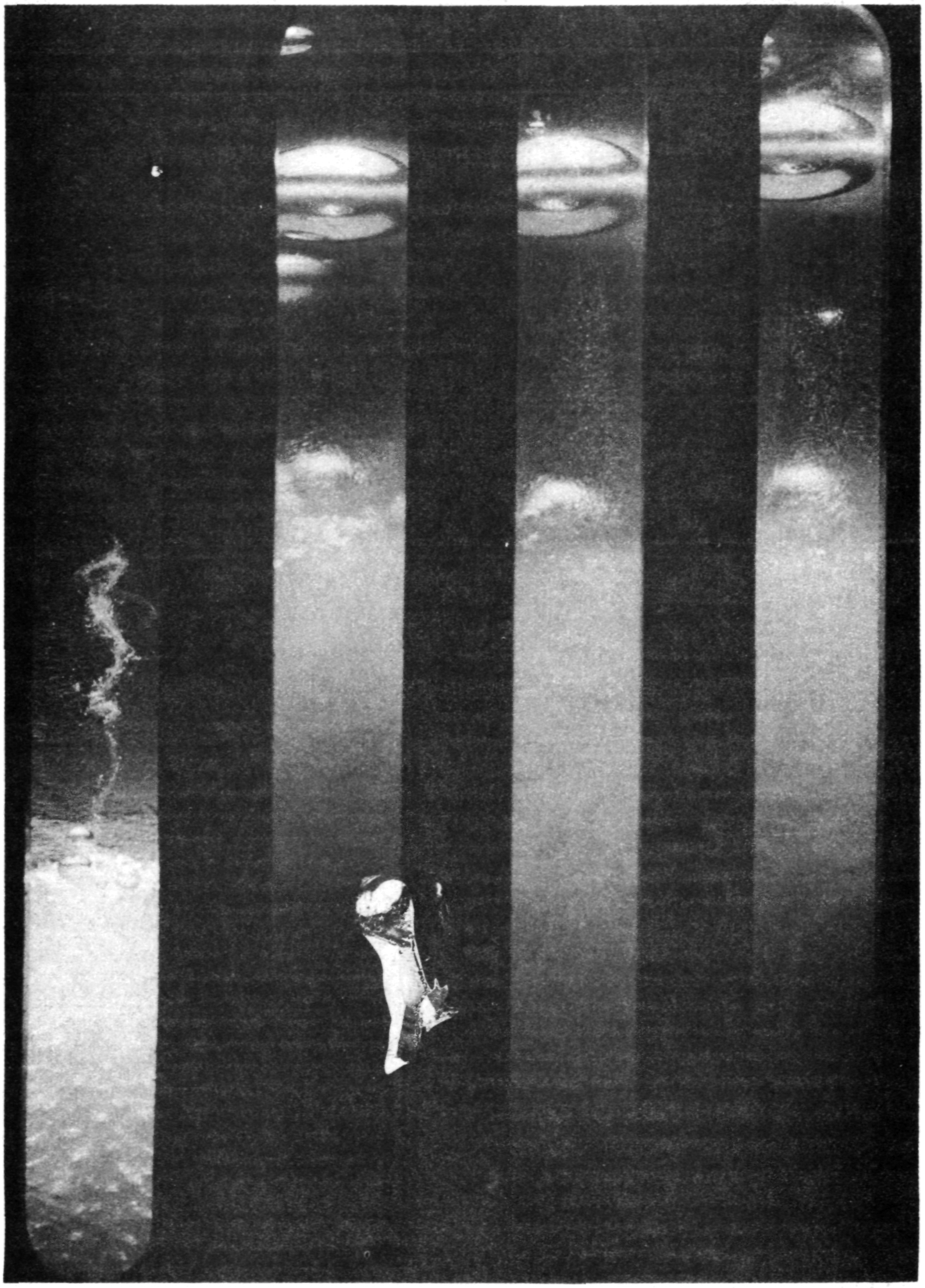

Figure 7. (Continued)

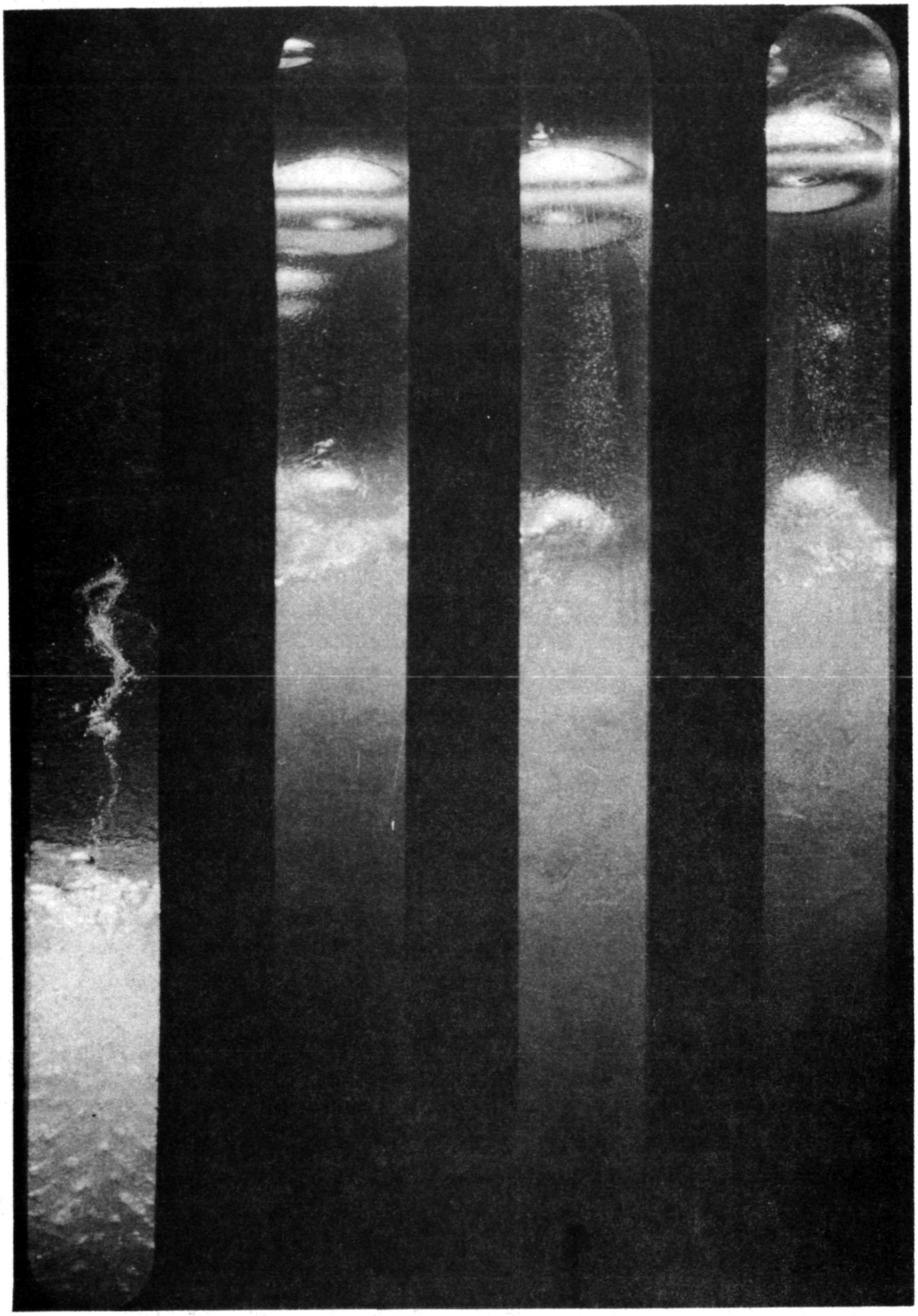

Figure 7. (Concluded)

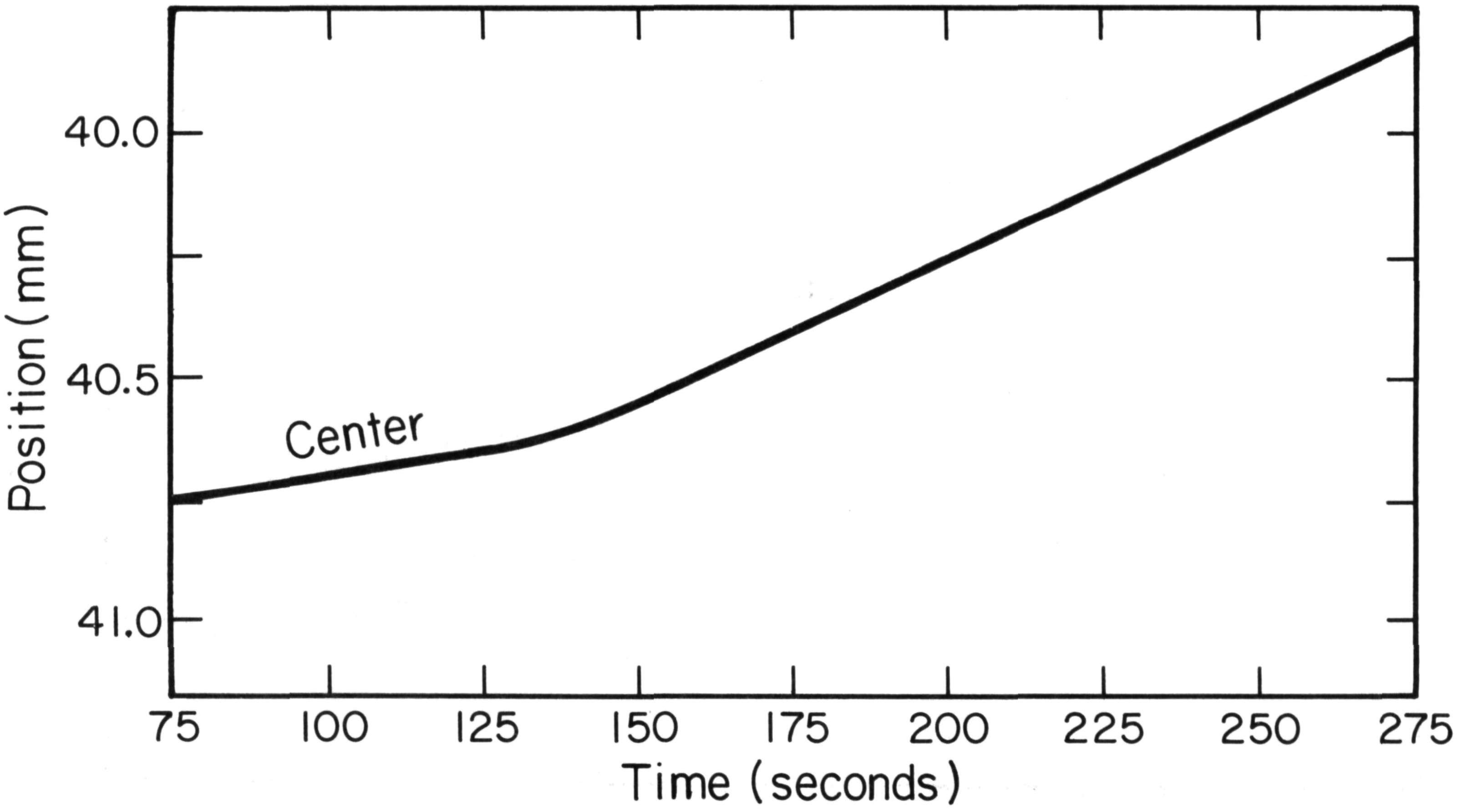

Figure 8. Position of the center of the sample at various times after lift-off, measured from flight photographs.

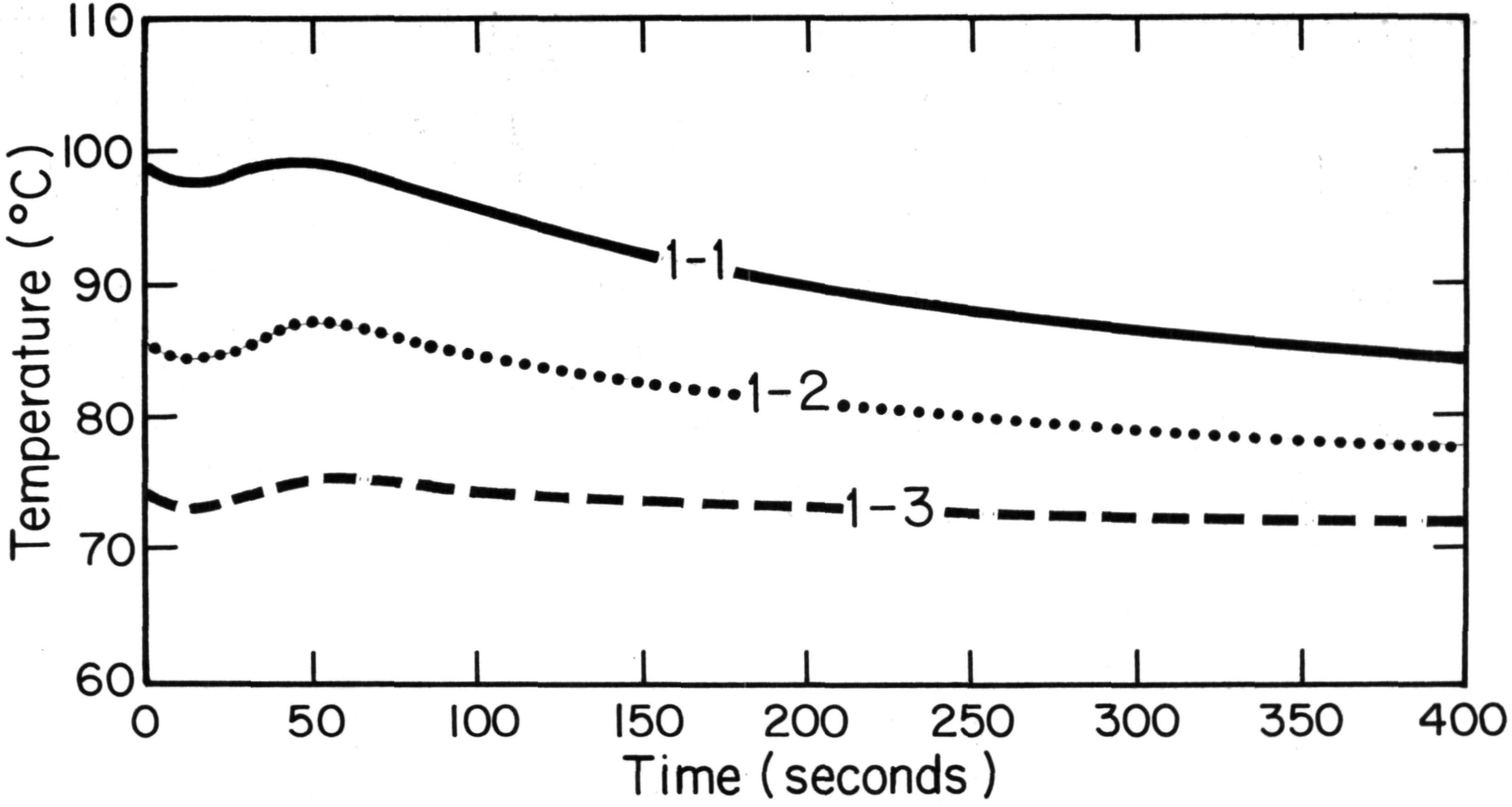

Figure 9. Temperature of the aluminum block surrounding the sample at various times after lift-off. (Curve 1-2 is at the center of the sample height; curves 1-1 and 1-3 are respectively 1.9 cm above and below the center.)

temperature as the aluminum block, a growth rate of about 50 microns sec^{-1} would be inferred from the change of the 80°C isotherm with time (assuming a negligible kinetic undercooling, which is reasonable for naphthalene). Use of somewhat lower isotherms would lead to similar estimates of the growth rates. The much smaller growth rates measured for the central region of the sample and the lack of significant growth in the peripheral region reflect the expected poor thermal coupling between the walls of the glass sample tube and the aluminum block.

A further manifestation of the thermal lag in the system is provided by the fact that 75 sec after launch, the location of the interface visible at the center of the photographs corresponds closely to the 80°C isotherm in the aluminum block. In contrast, 250 sec after launch, the central region of the interface is located at a level where the temperature of the aluminum block is about 76°C. Hence, on the basis of interface location as well as interface shape, it is concluded that conduction through the solid sample is the primary path for removal of the heat of fusion from the interface.

Careful examination of the sequence of photographs taken during the experiment (Fig. 7) and comparison with the solidified sample after recovery led to the conclusion that the interface slopes downward from the back of the sample tube to the front at the start of the microgravity experimental period. This conclusion is based on the following observations. First, as the crystal grows at the center of the sample, it appears to grow in front of and obscure a dark band of zinc particles visible at the top of the crystal. It is concluded, therefore, that the band of particles is at the rear of the sample tube and is somewhat higher than the rest of the sample. A band of particles similar in shape to that seen in the photographs was observed at the periphery of the solidified sample near the vertical position where growth in the central region took place. The suggested uneven form of the interface can be associated with uneven melt-back from connective motion following launch, but the details of this connective motion remain to be elucidated satisfactorily.

The exact shape of the interface during the experimental period could not readily be determined from the photographs taken during the flight. This difficulty is associated primarily with the circular geometry and relatively large diameter (8 mm) of the sample tube, together with the illumination of the sample from above the interface rather than transverse to it (chosen for optimum illumination of the bubbles in the Grumman experiment).

After photographing the recovered sample inside the glass test tube, the sample was cut in half longitudinally (along its axis) with a diamond saw and then removed from the test tube and photographed. Figure 10 shows a portion

Figure 10. Central longitudinal cut through flight sample. (The dark mass near the center of the photograph is the large clump of particles discussed in the text. Above the clump is a large void formed during rapid cooling at the termination of the experiment.)

of the cut surface of one of these half-samples. A sizable dark clump of zinc and glass particles is noted near the center of the sample. This clump of particles is approximately 1.5 mm high and about 4 mm in lateral extent. This clump is rich in particles, but it consists mostly of naphthalene since the volume of the clump exceeds the total volume of particles originally present in the molten portion of the sample.

Above the clump of particles is a large cavity which presumably formed in the period of rapid cooling after termination of the experiment. During this period, the crystal grows radially from the walls of the sample tube toward its center.

The sample halves were next embedded in a Clear Cast resin, and were ground and polished as described previously.

Figure 11 is a photograph of the sample close to its center. Again there is a large clump of particles (about 2 mm high × 3.3 mm in lateral extent). Seen clearly in this photograph is the transition from the nearly-circular gas bubbles in the originally-prepared, rapidly crystallized material to the highly elongated bubbles in the material which was slowly crystallized under microgravity conditions. The bubbles thus indicate the direction of growth and help delineate the region of directional growth in microgravity. From the extent of the elongated bubbles in the crystal under the clump of particles and the absence of particles in the region of these bubbles, it is estimated that the particles were pushed by the interface over slightly more than 2 mm.

Figure 12 shows a closer view of the region of crystal below the clump of particles. The section is located approximately midway between the center of the sample and its periphery. Note that the region of crystal below the clump has been effectively cleared of particles by the passage of the solidification front.

By use of the sectioning, grinding, and polishing procedure, the distribution of particles has been determined as a function of position in the sample. Figure 13 indicates the distribution of masses of particles in sections through and adjacent to the region in which growth took place during the experiment. Below the large clump of particles the naphthalene is free of particles. They have all been pushed by the advancing solidification front. The band of particles which is visible in the flight photographs appears in Sections B and C of Figure 13. The band of particles visible on the right side of the flight photographs appears only in view B and are located at the wall at the glass tube. The lower band of particles on the left side of the flight photographs appears in views B and C. A portion of these particles (specifically those closer to the center of the sample tube) were pushed by the advancing solidification front. Primarily, however, the particles in the large clump were cleared out of Section D, and deposited in a region extending from Section C to Section A.

The information obtained in this experiment is discussed in the following section.

Figure 11. Longitudinal section of flight sample close to its center. (The originally-prepared crystal at the bottom of the photograph is marked by round gas bubbles. The crystal grown during the experiment contains bubbles elongated in the direction of growth. The particles have been pushed by the interface over more than 2 mm.)

Figure 12. Longitudinal section of flight sample approximately midway between center and periphery. (The region of the crystal below the clump which is free of particles is shown in greater detail than in Fig. 11.)

DISCUSSION AND CONCLUSIONS

The results of the 74-36/15 experiment on the SPAR 1 flight indicate that rejection of particles at the crystal-liquid interface in naphthalene took place during solidification in the microgravity environment. The results also indicate that a large pile-up of particles was pushed by the solidification front over distances of millimeters. The occurrence of discrete clumps of particles, their location in the sample, and the form of the interface at the start of data recording remain to be explained in detail. They very likely reflect the initial distribution of particles prior to launch and the complex fluid motions which took

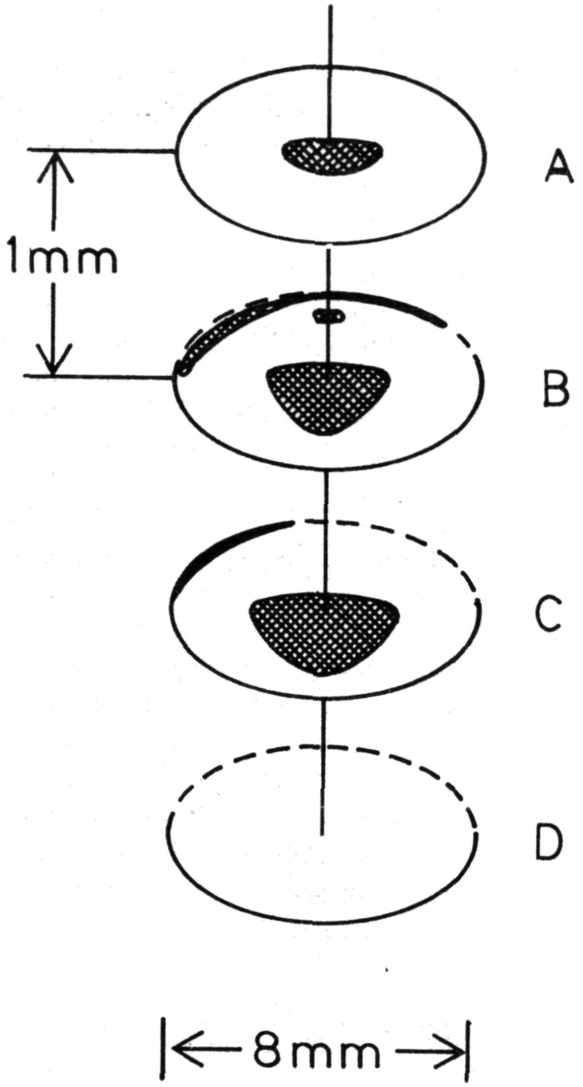

Figure 13. The distribution of particles in the flight sample determined from post-flight analysis. (Sections A and C show the limits of the large clump of particles in the central region of the sample.)

place after launch. Despite the extensive and complex motion in the period after launch, good evidence has been provided for the absence of significant motion in the liquid during the microgravity period of the experiment.

While these results are notable, the principal value of the experiment run on the SPAR 1 flight was the insight which it provided — not directly into the behavior of second-phase particles at a solidification front, but into the material and environmental factors which are important in elucidating the phenomenon from rocket experiments. This insight has already been important in the design of the controlled solidification apparatus which will be built by the Charles S. Draper Laboratories (which will be flown on the SPAR 4 and SPAR 5 flights).

Among the significant insights which were obtained, the following should be noted:

1. A meaningful determination of the effects of important experimental variables on the behavior of second-phase particles at solidification fronts requires careful and detailed control of experimental conditions as well as a carefully selected range of solidification conditions. Such control will be provided by the apparatus which is now being designed at the Draper Laboratories.

2. The sample chamber should be relatively thin (but thick relative to the diameter of the largest particles being studied), and should be constructed with flat walls. This will permit better control of the solidification conditions and better determination of the interface shape. It would also permit effective photographic recording at reasonable magnifications.

3. Provision should be made for photographic recording of the solidification process at sufficiently high magnifications that individual particles can be seen interacting with the interface. This will provide a much better understanding of the interactions, and permit a better determination of the critical velocity for trapping.

4. The sample should not be melted prior to launch, but melting should be carried out in the microgravity environment. This will avoid the problems associated with highly nonuniform distributions (clumps) of particles.

5. The total concentration of particles should be kept small (0.1 percent or less), and a single size and type of particle should be investigated in a given run. This will avoid complications associated with pile-ups and with large particles pushed by small particles.

6. The sample materials should be partially degassed prior to insertion in the sample chamber. A small concentration of air bubbles generated at the interface should provide valuable information for the post-flight analysis, but should avoid problems associated with copious generation of gas at the interface.

7. For sample capsules in which photographic recording at magnification is not provided, careful recording should be taken of the the thermal conditions, and the thermal conditions must be carefully controlled. This will permit meaningful results to be obtained from post-flight analysis of the solidified samples.

As indicated above, these considerations are being incorporated into the design of the apparatus which will be flown on the SPAR 4 and SPAR 5 flights. With this apparatus, it is expected that definitive information can be obtained from the planned future experiments in the microgravity environment. These experiments on the rocket flights, coupled with ground-based experimental and theoretical studies, should provide a greatly improved understanding of the interaction of second-phase particles with a solidification front. This, in turn, should lead to a better understanding and control of several solidification processes, on Earth as well as in space, and perhaps to technologically important new products.

REFERENCES

1. Corte, A. E.: J. Geophys. Res., vol. 67, 1085, 1962.
2. Uhlman, D. R.; Chalmers, B.; and Jackson, K. A.: J. Appl. Phys., vol. 35, 2896, 1964.
3. Bolling, G. F. and Cisse, J.: J. Crystal Growth, vol. 10, 56, 67, 1971.
4. Neumann, A. W.; Van Oss, C. J.; and Szekely, J.: Kolloid Z.u.Z. Polym., vol. 251, 415, 1973.
5. Kuo, V. H. S. and Wilcox, W. R.: I&EC Process Design and Develop., vol. 12, 376, 1973.
6. Lifshitz, E. M.: Soviet Phys. — Theoretical Physics (JETP), vol. 2, 73, 1956.
7. Neumann, A. W.: Adv. Colloid and Interface Sci., vol. 4, 105, 1974.
8. Hunt, J. D.; Jackson, K. A.; and Brown, H.: Rev. Sci. Inst., vol. 37, 805, 1966.
9. Jackson, K. A.: In Progress in Solid State Chemistry, vol. 4, ed. by H. Reiss, Pergamon Press, New York, 1967.
10. Hunt, J. D. and Jackson, K. A.: Acta. Met., vol. 13, 1212, 1965.

CHAPTER IV

LIQUID MIXING EXPERIMENT

Experiment 74-18

By

Charles F. Schafer

Marshall Space Flight Center

BACKGROUND AND INTRODUCTION

Part of the rationale for performing materials science experiments in space has been that convective flow in fluid systems with density gradients could be suppressed by removal of the accelerating force of gravity. These convective flows were known to influence the quality of crystals grown from a liquid (either melt or solution). It was postulated that superior dopant homogeneity and lower dislocation densities would result in these systems by performing the experiments in the absence of gravity. Skylab experiments have demonstrated that these aspects of crystalline perfection can indeed be improved in low-g crystal growth. Specifically, Experiment M560 [1] showed improvement in dislocation density, and Experiment M562 [2] demonstrated improved dopant homogeneity due to growth in the absence of gravity. The absence of convection as a mass transport mechanism in the Skylab environment was demonstrated in the Radioactive Tracer Diffusion Experiment M558 [3]. In this experiment, the mixing of radioactive zinc with normal zinc was shown to be purely a diffusion-controlled process. That is, no convective mixing was evident.

The sounding rocket project provides a platform for further low-g studies which will surely include fluid systems containing density gradients. This experiment is aimed at characterizing the rocket environment for these systems by providing an indicator of whether and under what conditions a diffusion-controlled mass transport regime will be experienced by fluid systems with density gradients.

This experiment was designed to illustrate the nature of the Space Processing Sounding Rocket accelerational environment by its effects on a confined fluid system containing density gradients. Results from this experiment should serve several purposes. First, they should aid in characterizing the rocket environment. Second, they should emphasize to any potential experimenter the necessity of planning his experiment carefully with respect to possible fluid motions even at very low acceleration levels. Third, they will furnish further data for evaluating the usefulness of simple computations for predicting onset of flow.

This experiment was conducted by observing the mixing behavior of two fluids of differing density during the low-g coast phase of the sounding rocket trajectory. Three samples were used. Each sample was composed of cylindrical sections of two materials having density differences. These were melted during the low-g coast phase of the flight. The density difference between the two materials was designed to enable convective mixing to occur if sufficient

Preceding Page Blank

residual accelerations were present. (The melt time was too short for significant diffusive mixing to occur.) The melts were water-quenched to resolidification before leaving the low-g phase. The samples were returned to the laboratory and analyzed to determine the degree of mixing in each.

EXPERIMENT DESIGN

In order to accomplish the objective of characterizing the effect of the rocket residual acceleration environment on an experimental fluid, the most important criterion was selection of a meaningful model system. The experiment was designed to yield results that can be interpreted as being relevant to a broad range of other experiments involving fluids containing density differences. First, the shape and size of the sample was chosen to be representative of experiments which would use a rocket multipurpose furnace facility. Second, the kinematic viscosity is in the range of kinematic viscosities of materials of interest to other investigators (e.g. liquid metals). This follows from the fact that for a fixed geometry, the kinematic viscosity of a fluid is a fundamental parameter governing flow due to accelerations which act through density differences.

Third, the materials chosen for sample preparation were selected so as to minimize spurious flow effects. For example, low volume change with phase change was required. In addition, high thermal conductivity is required to minimize Marangoni convection, thermally induced density gradients, and to assure melting and rapid quench. With these selection criteria in mind, the samples were composed of indium and an indium-lead alloy (80 wt % In, 20 wt % Pb).

Aluminum cylinders served as sample containers (Fig. 1). (The high thermal conductivity of the aluminum serves to minimize temperature gradients and aid in rapid quench.) Each sample container holds a sample composed of a 7/16 in. long by 1/4 in. diameter solid cylinder of indium joined to a cylinder of In-Pb of the same size, forming cylinders 7/8 in. long by 1/4 in. in diameter (Fig. 1). Three samples were mounted in a Thermal Control Unit (Fig. 2) which provided a water quench system, thermistors for monitoring sample temperatures, and electrical connections for heater power. Associated with the Thermal Control Unit was a voltage regulator, timing circuits, and relays for control and sequencing of the heating cycle. A system schematic is shown in Figure 3.

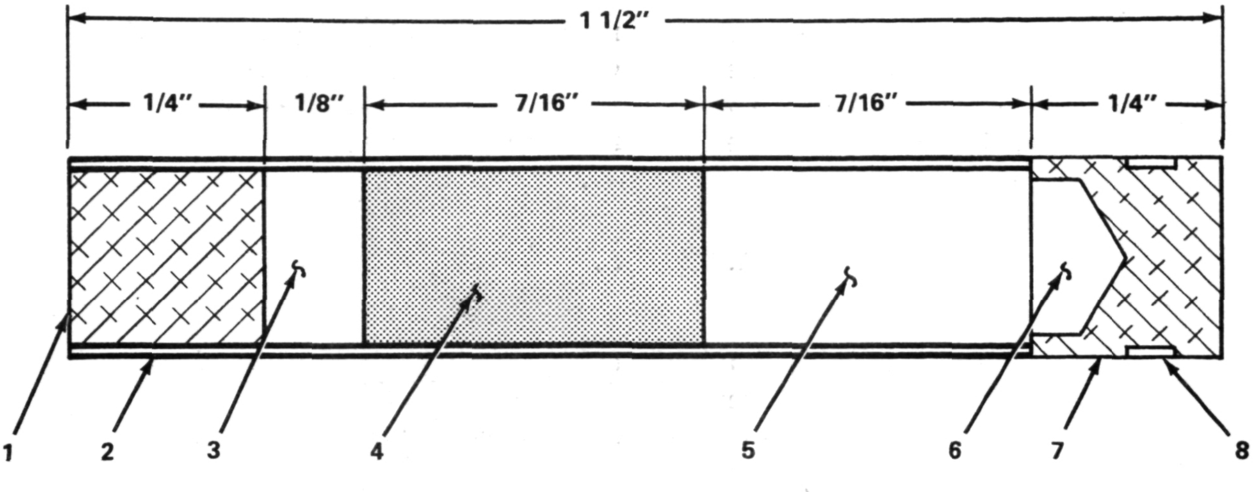

1. ALUMINUM END PLUG (WELDED IN PLACE)
2. ALUMINUM TUBING
3. EXPANSION VOLUME (WALLS COATED WITH AQUADAG)
4. IN – PB ALLOY
5. PURE IN
6. EXPANSION VOLUME (WALLS COATED WITH AQUADAG)
7. ALUMINUM END PLUG
8. GROOVE FILLED WITH EPOXY

Figure 1. Sample and sample container (cross-section).

The Thermal Control Unit was mounted in the sounding rocket payload section as shown in Figure 4. The flight samples had orientations with respect to the payload longitudinal axis as shown in Figures 5 and 6. It will be noted that the longitudinal axis of sample 6 is rotated by 7.5° with respect to a radius from the longitudinal axis of the payload section. Sample 1 is perpendicular to sample 6 and in the plane of rotation, so its axis is rotated by 7.5° as well. This rotation makes the sample longitudinal axes parallel to the onboard accelerometer axes. Samples 1, 6, and 2 are parallel to the accelerometer x, y, and z axes respectively.

Through extensive ground-based testing, a time line was established for conducting the experiment within the low-g portion of the payload trajectory. Sample heating was initiated at launch plus 45 seconds. Heaters were turned off at launch plus 225 seconds, and quench occurred at launch plus 345 seconds.

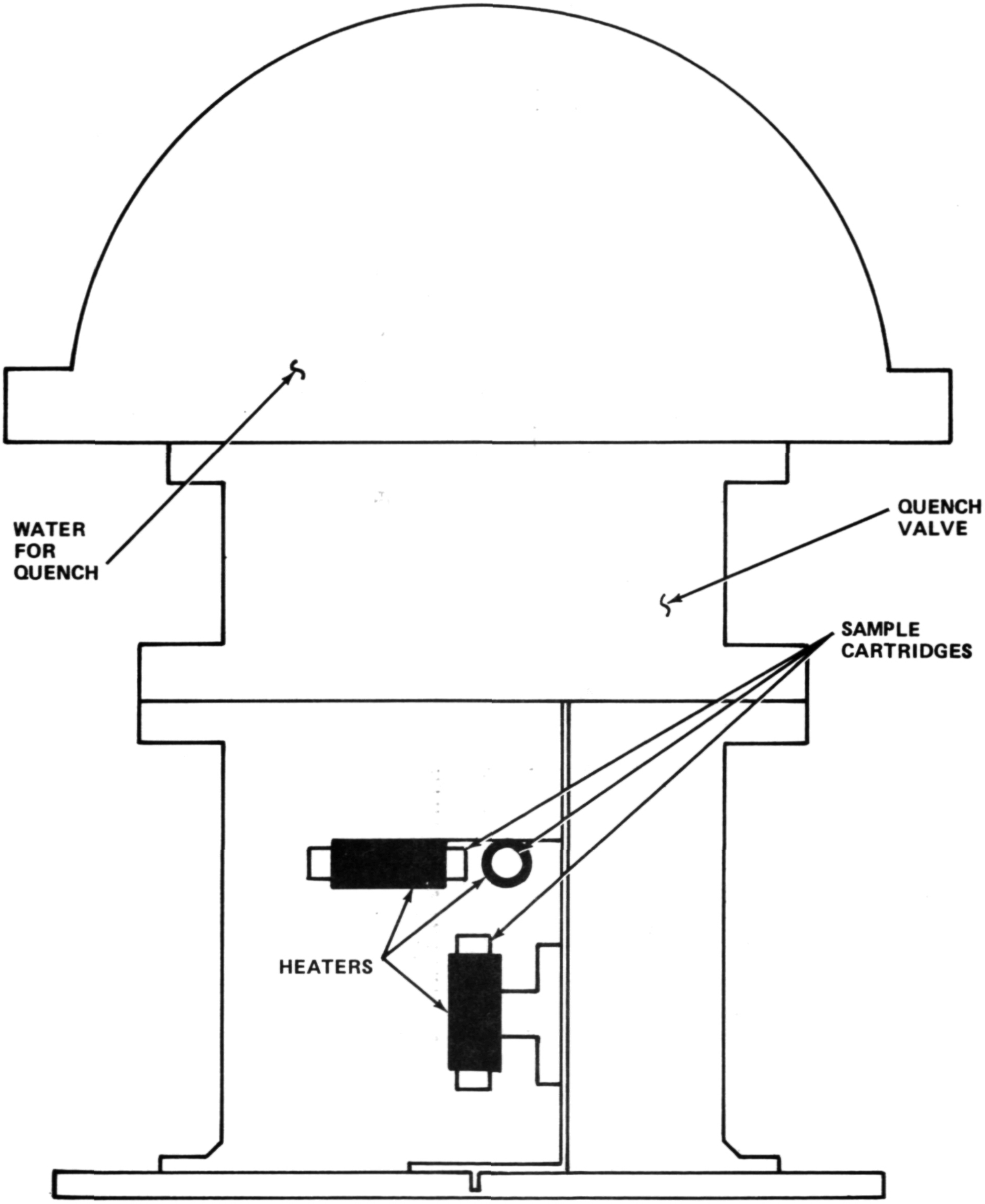

Figure 2. Thermal Control Unit.

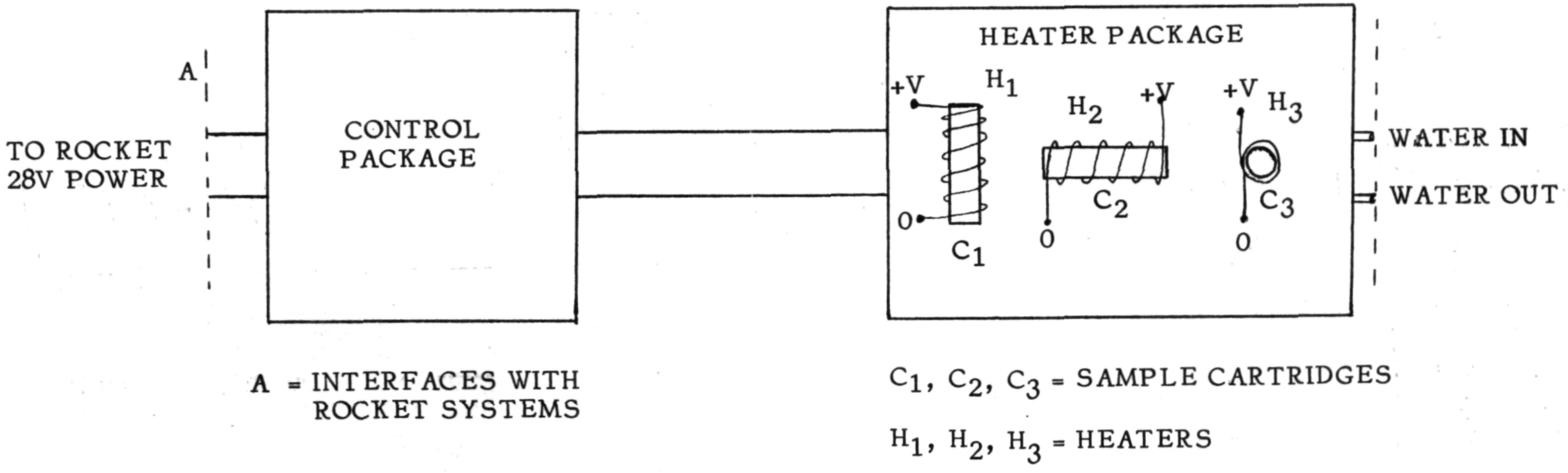

Figure 3. Experiment system schematic.

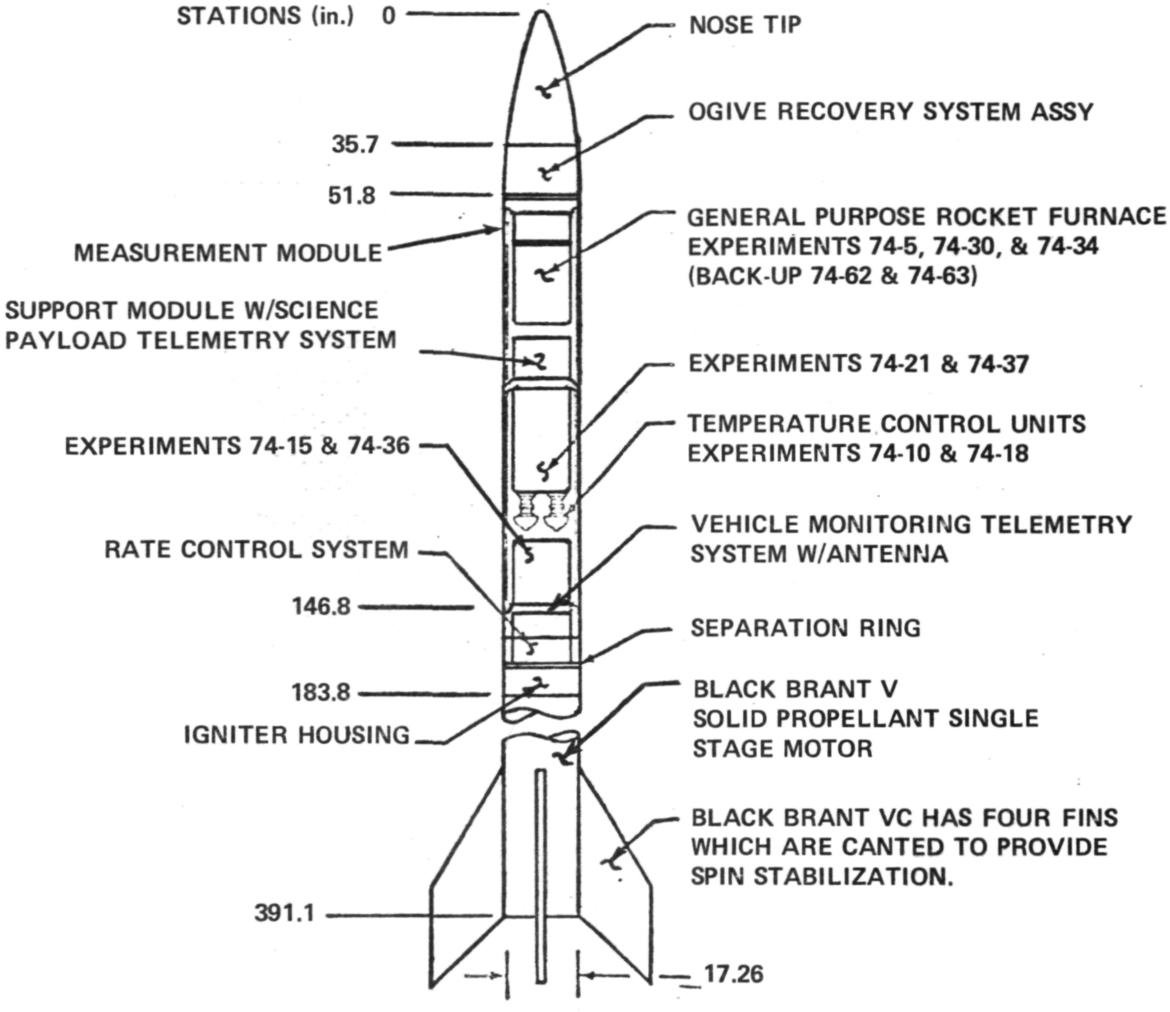

Figure 4. Payload 1, Black Brant VC sounding rocket with the space processing payload mounted on the forward and aft baseline science payload housing pads (nonspin platform is not used).

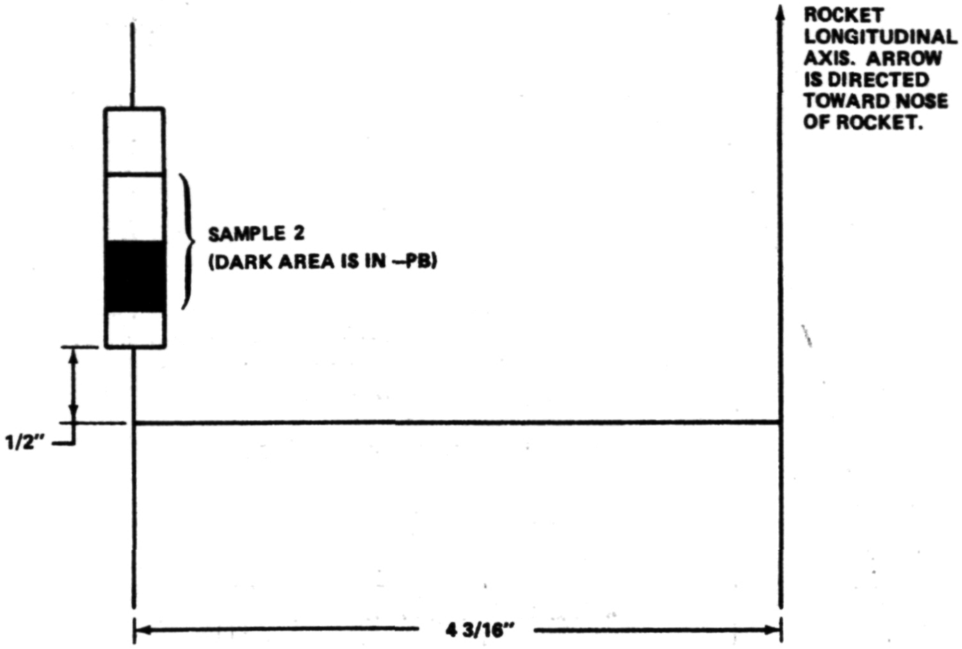

Figure 5. Orientation of sample 2.

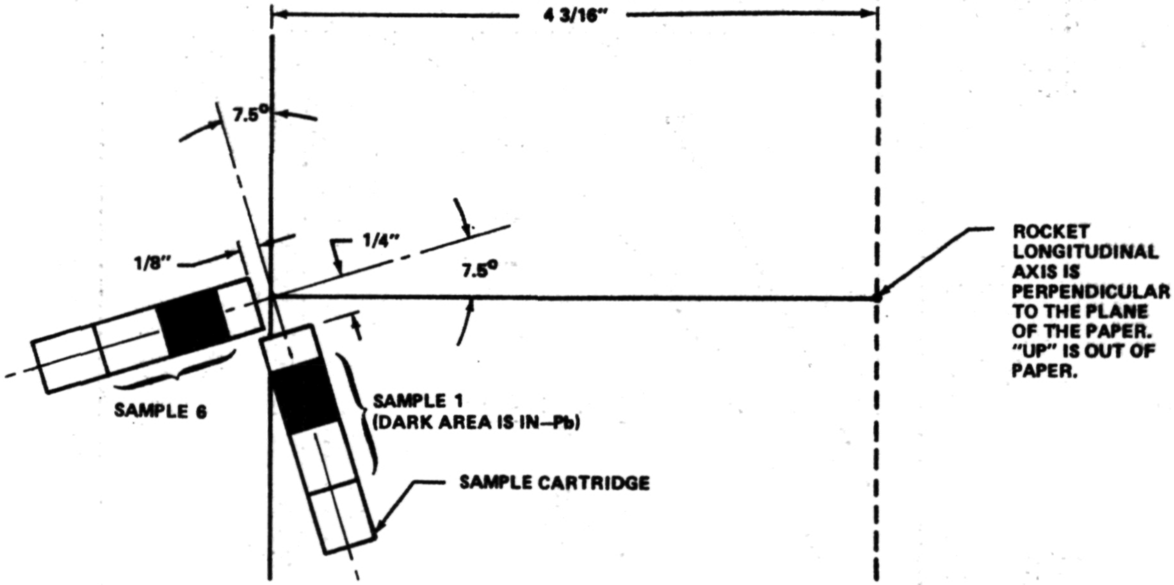

Figure 6. Orientations of samples 1 and 6.

SAMPLE PREPARATION

Samples were prepared from 5N pure indium and 5N pure lead. Samples were weighed on a Mettler electrobalance and placed in a pyrex preparation chamber (Fig. 7). The chamber was purged for 30 min with flowing N_2 gas, and then the end of the pyrex chamber was sealed. The chamber was placed in a tubular furnace (Fig. 8) and heated to 400°C while maintaing an N_2 atmosphere. The chamber containing the molten mixture was held at 400°C for 3 hours and shaken every 15 min to assure complete mixing. The molten material was then poured into room temperature graphite molds (Fig. 9) to form 1/4 in. diameter cylinders. Cylinders of pure indium were cast in a similar manner. Cylindrical sections of indium and indium-lead alloy 7/16 in. long were cut with a microtome and the freshly-cut ends pressed together to form the coupled sample.

ENGINEERING DATA

A thermal analysis was conducted to assure that design of the cartridge and heating unit allowed for proper conduct of the experiment. A computed thermal profile for a sample in low-g is shown in Figure 10. It is compared to a laboratory run using flight hardware in which the pressure was reduced to 0.1 atmosphere to simulate the reduced convective heat transfer experienced in a low-g environment. These simulations and ground-based tests indicated a high probability of successful experiment operation. Temperature data taken during flight indicated that the heating cycle followed predicted behavior.

Pressure change within the sample cartridge was computed to determine whether evacuation of the sample was required. Assuming a pressure of 1 atmosphere inside the sealed cartridge at room temperature and allowing for expansion of the sample due to phase change and temperature increase, and of pressure increase of the air due to temperature change, the force tending to blow out the sample cartridge end cap was less than 1 pound. It was determined that container evacuation was not necessary.

PHYSICAL PROPERTIES OF THE SAMPLE MATERIALS

The In-Pb phase diagram is shown in Figure 11 [4]. The range of alloys in the samples will be in the less than 0 to 20 wt % Pb range. There is no apparent unusual behavior in this range. Over this range the melting point

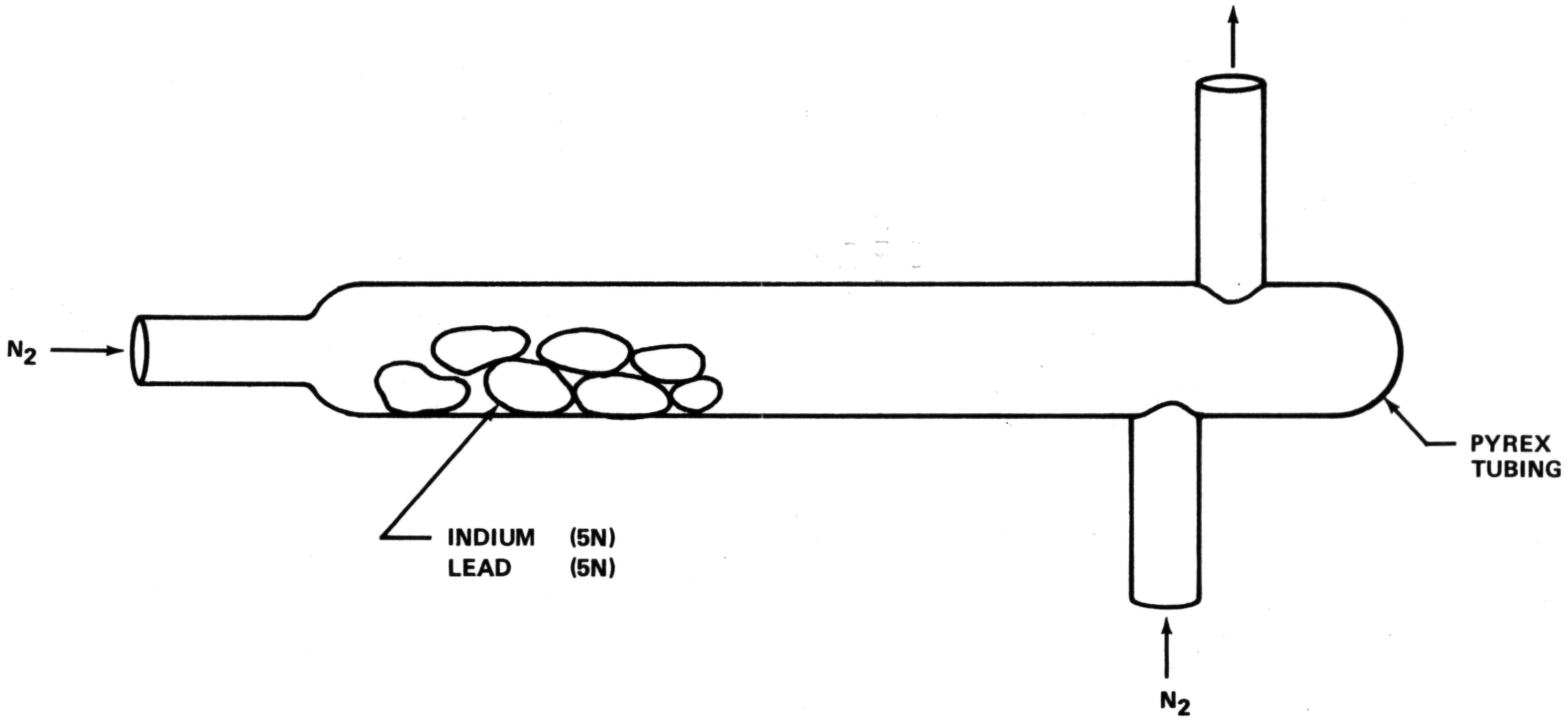

Figure 7. Pyrex preparation chamber.

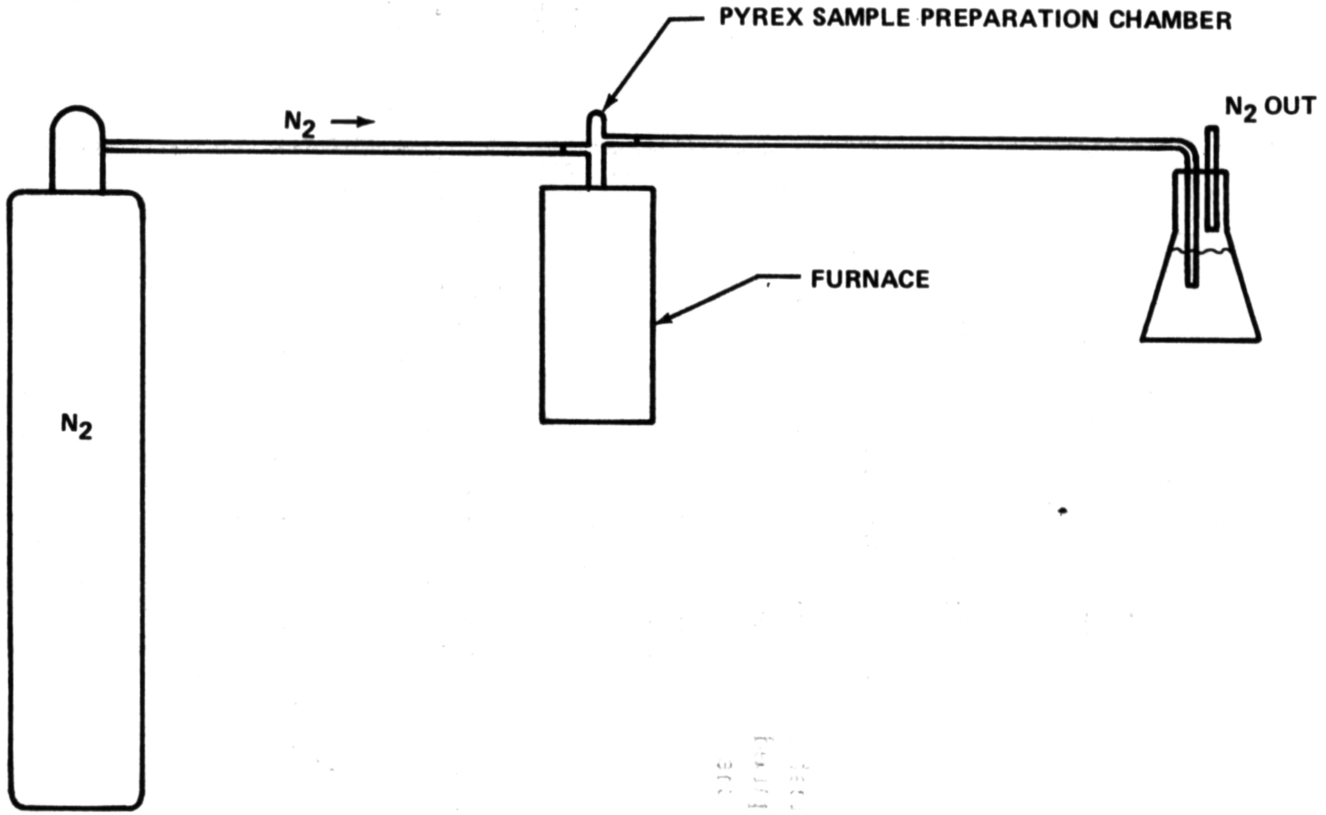

Figure 8. Tubular furnace.

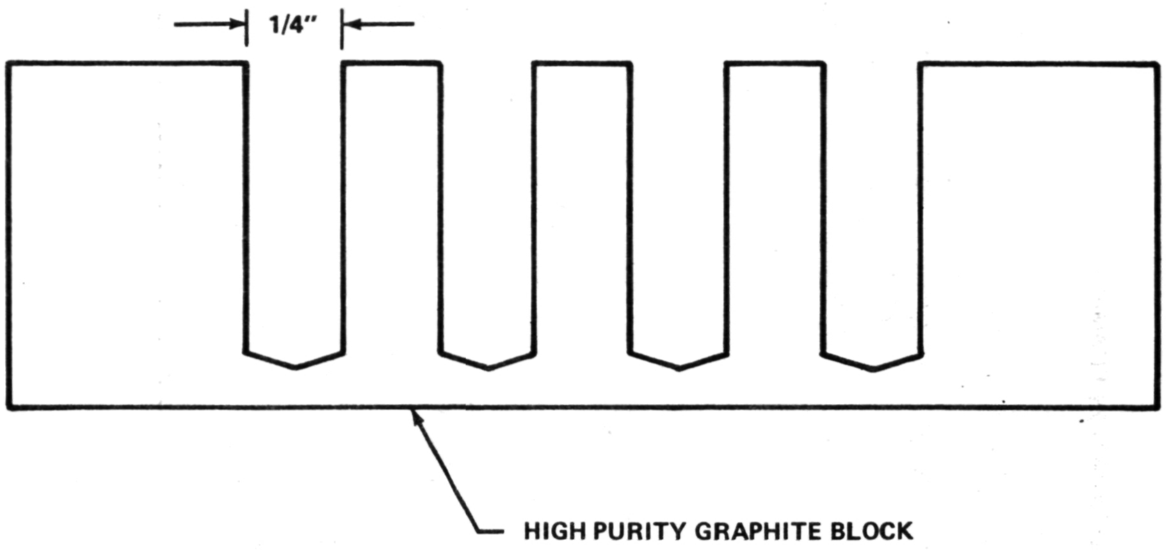

Figure 9. Sample mold.

varies very little indicating that the samples should melt rather uniformly. Figure 12 shows computed densities (from empirical relations) [5] for various alloy compositions in the 0 to 20 wt % Pb range and over the 160°C to 400°C temperature range. There is a density difference of about 7 percent between In and In(80), Pb(20) over this temperature range.

One of the characterization schemes discussed later requires knowledge of the densities of the solid alloys. Figure 13 shows calculated values for density as a function of composition. Figure 14 [6] shows measured density values. Figure 15 [7] shows x-ray diffraction results indicating that the c/a ratio increases smoothly and monotonically over the composition range of interest. This leads to the conclusion that density should be an unambiguous indicator of composition for this system.

Mutual diffusion coefficients for this system are shown in Figure 16 [8]. Other physical properties of interest are given in Table 1.

MASS TRANSPORT

As previously noted, sample and cartridge design minimize unwanted flow effects. Calculations indicate that no mass transport effects would be observed in the 10^{-4} g range and less, except solutal convection and diffusion. Time for diffusion to act is small (about 200 seconds), so that a diffusion front

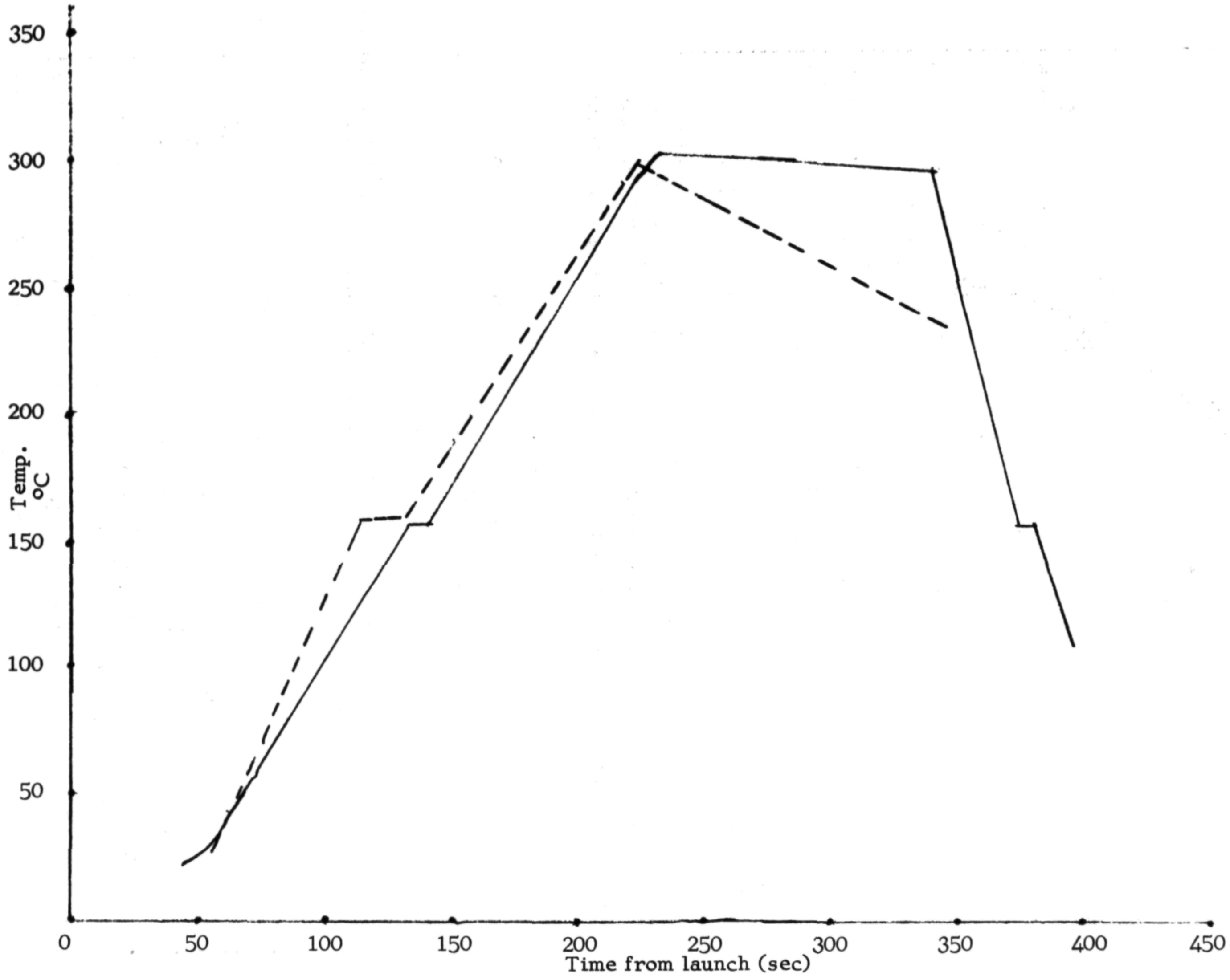

Figure 10. Computed thermal profile for a sample in low-g.

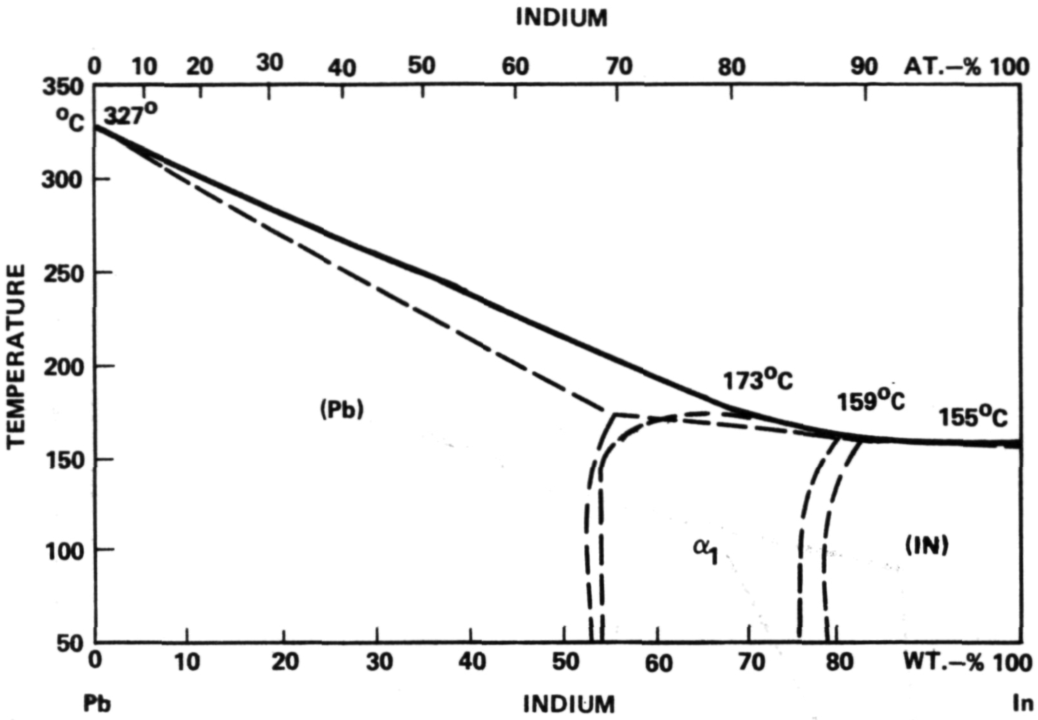

Figure 11. Indium-lead equilibrium phase diagram [4].

can progress only a distance less than 1 mm (Fig. 17). We can assume then that any appreciable fluid motion experienced by the samples will be due to solutal convection (residual accelerations acting on concentration induced density gradients).

CHARACTERIZATION

Four schemes for characterizing the composition as a function of position in the processed samples were developed.

(1) X-ray radiography was considered. Samples were inserted into an indium block placed on an x-ray film package, and exposed (Fig. 18). The differences in x-ray absorption coefficients for the two materials composing each sample cause different exposure levels on the film. These exposure level differences yield visual images of the flow fronts. X-ray exposures from multiple angles with subsequent image analysis can be used to construct a three-dimensional picture of the flow without damage to the sample. After these studies, sample sectioning was begun. Sample sectioning is done using

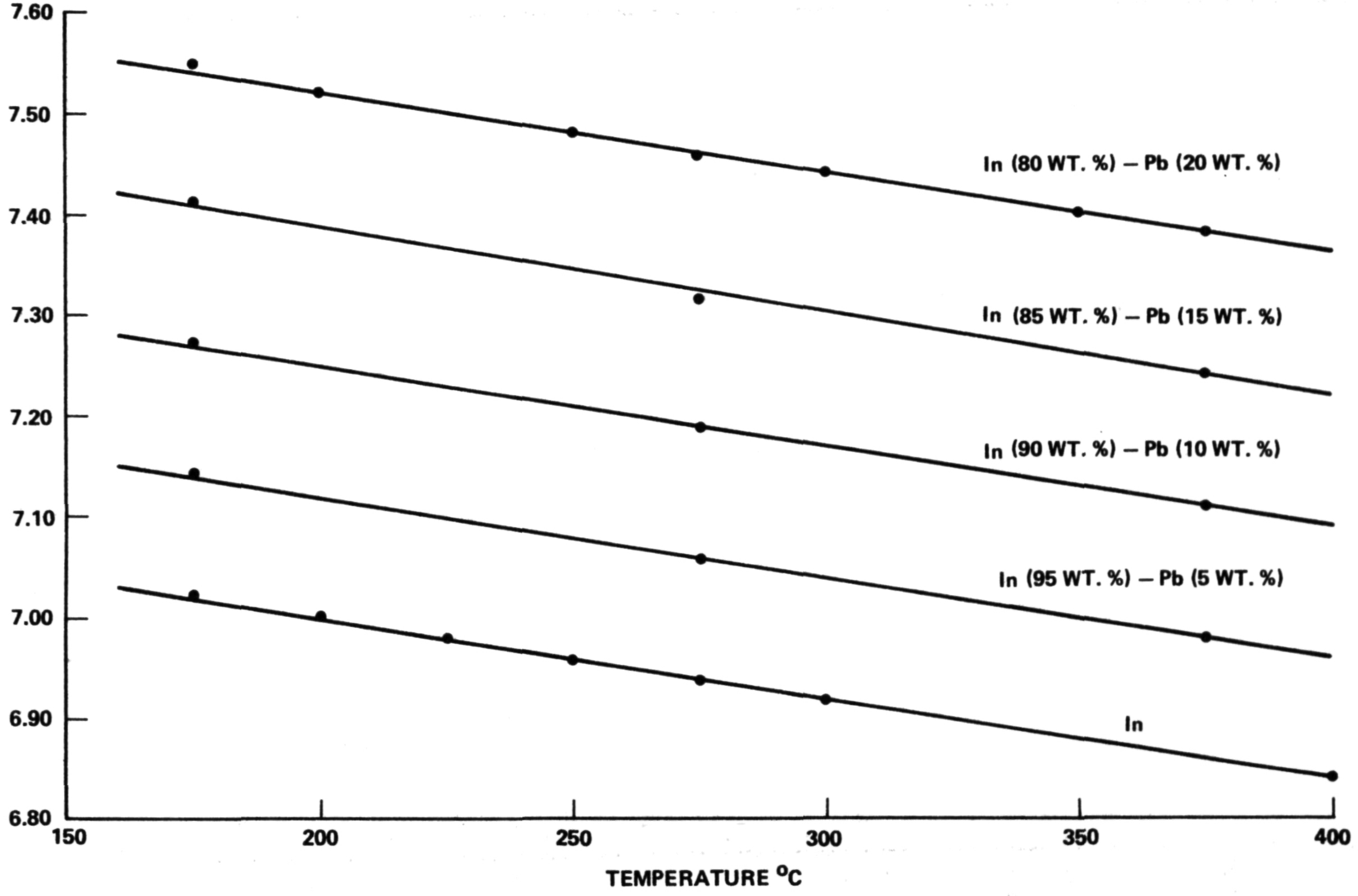

Figure 12. Densities of molten In-Pb alloys (calculated from empirical laws).

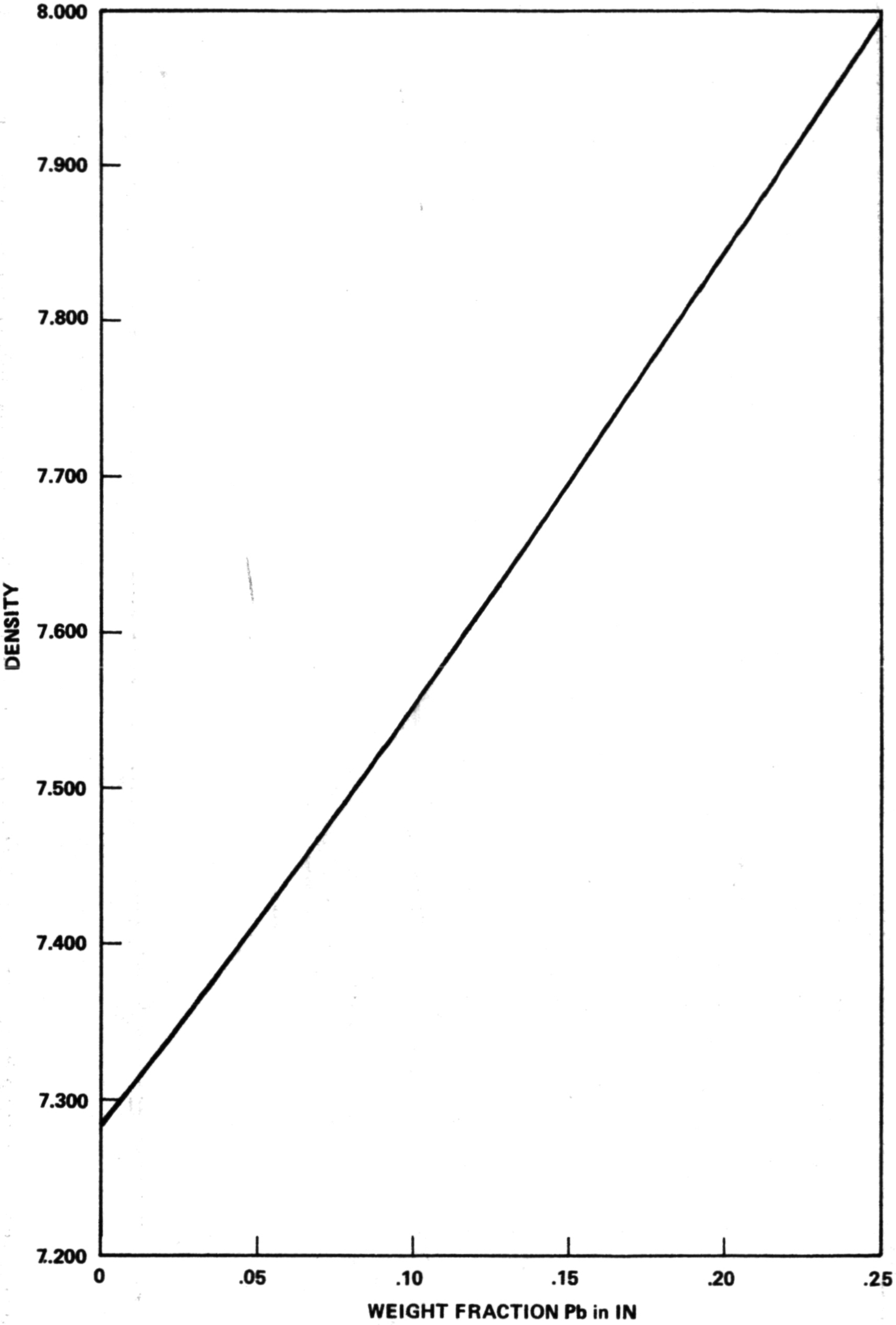

Figure 13. Calculated densities of Indium-lead alloys.

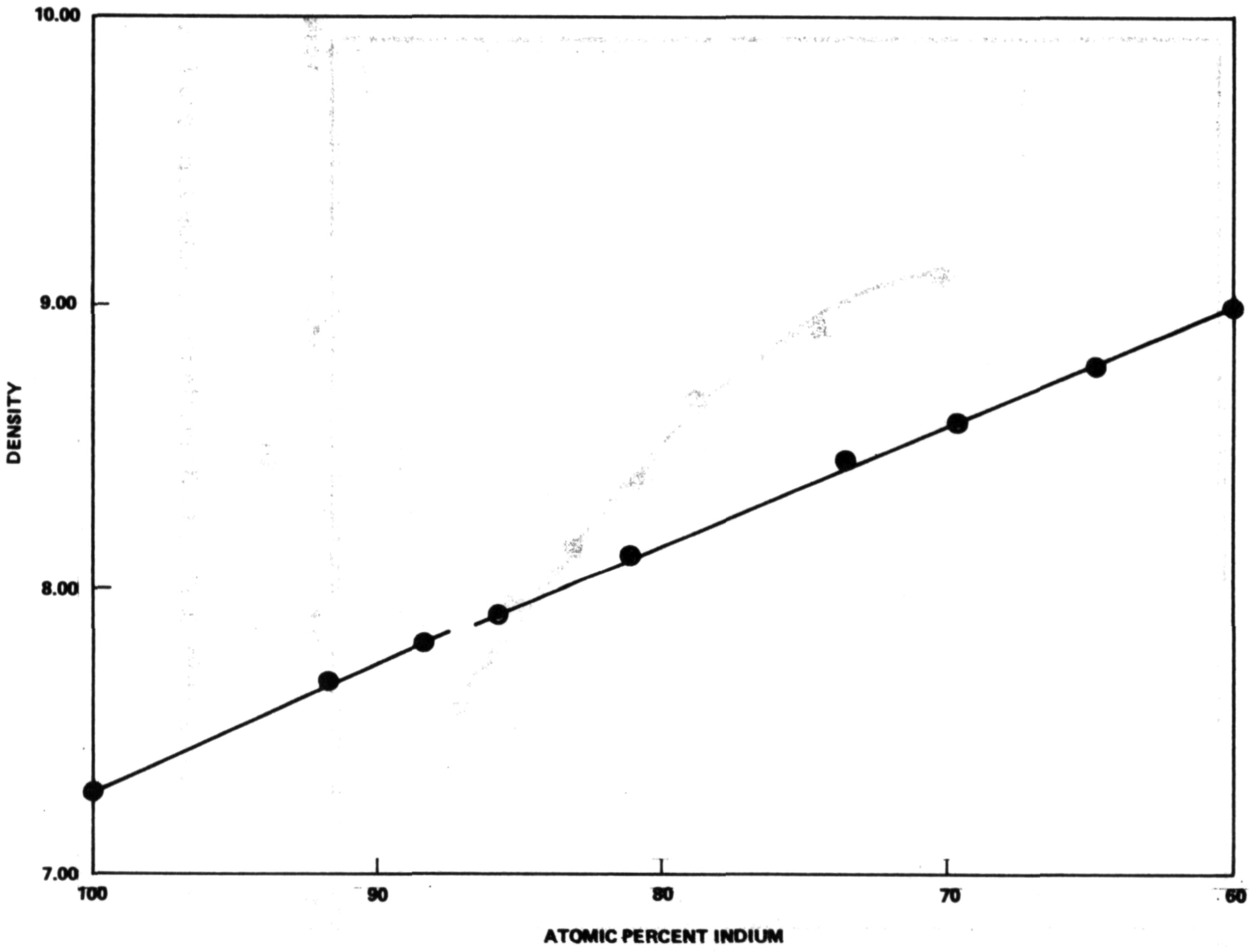

Figure 14. Densities of Indium-lead alloys at 25°C [6].

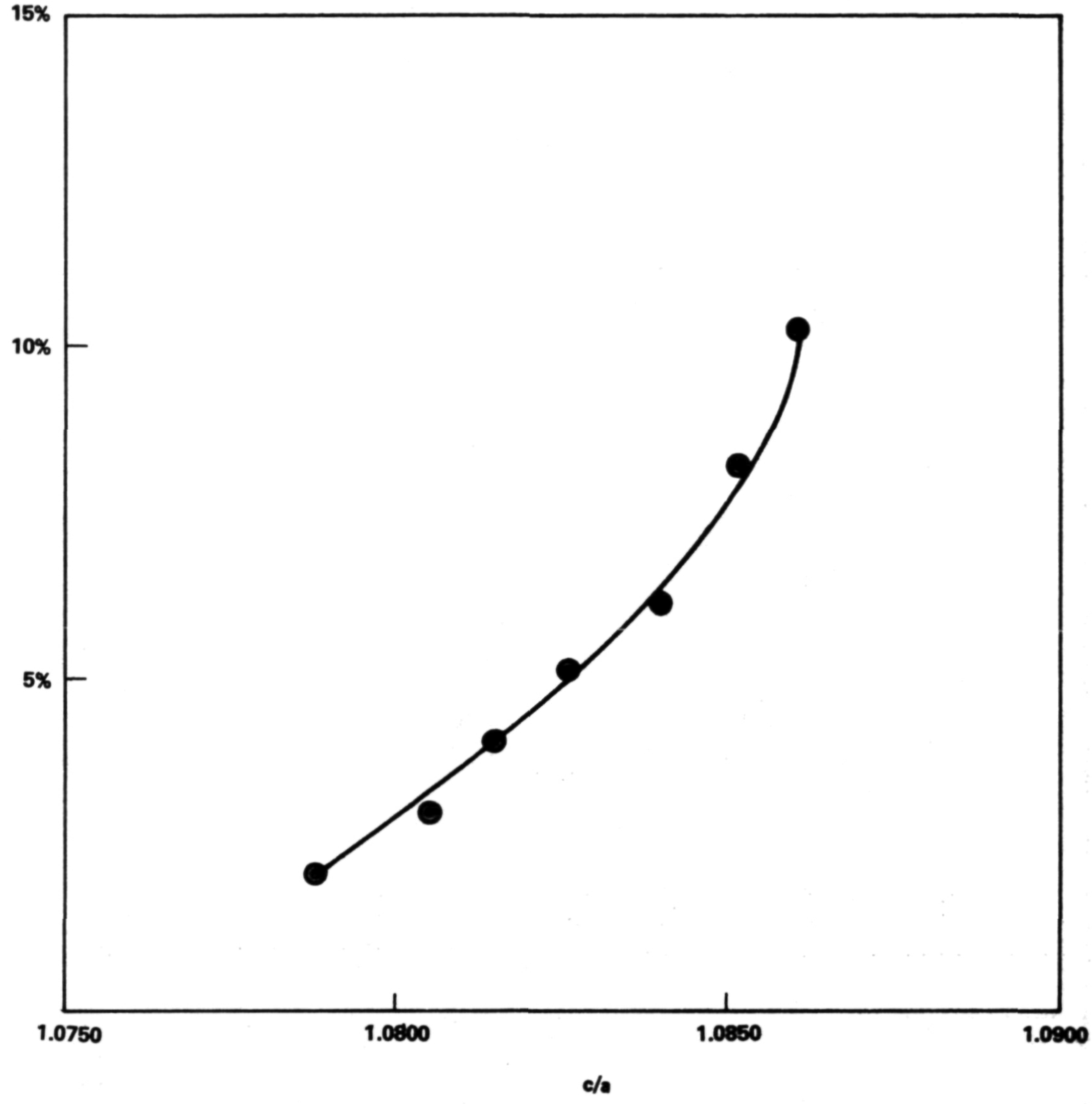

Figure 15. Atomic percent Pb in In versus lattice spacing ratio c/a [7].

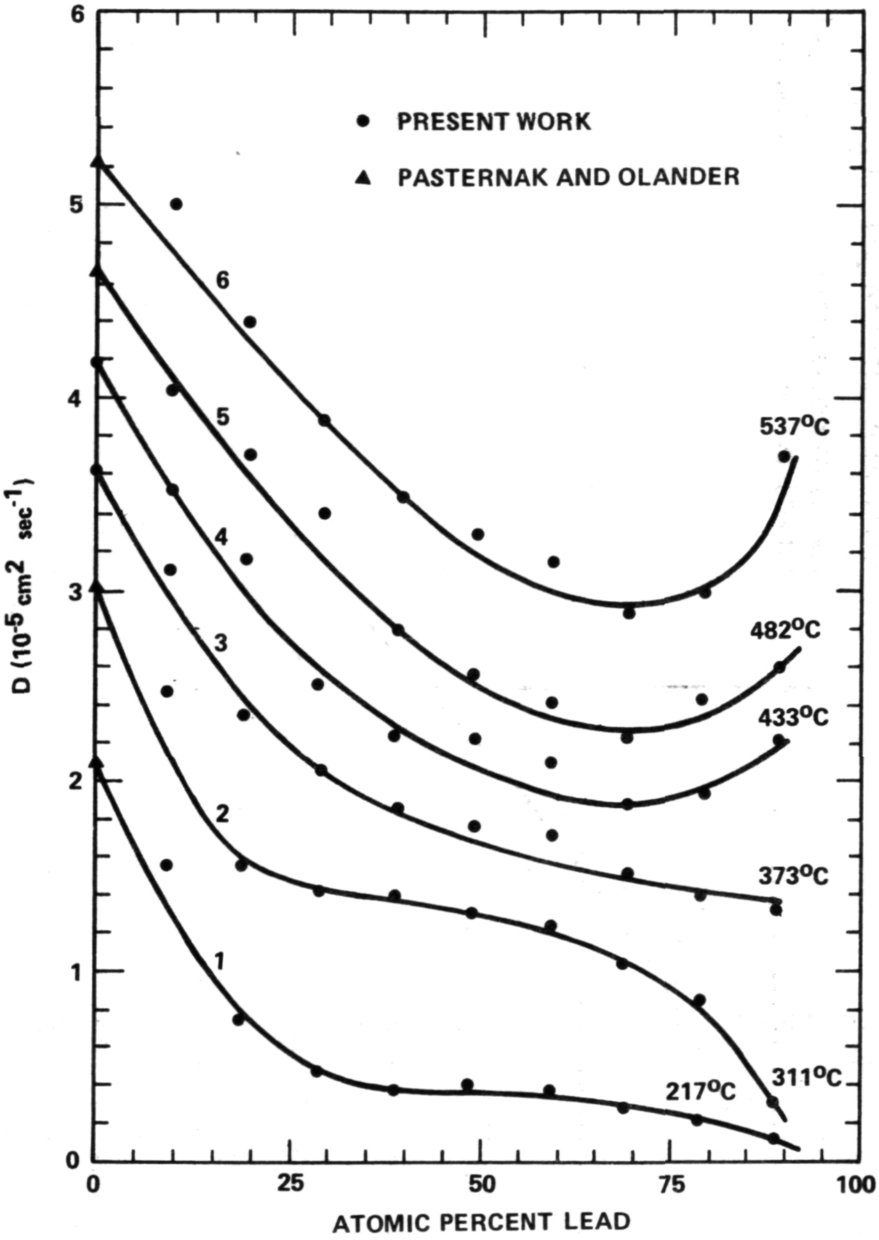

Figure 16. Mutual diffusion coefficients for the system In–Pb [8].

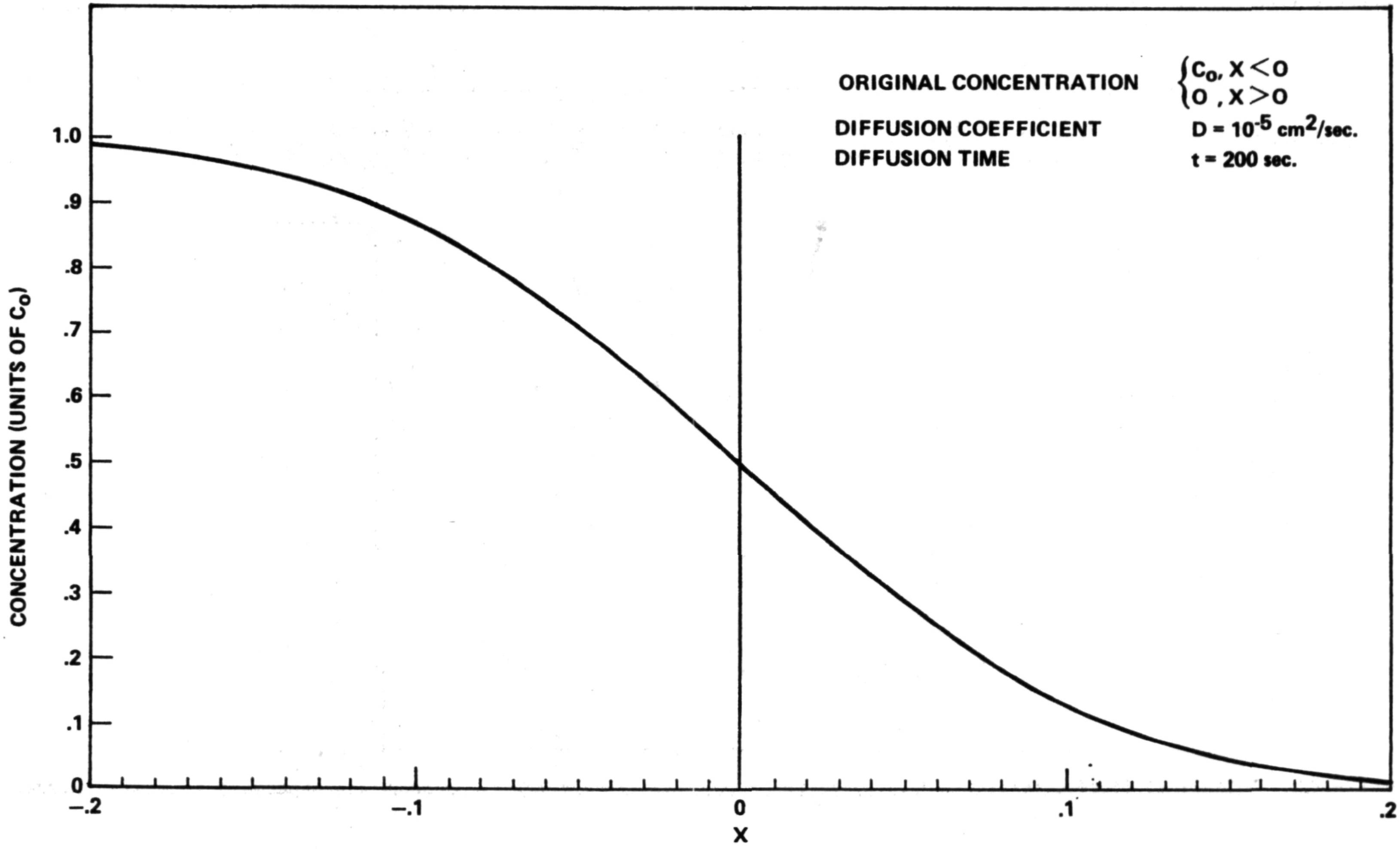

Figure 17. Concentration profile for diffusion in an infinite cylinder.

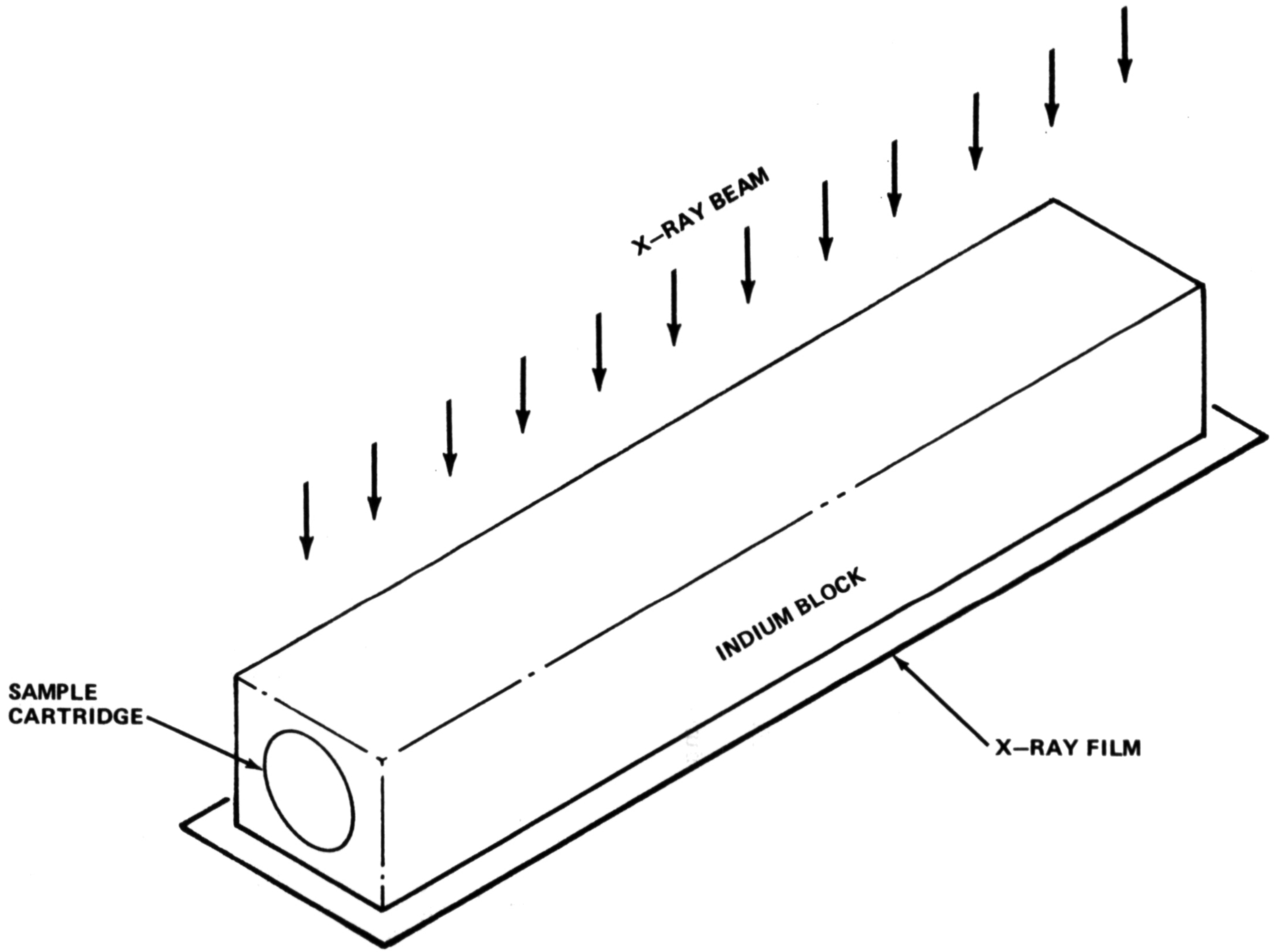

Figure 18.. Indium block on x-ray film package.

a microtome with specially designed tubular feed mechanism. Cylindrical sections 1 mm thick are made (Fig. 19). These sections are then available for further x-radiography and the other characterization methods.

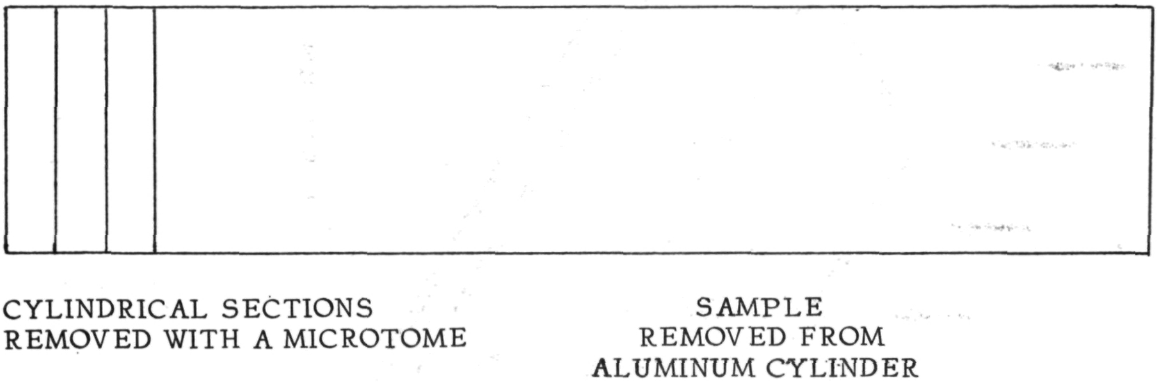

Figure 19. Sample sectioning technique.

(2) The indium-lead system was calibrated for hardness using a Leitz microhardness tester. Curves for unpolished and polished samples are shown in Figures 20 and 21, which show microhardness as a function of composition.

(3) Arrangements have been made to perform electron microprobe analysis if required.

(4) An apparatus has been assembled for performing small sample (30 to 100 mg) density measurements on the sectioned samples. This apparatus is shown in Figure 22 and is similar to the apparatus described by Cawthorne and Sinclair [9]. Measurements of known samples using this system yield results consistent with the values reported by Rider and Roney (Fig. 14).

These techniques will be used as required, with emphasis on the x-radiography and subsequent image analysis.

RESULTS

Telemetered temperature data from the flight samples indicated that the experiment performed as scheduled and that the thermal profile was that expected. Discussions with test personnel who removed the heater assembly

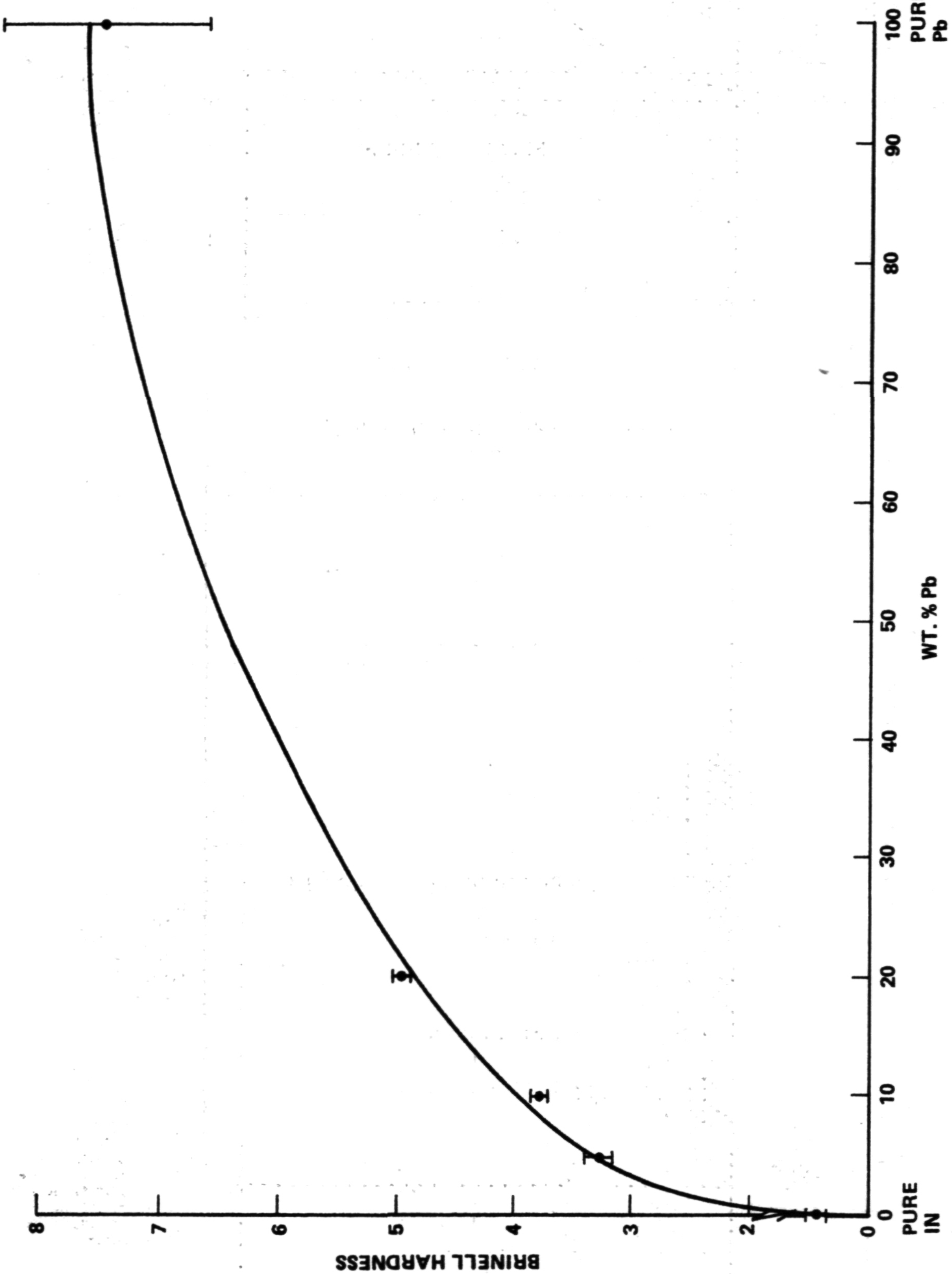

Figure 20. Microhardness of Indium-lead alloys (untreated specimens).

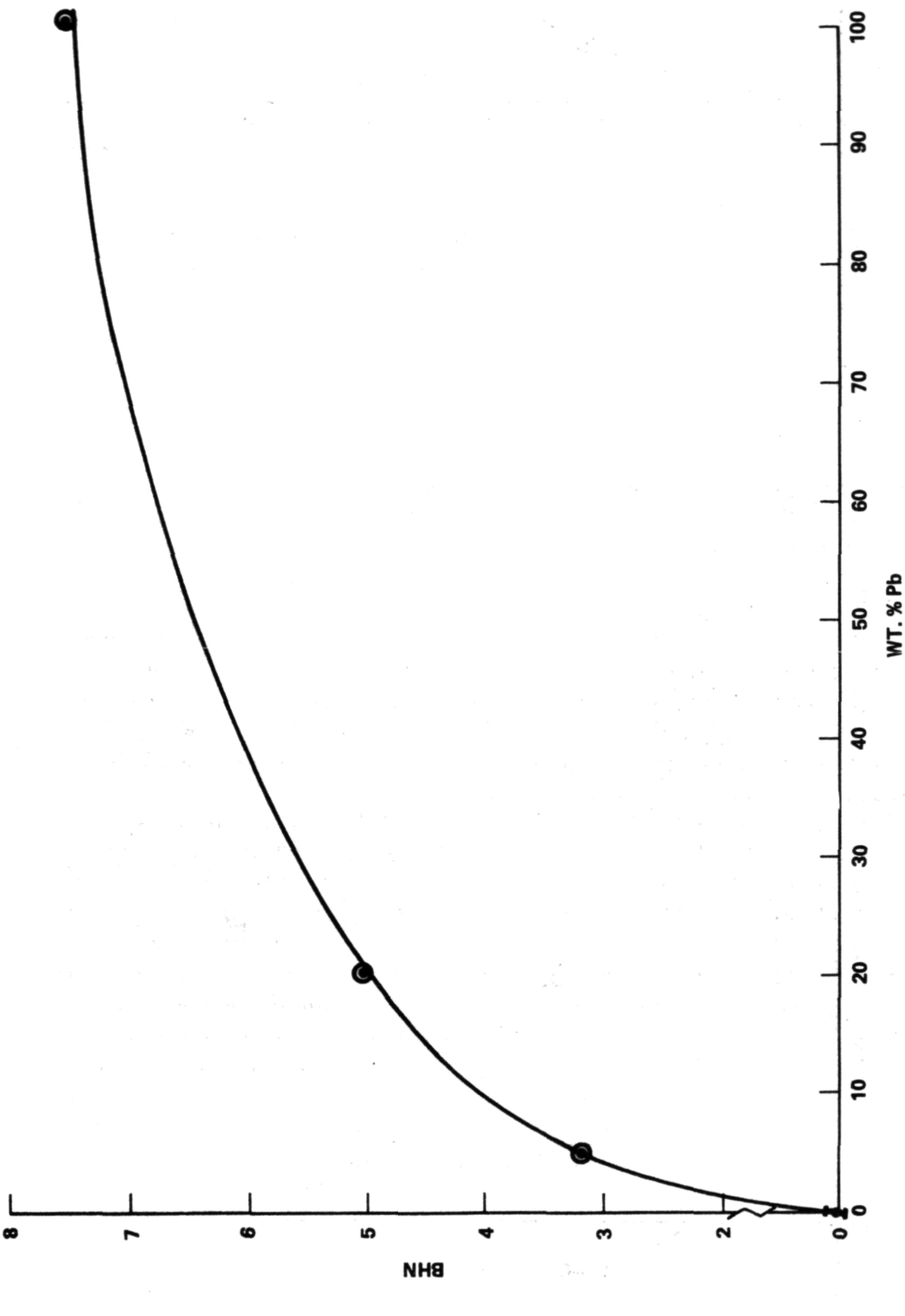

Figure 21. Microhardness of Indium-lead alloys (polished specimens).

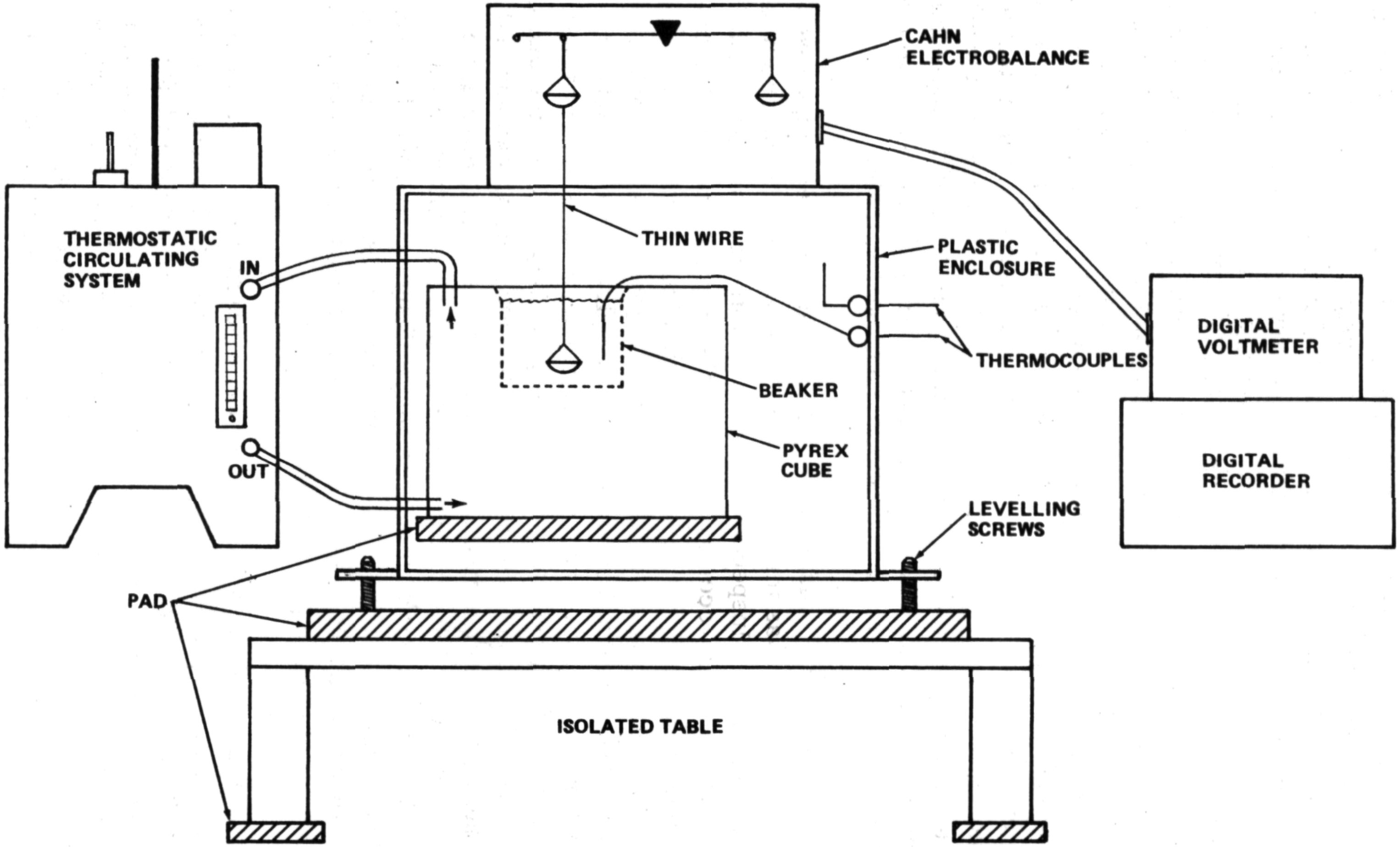

Figure 22. Small sample density measuring apparatus.

from the Thermal Control Unit indicated that the lower part of the unit was full of water adding further evidence that the quench system performed as expected. The heater unit with samples still installed was returned to MSFC, where the samples were marked for orientation and removed. The samples were subjected to x-ray radiography at two exposure levels. First, they were exposed to reveal the shape of the processed samples (Fig. 23). These exposures revealed that all the samples had melted (the edges were rounded) and had resolidified during low-g (samples remained centered in the cartridge). Next, the samples were inserted in an indium block (to yield more uniform exposure, i.e., reduce geometry effects) and subjected to a higher level of x-ray exposure to reveal the In-(In-Pb) interfaces. Sample 2 (oriented parallel to the payload longitudinal axis) experienced interface motion near that expected from diffusion (Fig. 24). Sample 1 (aligned parallel to the accelerometer x-axis) experienced a small amount of interface motion (Fig. 25) which may be slightly more than that expected by diffusion. Sample 6 (aligned parallel to the accelerometer y-axis) experienced flow down one side of the container (Fig. 26).

The sample cylinders were then placed in a lathe and the section containing the end cap was machined away. The end of each sample was marked to record orientation. Inspection of the ends of the samples revealed that very little wetting, if any, occurred between the samples and the aluminum cartridges. It had been planned to machine away the aluminum cartridge from the samples, but the lack of wetting suggested a change in procedure. A groove was carefully filed down the length of each side of the sample cartridge. When the groove was nearly through the aluminum, pliers were used to split the cartridges away. The samples were than removed without damage. Inspection of the samples revealed that the cleaning agent used to prepare the sample container and end cap for epoxying together had spread over much of the sample, leaving a residue. This residue combined with an oxide film could have prevented wetting of the aluminum by the sample material. Some shape changes were noted in the processed samples. Sample 6 had the most pronounced change, with a somewhat flattened side over about half the sample length. Photographs are shown for three orientations of the samples in Figure 27.

The samples were then subjected to another complete set of x-ray radiographs. Each sample was x-rayed in at least eight different orientations. That is, a radiograph was made for each of eight positions rotated about 22.5° from each other around the longitudinal axis. From these radiographs, image analyses are being performed which attempt to remove geometry effects and impose calibrations such that an effective thickness of the In-Pb alloy can be found for each position of the image. By performing this for various rotations, three-dimensional concentration profiles can be generated without damaging the

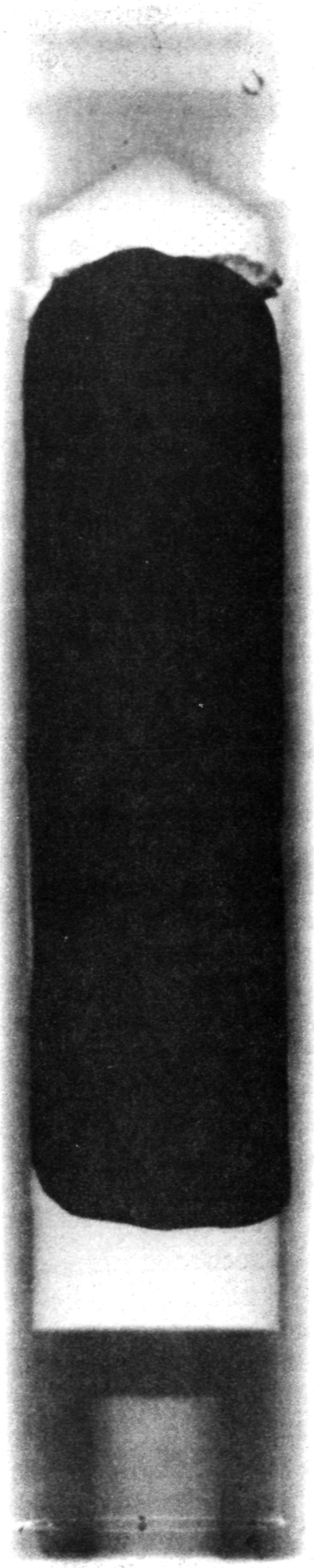

Figure 23. Sample 2 at 45°.

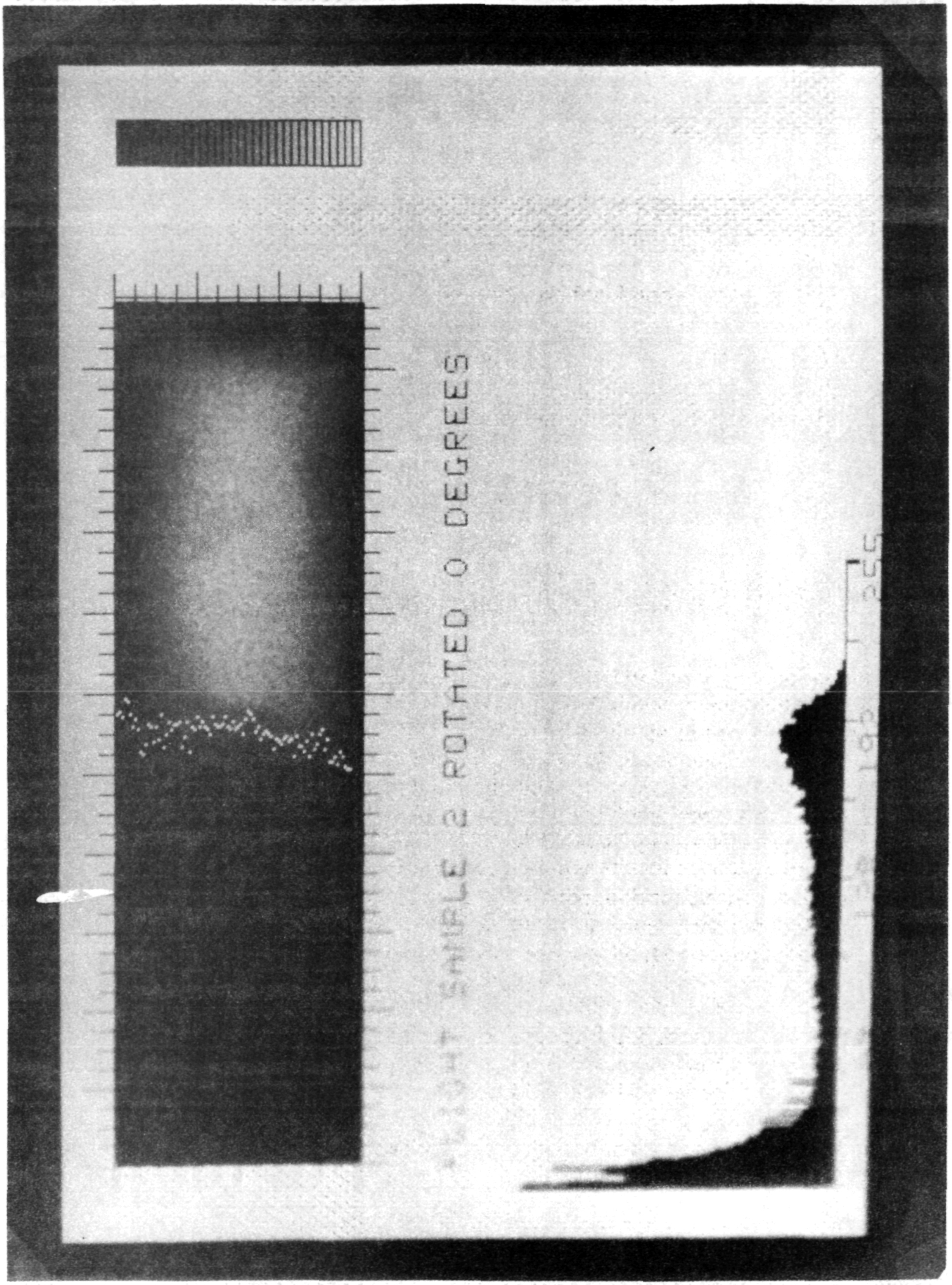

Figure 24. **Sample 2 at 337^0 for 2 min.**

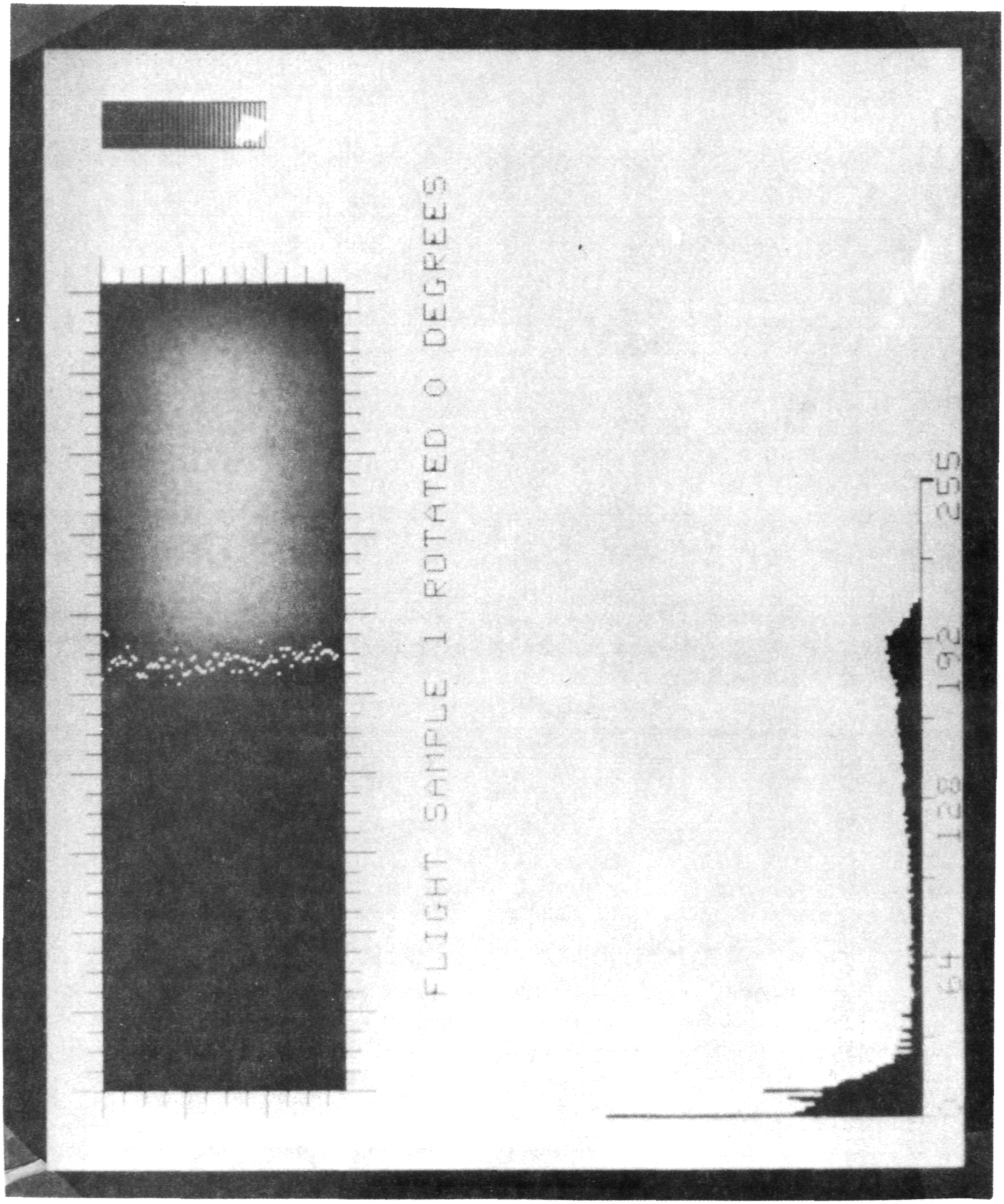

Figure 25. Sample 1 at 22° for 15 sec.

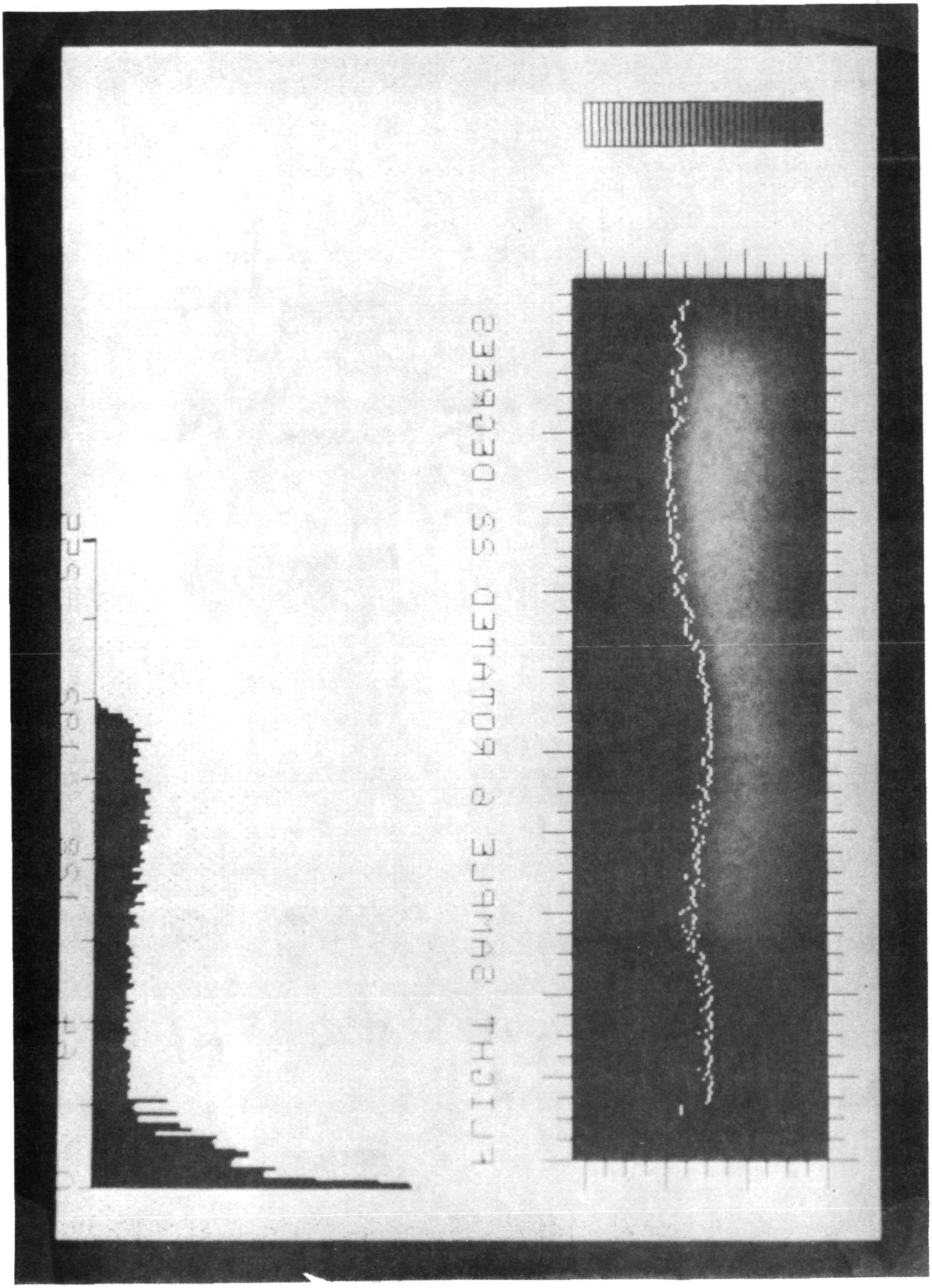

Figure 26. Sample 6 at 22°.

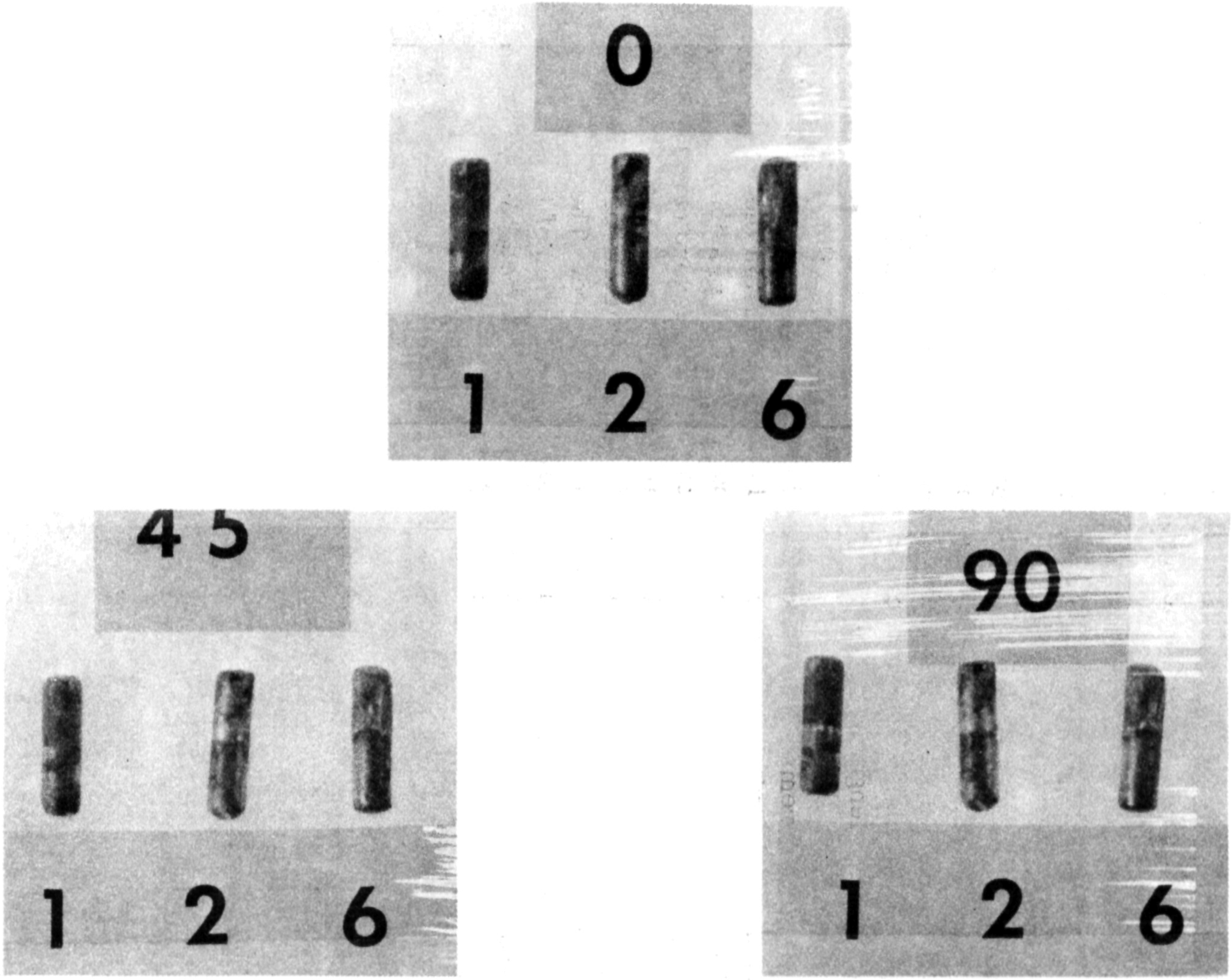

Figure 27. Orientations of samples 1, 2, and 6.

sample in any way. An example of the type of operations being performed on these radiographs is shown in Figure 28. Here the radiograph was scanned, displayed on a screen, and an automatic scan made of illumination level versus position along a line through the image. Analysis of the radiographs is still under way.

Sample 6 has been sliced into 1 mm thick sections and the sections subjected to x-ray radiography. These radiographs substantiate what was revealed in the work with the whole samples, that is, that flow occurred down one side of the sample. A sketch of a typical radiograph image of these sections is shown in Figure 29.

The results we must account for are now presented in summary.

Radiographic analyses provided magnitudes of interface motion for the two samples which encountered very little flow. If we assign a value $x = 0$ for the original interface position, then the post-processing interfaces for both samples were within the range $-0.1 \text{ cm} \leq x \leq +0.1 \text{ cm}$. Sample 6 experienced flow down its entire length.

The problem remains, then, of correlating these observations with the rocket acceleration environment. Both angular rate data from the rate control system gyros and three axis accelerometer data have been provided. In addition, information on moments of inertia, location of the payload center of mass, and confirmation that the payload body axes are principal axes for the system have been received. It is now believed that the accelerometers are reading down in their noise levels, so this set of data cannot be used. The rate gyro data show an increase in roll rate magnitude over the duration of the flight, but almost constant pitch and yaw rates over the same time period. We write the Euler dynamical equations for rocket payload:

$$I_x \dot{w}_x + (I_z - I_y)\, w_y w_z = L_x$$

$$I_y \dot{w}_y + (I_x - I_z)\, w_z w_x = L_y$$

$$I_z \dot{w}_z + (I_y - I_x)\, w_x w_y = L_z$$

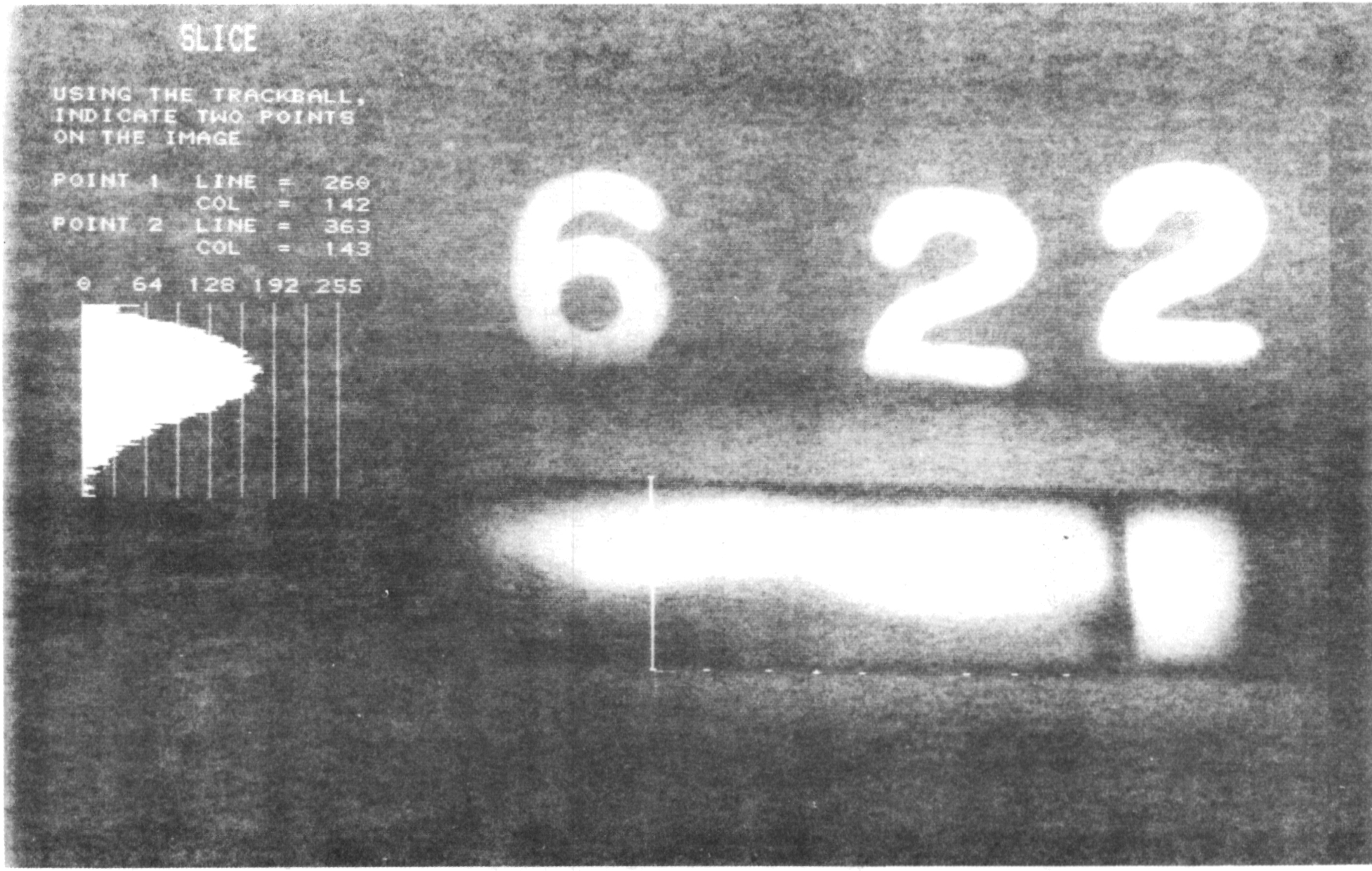

SLICE

USING THE TRACKBALL,
INDICATE TWO POINTS
ON THE IMAGE

POINT 1 LINE = 260
COL = 142
POINT 2 LINE = 363
COL = 143

Figure 28. Example of types of operations performed on the radiographs.

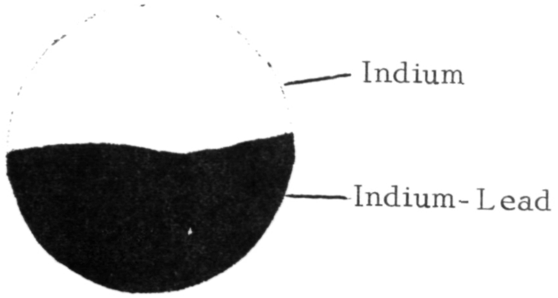

Figure 29. Sketch of appearance of radiograph of sample 6 cross-section.

We know from the dynamical data that $I_x = I_y$, $\dot{w}_x = \dot{w}_y = 0$, $\dot{w}_z$ = a constant, and that $I_z - I_x = I_z - I_y \cong I_z$ (i.e. $I_z >> I_x$). We must conclude from this that either:

(1) there are external torques, or

(2) the angular rate data signal levels are also down in the noise.

Given that no consistent picture of payload motion exists, but that some motion did exist to cause the flow experienced by the samples as described above, we now will construct a self-consistent model of payload motion. The simplest motion which would qualitatively explain our observations is a roll about the longitudinal axis. This would produce an acceleration directed along a radius and would act on samples 1 and 2 from the side (nearly perpendicular to the samples' longitudinal axes, Figs. 5 and 6). The force on sample 6 would be directed nearly along the longitudinal axis, with the heavier material "on top" (Fig. 6).

An analysis by Cormack, Leal, and Imberger [10] studied convection in a rectangular box lying on its side with a horizontal density gradient in the fluid. Applying this model to samples 1 and 2, and assuming interface motion of 2 mm, we find the acceleration required to cause this motion in 200 sec to be 2.6×10^{-5} g.

Sample 6 may be represented as a vertically stratified fluid. The problem of stability in this type of system has been treated extensively in the literature [11-14]. If we use the value of the critical Rayleigh number computed by Verhoeven [14] for this configuration, we find the acceleration value for threshold convection to be 1.5×10^{-5} g.

SUMMARY AND CONCLUSIONS

The magnitudes of flow experienced by the three samples in this experiment are consistent with an acceleration arising from rotation of the payload about its longitudinal axis. The level of this acceleration would be a few times 10^{-5} g or less. Two conclusions must be reached from these results. First, the residual accelerations aboard the SPAR are very low so that the SPAR experiment package provides a good platform for experiments requiring up to 5 minutes of low-g time. Second, even at very low-g levels, convective fluid motion can occur. Computations can be made for a given experimental configuration to estimate levels of effective gravity for which convective flows become significant. This type of computation should be done as a part of experiment design for each proposed experiment.

REFERENCES

1. Proceedings Third Space Processing Symposium, Skylab Results, vol. 1, p. 257.

2. Proceedings Third Space Processing Symposium, Skylab Results, vol. 1, p. 275.

3. Proceedings Third Space Processing Symposium, Skylab Results, vol. 1, p. 425.

4. Hansen, M.: Constitution of Binary Alloys. McGraw-Hill, New York, 1958, p. 854.

5. Ukanwa, A.: Diffusion in Liquid Metal Systems. NASA Contract NAS8-30252, Final Report, June 1975.

6. Rider, J. G. and Roney, P. L.: J. of the Inst. of Metals, vol. 91, 1962-63, p. 328.

7. Tyzack, C. and Raynor, G. V.: Faraday Society Transactions, vol. 50, 1954, p. 675.

8. Rialland, J. F. and Robert, J.: Proceedings of the 2nd Int. Conference on Properties of Liquid Metals. Tokyo, Japan, Sept. 1972, p. 549-553.

9. Cawthorne, C. and Sinclair, W. D. J.: Journal of Physics E, Scientific Instruments, vol. 5, 1972.

10. Cormack, D. E.; Leal, L. G.; and Imberger, J.: J. Fluid Mech., vol. 65, part 2, 1974, pp. 209-229.

11. Chandrasekhar, S.: Proceedings of the Cambridge Philosophical Society, vol. 51, 1955, p. 162.

12. Nield, D. A.: Water Resources Research, vol. 4, no. 3, June 1968.

13. Schein, V. B.: Translated from Zhurnal Technicheskoi Fiziki, vol. 29, no. 9, Sept. 1959, pp. 1162-1166.

14. Verhoeven, J. D.: Trans. Met Soc. of AIME, vol. 242, Sept. 1968, p. 1937.

CHAPTER V

THE DIRECT OBSERVATION OF SOLIDIFICATION AS A FUNCTION OF GRAVITY LEVELS

Experiment 74-21

By

M. H. Johnston and C. S. Griner

Marshall Space Flight Center

ABSTRACT

The solidification of a metal-model material was directly observed on Earth at one-g and at 10^{-5} g on a suborbital rocket flight. In the one-g experiments, nucleation started at the cold walls, and then dendrites and dendritic debris were swept into the central region by fluid flow. The numerous crystals in the central zone created an equiaxed zone. Secondary dendrite arms were oriented toward the cold wall with suppressed arm growth in the direction of the flow pattern. The necking and remelting of secondary arms was observed. The variation in secondary and tertiary arm spacing ranged from 27 to 38 percent. Individual dendrites grew at similar rates to interface fronts.

When solidified in low-g, only four nuclei grew to form the complete casting. There were no free floating crystals or visible dendrite remelting. Symmetrical dendrite growth into the fluid and some necking of secondary arms occurred, but no coarsening or fragmentation resulted. The growth rate of interfaces was less than that of individual dendrites. Total growth was columnar with no equiaxed zone being formed.

INTRODUCTION

The NASA Space Processing Program is developing applications of space flight that will advance materials science and technology. This objective is met by obtaining research results which contribute to understanding and improving processes used on the ground and developing means to process products of high value in space.

Opportunities to perform experiments in low-g (where g is defined as 980 cm/sec^2) are, therefore, essential for progress in space processing, and the Space Processing Program has been active in experimentation on all available manned space flights.

The condition of near weightlessness obtained in suborbital or orbital flight cannot be duplicated on Earth except in free-fall experiments where the maximum duration is on the order of seconds. The Space Processing Rocket Experiment Project continues to develop materials science experiments through the remainder of the 1970's. Approximately 5 to 7 minutes of acceleration levels of 10^{-5} g are available with the Black Brant VC sounding rocket. This chapter will present the results of a casting experiment performed under these low-g conditions.

The transition between the columnar and the equiaxed zone in castings has been the subject of numerous publications [1-3]. Theories dealing with this phenomenon have depended on gravity as the driver for fluid flow and subsequent crystal multiplication [3,4]. The only theory which is active in the absence of gravity [1] suggests that the equiaxed zone forms due to constitutional supercooling ahead of the interface.

Experimenters have attempted to circumvent the gravity influence by use of magnetic fields [5], metal screens [6], or other impediments to fluid flow. None of these techniques actually eliminates the gravity force. Through the Space Processing Applications Rocket (SPAR) project, the present experiment was operated at a gravity acceleration around 10^{-5} g, a level perfectly adequate for eliminating acceleration influences on casting phenomena. The purpose of the experiment was to observe the growth of dendrites in the columnar solidification region in order to determine the influence of gravity driven flow on the formation of the equiaxed zone. In order to observe the actual solidification process in low-g, a transparent "metal-model" material was selected for this experiment.

The H_2O-NH_4Cl system has been used extensively as a metal-model material in the investigation of solidification phenomenon [7-9]. Experimentation has included such areas as growth morphology [10], growth kinetics [11], gravity segregation [12], and dendrite remelting and coarsening [13]. The observation of the remelt process during growth in the low-g environment was a primary objective of this experiment. Although several metallic systems have been solidified in space on Apollo, Skylab, and ASTP, this was the first direct observation of metallic-type solidification at low-g acceleration levels.

EXPERIMENTAL PROCEDURE

For all experiments, a solution of NH_4Cl was prepared by saturation at 72°F. The resultant composition from the phase diagram [14] was 28.4 wt.% NH_4Cl. This concentration was selected to preclude the presence of any solid NH_4Cl prior to initiation of solidification. The solution was encapsulated in a plexiglass cuvette. The cuvette was completely filled and sealed to eliminate air bubbles which, as a free surface, could become a nucleation site.

The capsule was mounted into a cuvette assembly (Fig. 1), consisting of two thermoelectric cooling units, three thermistors, and the mounting bracketry which also provided the heat sink for the thermoelectric devices. Power was supplied to the thermoelectrics by two HR5DC-7 3 volt batteries in series. The assembly was backlighted by a single tungsten filament lamp. The solidification process was photographed from the front of the cuvette with a 35 mm Nikon F2 camera. Using a motor drive unit and a 250 magazine back, it was possible to photograph a total of 240 frames at one frame per second.

A series of ground-based tests (GBT) was made in the "flight" hardware to characterize the solidification process in the one-g environment. All tests were made in a vacuum chamber with a thermally controlled shroud. As can be seen in Figure 2, the cuvette temperature versus time curve for the GBT runs and the low-g flight were comparable. The direction of the gravitational force directly affected the fluid flow in the cuvette. One-g tests were therefore made with the cuvette perpendicular (horizontal) as well as parallel (vertical) to the gravity force. Differences in temperatures for the two orientations are attributable to the thermal transfer caused by convective fluid flow.

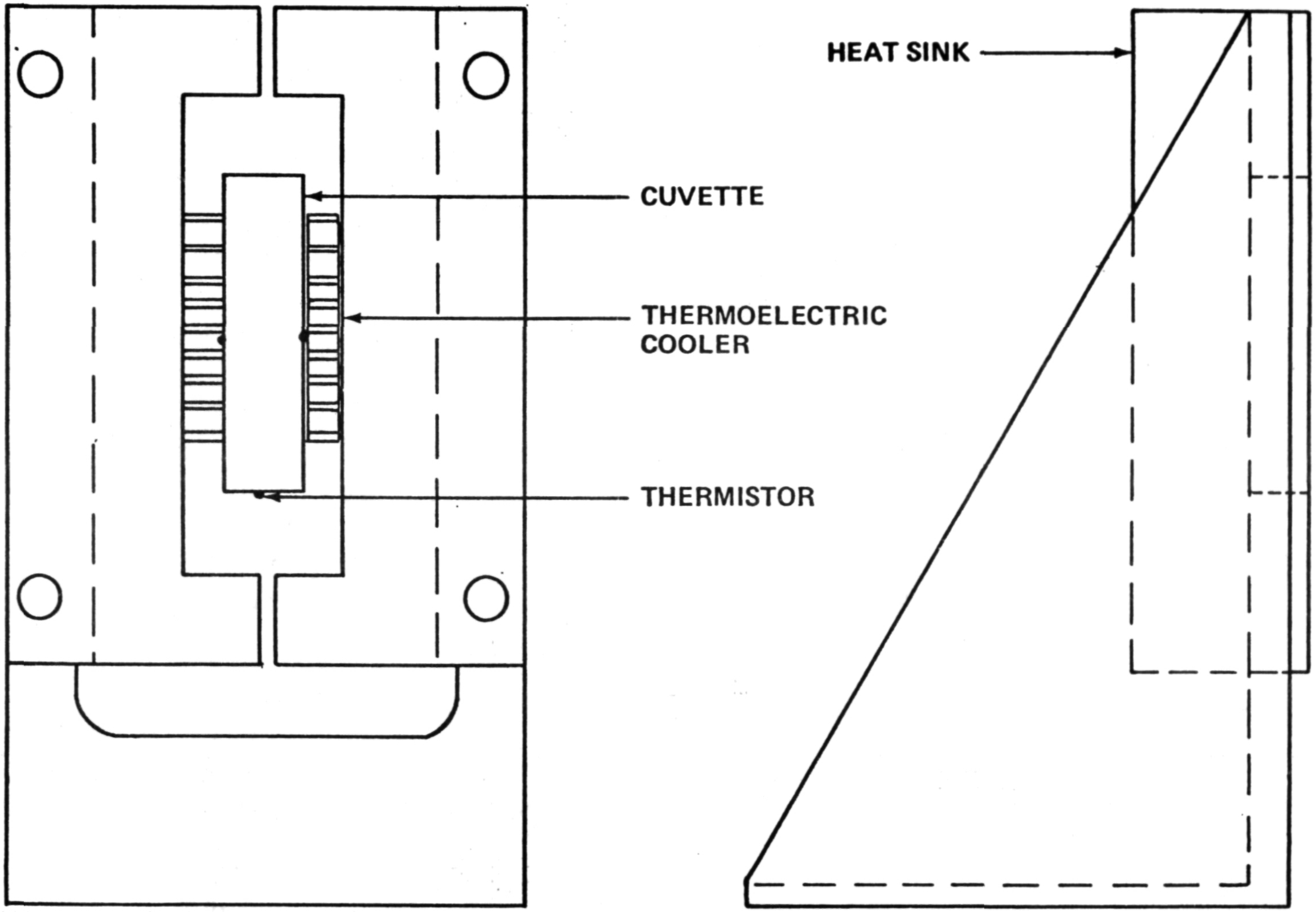

Figure 1. Cuvette assembly schematic.

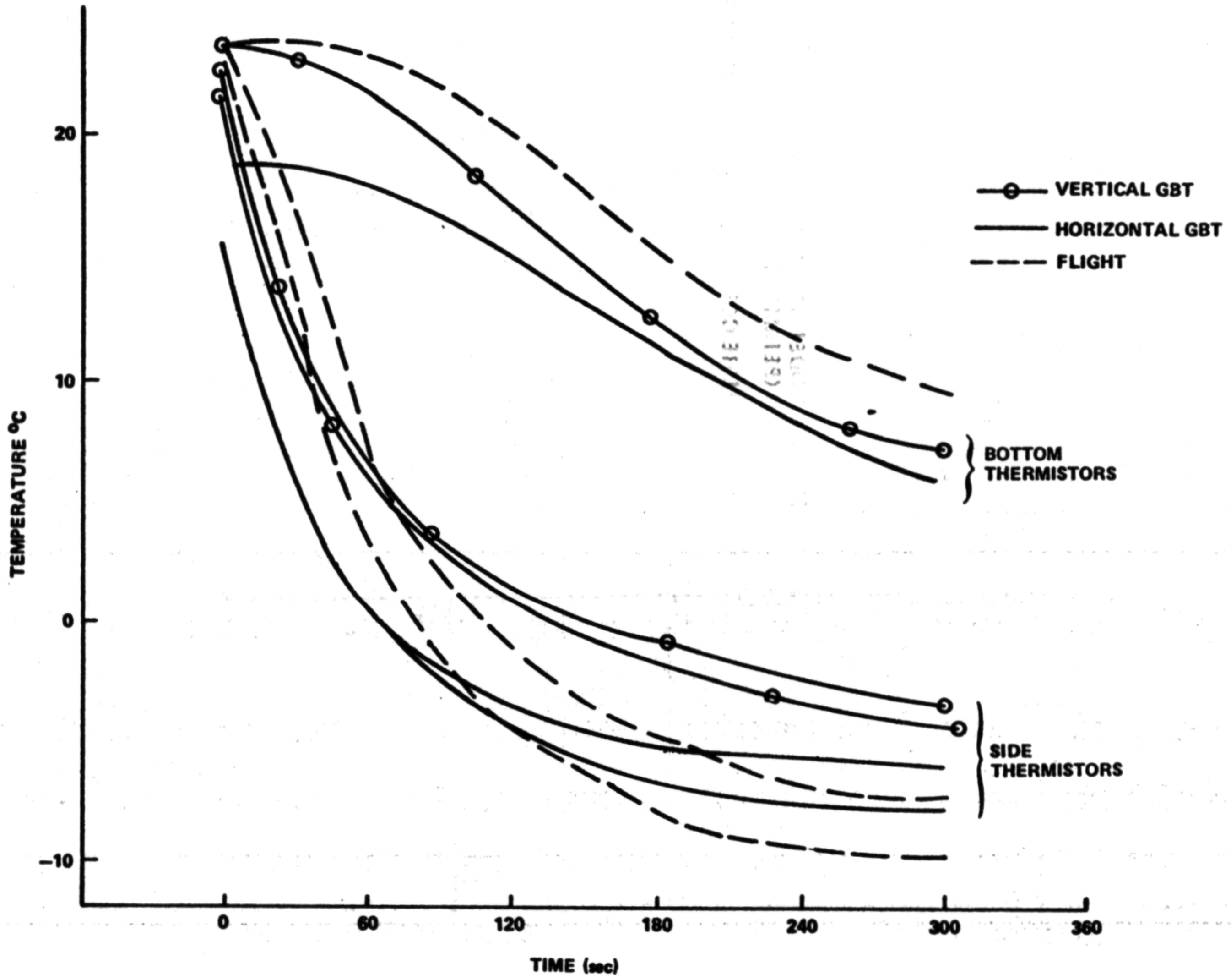

Figure 2. Time versus temperature cooling curve.

The apparatus was mounted in the sounding rocket in the location shown in Figure 3. The accelerations experienced by the experiment during the flight are shown in Figure 4 for the three axes of the rocket as a function of time. The timing sequence of the experiment during flight is also shown in Figure 4.

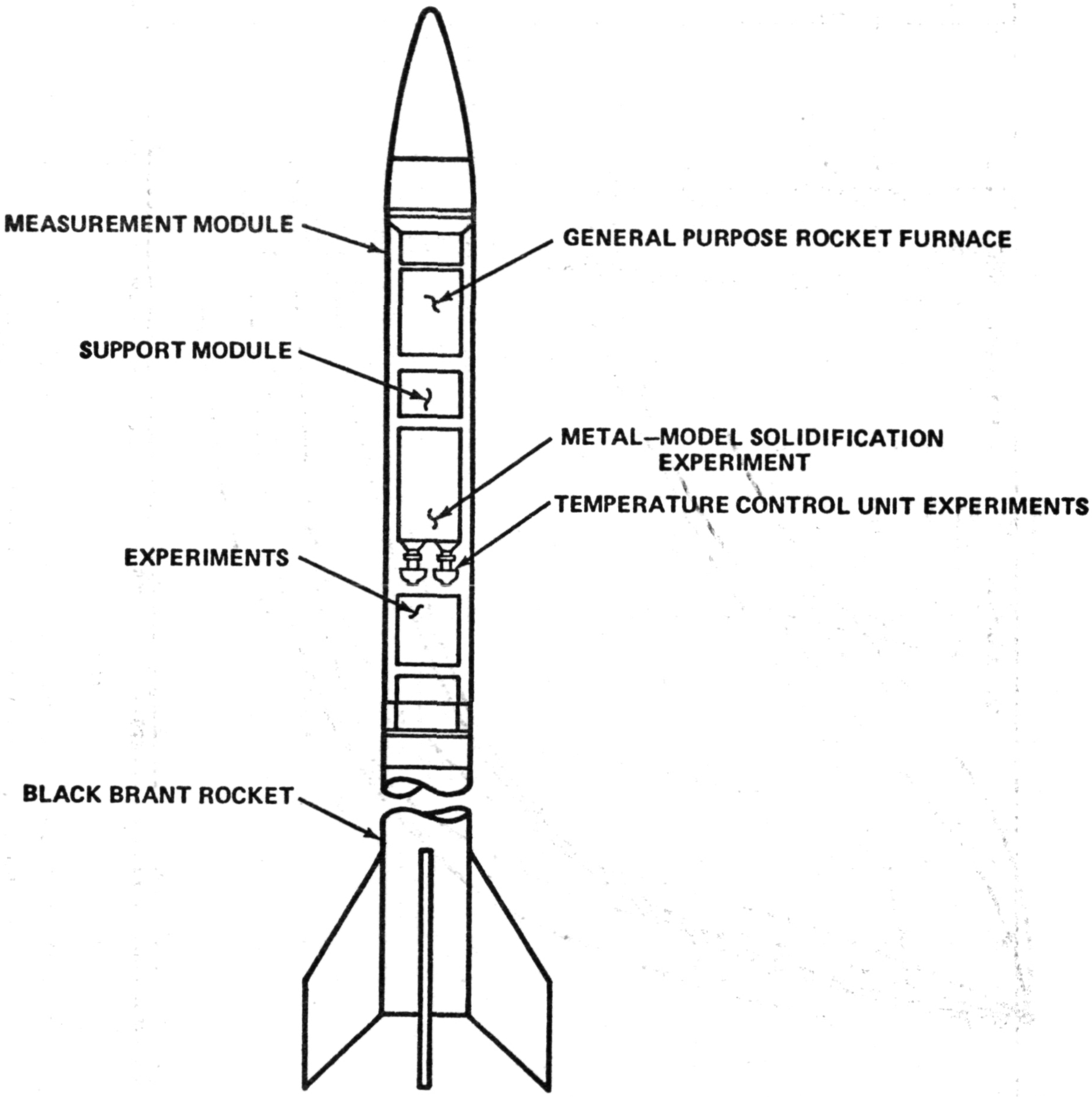

Figure 3. Diagram of Black Brant Rocket showing experiment location.

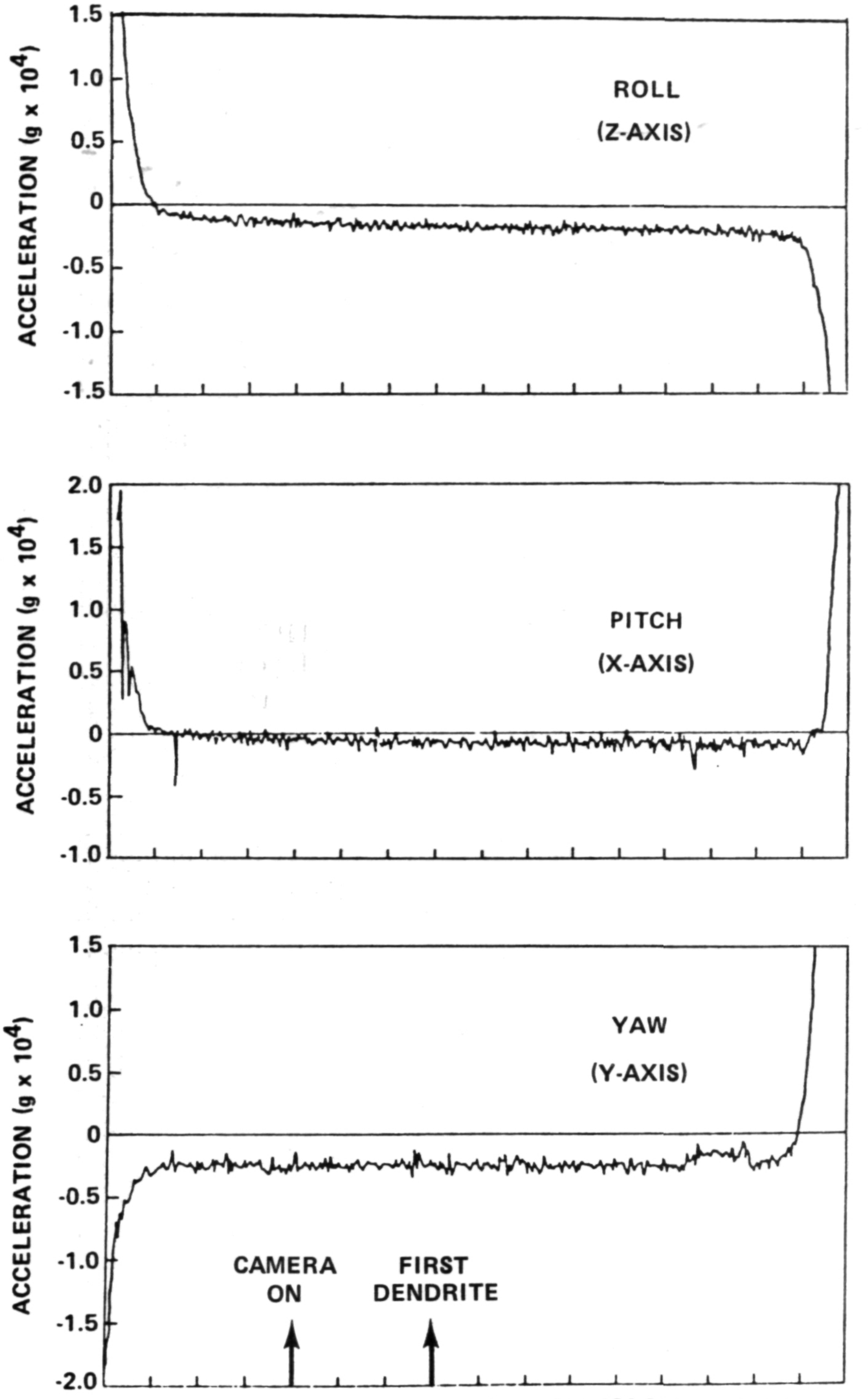

Figure 4. SPAR I - 21.032 np measured acceleration (low-g environment).

EXPERIMENTAL RESULTS

During the low-g portion of the rocket flight, the entire solidification sequence occurred and was photographed. Selected photographs are shown in Figures 5 through 8 along with photographs of ground-based solidification in the same time frame.

Length versus time measurements of secondary dendrite arms and dendrite array "interfaces" for low-g and one-g growth are shown in Figure 9. The first crystal to appear in the low-g solution had what appeared to be a [100] growth direction and a slow growth rate of 0.29 cm/min. This corresponds with earlier published data by Chan and Kahlweit [15]. Other dendrites in the low-g case, and all measured dendrites that were attached to the wall in the one-g experiment, grew at rates ranging from 0.85 to 1.0 cm/min and apparently had a [110] growth direction. Except for the initial low-g dendrite, there was no significant difference in individual dendrite growth rates between the low-g and one-g crystals; however, there was a difference in the rate of interface growth. The low-g interfaces grew at approximately 25 percent of the rate of individual dendrites, while the one-g interfaces grew at the same rates as individual dendrites. This indicates that the controlling factor on the single dendrite growth rates is the cooling rate and crystallographic direction of the system. During interface growth, the matrix depletes the surrounding solution. In the one-g experiment, there is fluid flow supplying fresh solute to the growing interface. In the low-g experiment fluid flow does not occur so growth is limited by diffusion in the quiescent liquid. This diffusion limited phenomenon could also be seen in the low-g experiment when an individual dendrite merged into a dendrite array. The growth rate decreased and momentarily halted.

The measured spacing of secondary and tertiary dendrite arms for both one-g and low-g crystals is shown in Table 1. The flight secondary arm spacing is greater than that of the one-g material. Tertiary arm spacing is less affected by the gravitational levels. It was found, however, that the standard deviation for ground-based material ranged from 26 to 38 percent. This constrasts sharply to the deviation of only 13 to 20 percent for low-g arms. The greater deviation in one-g arm spacing is most likely a result of breakoff caused by convective fluid flow. This flow leads to an enhanced coarsening process, whereas the absence of fluid flow causes the low-g material to retain more of a fine substructure.

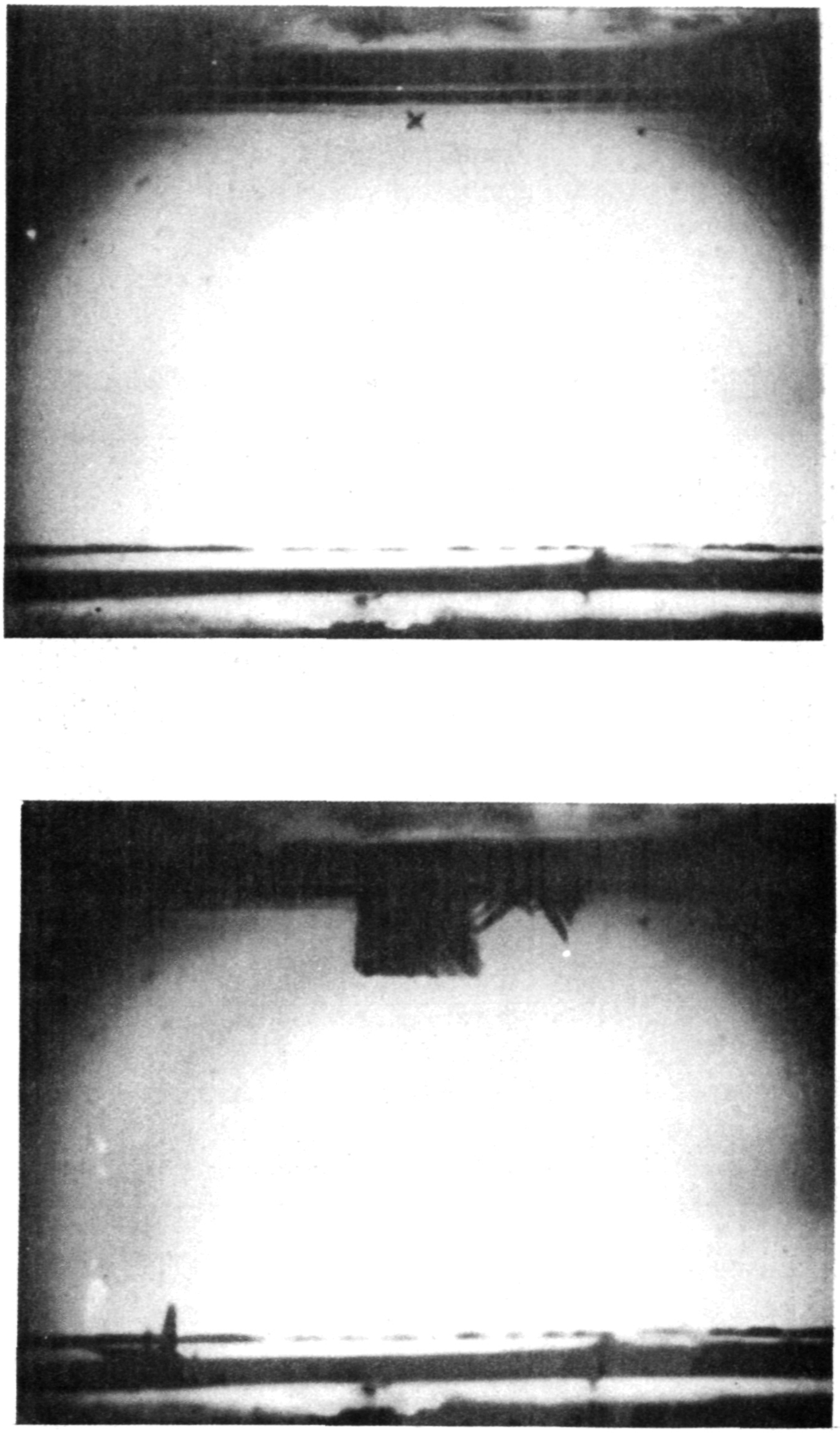

Figure 5. Photographs of low-g solidification — initiation and growth.

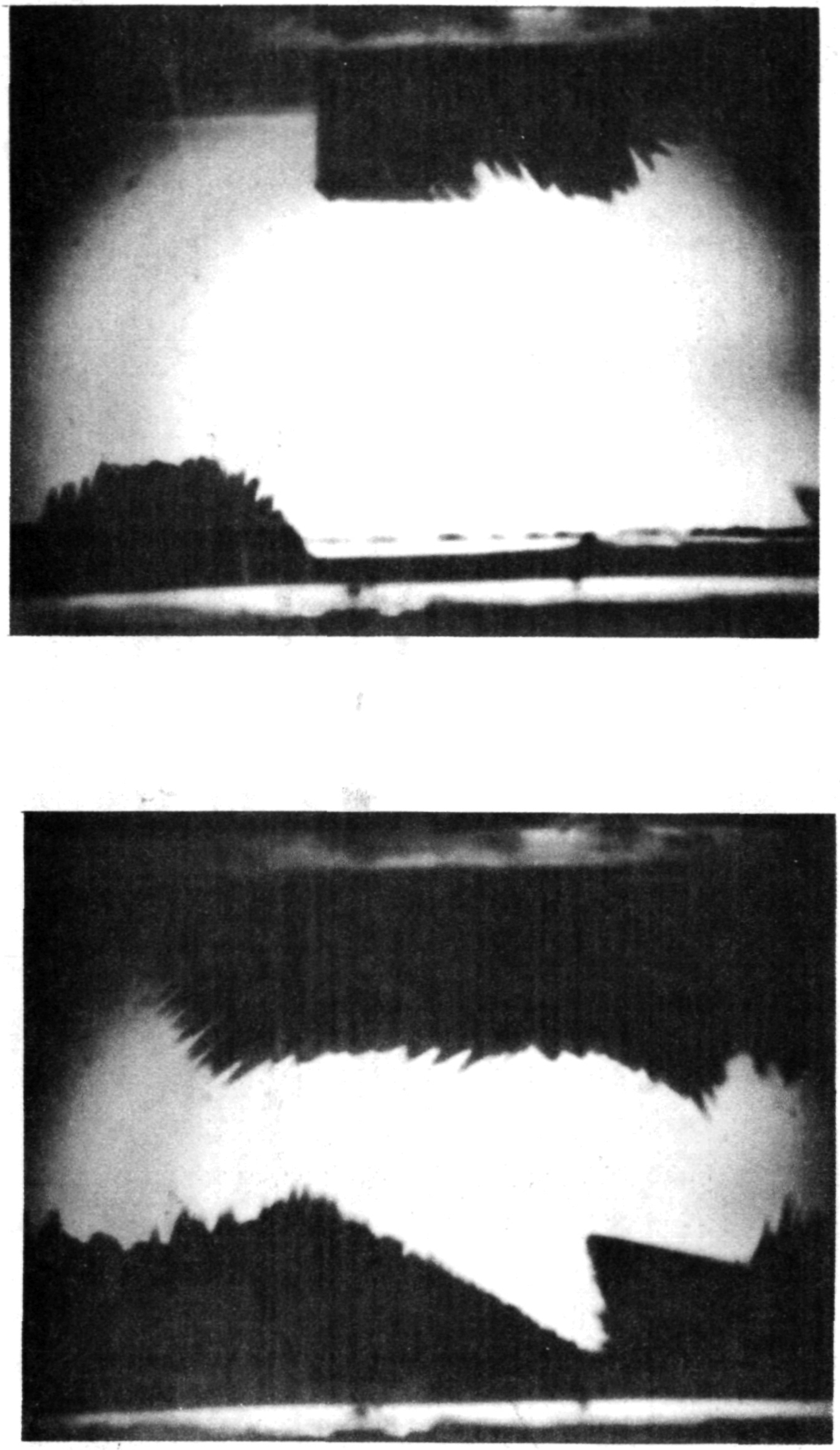

Figure 6. Photographs of low-g solidification — advancing growth.

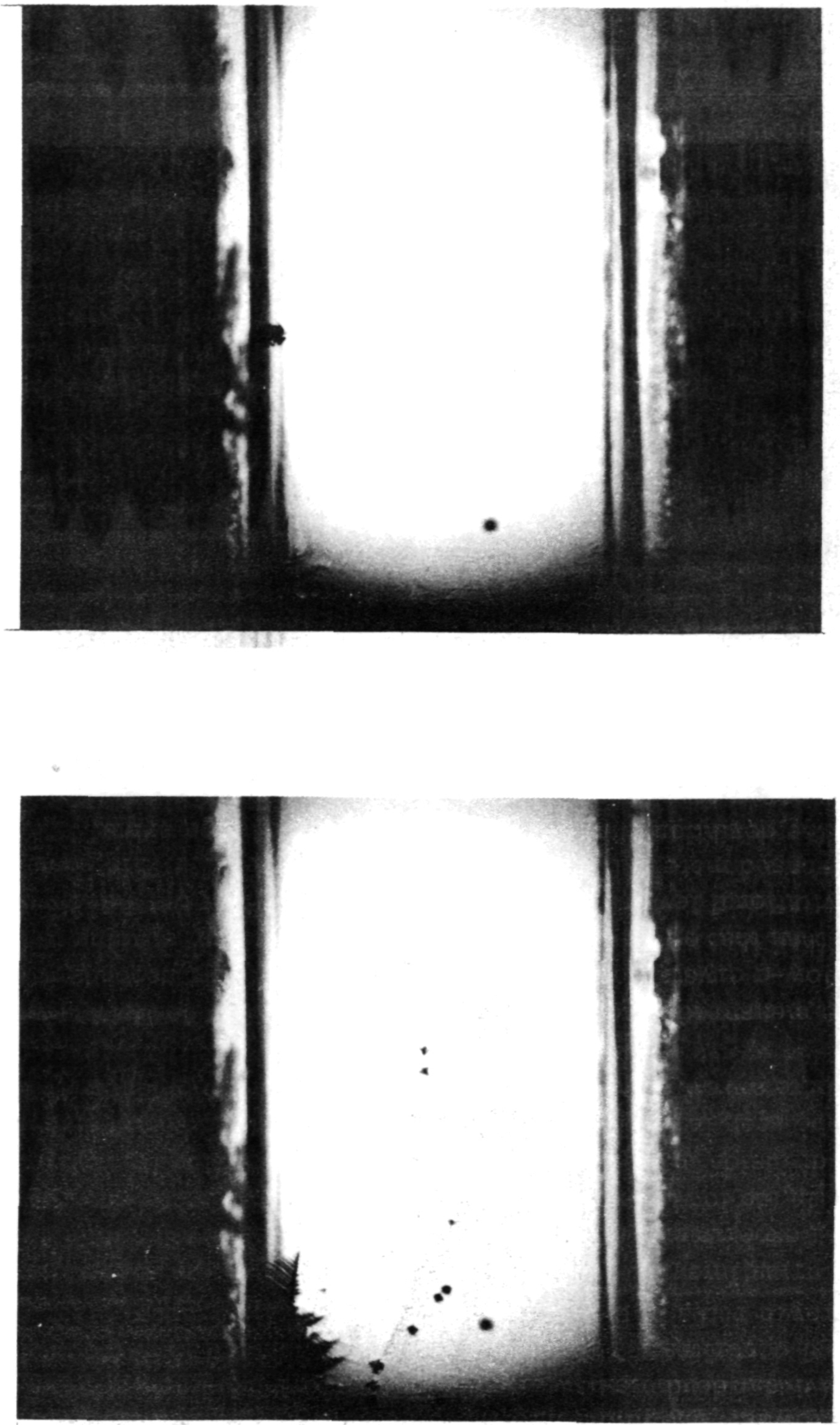

Figure 7. Photographs of one-g solidification — initiation and growth.

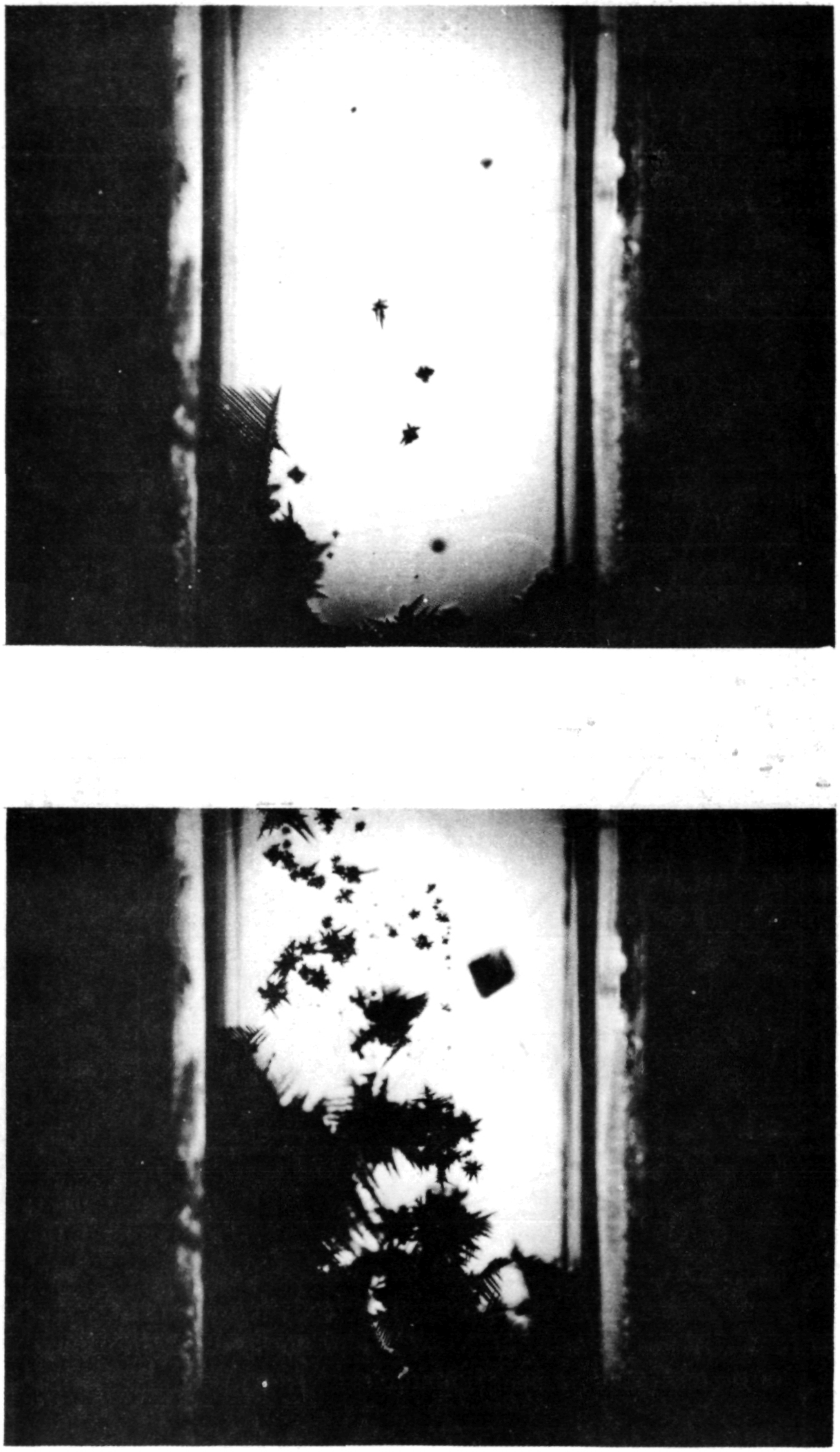

Figure 8. Photographs of one-g solidification — advancing growth.

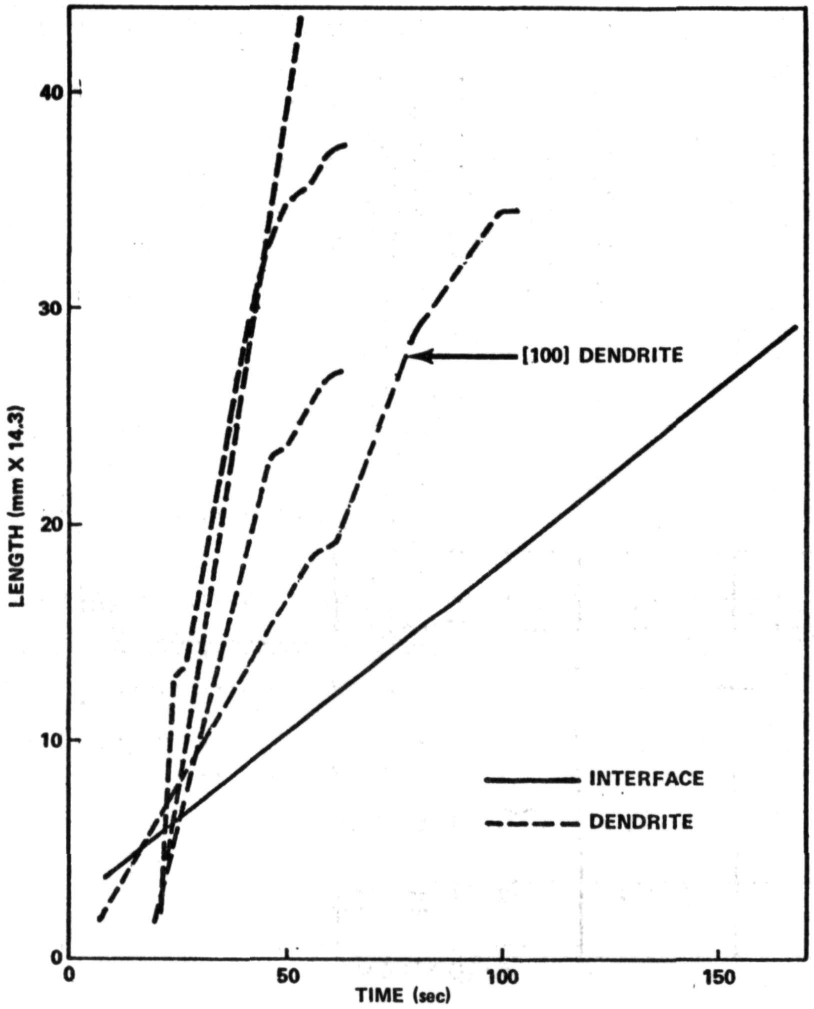

Figure 9(a). Interface and dendrite growth for low-g flight.

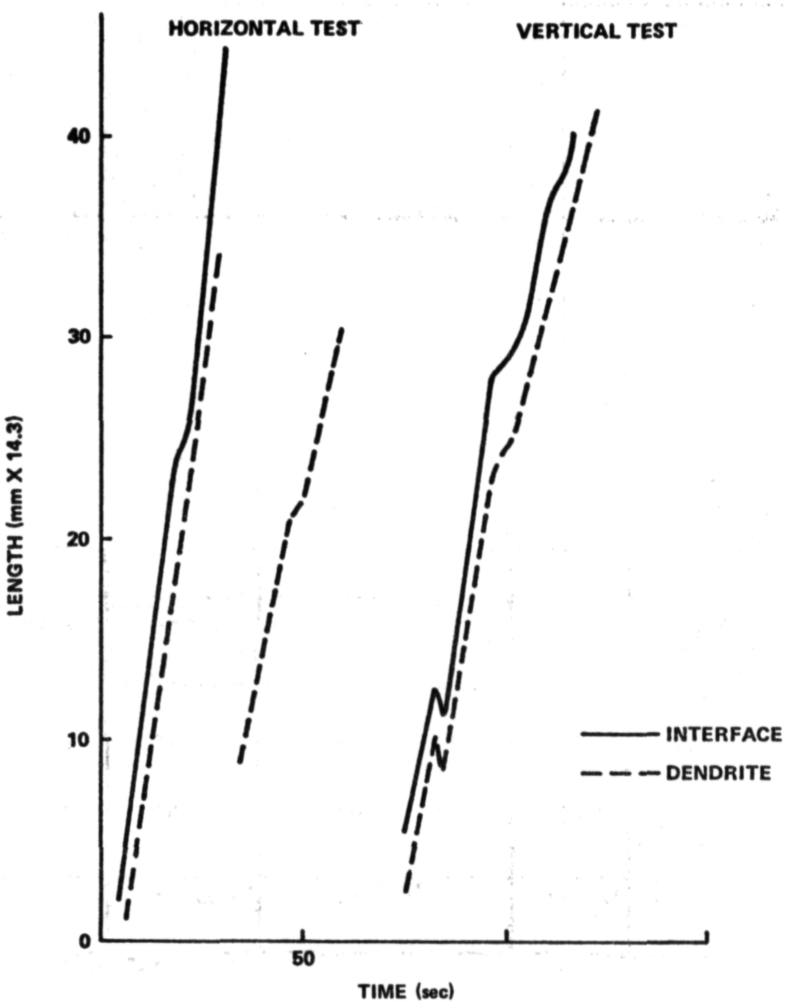

Figure 9(b). Interface and dendrite growth for ground-based tests.

TABLE 1. DENDRITE ARM SPACING

	Secondary		Tertiary			
	X ± σ, mm	σ, %	Side	σ, %	Center	σ, %
Flight	0.102 ± .020	19.6	.034 ± .005	14.7	.044 ± .006	13.4
Vertical GBT	0.072 ± .019	26.4	.031 ± .012	38.0	.056 ± .015	26.8
Horizontal GBT	0.061 ± .020	32.3	.030 ± .009	30.0	-	-

An obvious but immeasurable difference between the one-g and low-g solidification was seen in the growth symmetry. During the early stages of one-g solidification (Fig. 10), secondary and tertiary arms grew almost exclusively towards the wall. Growth of arms towards the center was impeded by the upward flow of warm liquid.

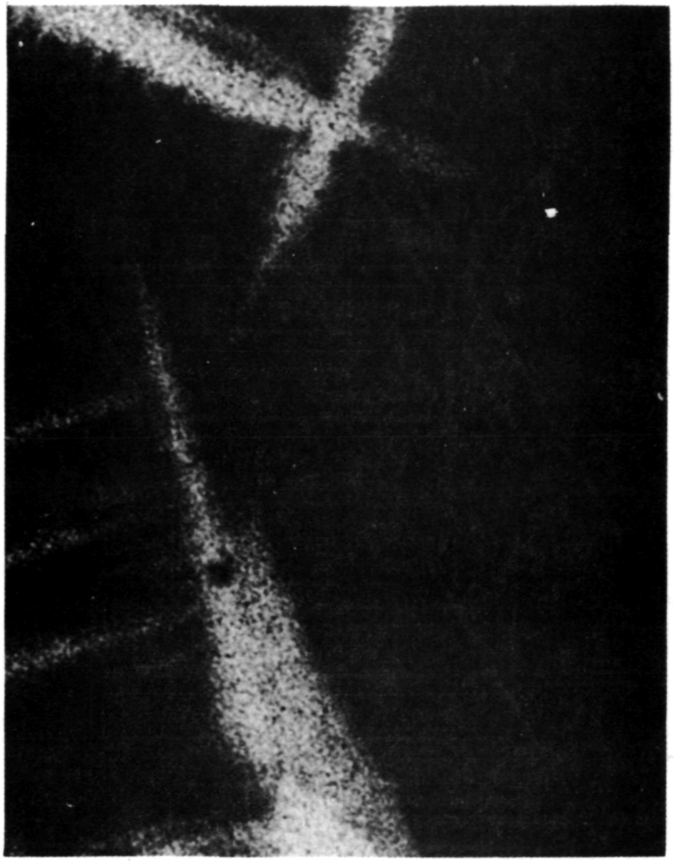

Figure 10. Dendrite asymmetry during one-g solidification.

In the low-g experiment during the rocket flight, the dendrite arms grew symmetrically, regardless of their orientation in the assembly. There was obviously no inhibiting influence such as fluid flow to disturb the crystal symmetry.

Although necking was observed in all experiments, no actual remelting was visible. This is due to the short period of time available for the experiment. According to Kattamis, Coughlin, and Flemings [13], for dendrites with the stated arm spacings, it would take 3×10^4 minutes for secondary and 1.2×10^3 minutes for tertiary arms to melt off.

Some fragmentation or breakoff of dendrites was observed in the one-g experiments as shown in Figure 11. The results of the fragmentation were apparent in the numerous crystallites being carried by the convection currents. No fragmentation was observed in the low-g samples. This supports the conclusion that there was negligible fluid flow in the low-g case.

Castings solidified under the experimental conditions would be comprised of exclusively columnar grains in the low-g case, and of both columnar and equiaxed grains in the one-g case. It can therefore be concluded that gravitational acceleration is the dominating influence on the zone transitions in casting structure. Without grain fragmentation and the subsequent flow of the particles into the central fluid, there is no equiaxed center zone. The obviously quiescent liquid ahead of the low-g interfaces was not conducive to secondary nucleation and growth.

CONCLUSIONS

A saturated solution of NH_4Cl was solidified on Earth at one-g and in a suborbital rocket at 10^{-5} g. In the one-g experiments, macrosegregation caused by the gravitational acceleration was marked. Nucleation started at the cold walls after which dendrites and dendritic debris were swept into the center of the cuvette by the convective fluid flow. The numerous crystals in the central region created an equiaxed zone. During the growth process, secondary dendrite arms were oriented toward the cold wall. Arm growth in the direction of the flow pattern was suppressed. The necking of secondary arms was observed. The variation in secondary and tertiary arm spacing ranged from 27 to 38 percent. Individual dendrites grew at similar rates to interface fronts.

When solidified in low-g, only four nuclei grew to form the complete casting. There were no free floating crystals or visible dendrite remelting. The lack of fluid flow allowed symmetrical dendrite growth into the fluid. Some necking of secondary arms occurred, but no coarsening or fragmentation resulted. The growth rate of interfaces was less than that of individual dendrites. Total growth was columnar with no equiaxed zone being formed.

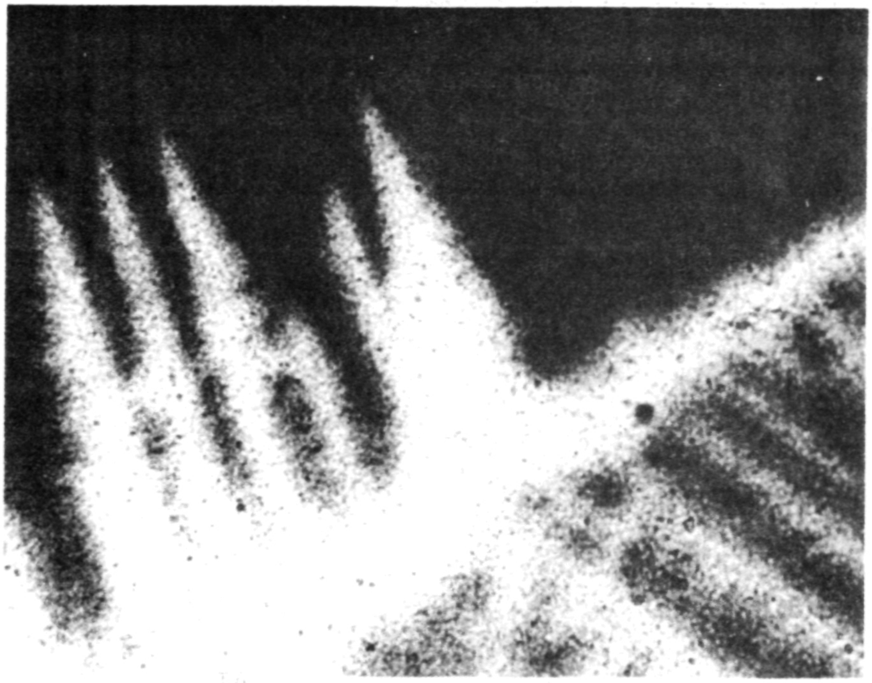

(a) Dendrite structure at t = 15 sec.

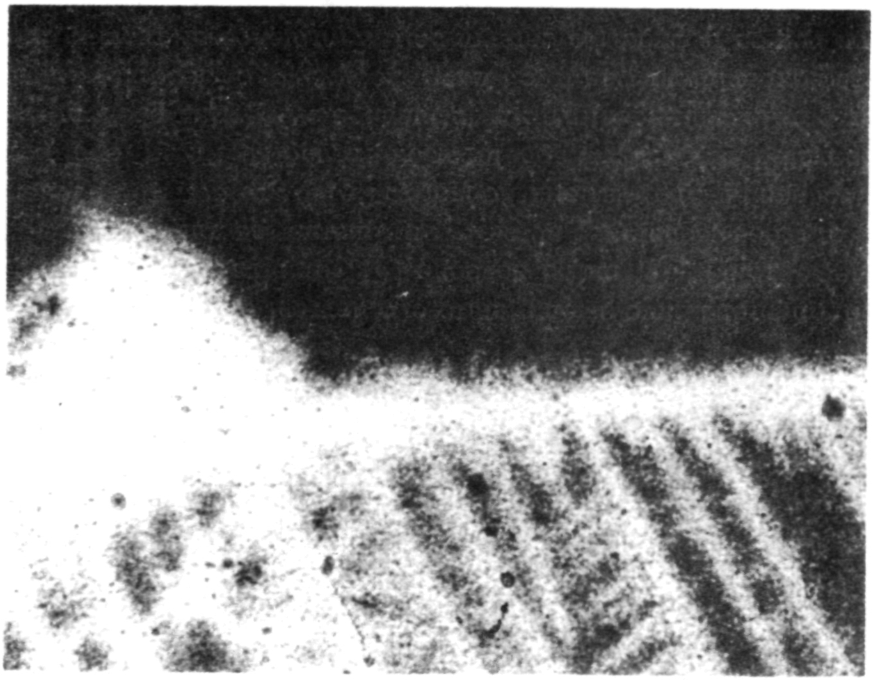

(b) Dendrite fragmentation at t = 17 sec.

Figure 11. Photographs of dendrite fragmentation.

REFERENCES

1. Chalmers, B.: Principles of Solidification. John Wiley and Sons, Inc., New York, 1964, p. 265.

2. Fredriksson, H., et al.: Met. Trans. AIME. vol. 3, 1973, p. 565.

3. Jackson, K. A., et al.: Trans. Met. Soc. AIME, vol. 236, 1966, pp. 149-158.

4. Strangman, T. E., et al.: Journal of Crystal Growth, vol. 18, 1973, pp. 209-211.

5. Johnston, W. C., et al.: Trans. Met. Soc. AIME, vol. 227, 1963, p. 890.

6. Cole, G. S., et al.: Trans. of Met. Soc. AIME, vol. 233, 1965, p. 1568.

7. Jackson, K. A., et al.: Acta Met., vol. 13, 1965, p. 1212.

8. Sharma, S. D., et al.: JAP, vol. 45, 1974, p. 4120.

9. Kahlweit, M.: Journal of Crystal Growth, vol. 6, 1970, pp. 125-129.

10. Hunt, J. D., et al.: Trans. Met. Soc. AIME, vol. 236, 1966, p. 843.

11. Kahlweit, M.: Journal of Crystal Growth, vol. 7, 1970, pp. 74-78.

12. Mehrabian, R., et al.: Met. Trans., vol. 1, 1970, pp. 1209-1220.

13. Kattamis, T. Z., et al.: Trans. of Met. Soc. AIME, vol. 239, 1967, pp. 1504-1511.

14. Copley, S. M., et al.: Met. Trans., vol. 1, 1970, pp. 2193-2204.

15. Chan, S. K., et al.: Journal of Crystal Growth, vol. 32, 1976, pp. 303-315.

CHAPTER VI

CASTING DISPERSION-STRENGTHENED COMPOSITES AT ZERO GRAVITY

Experiment 74-34

By

Louis Raymond and Choh-Yi Ang

The Aerospace Corporation

SUMMARY

The SPAR I flight test for Experiment 74-34, Casting Dispersion-Strengthened Composites at Zero Gravity, has been successfully completed. As the first of a series of two experiments, the sample processed in SPAR I was a composite containing 2.4 vol % thoria particles in a matrix of magnesium. Since the issuance of the preliminary technical report, characterization of the flight and several ground-processed samples had progressed to a point whereby conclusions can be drawn and recommendations of certain changes on process parameters for the SPAR II experiment can be made.

In comparison with various one-gravity samples, the low-gravity effects on the relative motion of the melt and protective atmosphere have contributed to the production of a cast ingot that is internally sound and without gas voids or shrinkage cavities. It is believed that this beneficial phenomenon would have significant impact on future space processes that involve the melting and solidification of unique materials that require protective atmospheres and containers for configuration control.

The optimum dispersion of the oxide particles in the matrix was not achieved. Mechanisms causing the presence of dispersion-depleted regions in the flight sample have been postulated. The continuing characterization efforts and results of the forthcoming SPAR II experiment should help determine the validity of these postulations.

Although there is a mechanistic difference between the SPAR I and SPAR II experiments, certain changes in programming the SPAR II furnace operation have been suggested on the basis of SPAR I observations. These suggested changes are intended to minimize the possibility of inducing thermoacoustic convection effects during heat-up.

INTRODUCTION

This report covers the characterization efforts and analyses of results performed during the 10 week period after receipt of the SPAR I flight sample. Because of the complexity of the observed microstructural features of the flight and three ground-based test (GBT) samples, additional one-gravity samples are being processed in the laboratory and at MSFC to provide additional data for analysis. Consequently, the interpretation of observed phenomena presented in this report may be modified at some later date.

Experiment 74-34, Casting Dispersion-Strengthened Composites at Zero Gravity, is a series of two experiments. The SPAR I flight experiment involved the addition of thoria (ThO_2) particles to the magnesium (Mg) matrix. The forthcoming SPAR II experiment will attempt to investigate the gettering mechanism involving Th metal and magnesia (MgO) in the matrix of Mg, resulting again in a dispersion of ThO_2 in Mg. It is not feasible to conclude SPAR I before initiating SPAR II either technically or within the scheduled requirements. These two experiments represent a stepped attempt to explore the feasibility of casting dispersion-strengthened high temperature structural materials in space.

Much of the background information and experimental procedures such as sample preparation, cartridge construction, and cartridge examination were reported in the preliminary technical report [1]. These materials in general are not repeated in this report. However, certain presentations in the previous report are reintroduced to support the analytical interpretation of observations.

OBJECTIVES

The ultimate purpose of the SPAR I and the forthcoming SPAR II experiments is to develop techniques and establish the feasibility of casting dispersion-strengthened useful metal composites in space that are difficult if not impractical to cast on Earth. The objective of the flight experiment was to demonstrate the achievement of optimum distribution of dispersed thoria particles in an Mg matrix upon melting and solidification in short-duration at a low-gravity level.

FLIGHT DATA AND DISCUSSION

Complete SPAR I acceleration and thermal data related to Experiment 74-34 have been made available for examination. The acceleration data from the X-axis accelerometer (corresponding to the Z-axis of the rocket) and the furnace temperature profile are plotted in Figure 1. Included in this figure is a plot of the sample temperatures as predicted and extrapolated from one of the initial furnace test runs. Beyond 240 seconds, the sample temperature profile is extrapolated, but the initial segment of the sample cooling curve is a duplication of the furnace test data after gas injection.

The gravity level profile shows that indeed we had attained $\leq 10^{-4}$ g for 270 and 230 seconds when the furnace and sample temperatures were respectively above the melting point (651°C) of Mg. The sample was soaked in the molten

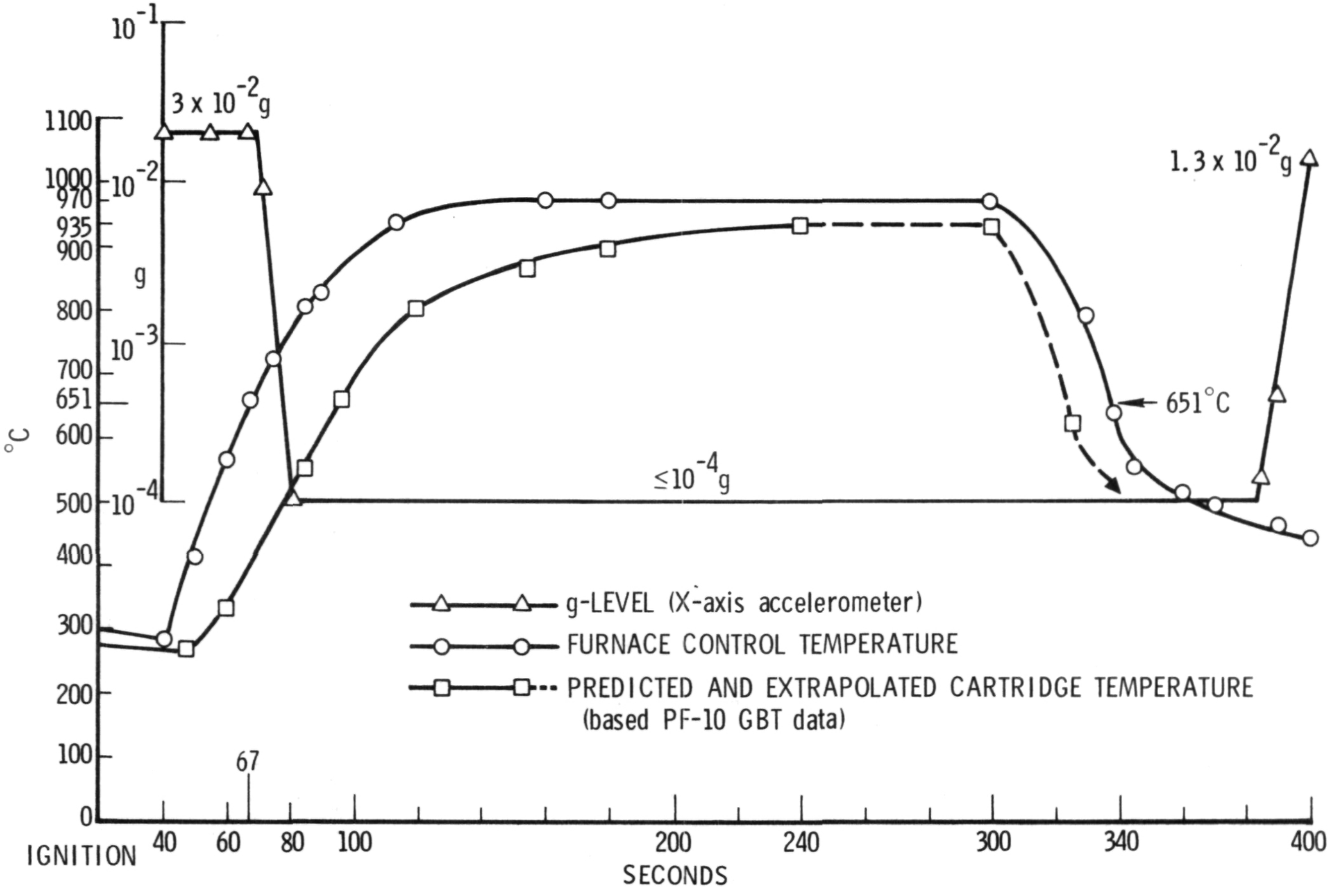

Figure 1. SPAR I flight gravity level and thermal profiles for experiment 74-34.

state at temperatures ≥800°C for at least 190 seconds at low gravity. Analysis of the rate gyro data [2] also indicates that there was no occurrence of "coning" or tumbling of the payload during the coasting phase of the flight. Neither were there any detectable gravity jitters.

It should be noted that the flight furnace did not follow the programmed cooldown rate after 340 seconds because of a malfunction of the gas injection system. However, we believe that the sample had already solidified completely by that time.

The possibility exists that the actual sample temperature during heat-up was much closer to the flight furnace temperature than the profile predicted from earlier ground-based furnace tests. For example, on the time scale, if the sample temperature lagged the furnace temperature by less than 50°C, then the Mg/ThO_2 sample could have been heated in the molten state for 10 seconds at gravity levels from 3×10^{-2} to 1×10^{-3}. The implication of this possibility will be discussed later in connection with observed microstructural features of the flight sample.

In the original experiment design, the furnace heat-up rate of 10°C/s had not been considered as having serious impact on the experiment. As will be discussed later, the thermoacoustic convection effects induced by this fast heating at low gravity may play a major role in the liquid-gas movement influencing the solidified microstructure.

MICROSTRUCTURAL CHARACTERIZATION OF SAMPLES

In addition to the single flight-tested sample and three ground-based tested samples, several laboratory samples at different stages of sample preparation have been examined metallographically. The samples included in this report are designated in the following manner for ease of identification:

Sample Designation	Description
SPAR-G1	Flight-tested sample
GBT-H4	One-gravity sample processed at MSFC
GBT-H5	One-gravity sample processed at MSFC
GBT-H6	One-gravity sample processed at MSFC
LT-G8	One-gravity sample processed in the laboratory at Aerospace
HP-G6	As-hot-pressed compact

The intended composition was 10.5% ThO_2 in Mg by weight. Chemical analysis of the ball-milled powder mix yielded an average content of 12.3 wt % ThO_2, which corresponds to a calculated 2.4 vol % ThO_2 in Mg. As will be seen later, optimum uniformity in dispersion has not been achieved in the low-gravity and one-gravity samples; therefore, it is not possible to determine, to any degree of accuracy, the actual vol % of dispersion in a given sample.

Microstructure of Hot-Pressed Compact

Sample HP-G6 was hot-pressed (at approximately 250°C) to a density that was 98% of the calculated theoretical value of 19.4 g/cm^3. The polished macrostructure and microstructure of the longitudinal section of this sample are shown in Figures 2(a), 2(b), and 2(c). Many darker inclusions are actually voids left by ThO_2 particles that were pulled out during polishing. Figure 2(c) shows quite clearly the flattened Mg powder grains (-200 mesh) and the ThO_2 particle aggregates and pullouts between Mg grains. Figures 3(a) and 3(b) are scanning electron microscope (SEM) photos of the ion-etched surface at 250X and 1000X. By using the technique of xenon (Xe) ion etching, one can minimize the problem of polishing pullouts. With this sample, there are some residual pullouts as shown by the small black spots in the white areas of ThO_2 particles. With the specimen tilted at 6 degrees in the SEM, the technique of energy dispersive X-ray analysis (EDAX) was used to identify the constituent between Mg grains as Th containing materials. The SEM photo and corresponding Th X-ray map are shown in Figures 4(a) and 4(b).

The purpose of studying the microstructure of an as-hot-pressed compact is to confirm our belief that the starting material (premelting sample) was dense, with the harder ThO_2 particles imbedded between grains of Mg powder. On a macroscale, the "dispersed" phase was as uniformly distributed as achievable using the powder metallurgy technique.

Comparison of Flight and GBT Samples

Magnesium does not wet POCO graphite. All the laboratory processed ingots could be removed from the crucibles with ease. However, there was no attempt to remove the flight and GBT ingots from their crucibles because the radiographic images [1] showed presence of low density areas as well as irregular ingot outline.

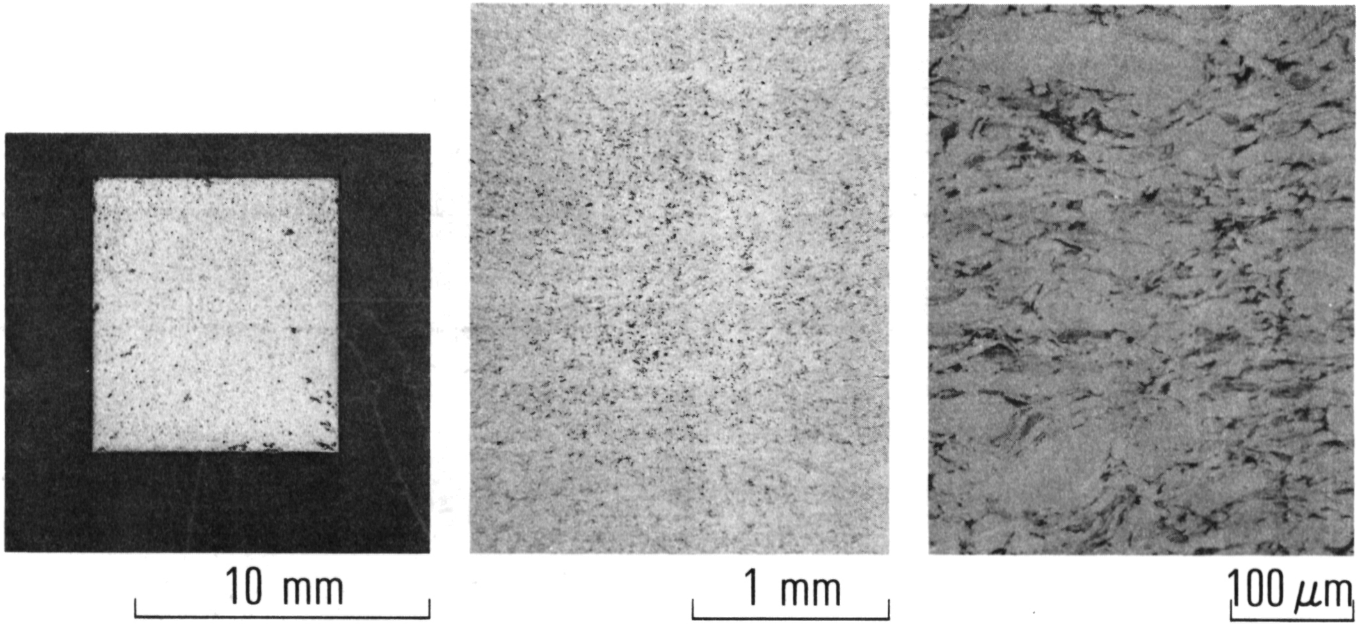

Figure 2. Macrostructure and microstructures of hot-pressed Mg/ThO_2 HP-G6 compact (White — Mg; Black — ThO_2).

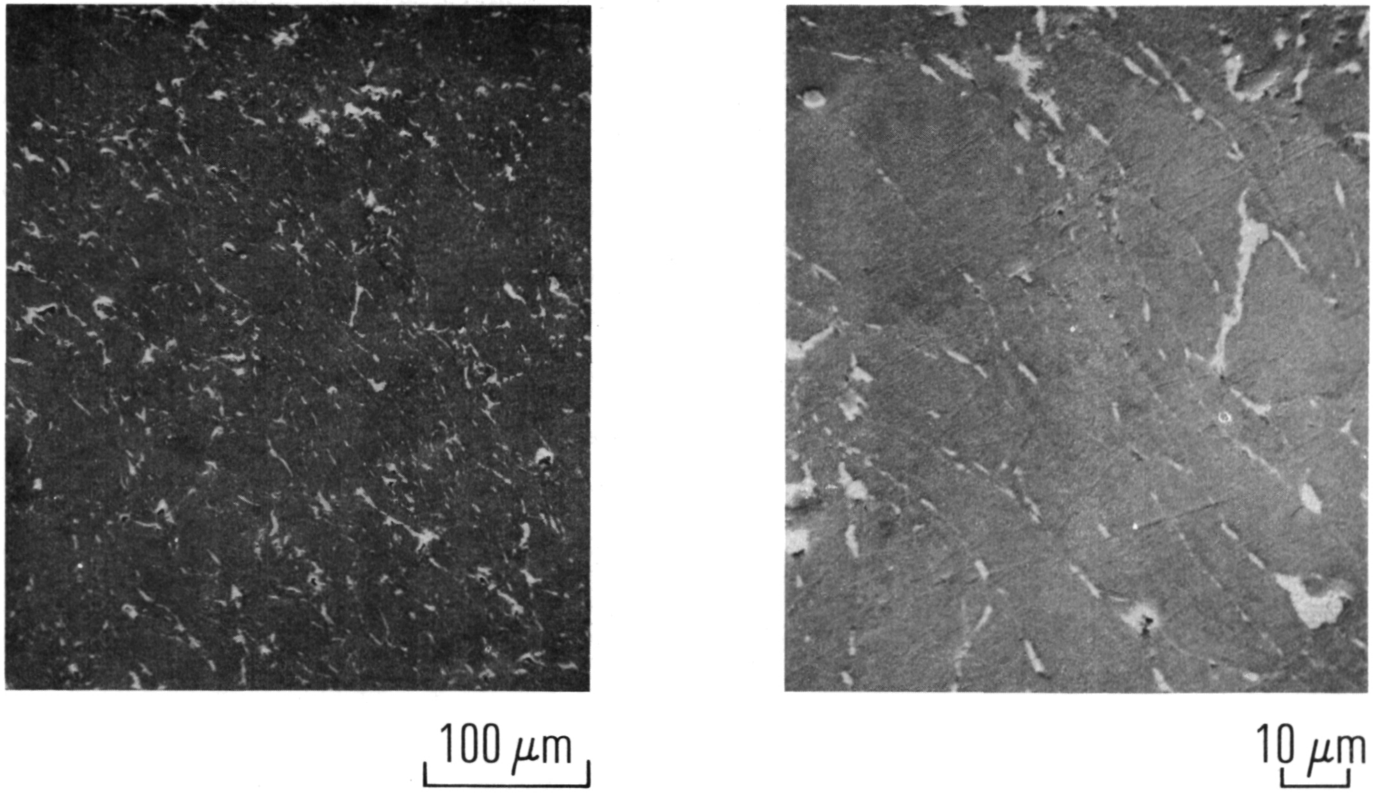

Figure 3. SEM's of ion-etched HP-G6 sample (Black — Mg; White — ThO_2).

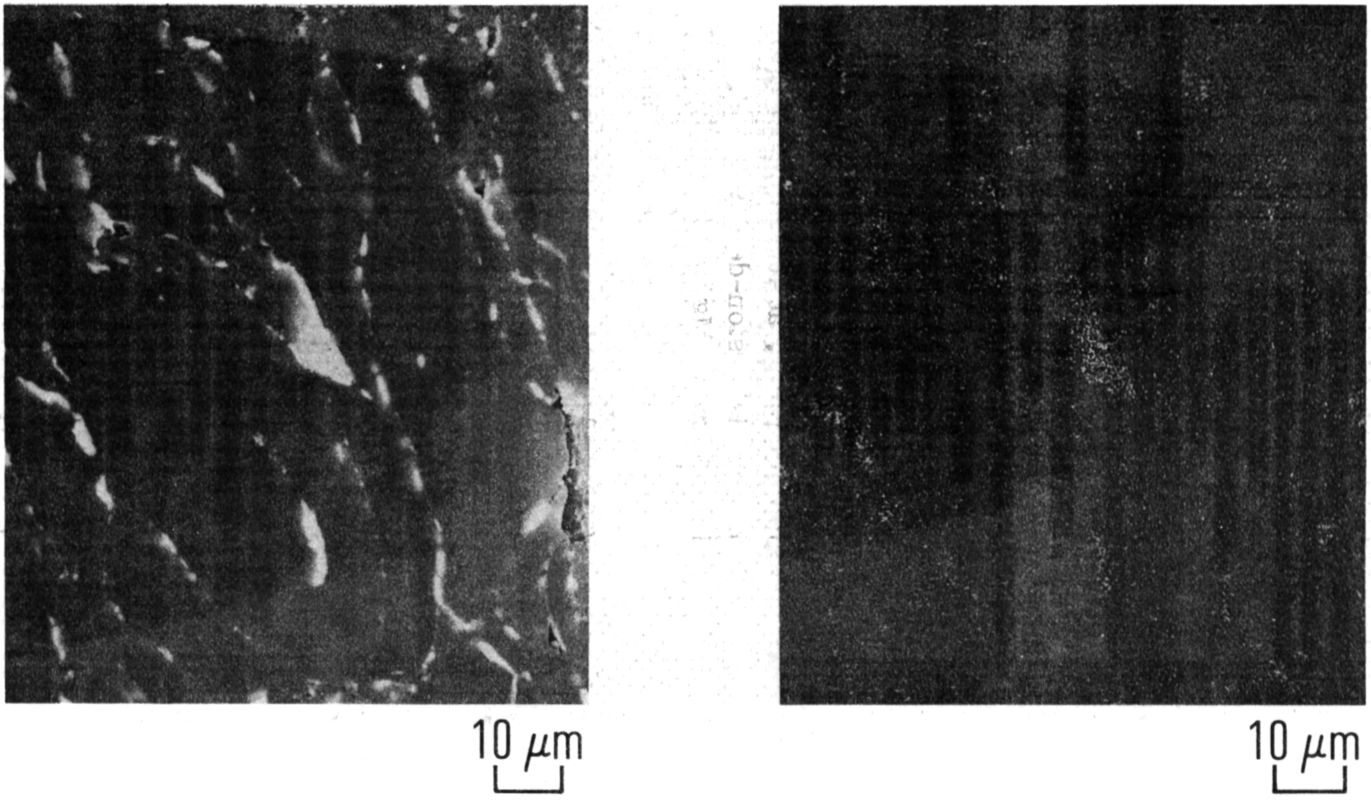

(a) SEM microstructure (Black — Mg; White — ThO_2).

(b) Th X-Ray Map (Black — Mg; White — Th and Background).

Figure 4. Identification of dispersoids in HP-G6 by energy dispersive X-ray analysis.

The macrophotos of longitudinal sections of the flight and three GBT ingots are presented in Figures 5 and 6. It is apparent that gas voids in the flight sample (SPAR-G1) are located next to the wall, whereas all three GBT samples are segmented by internal voids. It should be noted that GBT-H6 and SPAR-G1 were heated with the originally introduced argon atmosphere on top of the compact. Samples GBT-H4 and GBT-H5 were inadvertently heated with the argon gas on the crucible bottom. The fact that GBT-H6 was thermally cycled three times during the "all system test" makes it difficult to draw valid conclusions from the comparative characterization. A second GBT will be conducted, in the near future, with the flight backup sample G2 oriented as the SPAR-G1 sample, to provide additional one-gravity data for analysis.

The GBT samples all show the phenomenon of layered sedimentation of the dispersoids. The flight SPAR-G1 sample, on the other hand, contains dispersion-depleted areas, relatively large in size and similar in cross-sectional outline to the gas voids in the GBT-H6 sample [Figs. 4(a) and 4(b)]. There are also some layered areas depleted in dispersion in the SPAR-G1 sample.

Figures 7(a) and 7(b) are photomicrographs, at 40X and 250X respectively of the SPAR-G1 sample, showing the smaller dispersion-depleted layers and the presence of sparsely located ThO_2 particles between Mg grains within a dispersion-depleted area.

The 2% Nital etchant was applied to remove smearings due to polishing [Fig. 7(b)]. However, since chemical etchant cannot effectively eliminate the polishing pullouts, Xe ion etching was applied to the SPAR-G1 sample. Figure 8 presents three SEM photos of the dense and depleted areas of the sample ion-etched to minimize particle pullouts. The dense areas magnified to 1000X and 3000X are shown in Figure 9. At these high magnifications, it is possible to determine that the ThO_2 particle sizes range from 0.2 to 2 μm with the majority of particles being 0.7 to 0.8 μm in size. The interparticle spacings within a cluster vary from 0 to 1-2 μm. The intercluster spacings vary from 5 to 25 μm.

Figure 10(a) shows the microstructure of the transverse section cut through two of the near-circular areas in flight sample SPAR-G1 that are depleted in dispersion, as shown in the longitudinal section macrograph of Figure 5(a). It appears that these centrally located dispersion-depleted regions are spherical in shape and are not parts of solidification fronts originating from the cooler wall during cooldown. This particular transverse section also shows dispersion-depleted areas around the periphery of the ingot, either bordering

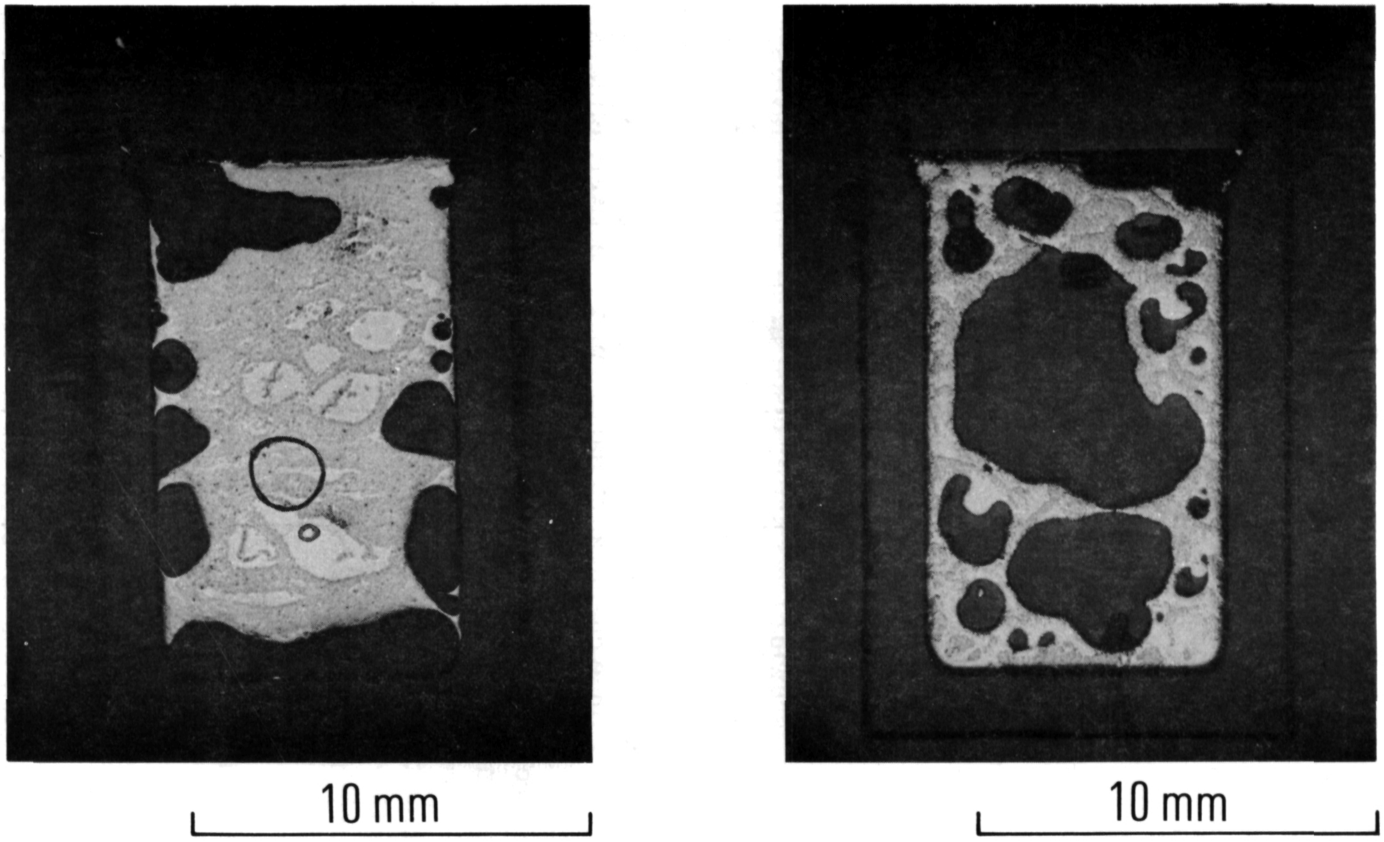

(a) SPAR-G1

(b) GBT-H6

Figure 5. Comparison of macrostructures of unetched SPAR-G1 and GBT-H6 ingots (circled areas are magnified in Figure 7). (Black — Argon; White — Mg rich material; Gray — Mg containing ThO_2 dispersion.)

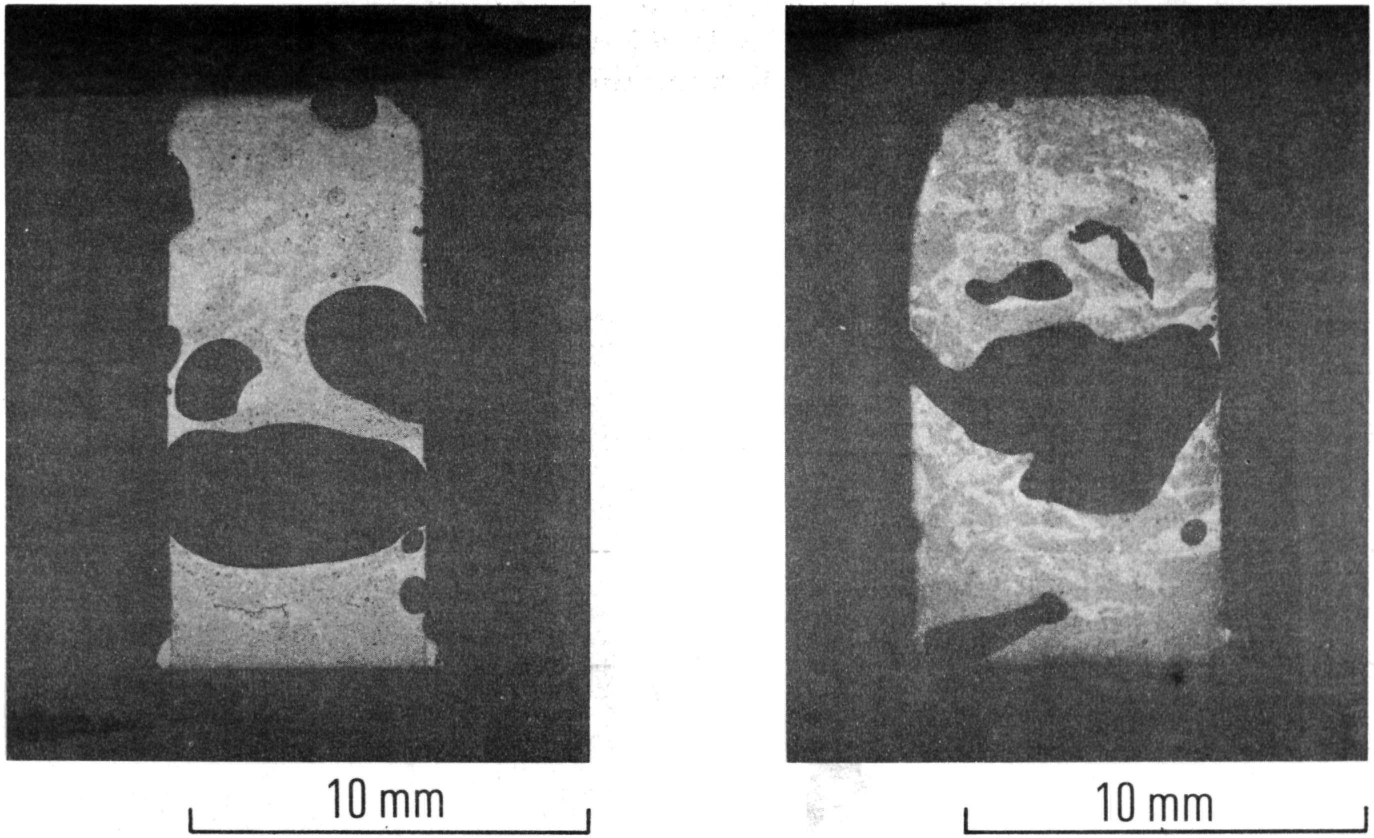

(a) GBT-H4

(b) GBT-H5

Figure 6. Macrostructures of unetched GBT-H4 and GBT-H5 ingots. (Black — Argon; Gray — Mg containing ThO_2 dispersion; White — Mg rich material.)

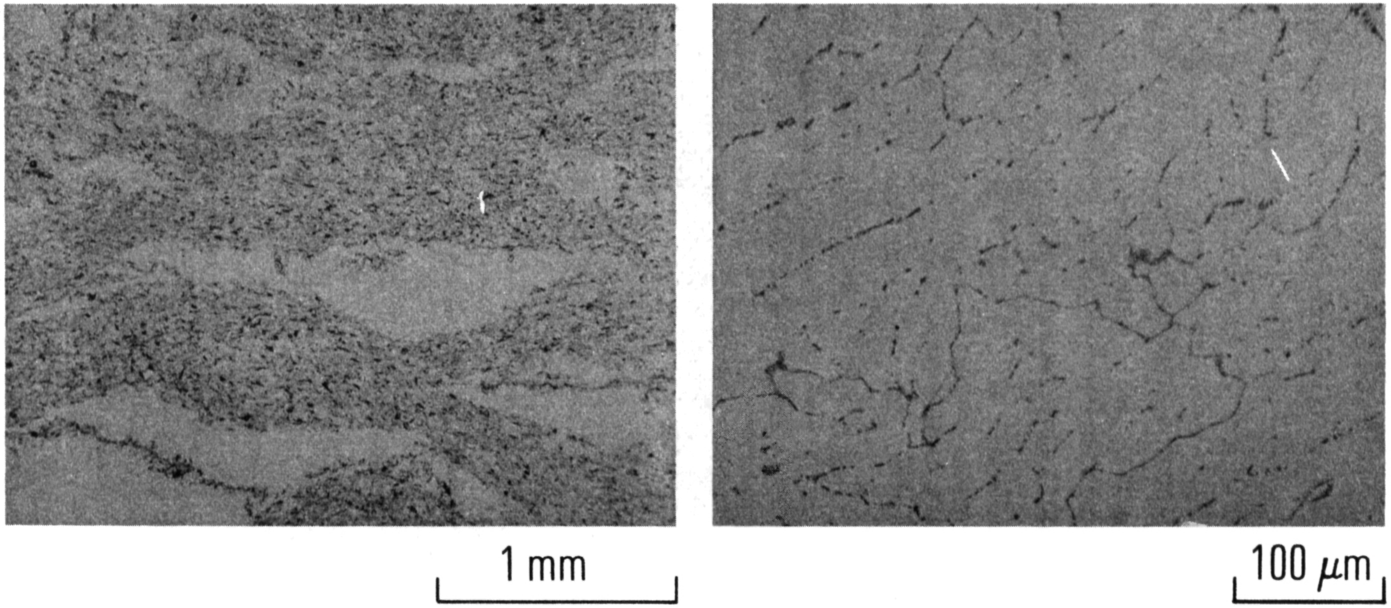

(a) UNETCHED

(b) 2% NITAL ETCHED

Figure 7. Microstructures of selected areas of the flight SPAR-G1 ingot [see Fig. 5(a)].

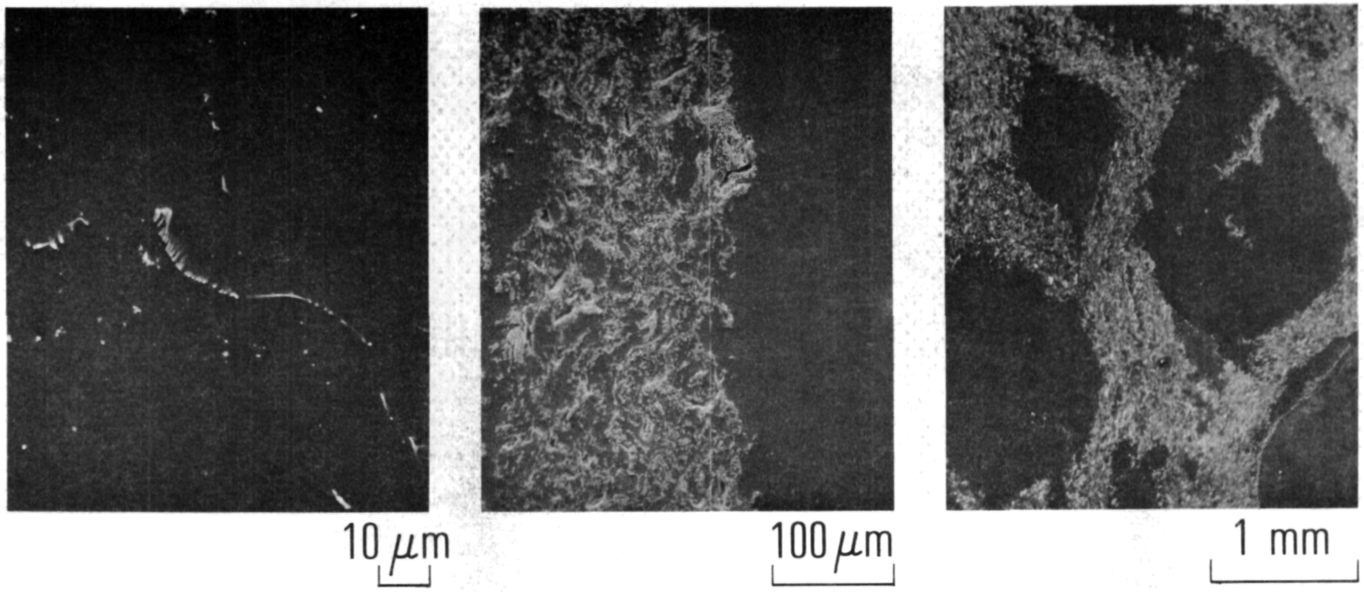

(a) Dispersion-Depleted Area (Black — Mg; White — ThO_2)

(b) Dense Area Adjacent to Depleted Zone

(c) Large Dispersion-Depleted Areas

Figure 8. SEM's of Xe ion-etched dense and dispersion-depleted areas of SPAR-G1 sample.

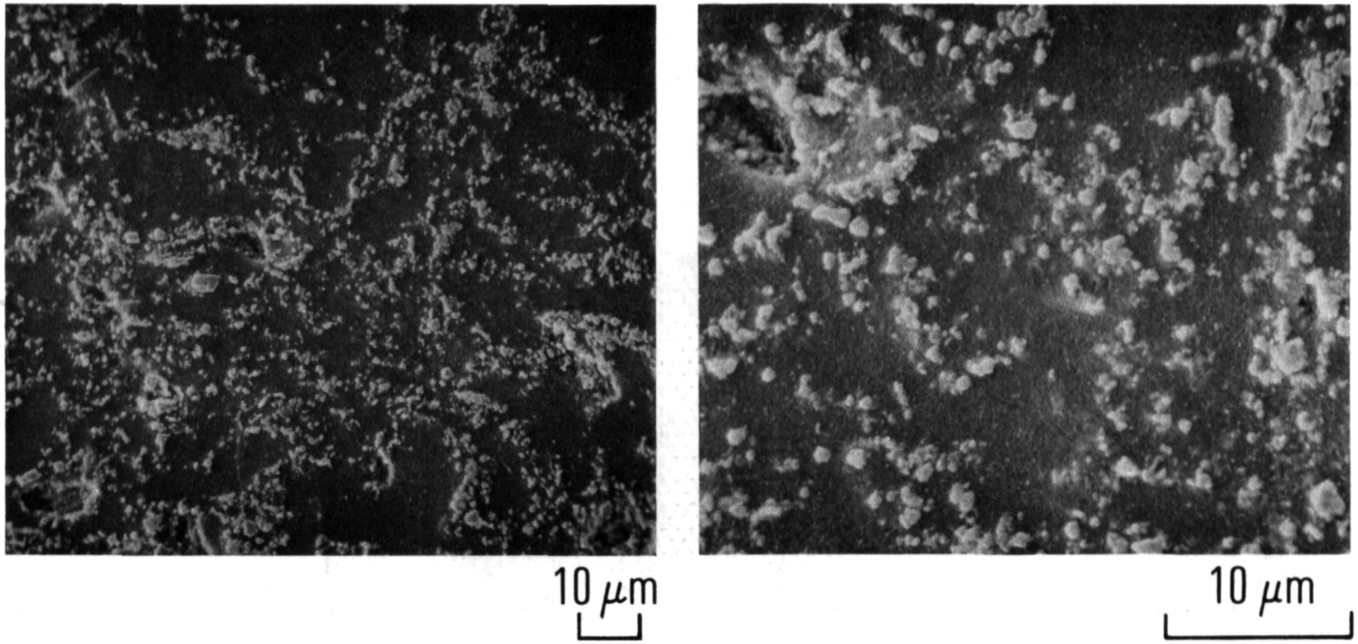

Figure 9. SEM' s of Xe ion-etched microstructure of THO_2 dispersed particles in dense area of SPAR-G1 sample (Black – Mg; White – ThO_2).

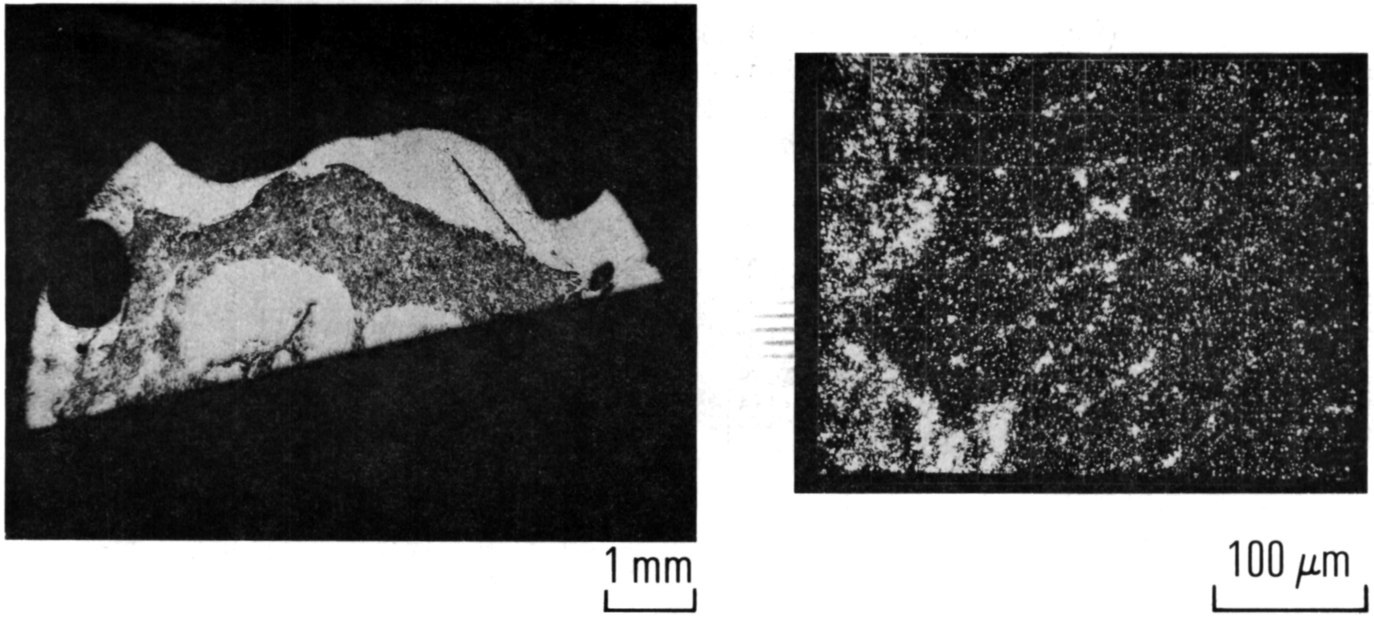

(a) Unetched Transverse Section (Gray — Mg plus ThO_2; White — Mg Rich)

(b) ThO_2 Map by IMMA (N_2^+ beam at 20 kV/1 nA) (White — ThO_2; Black — Mg)

Figure 10. Microstructure and ThO_2 IMMA map of SPAR-G1 transverse section.

the gas voids or touching the crucible wall. Small elongated Mg grains within the depleted areas that are outlined by thoria particles appear to have orientations that indicate the direction of directional solidification. However, if the directional solidification mechanism was operative during cooldown, it must have been modified by other mechanisms such as condensation of Mg vapor, motion of the gas bubbles, and the low thermal conductivity of the Ar gas.

The ion microprobe mass analysis (IMMA) is a powerful tool for positively identifying compound species. Figure 10(b) is a 250X ThO_2 map of an area in the SPAR-G1 transverse section [Fig. 10(a)] covering both dense and dispersion-depleted regions. Boundaries of Mg grains in the depleted region are outlined by ThO_2 particles. IMMA also reveals the presence of ThO_2 within the Mg grains that has not been clearly detected by either optical microscopy or EDAX.

The dense areas of sample GBT-H6 were also examined in the SEM. The microstructure as revealed by ion etching is shown in Figure 11 at 1000X and 3000X. In Figure 11(b), the presence of ThO_2 particles just beneath the surface of the space between clusters is evident.

Microstructure of Laboratory Processed Sample

Several samples encapsulated in cartridges have been processed in the laboratory. Two were vibration-heated to serve as quality control samples, while two others were heated to >950° C during the development of process parameters and temperature measuring schemes for induction heating. The sample LT-G8 was induction heated to approximately 825° C and held at that temperature for 3 minutes before turning off the power. The heat-up rate was approximately 4° C/s, and the cooldown rate was estimated to be 2° C/s. Metallographic preparation of sections of this sample has just begun, but some photomicrographs are presented here for discussion.

As shown in Figure 12(a), layered sedimentation of the dispersoids had taken place, but the Ar gas voids remained essentially on or near the top of the ingot. Figure 12(b) is an SEM photo at 40X of a layered area of the sample. Figure 13(a) shows the white stringers in one of the dispersion-depleted areas to be sites for ThO_2 particles that were pulled out during polishing. The improvement in microstructural analysis due to ion-etching is shown in Figure 13(b), where the ThO_2 particles are observed along an Mg grain boundary and particle pullout is absent, even at higher magnification.

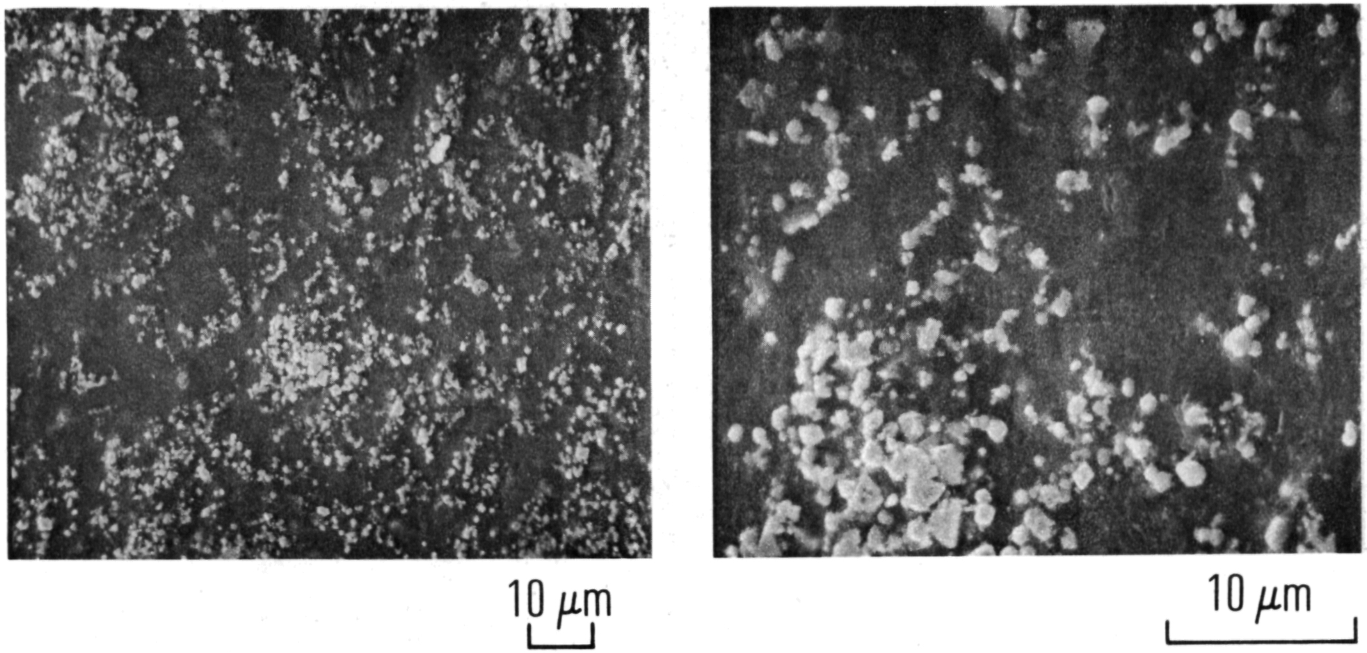

Figure 11. SEM's of Xe ion-etched microstructure of ThO_2 dispersed particles in dense area of GBT-H6 sample (Black – Mg; White – ThO_2).

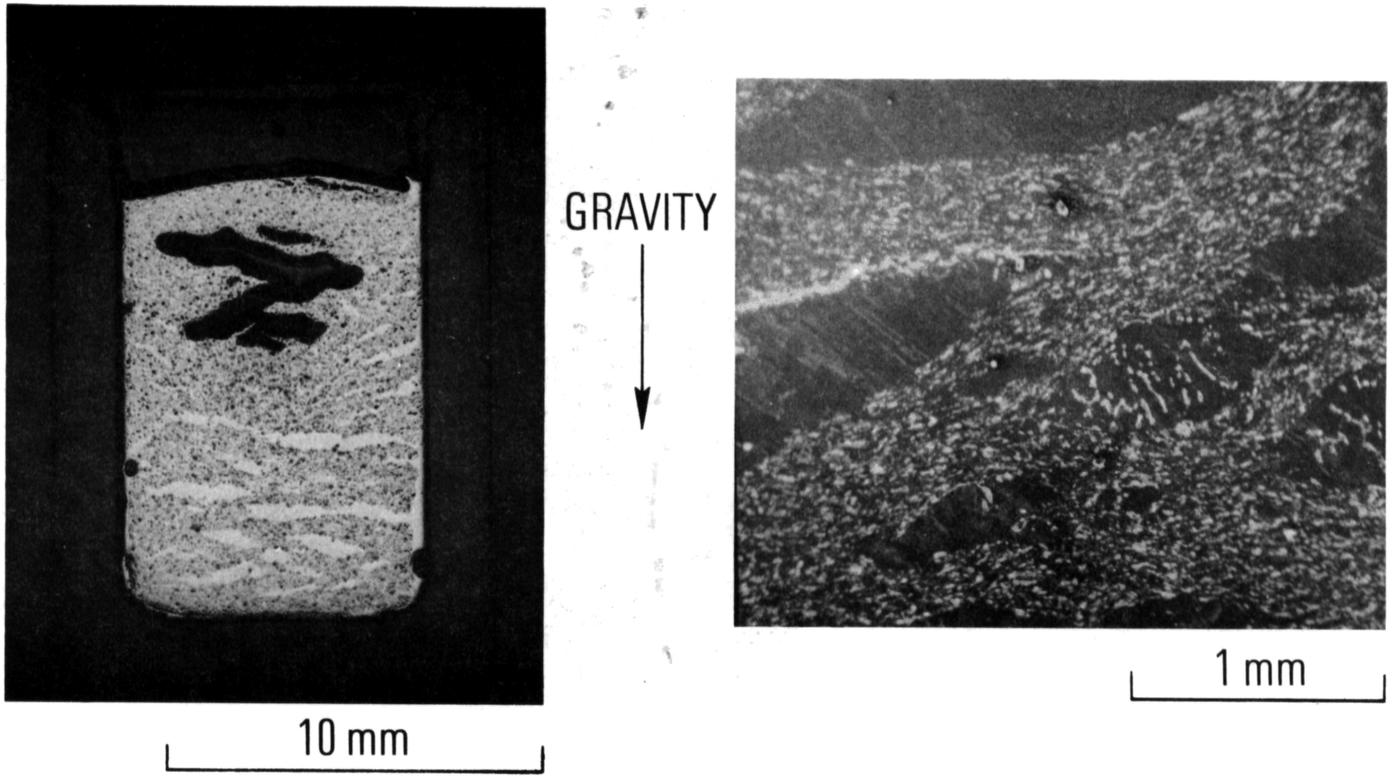

Figure 12. Longitudinal section of unetched macrostructure and microstructure SEM of LT-G8 sample processed in laboratory (Black — Mg; White — ThO_2; Scratches).

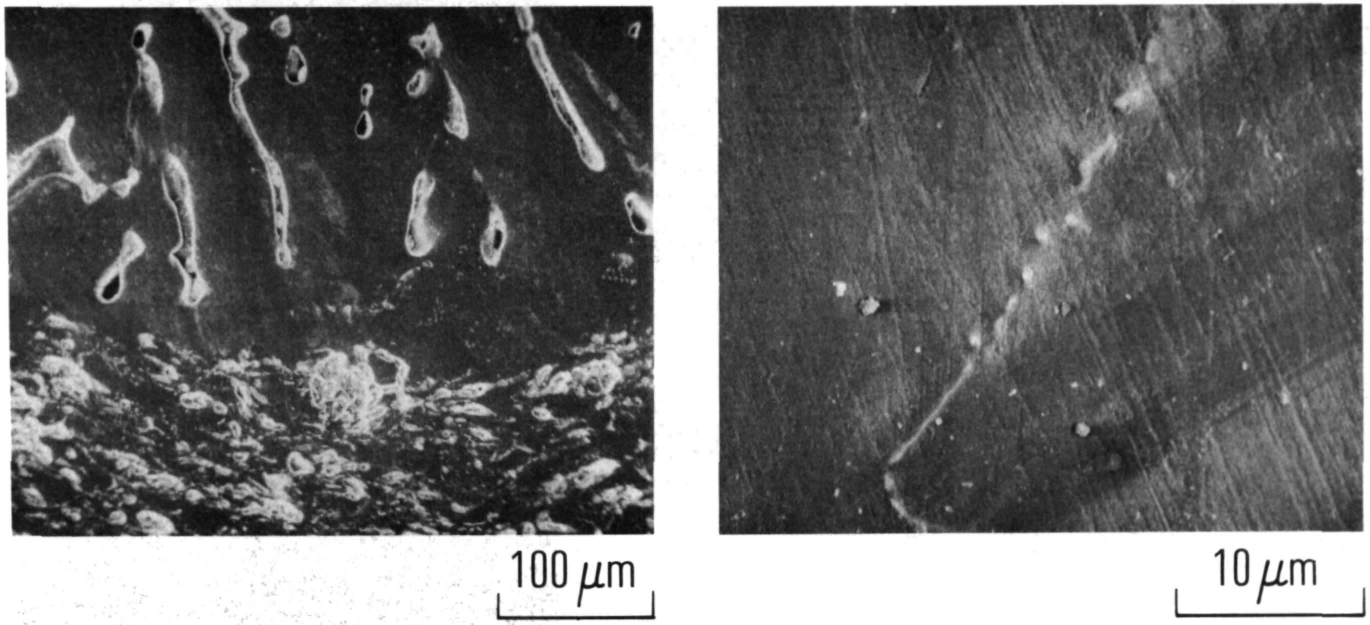

Figure 13. Microstructures of dense and dispersion-depleted areas of sample LT-G8 (Black — Mg; White — ThO_2; Particles in Grain Boundary).

The preliminary microstructural examination of the laboratory-processed sample shows that clustering of ThO_2 particles in the dense area is "coarse," in comparison with the flight sample SPAR-G1 [Figs. 8(b) and 9]. In other words, in the dense areas of the low-gravity sample, the clusters are less densely-populated than the one-gravity LT-G8 sample.

Effects of Dispersions on Microhardness

Originally it was intended to take regular arrays of microhardness readings on sections of the flight and GBT samples to examine the degree of uniformity in dispersion-strengthening. This plan has been abandoned because of the presence of dispersion-depleted regions in the flight sample SPAR-G1 and the large voids in the GBT samples. Nevertheless, by adopting an improvised scheme of using a 1.59 mm diameter Brinell ball indenter with a Tukon microhardness tester, several readings (diameter of the indentation) were taken on selected areas of the samples and the average values are listed below. It should be noted that hardness is inversely proportional to the indentation diameter.

	Dense Dispersion Area	Dispersion-Depleted Area	Hot-Pressed Compact
SPAR-G1	178	216	
GHT-H6	178	233	
LT-G8	220	253	
HP-G6	---	---	186

The above listed microhardness readings are presented for future reference in evaluating SPAR II samples. These data are insufficient to reach conclusions.

DISCUSSION OF MICROSTRUCTURAL OBSERVATIONS

The microstructural features observed in a hot-pressed compact are as expected. They show that the starting premelt sample was composed of fine ThO_2 particles imbedded between -200 mesh Mg grains that were flattened by compaction. There was no evidence of macrosegregations in a hot-pressed compact that might have led to the formation of dense and dispersion-depleted areas observed in the low-gravity and one-gravity processed samples.

There were gross and subtle microstructural differences between the flight-processed and ground-processed samples. The pertinent differences may be listed as follows:

- The flight-processed SPAR-G1 ingot does not have internal gas voids. The three GBT samples are segmented by large voids. The LT-G8 sample processed in the laboratory has voids on and near the top of the ingot.

- The SPAR-G1 sample contains relatively large, somewhat rounded areas that are depleted in dispersion and appear to have similar outlines to those of the internal voids in the GBT samples.

- Sedimentation of dispersoids or clusters in layers are observed in the SPAR-G1 and all four ground-processed samples. Layered sedimentation is, however, a predominent feature in the ground samples.

The discussions to follow will attempt to arrive at an understanding of the mechanisms causing these differences.

Low-Gravity and Crucible Effects on Gas and Liquid Movement

The use of argon atmosphere in sample preparation and cartridge assembly was based on the following reasons:

1. In Mg casting practice, high fluidity chloride fluxes [3] are used to protect the melt from oxidation and excessive evaporation. Low pressure or vacuum casting is not feasible because of the high vapor pressure of the metal even at temperatures below its melting point (e.g., 1 torr at 621°C for solid Mg, as compared with 973°C for liquid Pb and 1284°C for liquid Al). Therefore, in this series of space processing experiments, it is believed that a high purity inert gas atmosphere is preferable to vacuum in sample encapsulation.

2. Working with inert gas atmosphere inside a vacuum glove-box, involving powder weighing and mixing, hot-pressing of compacts, and sample encapsulation, is an established laboratory practice.

The effects of low gravity on the kinetics of liquids and gases within a container have been demonstrated by Reynolds [4] in his study on the behavior of mercury and oil in lucite boxes during free-fall. On the basis of the experiments, Reynolds concluded that under low gravity conditions, fluids that wet their container will crawl around the wall, leaving the gas pocket in the center. Nonwetting fluids, on the other hand, will kick themselves off the wall, leaving a blanket of gas in contact with the wall.

As mentioned previously, liquid Mg does not wet POCO graphite. Therefore, one would expect the cast ingot to shrink away from the crucible wall and form a sound casting. The fact that ingot SPAR-G1 did not completely shrink away from the crucible wall may be explained by quasi-wetting due to mechanical interlocking. The ID of the crucible has machining grooves and the POCO graphite materials as synthesized has noninterconnecting micrometer size pores. It is not unreasonable to speculate that, in the short time duration at low gravity followed by rapid cooling, the Mg ingot did not have sufficient time to completely break away from the locked position. Later we will discuss how the thermoacoustic convection effects at low gravity might have aided the movement of the Ar gas and liquid Mg and could have caused the formation of gas-void-like areas that are depleted dispersoids.

At one gravity, the melt should remain on the bottom of the crucible, unless secessive thermal agitation of the melt occurs from overheating. The LT-G8 sample serves to demonstrate this point. All three GBT samples, on the other hand, had been heated to temperatures approximately 100°C higher than LT-G8. Furthermore, GBT-H4 and GBT-H5 were inadvertently processed with the cartridges in the inverted position (gas below the compact). The sample GBT-H6, although oriented properly, was heated three times with an unknown thermal history. It is not surprising, therefore, to observe the excessive motion and entrapment of the gas bubbles. The motion and thermally induced pressure of the gas bubbles apparently further complicated the sedimentation of the dispersion in the Mg matrix.

The observed phenomena of relative motion of protective atmosphere and molten metal within a crucible or mold will have significant impact on other space processing experiments. In future space processing, "exotic" metals and alloys can be made without internal voids or shrinkage cavities even when reactivity and end-product configurations need the use of an inert atmosphere and container. A major consideration would be the proper selection of nonwetting container material or container coating material.

Phenomena of Layered Sedimentation

By assuming a high degree of sphericity of heavy particles in a liquid matrix, one may apply the well known Stokes Law [5] and estimate the gravity-induced terminal sedimentation velocity, V_t, for the particles from the equation

$$V_t = d^2 g \, \Delta\rho / 18\,\eta \qquad , \qquad (1)$$

where d is the diameter of the dispersoid, g is the gravitational constant, $\Delta\rho$ is the density difference between the settling particle and the liquid, and η is the viscosity of the liquid matrix. Since the ThO_2 particles have a size range from 0.2 μm to 2 μm, Figure 14 is constructed to illustrate the effects of gravity levels on the rate of particle sedimentation under ideal conditions. Two viscosity values are incorporated in the plots, i.e., $\eta = 1$ cp for molten Mg at the casting temperature ($\geq 750°C$) and $\eta = 3$ cp for Mg heated to just above its melting point (651°C).

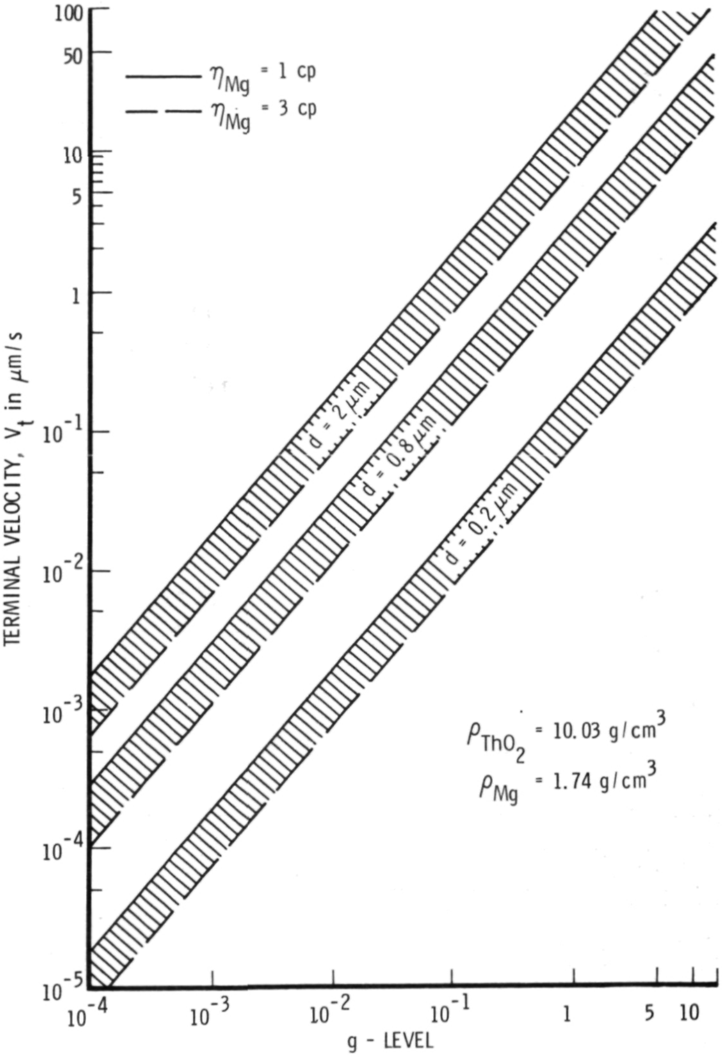

Figure 14. Sedimentation velocity for ThO_2 dispersoids in molten Mg under ideal conditions.

Sedimentation sizing is a well developed technique in powder metallurgy. Experience in applying equation (1) has shown that large deviations from the theoretical settling velocities of particles in a liquid will result if the following conditions exist.

- High viscous resistance — slower sedimentation
- Incomplete dispersion — slower sedimentation
- Suspension denser than 0.5% — slower sedimentation
- Wall effects from small container — slower along wall unless modified by convection currents
- Convection due to density gradients — slower when a denser region is adjacent to or above a less dense region.

It is obvious from the above discussion, that we do not expect the sedimentation of 2.4 vol % ThO_2 particles, irregularly shaped and ranging in size from 0.2 to 2 μm, to follow the Stoke's law even if thermally induced convection currents and wall effects are disregarded. The observed layered and irregular sedimentation in the one-gravity samples is, therefore, to be expected.

Neglecting the large and somewhat rounded dispersion-depleted areas in the flight sample SPAR-G1 for the moment, we still find it difficult to explain the observed layered sedimentation in the low-gravity processed ingot. From Figure 14, even under ideal conditions, an excursion for 10 seconds at the gravity levels from 3×10^{-2} to 1×10^{-3} would have resulted in clustering of the ThO_2 particles. The occurrence of clustering would, in turn, lead to density gradients that could further promote bunching or layering of dense regions in the sample. For this to occur, in view of the recorded gravity level and furnace temperature profiles, the sample temperature would have to lag by no more than 50°C in the molten state during heat-up, as discussed previously.

To remove this uncertainty, emphasis must be placed on attempts to simulate as closely as possible the flight-test conditions during preliminary furnace testing using samples that may be "sacrificed." With similar experiment materials and objectives (such as SPAR II Experiment 74-34) and under the constraints of sample size and configuration, it is not advisable to insert a thermocouple into the flight or GBT cartridge.

Low-Gravity Convection and Thermoacoustic Effects

Previous discussions have illustrated that large dispersion-depleted areas are observed in the microstructure of the flight sample but not in any of the ground processed samples. It has also been suggested that these areas have outlines not unlike those defining large gas voids in the interior of GBT ingots. The longitudinal and transverse sections [Figs. 5(a) and 10(a)] of SPAR-G1 clearly show that the near-spherical, dispersion-depleted areas are isolated within the ingot and are not parts of directional grain growth involving the rejection of particles. The fact that during cooldown the ingot center would always be hotter than the cartridge casing (which was in direct contact with the quenching gas) also rules out the possibility of solidification and grain growth originating from the ingot interior.

If one were to accept the suggestion that the observed regions depleted in dispersion were at one time occupied by expanded Ar gas containing Mg vapor, then the possibility of natural convection [6] should be explored in addition to the phenonmena of fluid/gas motion discussed previously.

Since our sample cartridge was heated from the side, the gravity-driven convective velocity, V_c, may be estimated from the following expression [7]

$$V_c = \frac{\Delta T}{L} \cdot \frac{\rho \beta g L^3 \delta}{12\eta} , \tag{2}$$

where g is the gravitational constant; ΔT is the temperature difference over a distance L, which is half way between the cartridge wall and the center of the molten sample; and β, ρ, and η are, respectively, the volumetric coefficient of thermal expansion, density, and viscosity of the melt. The δ in the equation is given by

$$\delta = \left(\frac{x}{L}\right)^3 - \frac{x}{L} , \tag{3}$$

where x is the distance at some point of interest in the melt along the direction perpendicular to gravitational pull. When $x = 2\,L/3$, δ has the maximum value of approximately 0.37. If we use the value of $1 \times 10^{-5}/^\circ C$ for β, 1.74 g/cm^3

for ρ, and 1×10^{-2} P for η, we can construct plots of V_c versus gravity levels for four temperature differences between cartridge wall and center of the melt, as shown in Figure 15. It should be noted that the temperature differences plotted are for 0.4 cm, or 2L, which is the radius of out cylindrical sample [1]. By using a self-diffusion coefficient of 1×10^{-4} cm^2/s for molten Mg, one can obtain an estimated diffusion velocity, V_D, of approximately 5×10^{-4} cm/s over the same distance. Comparing this V_D with the plotted V_c curves in Figure 15, one sees that the gravity induced convection currents will dominate over diffusion when gravity levels are higher than 2×10^{-3} for the specified temperature differences. As speculated previously, the possibility existed that sample SPAR-G1 could have had an excursion at the 10^{-3} to 10^{-2} gravity levels during the initial stages of melting. We should caution, however, that equation (2) does not describe accurately our heating scheme, which was cylindrical in configuration.

Perhaps a more plausible explanation for the induced liquid and gas motion at low gravity is the mechanism of thermoacoustic convection due to rapid heating. One-dimensional mathematical models for thermoacoustic convection have been developed and numerically investigated by L. W. Spradley [8]. His calculations show that the sudden expansion of liquid adjacent to a suddenly heated wall will set up an acoustic wave that propagates through the liquid. The magnitude of the effects of thermoacoustic convection is a strong function of the severity of the thermal boundary conditions. We lack well defined boundary conditions in our flight experiment for a quantitative analysis of the thermoacoustic effects. Nevertheless, it is our belief that the 10°C/s heat-up rate was rapid enough to have set up acoustic waves in the molten Mg, leading to the entrapment of argon bubbles just prior to reaching the quiescent soaking period.

During the soaking period at the $\leq 10^{-4}$ gravity level, the mechanism described previously took over, and nonwetting molten Mg would shrink away from the wall. At the same time, argon gas would diffuse to the wall to attain a lowest energy configuration. The original region once occupied by the relatively large Ar bubbles would then be filled by the low viscosity liquid Mg leaving behind most if not all of the ThO_2 particles. Solidification of this melt would then produce a microstructure consisting of, among other features, a number of dispersion-depleted regions in the interior that are similar in outline to gas voids seen in the GBT samples.

In future Spacelab space processing experiments in long duration missions, slow heat-up can be easily accomplished to avoid the problems associated with thermoacoustic waves. For SPAR furnace experiments,

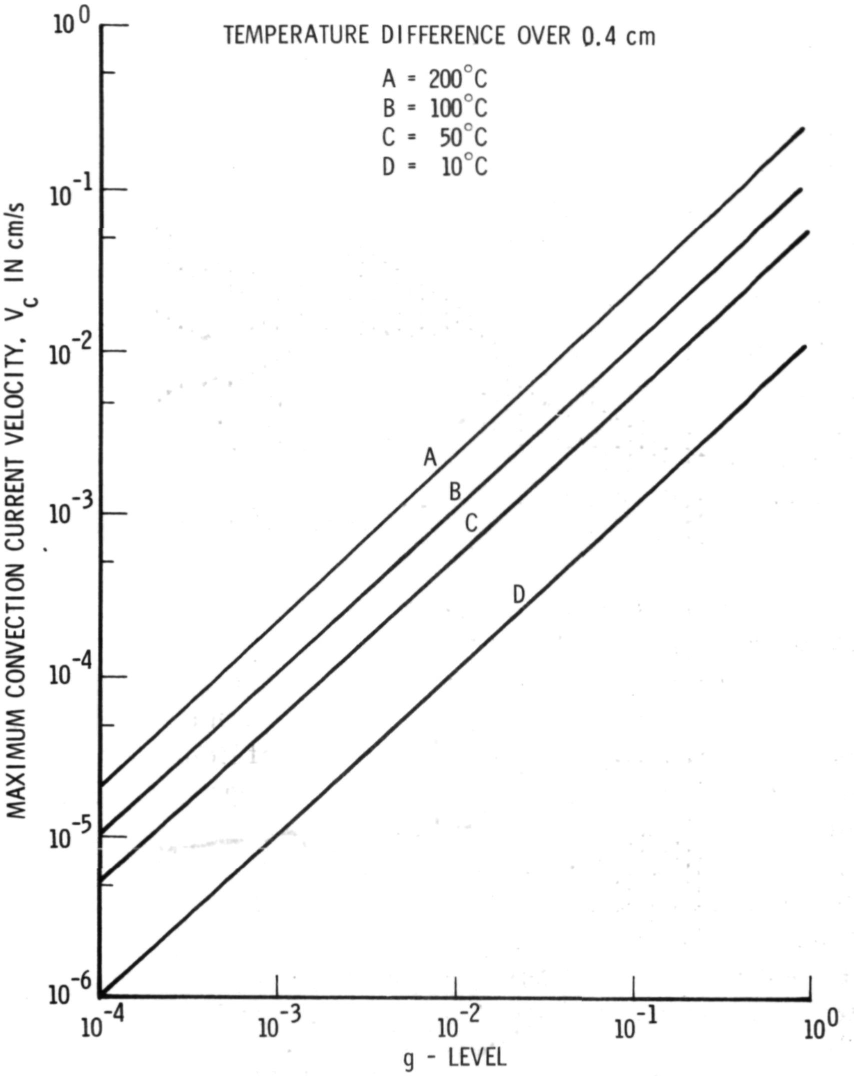

Figure 15. Convection velocity versus gravity level and temperature gradient.

thermal programming should be developed so that lowest possible heat-up rate can be applied within the constraints of flight time-line and soaking period requirements. With SPAR II Experiment 74-34, for example, if the sample temperature could approach closely the furnace temperature, then preheating the sample at, for example, 400°C to "ignition" would allow a programmed heat-up rate of <4°/s to reach 850°C, still providing a soaking period of 180 seconds or longer.

Directional Solidification and Particle Rejection

When a liquid containing a dispersion of small particles is directionally solidified, a critical growth velocity exists for the rejection or entrapment of particles along the moving solid-liquid interface. When the critical velocity, V_o, for a given system is exceeded by the rate of solidification, the particles will be trapped in the solid. The dependency of V_o on particle size and shape, and on other physical and chemical parameters of the liquid/solid system, is rather complex. However, it has been experimentally observed [9] that values for V_o for 1 to >100 μm metallic and refractory oxide particles in water and some organic solutions (η from 0.01 to 0.1 p) do not exceed 20 μm/s. Generally speaking, for small particles (< 15 μm), V_o is independent of particle size. For particle sizes greater than 100 μm, V_o has a smaller value and is shape-dependent, with irregularly-shaped particles having a higher V_o.

We have previously discussed the possibility of particle rejection in connection with the dispersion-depleted areas around the periphery of the flight sample SPAR-G1 [Fig. 10(a)]. Referring to the thermal profiles presented in Figure 1, it can be calculated that the cooling rate was approximately 15°C/s through the solidification temperature of 651°C. Even with an unreasonable assumption of a large temperature difference of 200°C between the ingot center and the cartridge casing, the estimated growth rate of 300 μm/s would still be orders of magnitude too fast for the rejection of particles. Should undercooling occur at low gravity levels (Fig. 1), the nucleation of solid grains would be almost instantaneous with no opportunity for particle rejection.

It should be mentioned that the small directionally oriented Mg grains within the dispersion-depleted areas are an indication of the existence of a temperature gradient, irrespective of the growth rate. The very fact that these grains are small (approximately 40 by 120 μm) is also an indication of rapid solidification. By eliminating the possibility of a slow growth rate promoting the particle rejection mechanism, the validity of the postulation is enhanced with regard to low-gravity effects on the relative motion of the gas and non-wetting liquid, and the surface tension induced movement of liquid Mg and condensation of Mg vapor during cooldown.

It should also be mentioned that with SPAR II experiment we expect to observe the product of Th plus MgO reaction to be extremely fine ThO_2 precipitates. Therefore, the layered sedimentation phenomena at related high-gravity levels of 10^{-3} to 10^{-2} should not occur. A slower heat-up rate, as previously suggested, should also lessen the chances of forming large dispersion-depleted regions in the center of the ingot. However, under the flight and experimental design constraints, it will probably not be possible to avoid the formation of dispersion-depleted areas at the periphery of the ingot.

Summary of Microstructural Analysis

The continuing characterization efforts related to all SPAR I samples may either strengthen the understanding of the observations discussed above or necessitate the modification of certain postulated mechanisms. The analysis of SPAR II experimental results will also have a bearing on the validity of some of the SPAR I conclusions. The presently postulated mechanisms for observed microstructures of the SPAR I samples may be summarized in the following.

1. The internally sound ingot cast under low-gravity conditions, in contrast to the one-gravity samples, is a beneficial manifestation of low-gravity effects which caused the protective gas to move to container walls and the non-wetting melt to move toward the center.

2. The presence of rounded regions that are depleted in dispersion can be attributed to thermoacoustic waves induced by rapid heating, coupled with the mechanism described in item 1 and accompanied by void-filling action of the low viscosity liquid.

3. Overheating and heating with gas beneath the melt under the influence of gravity will result in extremely unsound ingots with internal voids and shrinkage cavities, as evidenced by the three GBT samples and the laboratory cast sample.

4. Layered and nonuniform sedimentation of dispersoids in all ingots examined represents a deviation from the ideal Stokes law and is not unexpected with the present experiment design. It is necessary, however, to speculate on the possibility of the flight sample's excursion at the 10^{-2} to 10^{-3} gravity levels during initial melting to explain the observed layered sedimentation.

5. The presence of the dispersion-depleted periphery of the flight-processed ingot cannot be explained by the particle rejection mechanism because of the estimated high rate of solidfication. However, the mechanism of preferential gas motion at low gravity coupled with surface tension induced liquid motion and Mg vapor condensation can be used to explain this particular microstructural feature.

CONCLUSIONS

1. The flight sample SPAR-G1 was soaked in the desired range of temperature and time under low-gravity ($\leq 10^{-4}$) conditions.

2. The low-gravity effects have contributed to the soundness of the casting. The observation of this unique feature broadens the scope of space processing involving melting and solidification of materials that require protective atmospheres and containers in addition to low gravity.

3. Optimum distribution of dispersoids in the flight-tested sample was not achieved. Several mechanisms for the formation of undesirable microstructures have been postulated.

4. The formal GBT samples had not been processed under conditions expected by the experimenters. A new GBT run has been planned. Results of this new test and the in-progress analysis of other laboratory simulated castings should provide supplementary and additional data of scientific value.

5. Because of the mechanistic difference between SPAR I and SPAR II tests of this experiment series, some of the presently observed anomalies are not expected to occur in the second experiment. However, one specific recommendation relative to a change in thermal programming is made to minimize the possible thermoacoustic convection effects.

RECOMMENDATIONS

Overall recommendations on casting dispersion-strengthened materials at low gravity will be made after completion of the SPAR II experiment. The recommendations presented below are specifically related to the SPAR II flight and pre-flight tests.

1. Preheating of the two flight cartridges at 400 to 500°C until ignition time.

2. At ignition, the resumption of heating should be at a rate less than 4°C/s while allowing the sample to begin melting (651°C) at gravity levels not higher than 10^{-4} g.

3. The maximum power input to the furnace may be reduced to effect a lower heat-up rate. The soak temperature for the <u>sample</u> may be limited to the range of 800 to 850°C. The soak time at low gravity may be as short as 180 seconds.

4. Attempts should be made to reduce further the thermal lag between the sample and the furnace.

5. The quenching rate should be as fast as possible.

REFERENCES

1. Raymond, L. and Ang, C.: Casting Dispersion-Strengthened Composites at Zero Gravity. Post Flight No. 1 Preliminary Technical Report, NAS8-31539, Aerospace Corporation, December 1975.

2. Kissel, Ralph (MSFC), private communication.

3. Roberts, C. Sheldon: Magnesium and Its Alloys. John Wiley and Sons, New York, 1960.

4. Reynolds, W. C.: Behavior of Liquids in Free Fall. J. of Aerospace Science, December 1959.

5. Stokes, G. G.: Mathematical and Physical Papers, 1901.

6. Grodzka, P. G. and Bannister, T. C.: Natural Convection in Low-g Environments. Paper No. 74-156, AIAA 12th Aerospace Science Meeting, 1974.

7. Bird, R. B.; Stewart, W. E.; and Lightfoot: Transport Phenomena, Chapter 10, John Wiley and Sons, New York, 1960.

8. Spradley, L. W.: Thermoacoustic Convection of Fluids in Low Gravity. Paper No. 74-76, AIAA 12th Aerospace Sciences Meeting, 1974.

9. Uhlman, D. R. and Chalmers, B.: J. Applied Physics, vol. 35, October 1964.

CHAPTER VII

THERMAL MIGRATION OF BUBBLES AND THEIR INTERACTION WITH SOLIDIFICATION INTERFACES

Experiment 74-36

By

John M. Papazian

Grumman Aerospace Corporation

and

William R. Wilcox

Clarkson College of Technology

ABSTRACT

Specimens of gas saturated carbon tetrabromide were directionally solidified in a transparent furnace using a gradient freeze technique. The original temperature gradient was 5°C/cm and the cooling rate was 40°C/h. Progress of the experiment was monitored photographically. Gas bubbles were generated at the advancing solidification front in each of the three specimens (argon, hydrogen, and nitrogen saturated, respectively). The gas bubbles were observed to increase in size, coalesce, and eventually be grown into the solid specimen under low-gravity conditions. No bubble detachment from the interface was observed. Identical specimens processed in the laboratory showed bubble nucleation, bubble growth, and eventual bubble detachment due to buoyancy forces. Examination of the specimens showed a significantly greater void content in the low-gravity processed samples. The grain size was observed to be finer in the low-gravity processed samples. Bubbles, 50 μm to 4 mm in diameter, situated in the melt well ahead of the interface did not migrate to the hot end of the sample tube; this is contrary to predictions of thermal migration of bubbles in the absence of gravity. Reasons for this observation are discussed.

INTRODUCTION

This report presents the results obtained from Experiment 74-36 on the SPAR I sounding rocket flight. The primary objective of this experiment is to observe directly the interaction of solidification interfaces with bubbles in the absence of gravitational forces. In addition, we hope to generate some preliminary information on the rate of migration of bubbles in a quiescent liquid in a temperature gradient. These phenomena are of interest because bubbles are more of a problem in gravity-free materials processing due to the lack of buoyancy, the decreased hydrostatic head, decreased free convection, and increased dispersion of foreign particles. These factors lead to easier nucleation and slower motion of bubbles in microgravity. The understanding and control of bubble dynamics and bubble-interface interactions will be important elements in the development of sound materials processing practices in the orbital environment. Further, the microgravity environment allows us to perform experiments which are impossible on Earth but nevertheless produce results pertinent to problems encountered in Earth-based material processing.

The usual difficulties encountered in performing an experiment are exacerbated by the unique characteristics of a sounding rocket flight. The 300 s microgravity interval is preceded by violent accelerations due to engine thrust, spin stabilization, despin, and a complex vibrational spectrum. Thus, the apparatus must be robust and the experimental configuration must be designed to minimize the effects of the launch environment. In addition, a rapidly changing vacuum and thermal profile is imposed upon the apparatus by the rocket trajectory. Naturally, all manipulations must be performed by remote control. In view of these constraints, the philosophy adopted in this experiment was one of simplicity, redundancy, and low power requirements.

The philosophy led naturally to the choice of low melting point, transparent, organic materials to simulate the solidification behavior of metals. Prior experiments have clearly established the utility and applicability of this technique [1]. Besides their attractive low melting points, these materials possess the unique advantage of being transparent. Thus the progress of the experiment can be monitored photographically to produce a record of the sequence of events. This adds an extra dimension of insight into the physical processes and is a decided advantage over simply trying to reconstruct the sequence of events through specimen analysis.

Unstated, but very important, additional objectives of the first flight were to evaluate the effects of launch induced fluid motion on a partially liquid-partially solid specimen, to gauge the time required for damping of such fluid motion, and to gain a better understanding of the thermal and barometric environment seen by the apparatus during the rocket flight.

EXPERIMENTAL PROCEDURE

Apparatus

In its simplest form the apparatus for this experiment was required to perform the following functions:

- Establish a predetermined temperature gradient along the length of three specimens
- Freeze the specimens at a predetermined rate during the microgravity interval of the flight
- Photographically record the progress of the solidification front and the motion of any bubbles
- Provide a record of the thermal history of the specimen.

Such an apparatus was designed, built, qualification tested, and then successfully flown on SPAR I. An overall view of the apparatus is shown in Figure 1. The apparatus consists of four basic units. The first is the frame, which serves to physically support the three working components and attaches directly to the mounting tabs of the Black Brant rocket. The second component is an electronics package, which contains an analogue timer-sequencer controlling the operation of the camera and lights, a power supply for the camera and lights, and a 15 channel signal conditioner to convert the thermistor outputs to a 0 to 5 Vdc signal suitable for the rocket's telemetry system. The electronics package was powered by the main onboard 28 V rocket battery and started by the lift-off switch. The third component was the GFE motorized 250 exposure 35mm Nikon F2 camera which was contained in a supporting box. The camera used a Nikon 55mm MICRO lens set to photograph at 1/2X magnification. The fourth component was the specimen holder/furnace assembly. This consisted of an aluminum block which accommodated the four 10 by 100 mm sample tubes, housed the lighting system, and contained the heaters. The heaters were located at the top and bottom of the block and were powered by 110 Vac through the umbilical cable. The temperatures of the top and bottom portions of the specimen holder are preset and controlled independently by two temperature

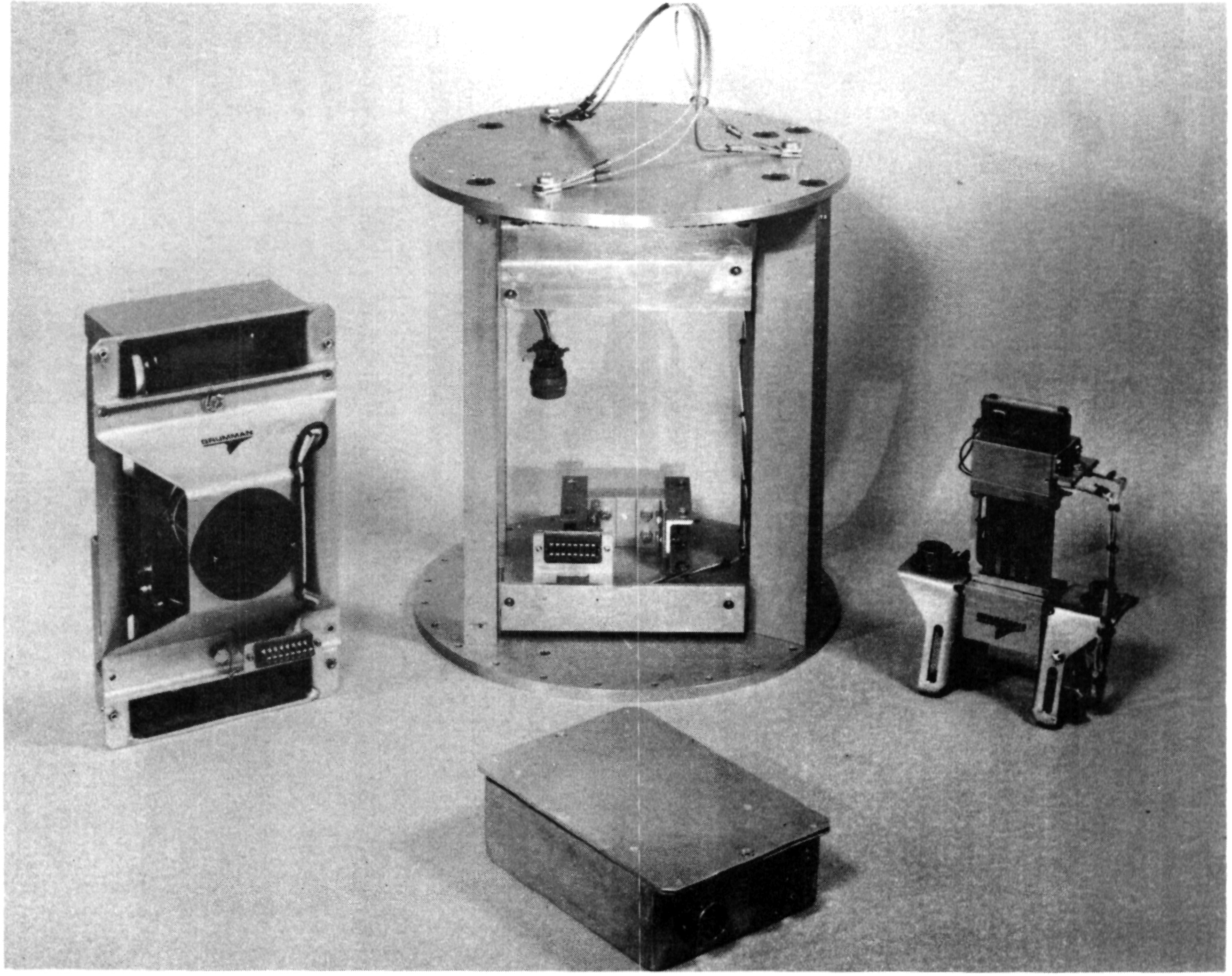

Figure 1. Gradient freeze apparatus built for Experiment 74-36, SPAR I.

controllers housed in the ground support equipment electronic package. Specimen temperature measurements were made by an array of 14 thermistors which were bonded to the back of the specimen holder.

In operation, the heaters were activated 30 to 45 min before launch, and thereby a stable temperature gradient was established and maintained along the length of the specimen holder. Upon launch the umbilical connection was ruptured and the specimen holder began to cool at a rate determined by the ambient temperature and pressure and by the thermal conductivity of the specimen holder mounts. This was adjusted in the laboratory to provide approximately the desired solidification rate of 10 μm/s. The block temperatures recorded during a ground-base simulation (GBS) are shown in Figure 2. This GBS was performed by turning off heater power and rough pumping the bell jar in which the apparatus was installed at time zero. The actual cooling rate during flight I is shown in Figure 3. It is seen that cooling was slower during the rocket flight. Since no change was detected in the temperature of the base plate during the flight we conclude that atmospheric conduction losses were lower during the flight and, thus, we must pump out the system more quickly to perform an accurate GBS.

Specimen Preparation

Carbon tetrabromide was chosen as the sample material for this investigation. The choice was made on the basis of previously published results, melting point (90°C), and availability. The material was from lot No. A4C of Eastman Chemicals. The samples were contained in 10 by 100 mm pyrex tubes which were sealed at one end by a glassblower. The seal at the other end was effected by a nylon stopper having two O-rings. The stopper was at the bottom (cold} end of the tube. Numerous GBS tests were performed to establish conditions of sample preparation which would ensure reliable and copious evolution of bubbles during the experiment. The preparation sequence finally chosen was as follows:

- Melting of as-received crystalline CBr_4 in the sample tube in a thermostatically controlled 95° C furnace
- Bubbling of A, H_2, or N_2 through the molten CBr_4 for 5 min
- Stopper insertion and rapid cooling.

All of these manipulations were carried out in an argon-filled dry box which was shielded from short wavelength light by filters. It had previously been determined that liquid CBr_4 decomposes rapidly in the presence of light. Numerous

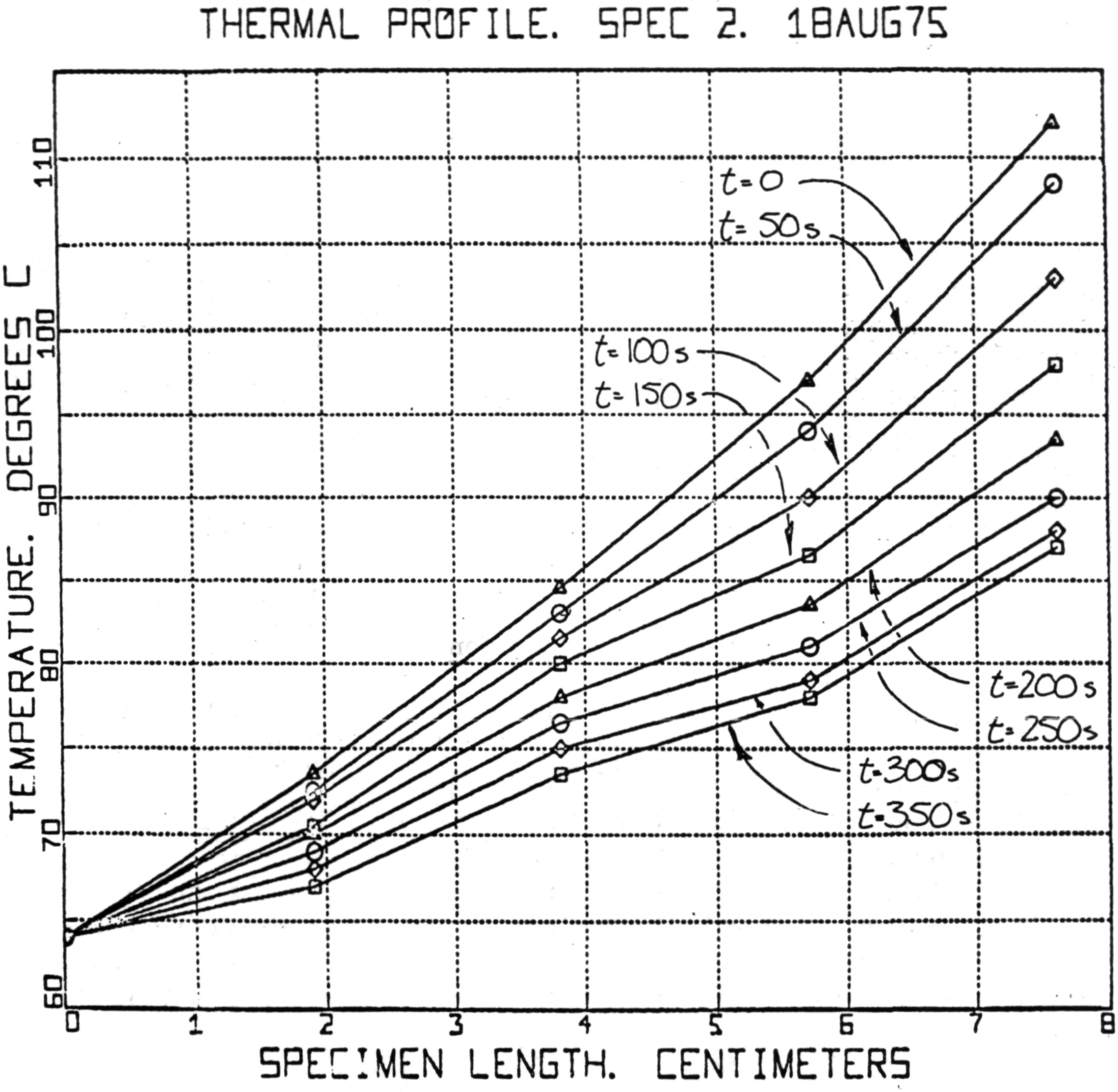

Figure 2. Thermal history of furnace block, GBS, August 18, 1975.

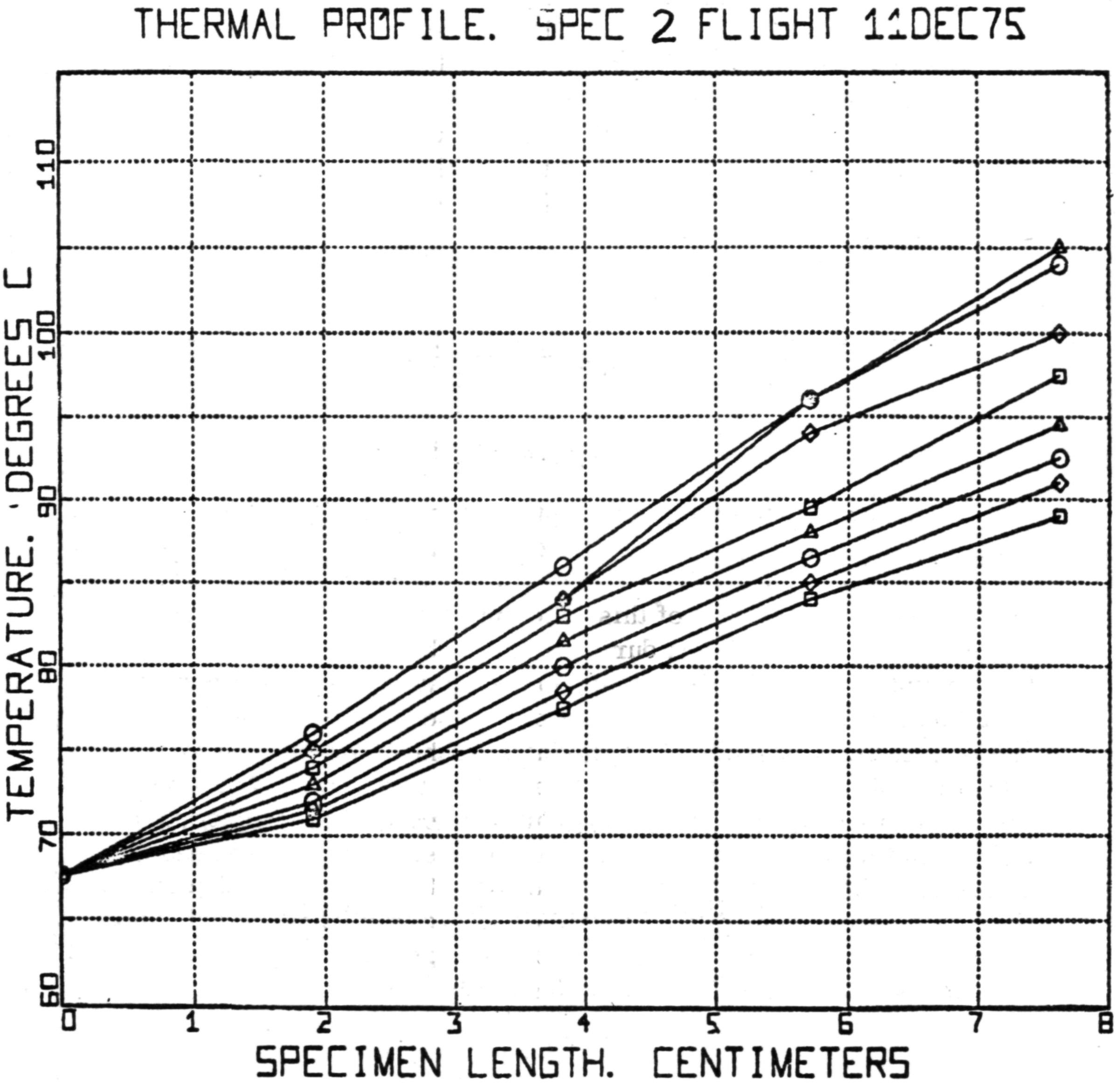

Figure 3. Thermal history of furnace block, flight, December 11, 1975.

reactions are possible; in most cases, highly reactive bromine radicals and free bromine are produced. These reaction products caused rapid discoloration of the specimen and vigorously attacked the stopper and O-rings. In order to suppress this photolysis, filters were installed on the specimen holder and dry box such that no light with a wavelength of less than 420 nm could reach the specimen. In addition, dwell time in the liquid state was kept to a minimum. The gas filled volume in the sample tube (ullage) was adjusted to be approximately zero when the sample was half molten-half solid, the anticipated launch configuration.

RESULTS

Initial Observations

During the actual rocket flight the apparatus functioned perfectly and the experiment was performed according to plan.

The major results of this experiment are contained in the 220 exposure 35mm film which was taken during flight. The camera began framing 80 s after lift-off and recorded at the rate of approximately one frame per second. This time lapse sequence of pictures has been made into a 16mm film.[1] Each original image was repeated eight times on the 16mm film in order to partially adjust the one frame per second filming rate to normal projection rate (24 fps). Thus, when viewing the film, the actual experiment is speeded up by a factor of three. Initial observations of the film show significant generation, motion, and inclusion of bubbles in the mushy zone, the disappearance of small bubbles in the liquid, and little, if any, motion of bubbles in the quiescent liquid. In addition to the film record, other data were generated by analysis of the returned specimens. Results from these two sources of information are discussed below.

Photographic Observations

Three frames from the 220 exposure flight sequence are reproduced in Figures 4, 5, and 6. These photos cannot adequately portray the dynamics of the experiment but they are intended to show a rough outline of the results. Figure 4 shows the appearance of the samples at $t = 85$ s. The extreme left hand tube, specimen A, is from Experiment 74-15 of MIT and contains naphthalene to which various small particles had been added. The next tube, specimen B, was argon saturated CBr_4; specimen C was hydrogen saturated CBr_4, and

---

[1] One copy of this film has been submitted to the SPAR Program Office at MSFC. A loan copy is available to interested parties from the authors.

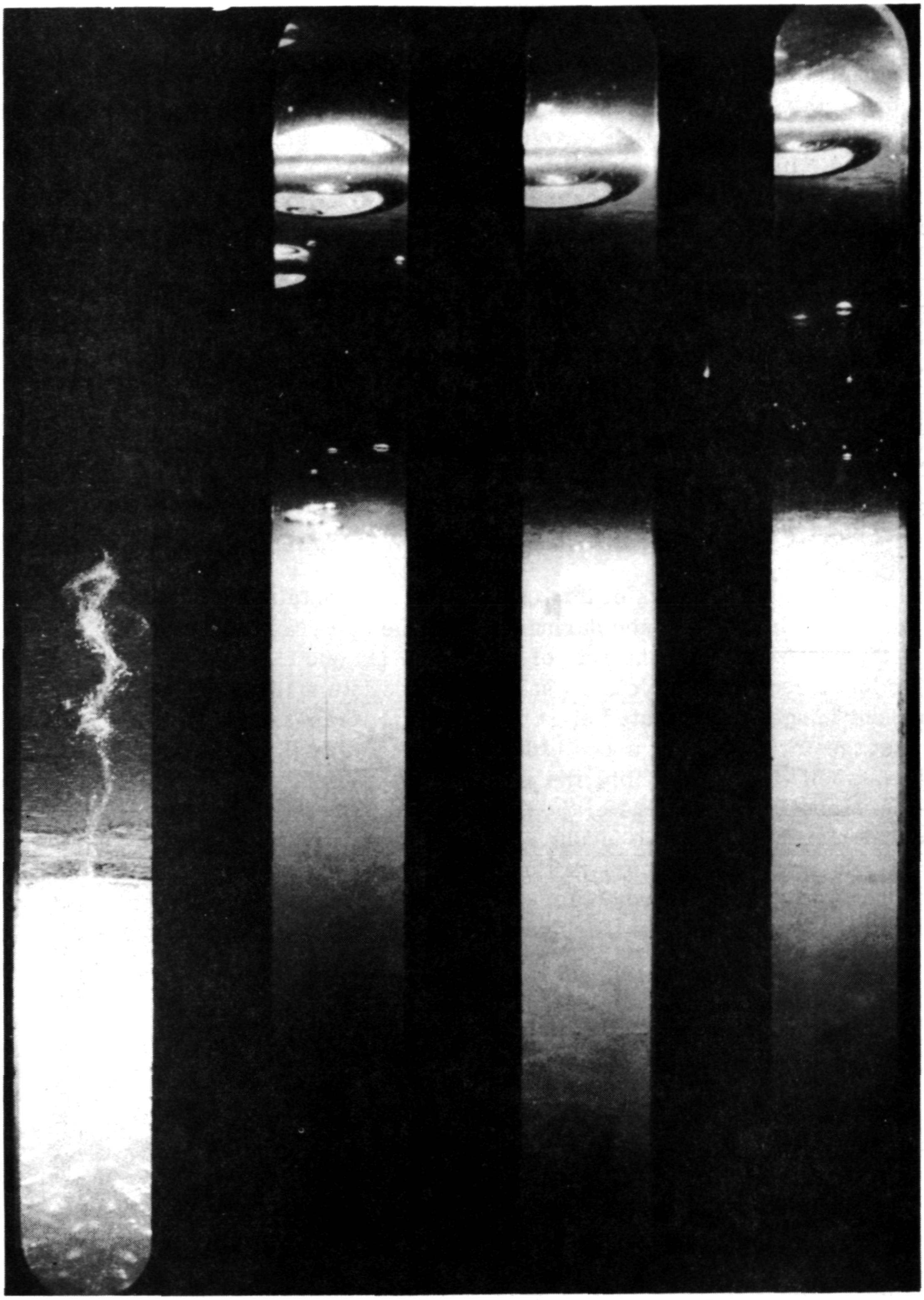

Figure 4. Photograph of experiment at t = 88 s after lift-off.

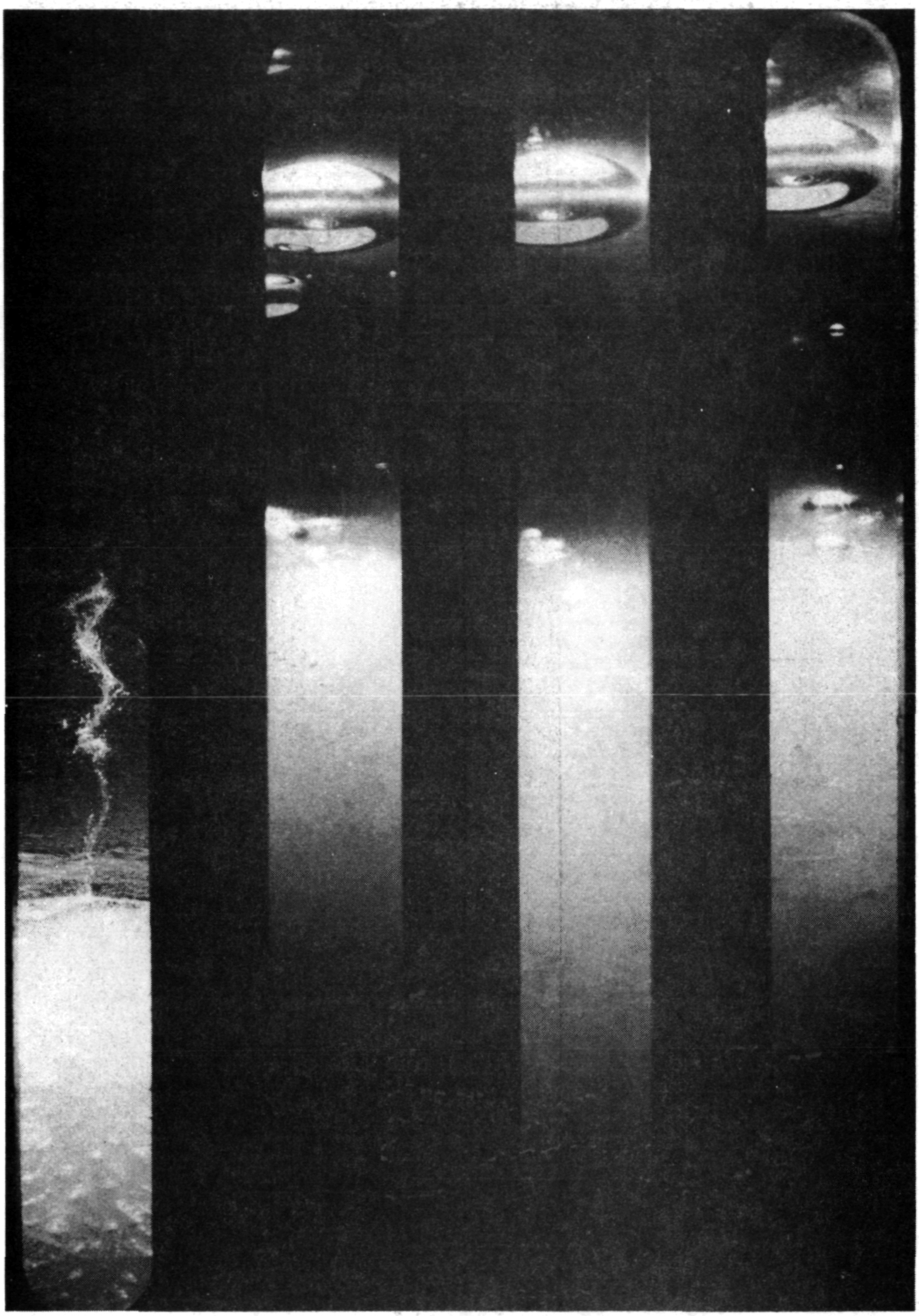

Figure 5. Photograph of experiment at t = 155 s.

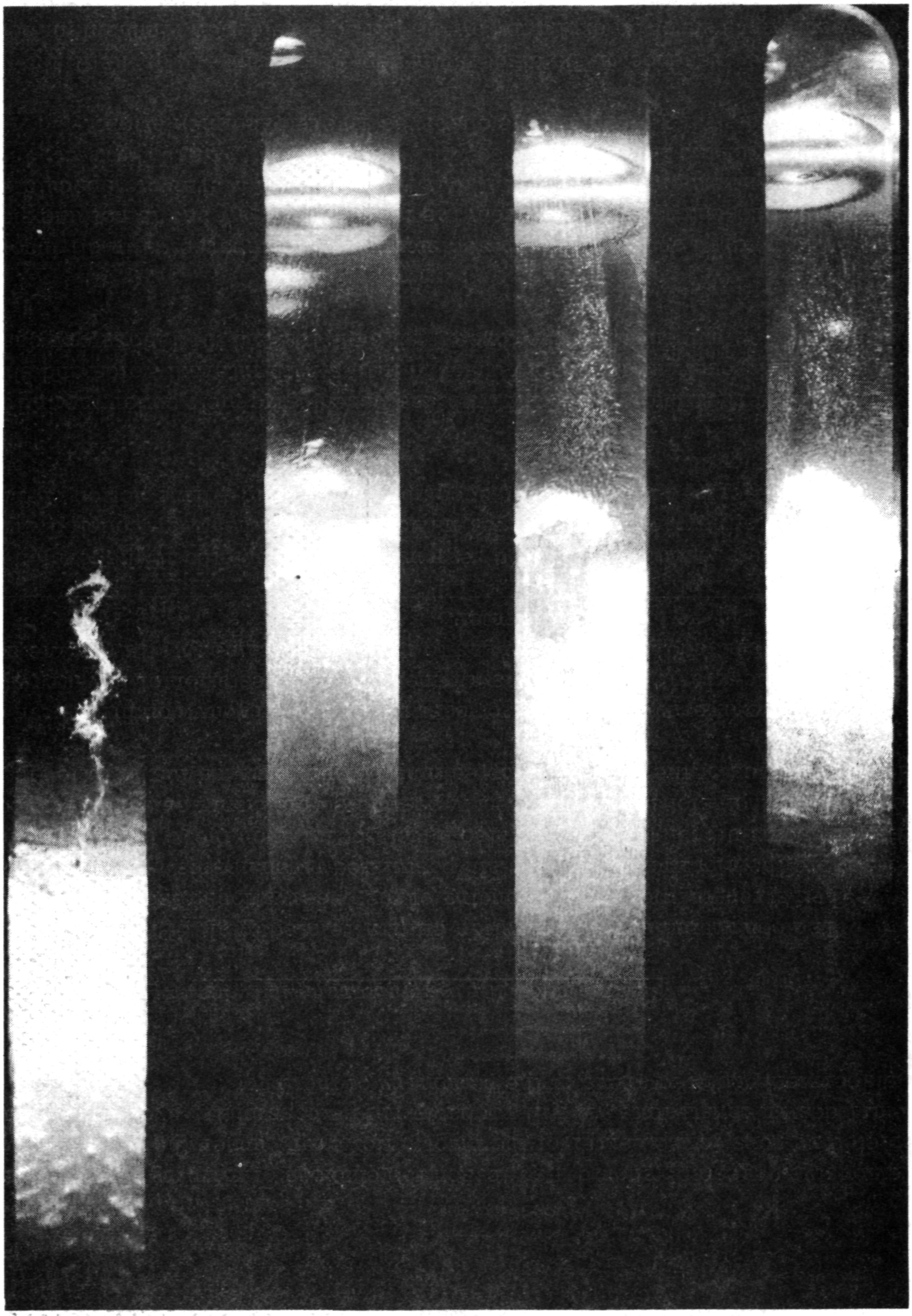

Figure 6. Photograph of experiment at t = 305 s.

specimen D was nitrogen saturated CBr_4. All of the specimens were situated in the thermal gradient shown in Figure 3. The bottoms of the specimens were at the cool end, thus the lower portions of all the specimens were solid. (Naphthalene melts at 80°C and carbon tetrabromide melts at 90°C.)

Specimen A shows a vortex-like structure in the liquid just ahead of the interface. This feature is interpreted as being the image of small particles that were resting on the liquid-solid interface before launch and that were swept up by fluid motion during rocket spin and despin. The shape of this feature does not change during the 220 s series of photographs. This observation leads to these conclusions: (1) that significant fluid motion occurred during launch, (2) that the fluid motion was predominantly axial rather than longitudinal, and (3) that fluid motion had been damped out by $t = 80$ s. The viscosity of naphthalene varies from 0.97 at 80°C to 0.78 at 100°C [2], and microgravity was not completely established until approximately $t = 75$ s. Thus, the damping occurred very rapidly, even more rapidly than had been expected [3]. Comparison with photographs taken immediately before launch shows that the fluid motion during launch caused approximately 1 to 2 mm of melting back or erosion of the solid-liquid interface in the CBr_4 specimens.

Specimens B, C, and D contained bubbles in the liquid portion of the sample tubes. The images of the bubbles were all distorted by the cylindrical sample tubes. Control experiments in which transparent plastic spheres were photographed at different positions in the sample tube showed that a spherical object is distorted such that the vertical dimension (along the length of the tube) is unchanged but the horizontal dimension is greatly magnified. Thus, the bubbles were in fact spherical and had a diameter equal to their apparent height.

Large bubbles of approximately 4 mm diameter are present in all three tubes, and smaller bubbles, down to 40 μm diameter, were present in tubes B and D. The bubbles were generated during the launch phase of the flight and were probably dispersed through the liquid by buoyancy and launch-induced fluid motion. The bubbles could have been due to evolution of trapped gas during melt-back, nucleation and growth of bubbles of gaseous solute rejected during solidification, or dispersal of gas present before launch. They probably are due to a combination of the three mechanisms. It seems likely that the 4 mm bubbles near the top of each tube were gas that had been pushed down from the top of the tube by launch-induced fluid motion and that the smaller bubbles were generated by the other two mechanisms.

Figures 5 and 6 show that during the course of the experiment the smaller bubbles disappeared and the large bubbles remained stationary. The bubbles at the interface grew larger and were incorporated into the growing crystal as the experiment proceeded. These observations are much more apparent in the motion picture. Figures 7, 8, and 9 are photographs of montages that were made by cutting 8 by 10 in. prints of selected frames and pasting them together. They show the sequence of events more clearly than individual still photos. Figure 10 is a similar montage from a ground-base simulation. These figures show that there was little, if any, motion of those bubbles which did not contact with the interface. They also show that nucleation and growth of bubbles occurs at the advancing interface in each of the three flight specimens and that these bubbles are sometimes displaced.

The motion of bubbles at the interface was sometimes abrupt, as is obvious in the motion picture. An example is shown in Figure 11 which shows two sequential views of specimen D. The two views were taken 1 s apart, and the bubble moved 0.8 mm in that time. It was stationary for many frames before and after. The ground-based simulation specimen produced almost no incorporation of bubbles at the interface. Numerous bubbles were generated at the interface, but they were eventually detached and rose rapidly under the influence of normal buoyancy forces.

Numerous small bubbles disappeared in the first 30 to 50 s, particularly in specimens D and B. The origin of this phenomenon is unclear. In general, the solubility of a gas in organic liquids increases as the temperature decreases. Thus, the small bubbles could have merely been dissolving into the melt as it cooled. However, data on the solubility of A, H_2, and N_2 in CCl_4 show mixed behavior, and in some cases the gas solubility decreases with decreasing temperature. We do not know how the solubility behaves in CBr_4, and ground-based experiments are planned to determine this. Other possibilities include Ostwald ripening or simply that the bubbles were transported during launch into a region of melt not saturated with gas.

Figures 7, 8, 9, and 10 allow us to estimate growth rate of the crystals. It is sometimes difficult to decide exactly where the crystals ended and the liquid began. This is not unusual since the material was not extremely pure and an extensive dendritic mushy zone was expected and found. Also, the lighting system was designed for bubble observations and was not optimum for observing the interface. However, we can subjectively define three "interfaces", namely, the fastest dendrite tip, a transparent interface, and a translucent interface. Measurements of the positions of these interfaces from specimen B are shown in Figure 12. The average growth rates of these three "interfaces" are 110, 10, and 4 μm/s, respectively. Measurements on the two other flight specimens gave similar values. Similar data for a ground base simulation specimen gave values of 2.5 and 120 μm/s for the transparent and fastest dendrite interfaces. We see

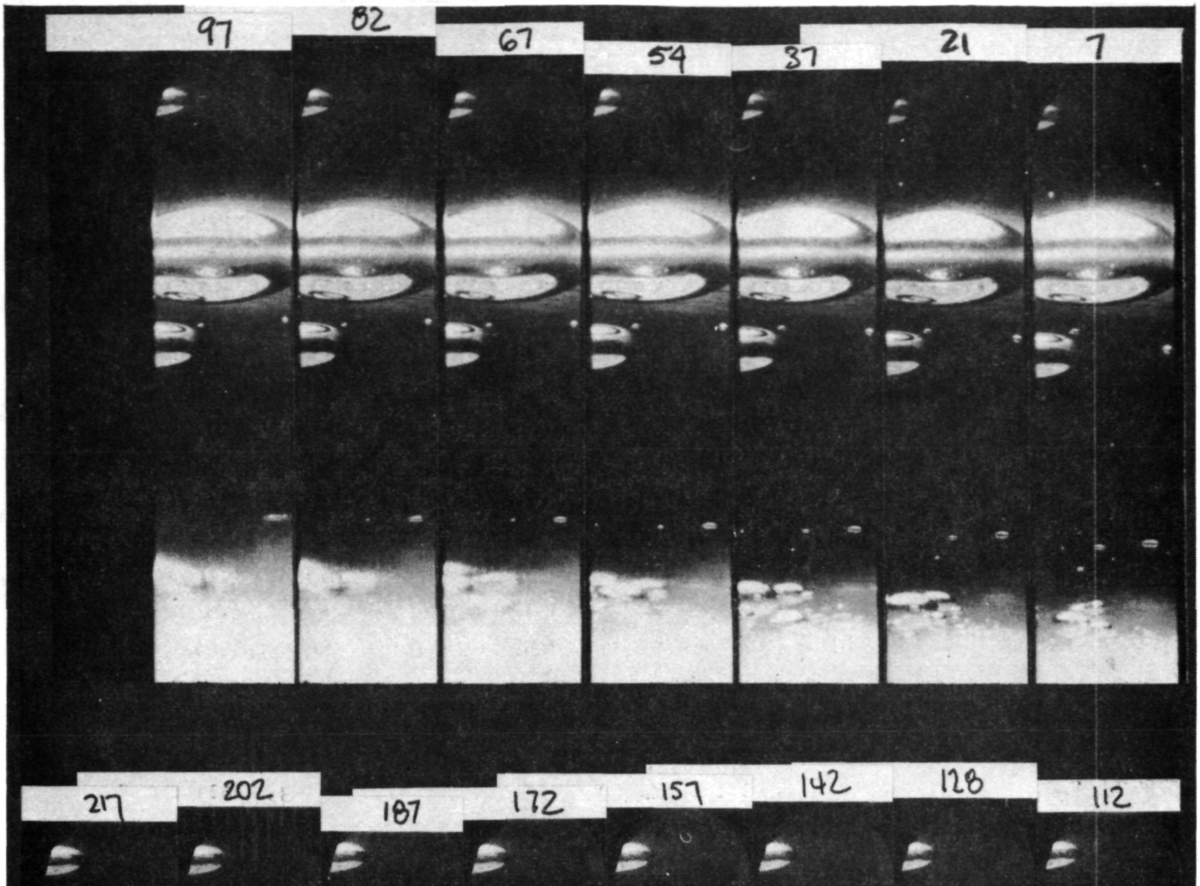

Figure 7. Composite photograph of specimen B (the frame sequence number, n, is above each view; the time since lift-off is n+80 s).

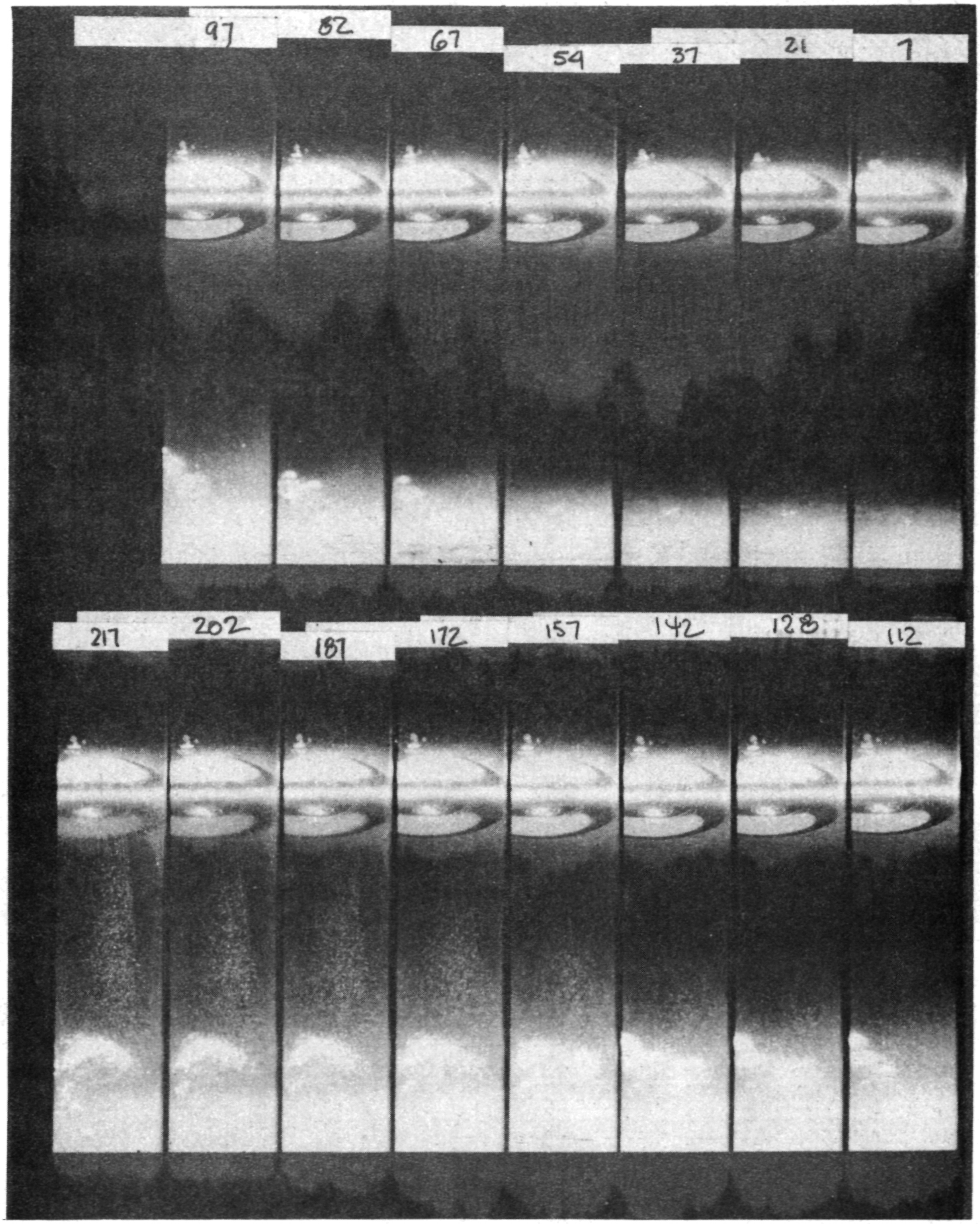

Figure 8. Composite photograph of specimen C (same conditions as Fig. 7).

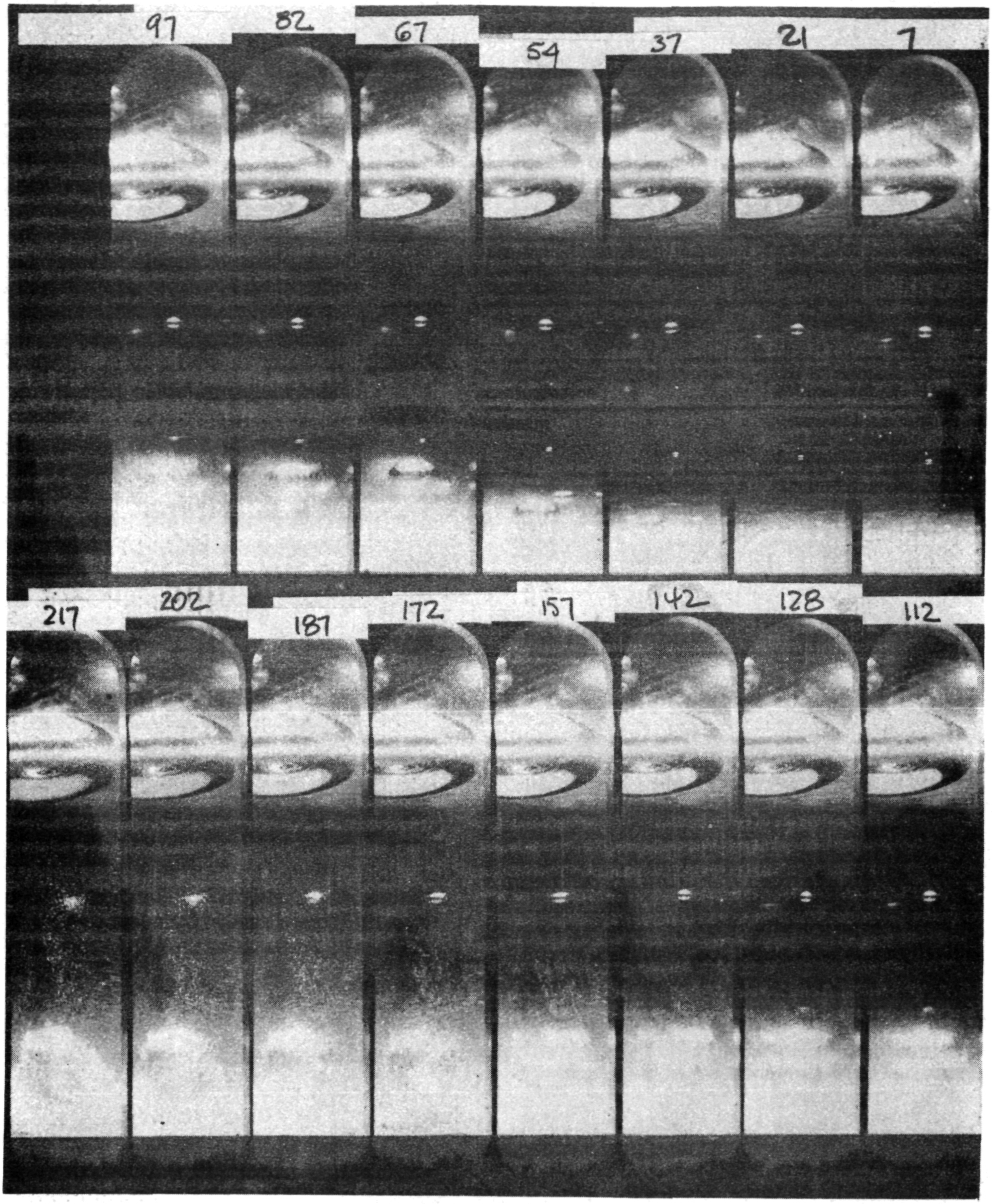

Figure 9. Composite photograph of specimen D (same conditions as Fig. 7).

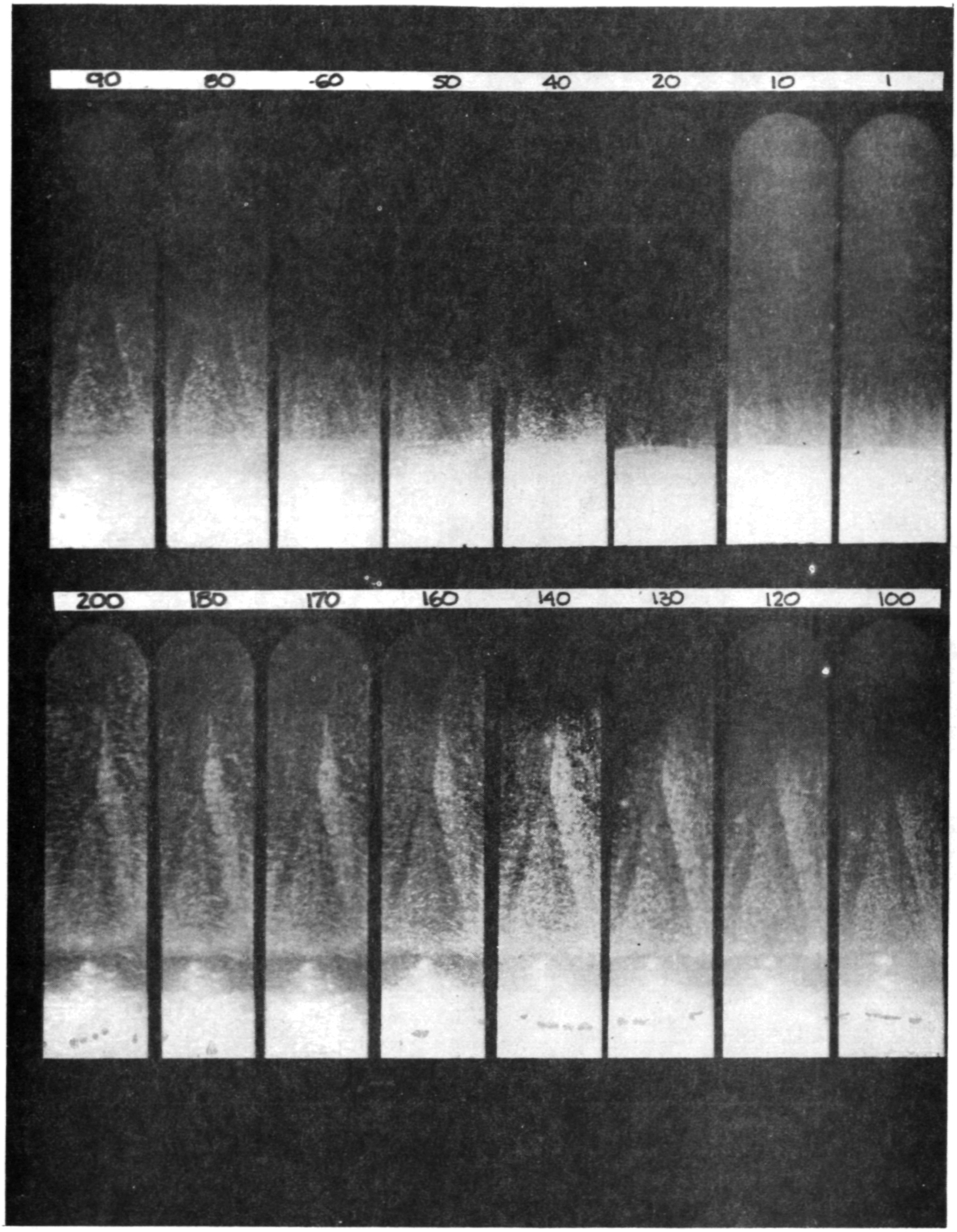

Figure 10. Composite photograph of a specimen from a ground-based simulation.

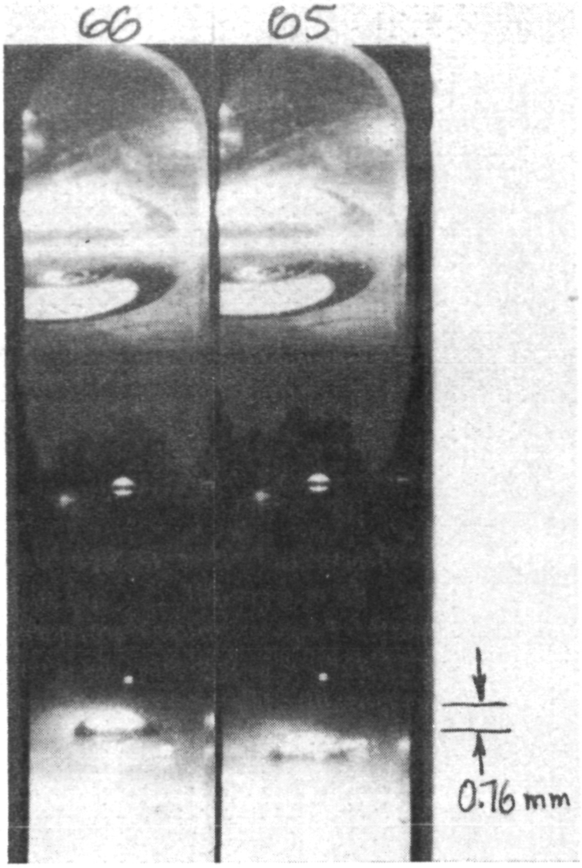

Figure 11. Sequence of two views of specimen D taken 1 s apart.

that although the block cooled significantly more slowly in flight than during the GBS, the crystals grew at much the same rate. This was due to poor heat transfer between the glass specimen tube and the aluminum block in a vacuum.

Structural Observations

The flight specimens contained large grown-in voids (gas bubbles). These are illustrated in the X-radiographs shown in Figure 13.[2] All three of the flight specimens contained voids in the portion of the crystal which was grown during the microgravity interval. The GBS crystals did not contain voids. Figure 14 is a macrograph of flight specimen D in which part of a subsurface void is visible. The circumference of the crystal was complete in all cases, i.e., the voids were confined to the center of the crystal and did not intersect the external surface. Figure 15 is a macrograph of a portion of the melt-back

---

[2] The size of the voids is exaggerated by the X-ray technique.

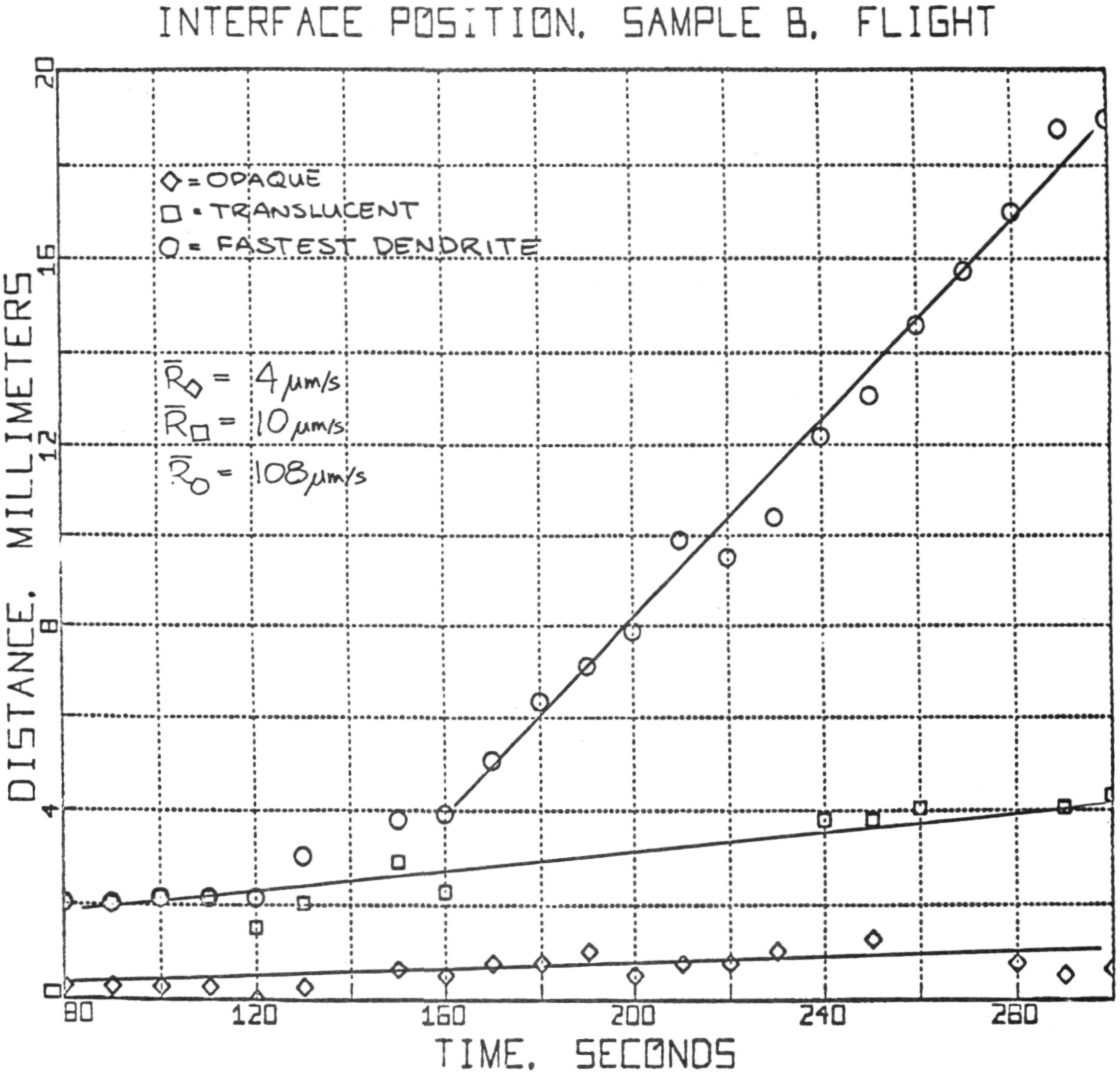

Figure 12. Interface position as a function of time, specimen B, flight.

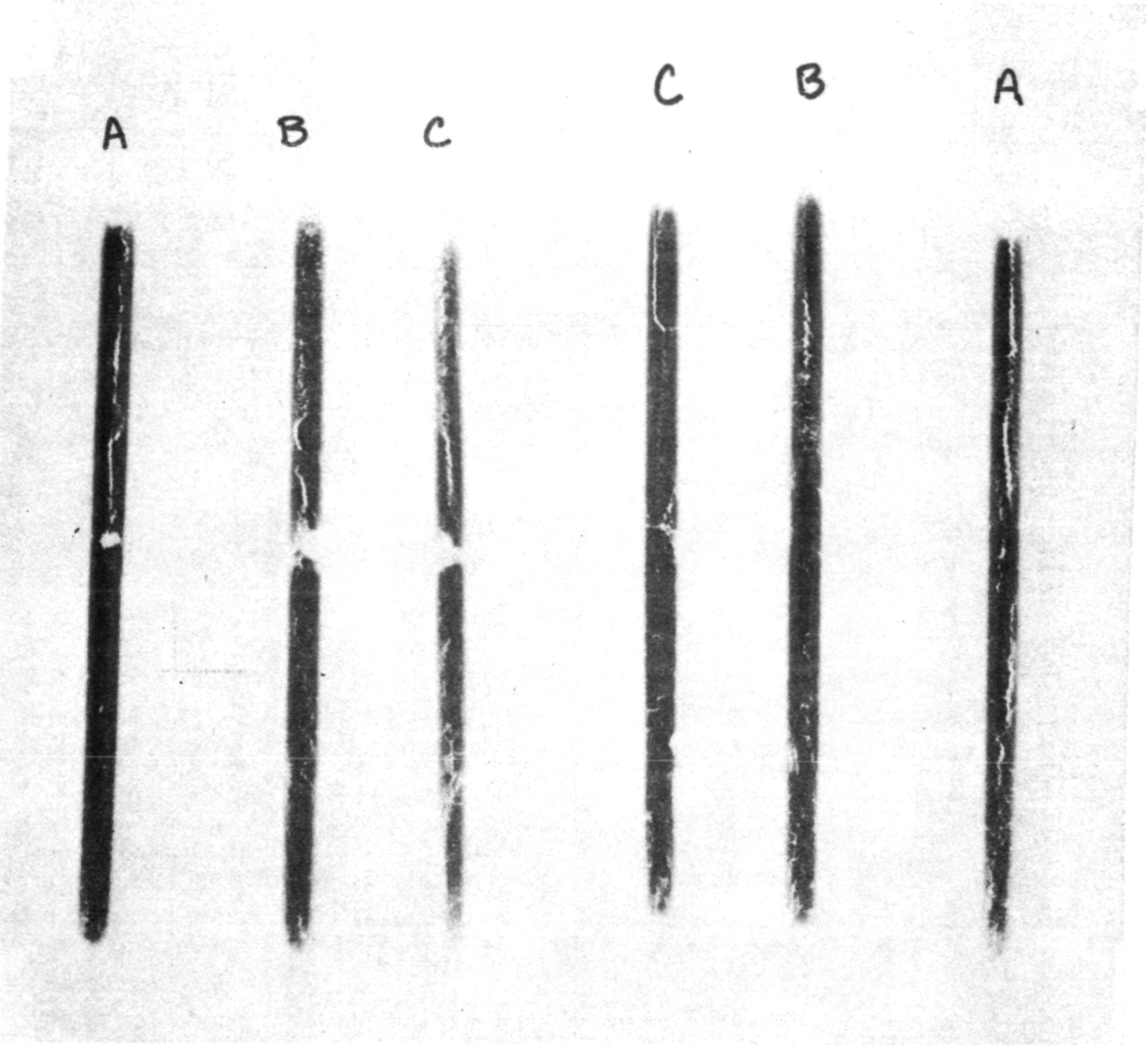

Figure 13. X-radiographs of the three flight specimens (left) and three GBS specimens (right).

interface and shows that a separation had occurred at the interface. Since the details on either side of the interface were almost exact replicas of each other, it is concluded that this separation occurred after solidification, perhaps during the shock of reentry or landing. It is also possible that the separation occurred because of thermal contraction, although this did not occur in the GBS samples. Thermal contraction is likely to be the cause of the observed separation of many of the grain boundaries in both flight and GBS specimens. It is interesting to

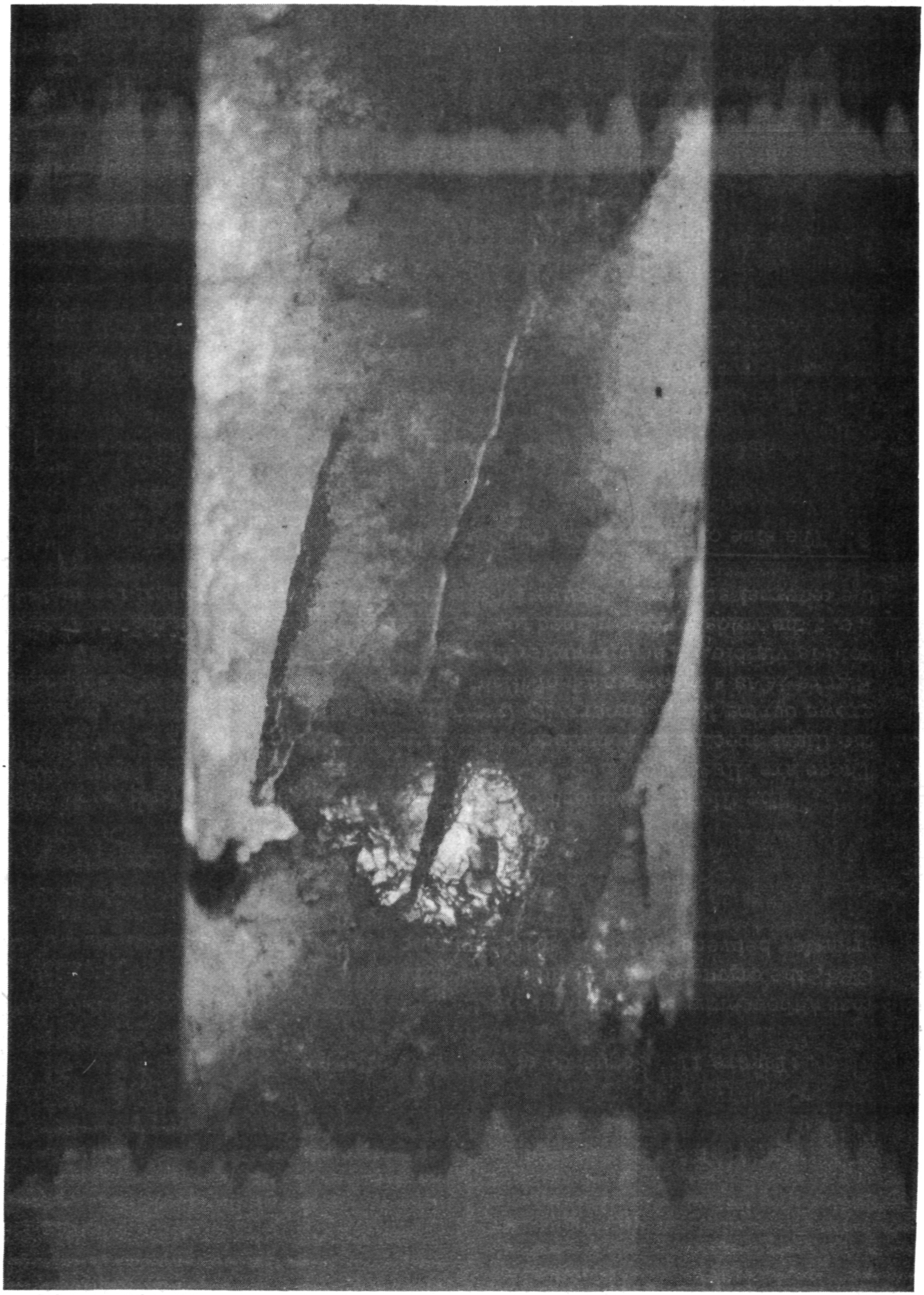

Figure 14. Macrograph of specimen D, flight (The melt back interface is roughly horizontal and located toward the bottom of the picture. The growth direction is upward. The total width of the specimen was 10 mm.).

Figure 15. Macrograph of specimen C, flight (same conditions as Fig. 14).

note that the surfaces of the CBr_4 grain boundaries revealed in this manner show a very rounded or pebbly topography (due to the dendritic solidification). This is in contrast to the more angular topography generally observed in embrittled metallic grain boundaries and is possibly due to smoothing after separation. The smoothing may have been due to a high evaporation rate. It is also possible that the boundaries are rounded in the as-grown conditions.

Figure 16 shows several grains in a CBr_4 specimen. The misorientation across the grain boundary can be readily seen from the dendritic pattern in each crystal. The pattern was probably caused by segregation of impurities to the regions between dendrite arms. Using this observation as a guide, the grain size of the specimens was estimated by simply counting the number of linear defects visible around the circumference of the crystal at the interface. The results are shown in Table 1. Note that the flight specimens were slightly finer grained than the GBS specimens.

DISCUSSION

The results of this experiment show for the first time generation, coalescence, and incorporation of bubbles at a solidification interface in the absence of buoyancy forces. The observations are not yet quantitative nor do they form part of a coherent scientific description of the process of bubble interface interaction. These tasks will be pursued on later flights. The motion picture record of the experiment adds an extra dimension of insight into the dynamics of the process. In addition, we have gained understanding of the sounding rocket environment.

The seemingly incredible juxtaposition of 7 s of rapid spin, violent acceleration and thrust, followed by 300 s in which all imposed accelerations are less than 10^{-4}g, does not appear to preclude meaningful experiments. Fluid motion seems to have been significant during the launch phase as evidenced by the particle decorated vortex in sample A and the distribution of bubbles in samples B and D. The sample tube was aligned with the axis of the rocket and approximately 100 mm off center. Each tube had an inside diameter of 8 mm and was launched with the hot end up. From the shape of the vortex and location of the bubbles, particularly the large bubbles, we conclude that the circumferential fluid velocity (i.e., in the plane normal to the rocket axis) was significantly greater than the axial velocity (along the axis of the rocket). Thus, there was significant interface erosion or melt-back, but the fluid motion was not vigorous enough to completely level the temperature gradient or distribute

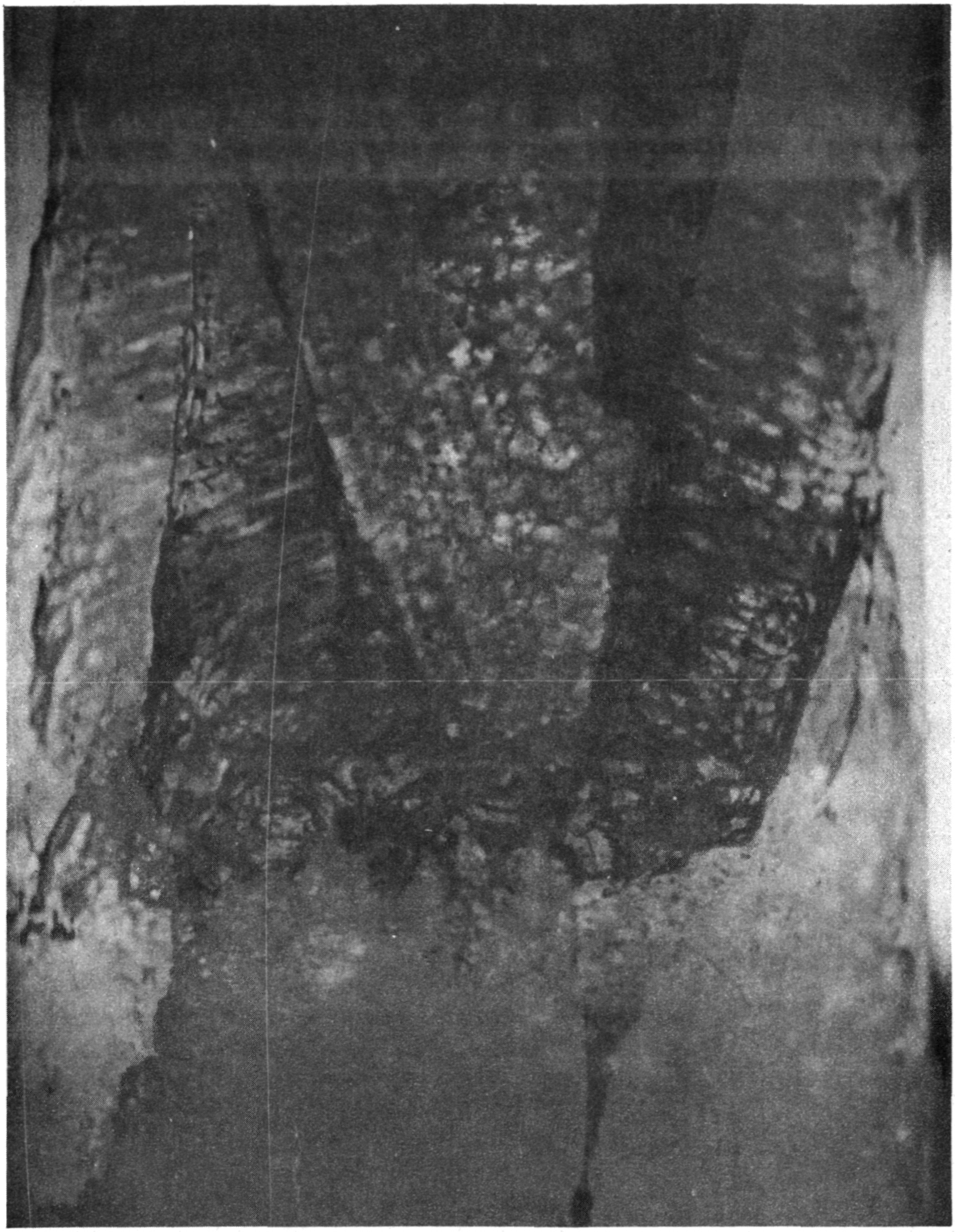

Figure 16. Macrograph of specimen D, flight (same conditions as Fig. 14).

TABLE 1. GRAIN SIZE (mm) OF THREE DIFFERENT TYPES OF SPECIMENS

	A	H_2	N_2
Flight	2.3	2.1	1.9
GBS August 18, 1975	2.8	2.5	2.8
GBS August 21, 1975	2.5	3.6	3.1
GBS September 4, 1975	4.2	3.6	3.1

the foreign bodies throughout the liquid. Some leveling of the temperature gradient did occur as is seen in Figure 3. It is not yet established how much of a thermal lag is present between the aluminum block and the specimen fluid, but the data in Figure 3 must underestimate the leveling effect. Nevertheless it is thought that a substantial temperature gradient remained in the liquid at the beginning of the microgravity interval. The damping of fluid motion was extremely rapid. Despin occurred at approximately 64 s and the rate control system was activated immediately afterward; microgravity conditions were established by 75 s. Our first photograph at 80 s showed no evidence of fluid motion; this macroscopically quiescent state persisted to the end of the experiment at approximately 300 s. This is a highly favorable result and removes a major uncertainty in plans for future experimentation.

The immobility of bubbles in a temperature gradient is the most surprising observation of this experiment. The only previous work in this field [4] leads to the prediction that bubbles should move with a velocity, v, given by

$$v = \frac{d\gamma}{dT} \cdot \frac{dT}{dz} \cdot \frac{r}{3\mu} \tag{1}$$

or

$$Re = \frac{M}{3} \quad , \tag{2}$$

where $d\gamma/dT$ is the temperature dependence of the surface tension, dT/dz the imposed temperature gradient, r the bubble radius, μ the fluid viscosity, Re reynolds number and M the Marangoini number. For a 1 mm bubble with $d\gamma/dT = -0.1$ dyne/cm°C, $d\gamma/dT = -0.1$ dyne/cm°C, $dT/dz = 5°C/cm$, and

$\mu = 2$ cp, this formula gives an expected velocity of approximately 4 mm/s. This prediction is not borne out in our experiment. Crude measurements of the bubble motion give an upper limit to the observed velocity of approximately 10^{-2} mm/s. Equation 1 is the result of simplifying assumptions, but should nevertheless give the correct order of magnitude for bubble velocity.

We can generate at least four hypotheses to explain the discrepancy as follows:

1. $d\gamma/dT = 0$. If the surface tension of CBr_4 does not vary with temperature in the region of interest, then there would be no driving force for bubble migration. We have measured $d\gamma/dT$ for our CBr_4 in the laboratory under conditions which should approximate those of the flight experiment. The results are shown in Figure 17 and give us $d\gamma/dT = -0.11$ dyne/cm°C, a fairly typical value for organic liquids. Thus, we discount this hypothesis.

2. $dT/dz = 0$. If no temperature gradient was present, there would be no driving force for migration. A stable temperature gradient certainly existed before launch, but perhaps this was almost completely eliminated by launch-induced fluid motion. As discussed in item 1, fluid motion did occur. The imposed accelerations were primarily downward, due to lift-off, and radial, due to spin and despin. The longitudinal forces would not tend to cause much mixing since the denser (cooler) fluid was at the bottom. Transient spin can be very effective at mixing, but in this case it did not seem to have been effective as evidenced by the position of the particles in specimen A. Further evidence that the temperature gradient was not eliminated is provided by the observation that the freezing rate was not much different in the flight and GBS tests. If the temperature gradient had been much lower, then we would have observed more rapid crystal growth.

3. Pinning. If the bubbles were pinned by being in contact with the tube wall or solid material, then they would not be free to migrate. It is thought that most of the bubbles were not in contact with solid CBr_4, at least at the beginning of the experiment, because we see no indication of solid being present in the liquid near the bubbles. It is possible that all of the bubbles were touching the tube wall; it is very difficult to evaluate this from the photographs. It is improbable, however, that all of the bubbles would be against the wall unless the fluid or heat flow had been such as to cause this. However, a hotter wall might have caused migration of the bubbles toward the wall and thus trapped them. Since the aluminum block cooled faster than the specimen tube, it is thought unlikely that the tube wall was hotter than the CBr_4. The fluid flow pattern may have thrown all of the bubbles to the wall, but it is impossible to evaluate the likelihood of this occurrence.

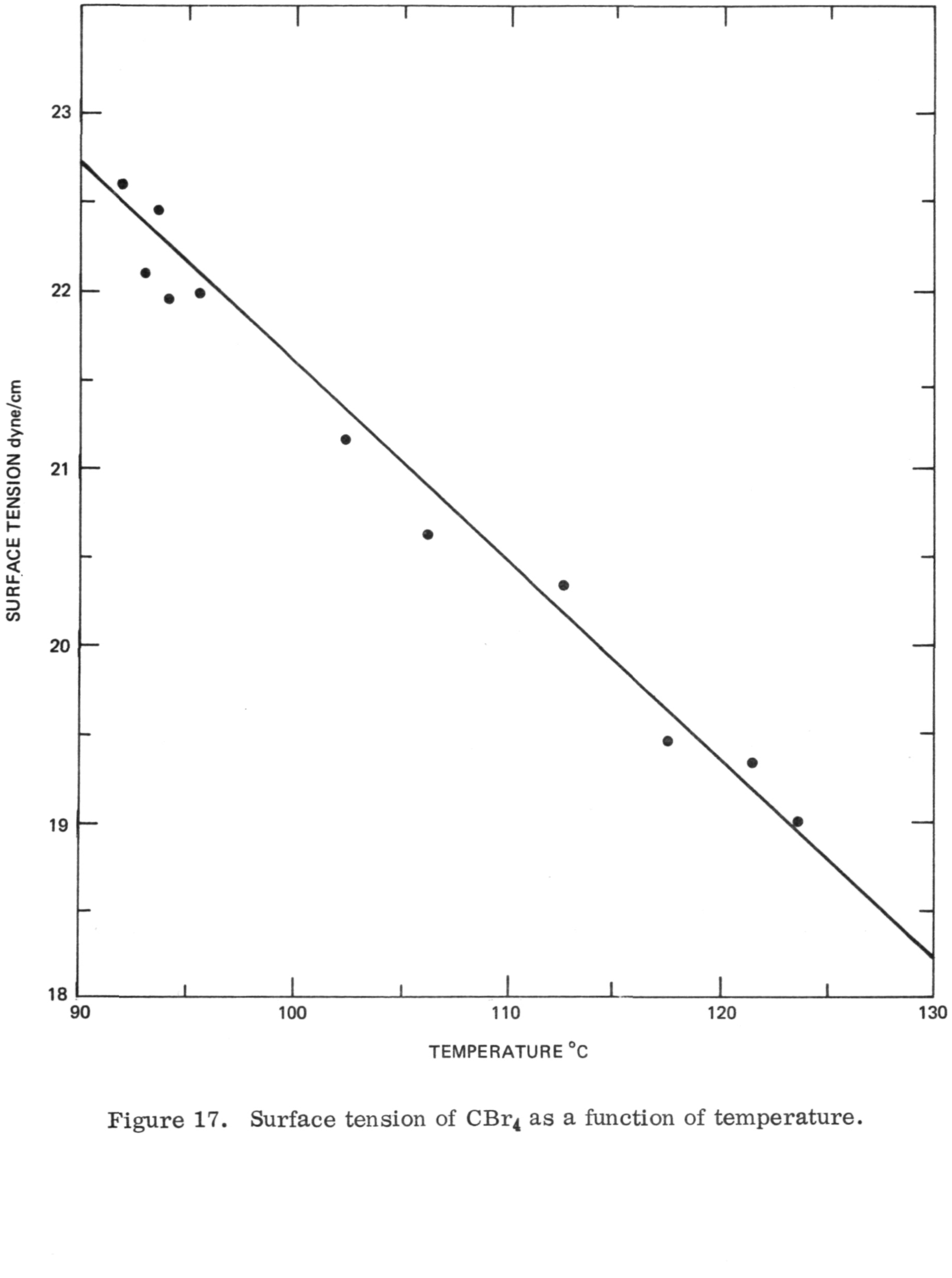

Figure 17. Surface tension of CBr_4 as a function of temperature.

4. Impurity Segregation. It is possible that impurities could have segregated to the surface and arrested bubble motion. We distinguish between two cases: (a) the lack of an energetic driving force due to equilibrium segregation, and (b) a kinetic limitation on the rate of matter transport. Equilibrium segregation, as defined in Reference 6, is limited to coverages on the order of a monolayer [7] and is strongly temperature dependent. This strong temperature dependence of adsorption can lead to a $d\gamma/dT = 0$ or even $d\gamma/dT < 0$ [8, 9]. This would naturally cause the bubble to be static or to migrate in the opposite direction. We do not believe this to have been the case in this experiment because our laboratory measurements of $d\gamma/dT$ would have shown this effect as mentioned in item 1.

A kinetic limitation might have arisen if a strongly segregating impurity was present and was concentrated to monolayer or greater thickness in the surface, and the rate of transport of an impurity molecule across the interface between the segregated layer and the bulk liquid was slow. This situation has been observed in bubble buoyancy experiments and might account for greatly reduced migration rates even though a negative $d\gamma/dT$ still existed. No extensive or obvious surface layer was observed in the photographs, in microscopic observations of GBS tests, or during the laboratory measurements of $d\gamma/dT$. However, this does not preclude its existence.

SUMMARY

The effect of gravity on the grown-in void content in our CBr_4 specimens strikingly illustrates the potential problem posed by bubble generation during solidification in the orbital environment. These results demonstrate the reality of the problem and confirm the viability of our experimental approach. We have observed that during terrestrial solidification bubbles nucleate and grow at the interface, but generally detach and float to the surface of the melt. Thus, we usually obtain a specimen which is free of large voids. However, in free-fall, bubble nucleation and growth also occur, but the bubbles do not detach from the interface and the dendritic growth front is able to go around the bubbles, thus forming a void.

Coalescence of bubbles trapped in the mushy zone was observed to occur in an abrupt manner, similar to the collapse of soap films. The grain size of the low-gravity specimens was finer than that of the GBS specimens. Bubbles, 50 μm to 4 mm in diameter, situated in the melt well ahead of the interface did not migrate to the hot end of the sample tube; that is contrary to the predictions of thermal migration of bubbles in the absence of gravity. Several possible explanations for this behavior are given.

REFERENCES

1. Jackson, K. A.; Hunt, J. D.; Uhlman, D. R.; and Seward, T. P.: TRANS. TMS-AIME, vol. 236, 1966, p. 149.

2. Hodgman, C. D., ed.: Handbook of Chemistry and Physics. 39th Edition, Chemical Rubber Publishing Co., 1958.

3. Papazian, J. M. and Wilcox, W. R.: Thermal Migration of Bubbles and Their Interaction with Solidification Interfaces. Research Proposal File No. 74-127 NAS, February 1975.

4. Young, N. O.; Goldstein, J. S.; and Block, M. J.: J. Fluid Mech., vol. 6, 1959, p. 350.

5. Grodzka, P. G.: Proceedings of the Third Space Processing Symposium Skylab Results. NASA G. C. Marshall Space Flight Center, 1974, p. 691.

6. McLean, D.: Grain Boundaries in Metals. Oxford Univ. Press, 1957, p. 116.

7. Cahn, J. W. and Hilliard, J. E.: Acta Met., vol. 7, 1959, p. 219.

8. Jones, H. and Leak, G. M.: Metal Science Journal, vol. 1, 1967, p. 211.

9. Jones, H. and Leak, G. M.: Acta Met., vol. 14, 1966, p. 21.

CHAPTER VIII

CONTAINED POLYCRYSTALLINE SOLIDIFICATION IN LOW GRAVITY

Experiment 74-37

By

John M. Papazian
Grumman Aerospace Corporation
and
Theodoulos Z. Kattamis
University of Connecticut

ABSTRACT

A 5×10^{-3} m solution of fluorescein in cyclohexanol was directionally solidified in a standard 10 by 10 by 45 mm ultraviolet silica cuvette using a bottom thermoelectric chilling device. Progress of the experiment was monitored by time lapse photography. During flight (SPAR I) the camera malfunctioned and only one-fourth of the expected data was collected. Comparison of flight and ground specimens indicated that: (1) the dark green layer observed ahead of the solid-liquid interface, which is most likely the solute-enriched zone, appears to be wider in the flight specimen; (2) parasitic nucleation ahead of the solid-liquid interface in the flight sample led to an irregularly shaped interface, smaller grain size, equiaxed grain morphology, and a larger average macroscopic growth rate; and (3) the formation of equiaxed grains ahead of the solid-liquid interface in the flight specimen may be attributed to ordered islands within the liquid, which survived remelting because of the low degree of superheating ($\simeq 1.5°C$), did not settle because of reduced gravity, and acted as nuclei during cooling.

INTRODUCTION

This experiment is designed to investigate the effect of a low-gravity environment on the columnar-to-equiaxed transition in polycrystalline metallic solidification. One portion of the experiment (Part A) will involve production of casting under low-gravity conditions; the other portion, Part B, is an attempt to measure the effect of reduced gravity on the width of the solute enriched zone ahead of the solidification interface. Part A will be performed in SPAR IV; Part B was performed on SPAR I and is the subject of this report.

This study was prompted by the unexpected occurrence of fine grained equiaxed microstructures in the Skylab M551 experiment [1] and in a drop tower metals melting experiment [2]. The significant effect of microstructures on the mechanical properties of castings and weldments cannot be overemphasized.

The unique and severe restrictions of the sounding rocket as a research vehicle and the desire to glean as much information as possible from a 300 s experiment led us to the choice of low melting point, low entropy of fusion organic materials as models for metallic solidification. These materials have been used successfully in the past and have the advantages of low melting point, ease of handling, and transparency [3]. Thus, the experiment can be performed quickly with low power requirements and can be observed directly with the aid of a camera. The general plan for Part B was to observe the buildup of a colored solute in transparent solvent ahead of the solidification interface.

PROCEDURE

Bench Tests

The optimum conditions for this experiment were established in the laboratory using bench-top simulations. The system cyclohexanol-fluorescein was selected because its melting point, 22° C, made it very convenient from an apparatus design point of view and because it had been used successfully in the past for a similar demonstration [3].

The desired experimental conditions consisted of a visually observable solute-enriched layer ahead of a stable, mascroscopically linear, solidification interface, producing directionally solidified crystal. These conditions were obtained using a 5×10^{-3} m solution of fluorescein in cyclohexanol contained in a standard 10 by 10 by 45 mm ultraviolet (UV) silica cuvette and solidified from the bottom by a thermoelectric chill. The solidification rate was approximately 10 μm/s, and optimum lighting was found to be reflected illumination by a tungsten filament microscope illuminator. Optimum photographic conditions were obtained by using a 35mm Nikon F camera with a 55mm Micro lens and extenders to increase the magnification to 1.5X. The lens had a filter whose transmission peaked at 540 nm, the wavelength of maximum fluorescence of the fluorescein, and Tri-X film was used. These experimental conditions were described in a document submitted to MSFC on July 1, 1975 [4]. A photograph taken in this manner is shown in Figure 1. A dark band, which in reality is green, is visible ahead of the interface. Microscopic observations led us to conclude that this band is not a Becke line. It could, therefore, be assumed that it is the solute-enriched layer.

The experimental parameters described were found to be of critical importance for a successful observation of the solute enriched zone. The solidification rate was chosen to be as slow as practically possible. The distribution of solute in the solute-enriched zone depends on the characteristic diffusion distance, $D_L R$, where D_L is the diffusivity of solute in the liquid and R is the growth rate. The width of this zone, δ , may be taken approximately equal to D_L/R. Assuming $D_L = 10^{-5}$ cm^2/s and R = 10 μm/s, δ is approximately 100 μm, an observable valve. Lower growth rates would lead to a larger δ , but might render observation inadequate in the allowed 300 s time.

Visual observation of the solute-enriched layer was found to be very sensitive to the lighting conditions. Optimum conditions would have required excitation by long wavelength UV and observation of the emitted fluorescent radiation. When this was attempted the intensity was too low for photographic recording at the minimum shutter speed of 1/4 s. This minimum speed was imposed by the motor drive of the camera. The observation that tungsten illumination produced more intense fluorescence was puzzling, and fluorescence spectometry was conducted on the solution to clarify this point. We found that in addition to an excitation peak in the long UV region, there was another excitation peak centered on 430 μm. This explained our observations.

Ground-Base Simulations (GBS)

An apparatus for the performance of this experiment was designed and built by MSFC, as shown in MSFC drawing number 95M31400. The heart of the unit is the cuvette/heat sink assembly which is shown in Figure 2 and consists

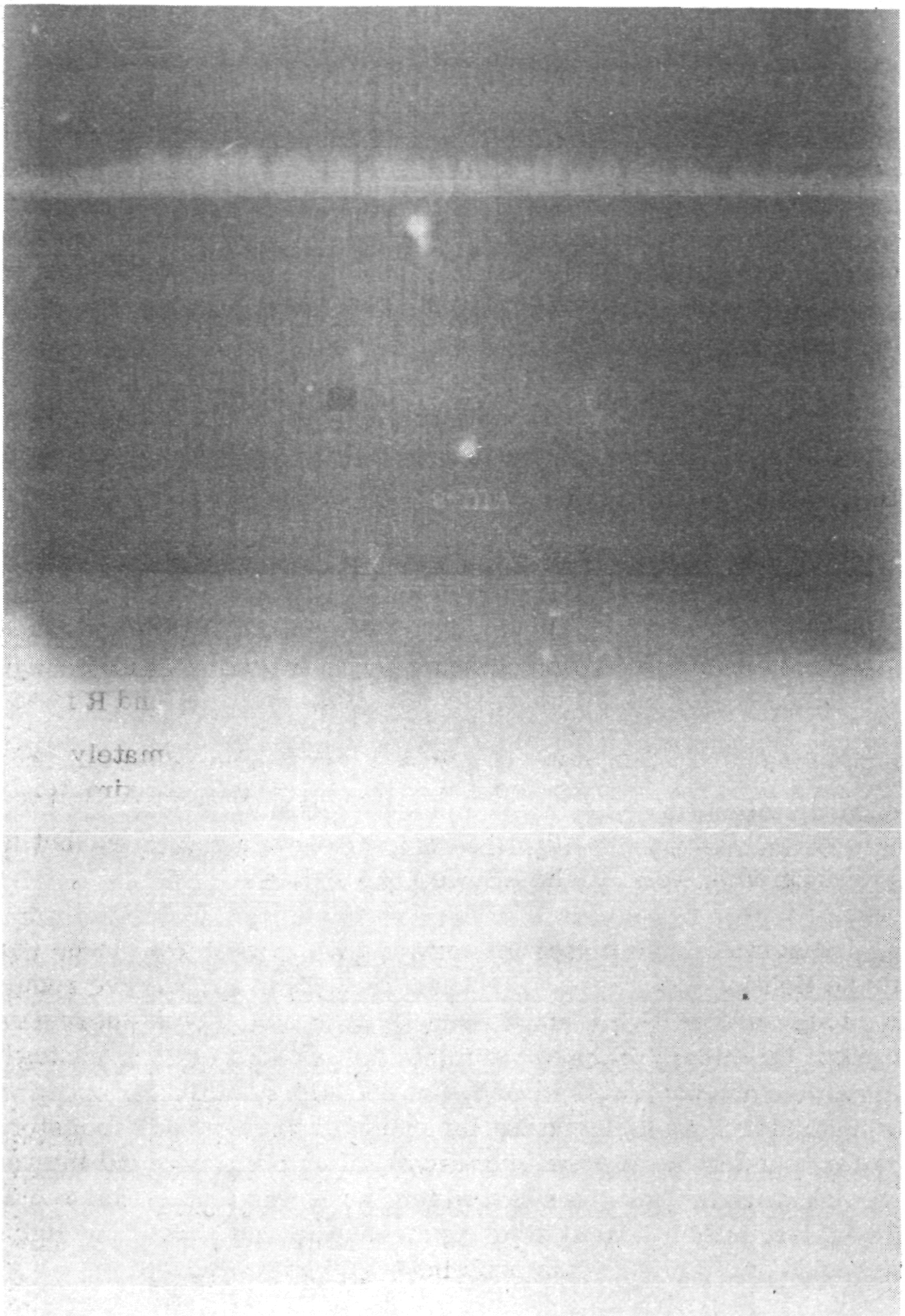

Figure 1. Solidification of cyclohexanol-fluorescein GBS, June 1975.

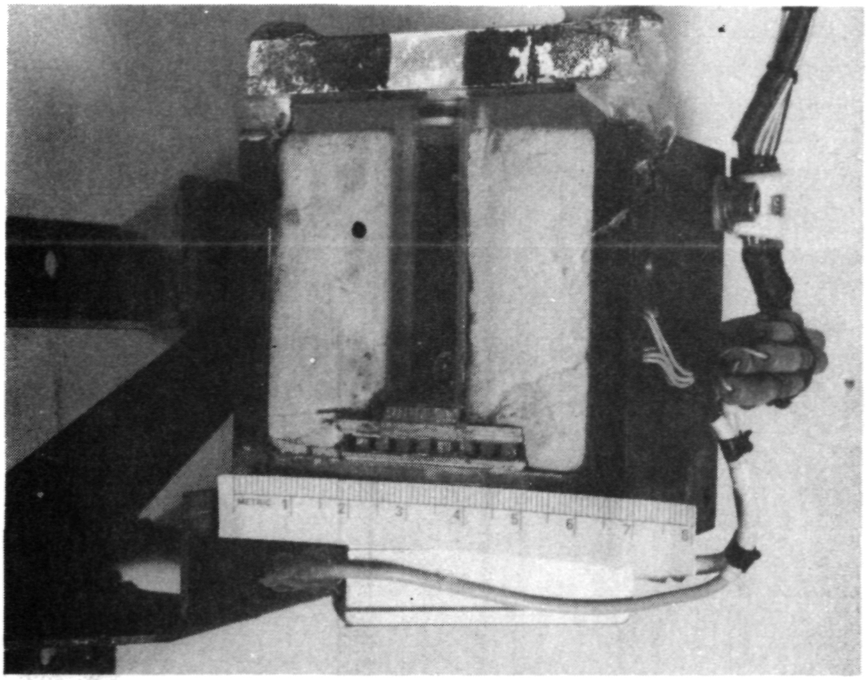

Figure 2. Flight cuvette/heat sink assembly.

primarily of an aluminum block, a thermoelectric cooling device, and the silica cuvette. To provide one-gravity baseline data, attempts were made to perform the experiment in the laboratory using the flight hardware. Despite our best efforts we were not able to successfully perform a valid ground-base simulation before the apparatus was installed in the rocket payload. This was due to many reasons. When the equipment was first delivered, it did not function properly, and when it was eventually functioning correctly, the data did not show the desired effects. The major problems with obtaining data were an improperly positioned light source, poor background, and too rapid solidification. Final adjustments and modifications including inversion of the cuvette assembly, installation of a resistor to slow the rate of solidification, and a change to color film were made very shortly before launch. It was found that the rate of solidification was relatively insensitive to external pressure between 10^{-2} and 760 torr.

The modifications to the flight hardware resulted in seemingly valid observations of a solute-enriched zone as shown in Figure 3, which was taken using the flight cuvette installed in a mockup apparatus in the laboratory. Subsequent GBS tests performed in the flight apparatus in the rocket payload on December 7 and 9, 1975, are shown in Figures 4 and 5. All of these films show a deeper green layer ahead of the interface, as confirmed by several observers in addition to the principal investigator. Thus, the experiment was adjudged ready to launch.

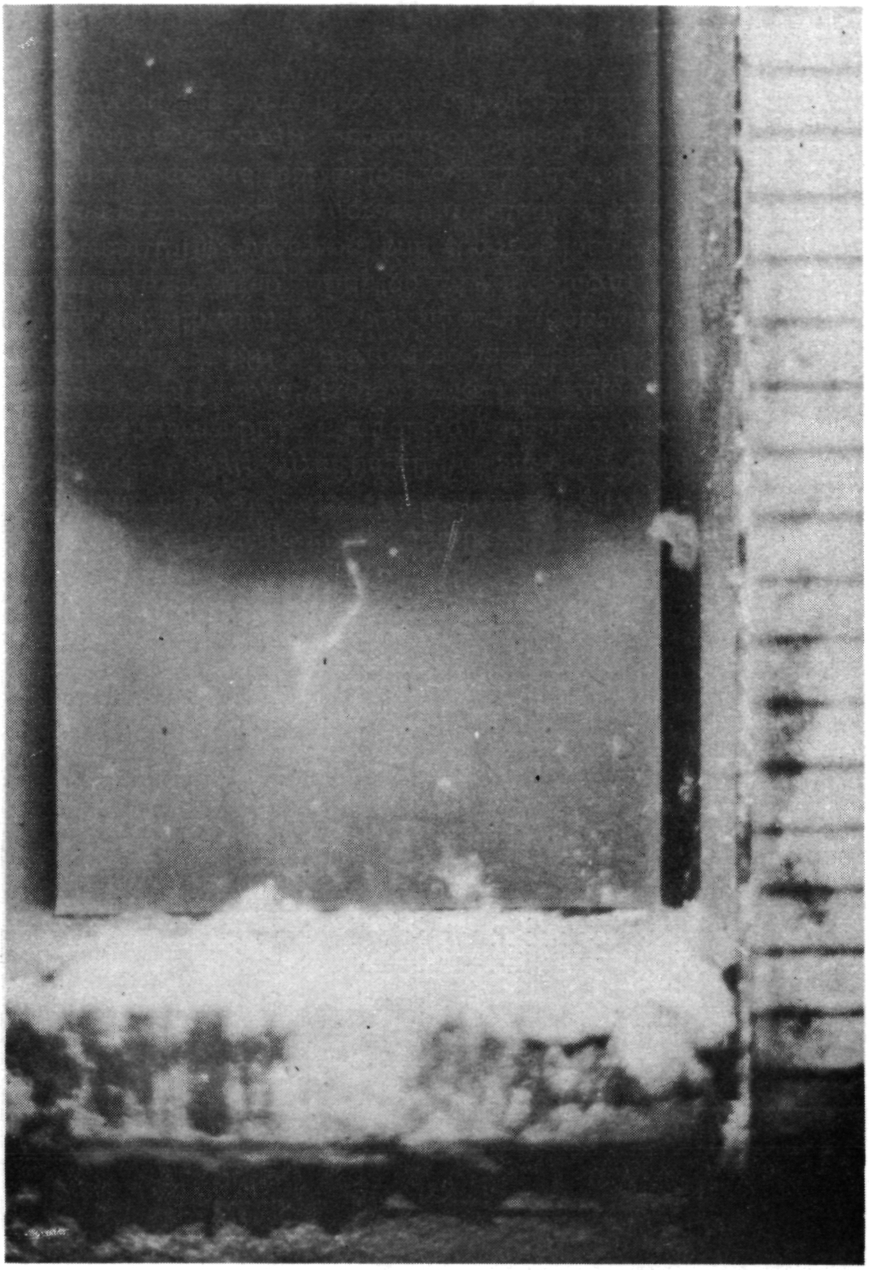

Figure 3. Solidification of cyclohexanol-fluorescein, GBS, November 1975.

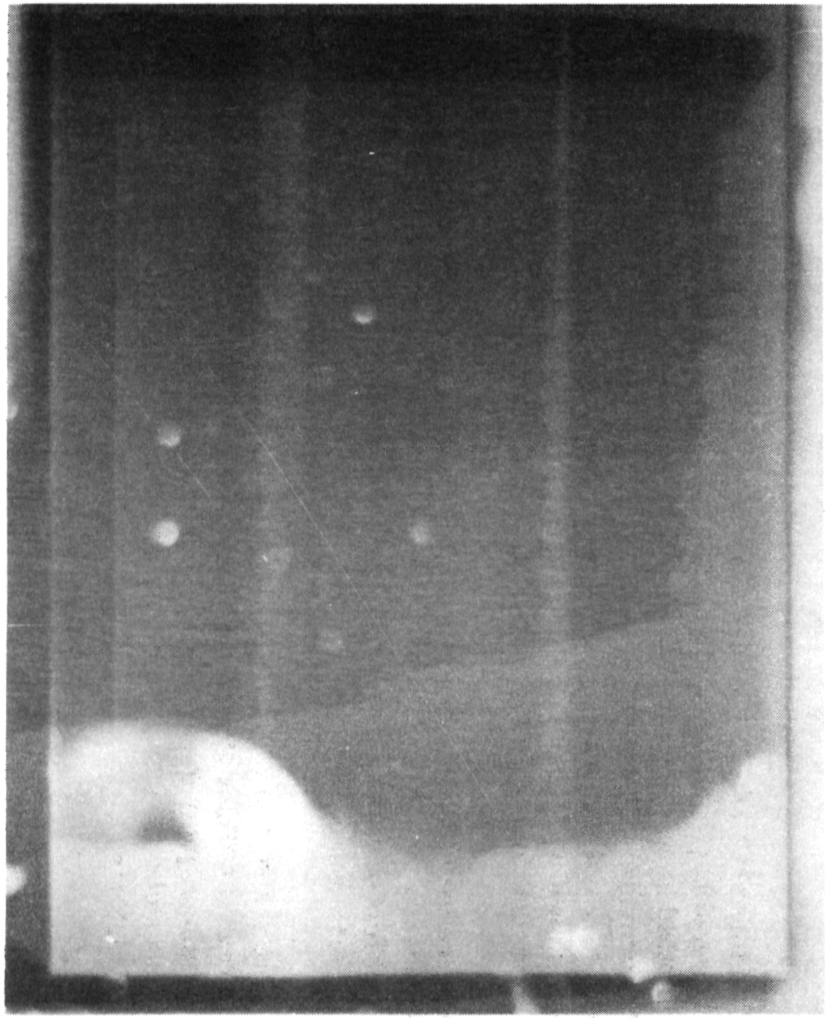

Figure 4. Solidification of cyclohexanol-fluorescein, horizontal all systems test, December 7, 1975.

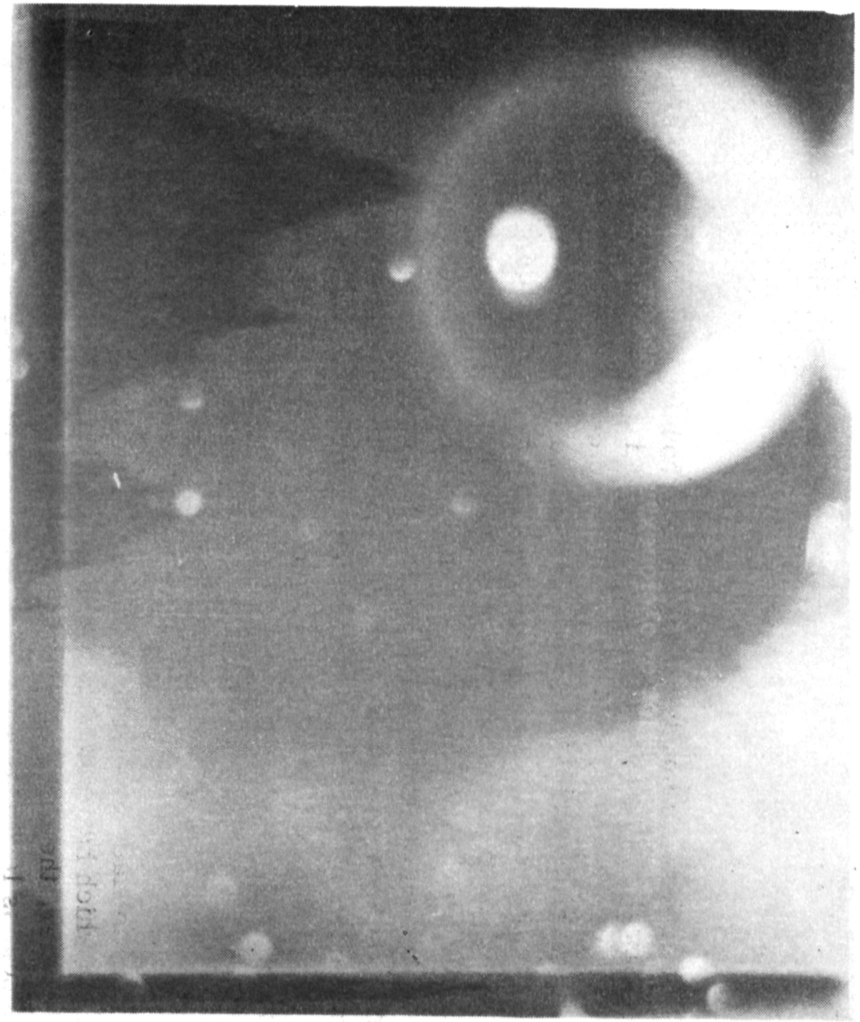

Figure 5. Solidification of cyclohexanol-fluorescein, vertical all systems test, December 9, 1975.

RESULTS

The expected flight data were to have consisted of a sequence of 220 pictures showing the progress of solidification and the buildup of the solute-enriched layer. The pictures were to be taken at 1 s intervals. Unfortunately, during flight, the government furnished (GFE) camera for this experiment malfunctioned. We obtained 4 test exposures before lift-off, followed by 13 exposures which seem to have been taken at the beginning of the low-gravity interval and 56 exposures which were probably taken toward the end of the cooling sequence. The first 14 low-gravity frames show that no crystallization had yet occurred; this is consistent with our ground-base results in which the first solid is observed at approximately 20 s. The 56 subsequent frames show approximately 6 mm of solid present; this solid continued to grow as the film sequence progressed. As is visible in Figure 6, the morphology of the solid cyclohexanol and the shape of the interface in the flight specimen are significantly different from those of the ground-base specimens.

The interface is seen to be much more irregular, there are several crystallites which have nucleated in the liquid ahead of the interface, the grain size is smaller, the grain morphology is columnar, and the green solute-enriched zone is less distinct. Upon receipt of the data, we began a series of experiments to determine to what extent these were genuinely gravity-related effects.

The telemetered thermal data portrayed a slightly different thermal history than had been obtained in the GBS, as shown in Figure 7 where the flight data are plotted as symbols and the GBS data as lines. It was thought that the different thermal history might be related to the low-gravity observations; thus, the cooling parameters were varied to match the flight data. The resulting curves are shown in Figure 8. Simulations performed with this thermal history were no different than in our previous attempts.

The relevant observations from pertinent tests are shown in Table 1. These tests were a systematic attempt to determine why the flight experiment displayed different growth morphology and nucleation characteristics. No explanation was found.

Table 1 also shows that we always observe a linear interface in GBS tests, whereas the flight experiment showed an irregular interface. By looking at the sequence of pictures, it can be seen that the irregularity of the interface in the flight specimen is caused by entrapment of crystals growing in the liquid ahead of the interface.

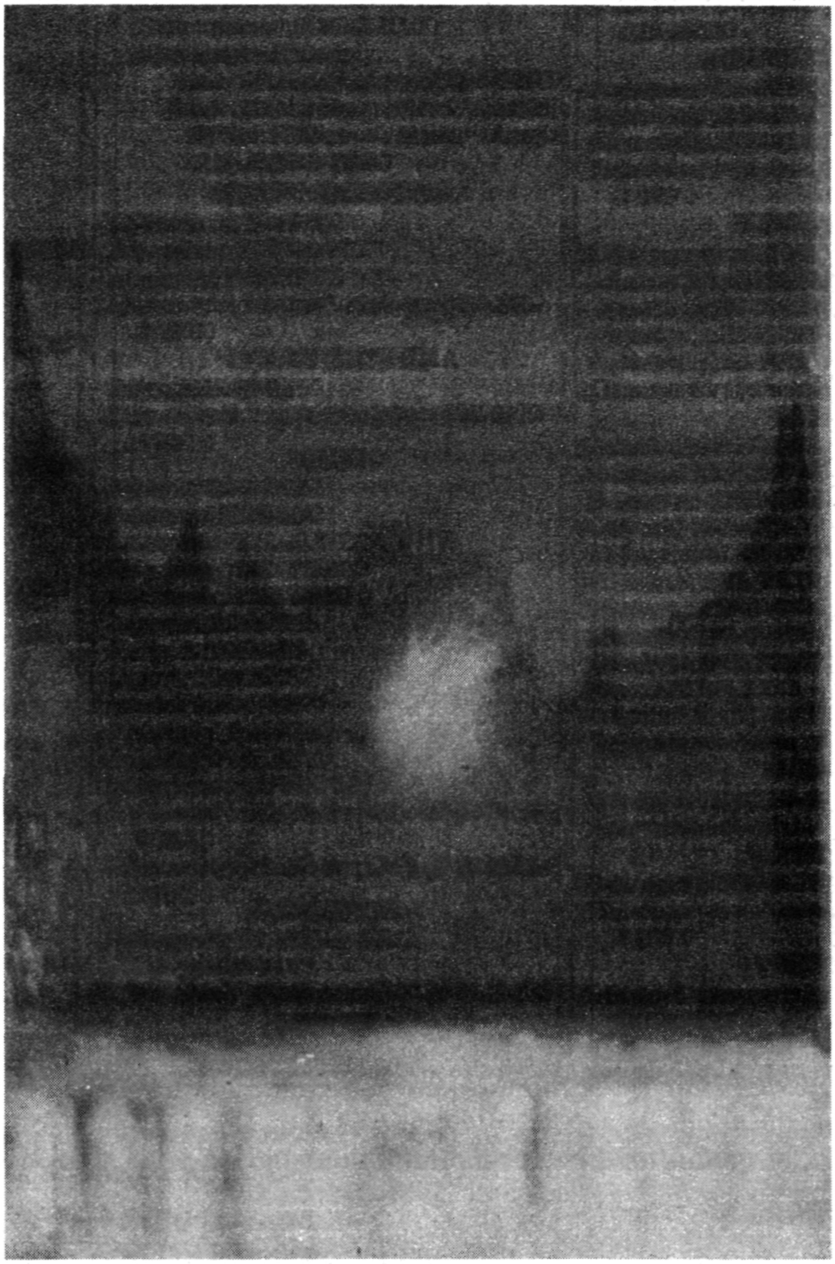

Figure 6. Solidification of cyclohexanol-fluorescein, flight test, December 11, 1975.

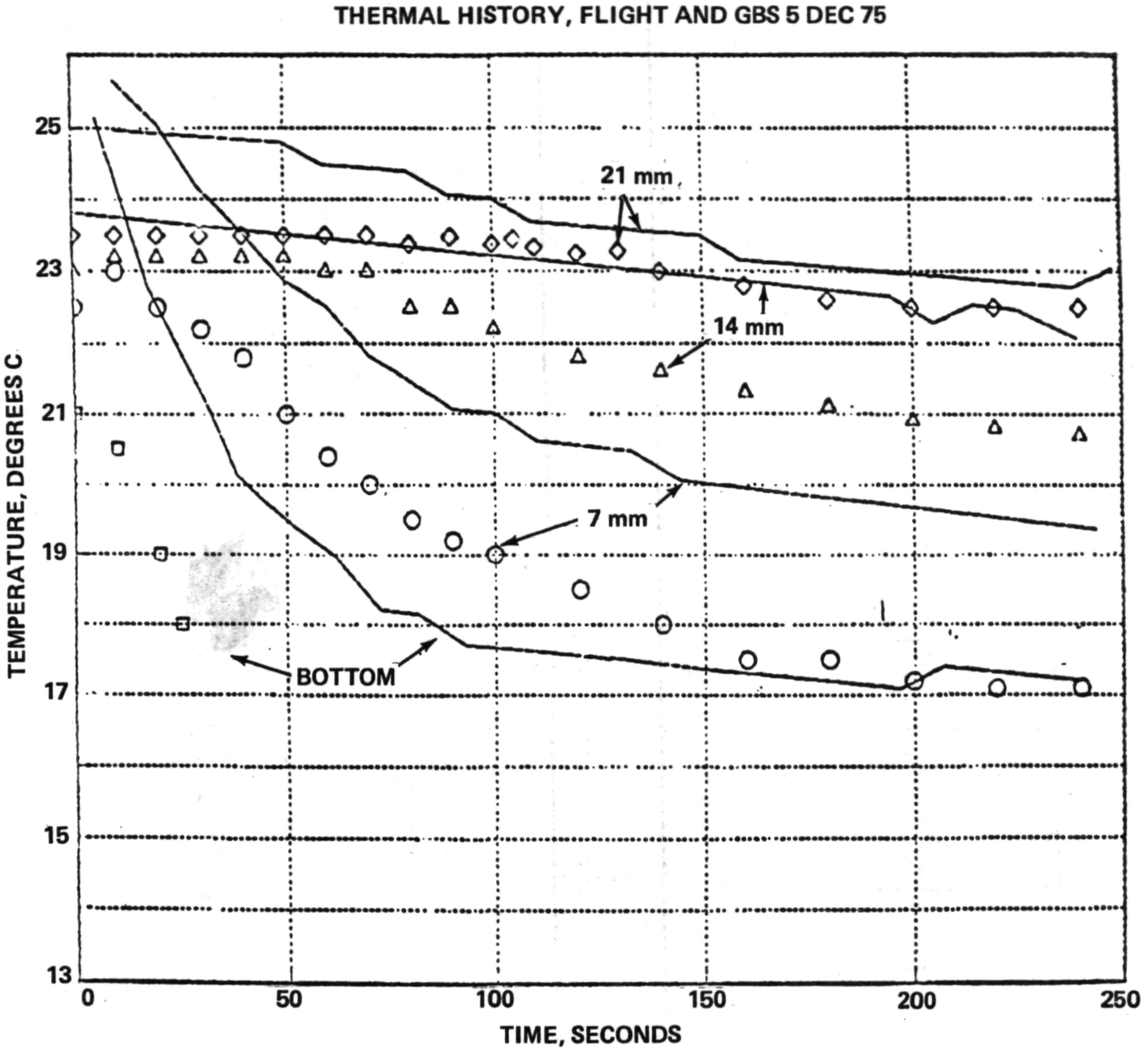

Figure 7. Thermal histories of a typical pre-flight GBS (solid lines) and the actual flight test (symbols).

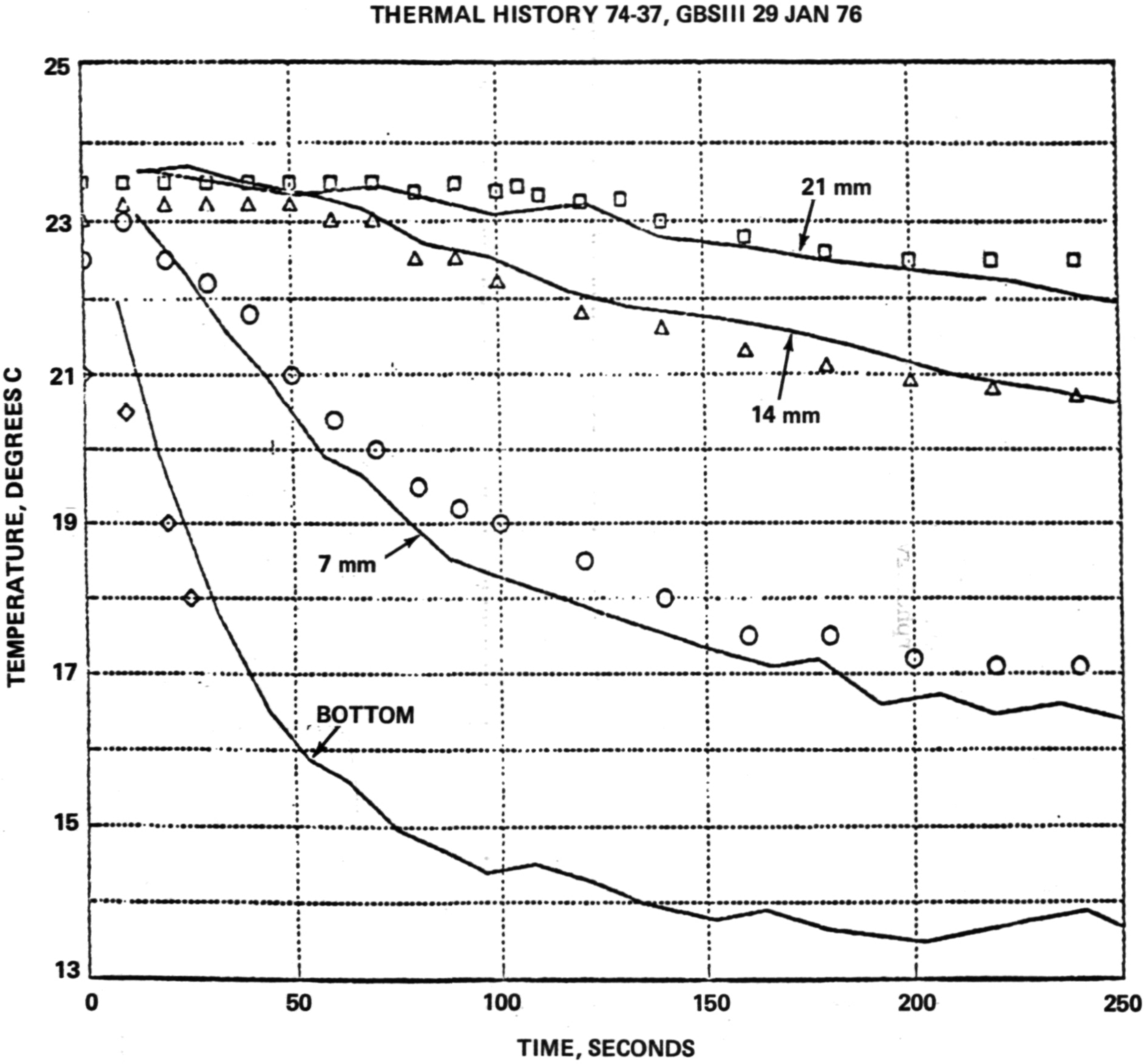

Figure 8. Thermal histories of a typical post-flight GBS (solid lines) and the actual flight test (symbols).

TABLE 1. TEST OBSERVATIONS

Test	Interface	Grain Size[a] (mm)	Grain Morphology	Nucleation[b] Events,		Green[c] Band (μm)	Bubbles
				$\underline{n}$	d_{max}(μm)		
GBS 5 Dec. 75	Linear	-	Columnar	-	-	-	None
Horiz 7 Dec. 75	Linear	2.5	Columnar	0	-	120-180	$\simeq$4 mm Dia.
Vert 9 Dec. 75	Linear	2	Columnar	3	450	70-140	None
Flight 11 Dec. 75	Irregular	1.2	Equiaxed	15	900	300-600	$\simeq$4 mm Dia.
GBS I 18 Dec. 75	Linear	3.5	Columnar	0	-	60-120	None
GBS II 18 Dec. 75	Linear	3.5	Columnar	0	-	60-120	None
GBS I 28 Jan. 76	Linear	2.5	Columnar	1	400	60-120	None
GBS II 28 Jan. 76	Linear	2	Columnar	0	-	60	None
GBS II 29 Jan. 76	Linear	2	Columnar	0	-	60-100	Simulated
GBS IV 29 Jan. 76	Linear	2.5	Columnar	1	600	75-150	Simulated

[a] In the case of Columnar Microstructures the smaller dimension (width) is reported

[b] Occuring in the liquid ahead of the interface during the 220s interval. The flight data was taken during a 60s interval. n is the total number of nucleii observed, d is the distance ahead of the interface.

[c] Visual observations from films, a dash indicates that no film record was made.

A columnar grain morphology was observed in all except the flight test. Likewise, nucleation ahead of the interface was rarely observed except in the flight test. Repeated nucleation ahead of the interface naturally leads to an equiaxed microstructure. The maximum distance from the interface to a nucleus in the liquid is also reported in Table 1. It is seen that the flight test showed nucleation at a much greater distance into the liquid than any of the GBS tests. It should be noted that the 15 nucleation events in the flight sample occurred during 56 s of observation, whereas all of the other tests were observed for a full 220 s.

The third column of Table 1 shows that the grain size obtained in the low-gravity test was significantly smaller than that obtained in the GBS tests.

In several tests, including the flight test, a 4 mm diameter bubble was present at the bottom of the cuvette. It was thought that the bubble might have sufficiently perturbed the heat and fluid flow to cause spurious results. To evaluate this possibility, a 4 mm diameter thin-walled glass sphere was installed in the bottom of the cuvette for several GBS tests. The presence of this simulated bubble had no significant effect on solidification, as shown in the last two rows of entries of Table 1. Further, the original bubble was present in the horizontal GBS and had no significant effect on solidification. Thus, the bubble did not affect the flight test results.

The average growth rate was deduced from measurements of the interface position as a function of time. Data from two GBS and the flight test are shown in Figure 9. Since the origin of time of the flight data cannot be located, it has been placed arbitrarily at t = 80 s. The slopes of the curves give average growth rates. In general, the GBS tests gave average growth rates of 20 to 30 μm/s, whereas the flight test showed a growth rate of 60 μm/s. This is simply explained as being due to nucleation ahead of the interface. Those nuclei which are situated ahead of the interface grow in all directions. If the dendrite tip velocity remains the same as that in columnar growth, then the average macroscopic interface velocity would be twice as high. Thus, this observation is taken as indicating that the dendrite tip velocity is practically constant in all of these tests.

The sixth column of Table 1 lists visual observations of the width of the darker green solute-enriched layer which is seen ahead of the interface. These values were obtained by looking at the original films on a lightbox and visually estimating the width of the deeper green layer, using a 7X magnifier and reticule. The reticule was calibrated in units of 0.1 mm, and the film magnification was typically 1.6X; thus, the smallest division represented approximately 60 μm.

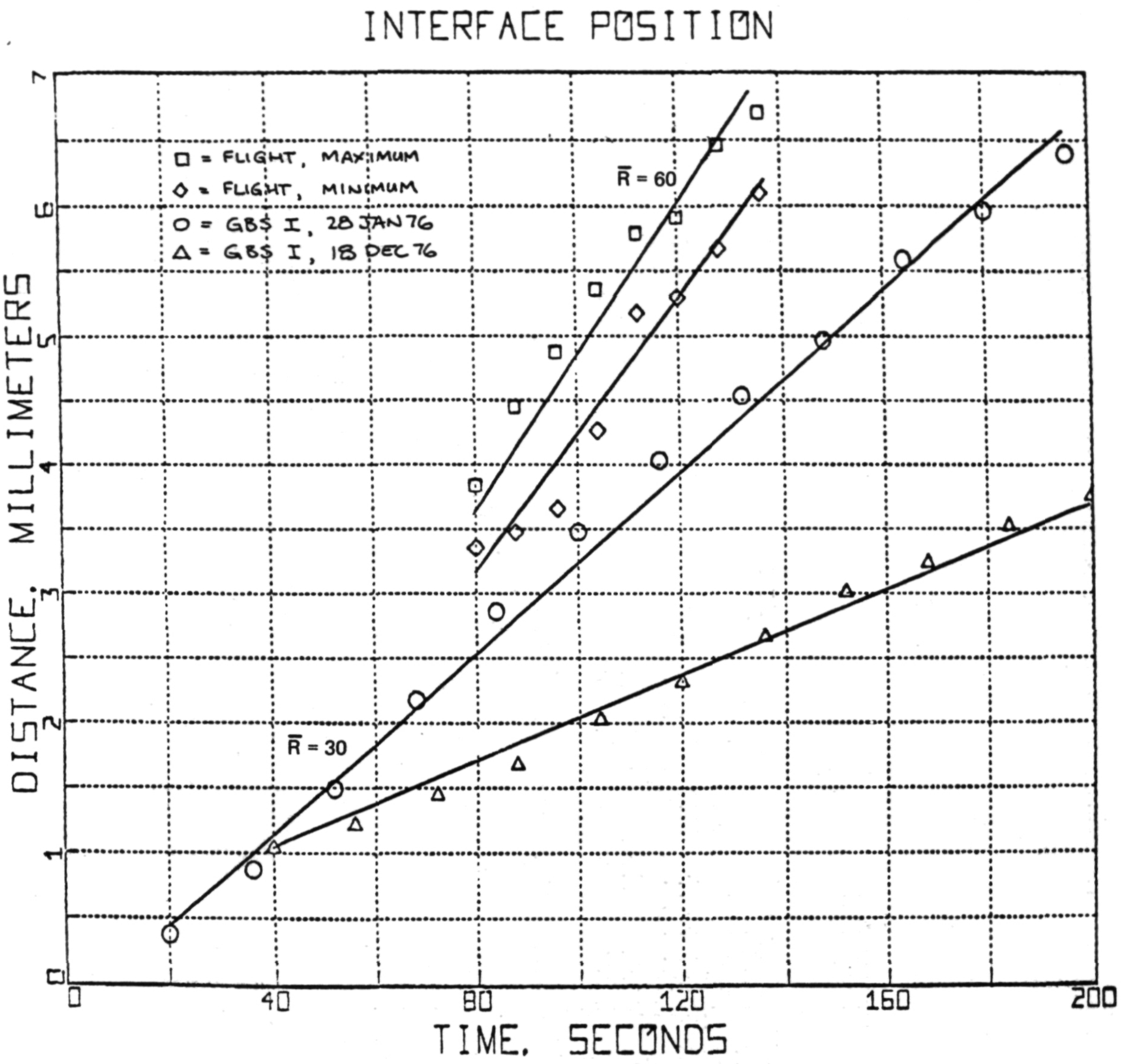

Figure 9. Interface position as a function of time for two GBS tests and the flight test.

In general, the green band was observed to be approximately 60 to 120 μm wide, but in the flight test it appeared to be larger by a factor of 5. We attempted to quantify this subjective observation.

Several of the films were analyzed using a Joyce-Lobel scanning microdensitometer. The instrument was set up to traverse from the crystal into the liquid. The spot size was approximately 15 μm on the film to be measured; this corresponds to approximately 10 μm linear distance on the actual specimen. Traverses were made using a green filter, thus only the green emulsion of the film was scanned, or without a filter in which case all three emulsion layers contributed to the observed density. Figure 10 shows a trace obtained from frame 674-1 of the vertical test in which a pronounced green layer was visible to the eye. No evidence of the solute-enriched zone is present in the trace. Figure 11 shows a similar trace which was made through a grain boundary groove in which a distinct, thick green band was visible. Again, no evidence for the green band was found. In no case were we able to make an objective, repeatable measure of the width of the green band. The human eye is unusually sensitive to color and can detect in the region of 10^7 shades of color; a microdensitometer does not approach this sensitivity. This is a possible explanation for this problem. However, it is well known that a human observer is highly prone to suggestion and, under difficult observational conditions, the eye often detects nonexistent objects. Numerous attempts were made to confirm these observations by impartial observers, and in all cases the observers claim to have seen the green layer. If the darker green layer is, in fact, the solute-enriched zone ahead of the solid-liquid interface, it can be concluded that it is wider in the flight specimen.

DISCUSSION

The darker green layer ahead of the solid-liquid interface is presumably the solute-rich zone, which appears to become wider in the flight specimen. Because of inadequate sensitivity of a Joyce-Lobel scanning microdensitometer, the detection of this zone and accurate measurement of its thickness was not possible.

Parasitic nucleation, or nucleation ahead of the interface, was the key feature of this experiment. This led to an irregular interface, a small grain size, an equiaxed grain morphology, and a large average macroscopic growth rate. This is in contrast to terrestrial experiments in which nucleation ahead of the interface was rarely observed and in which we observed a linear interface,

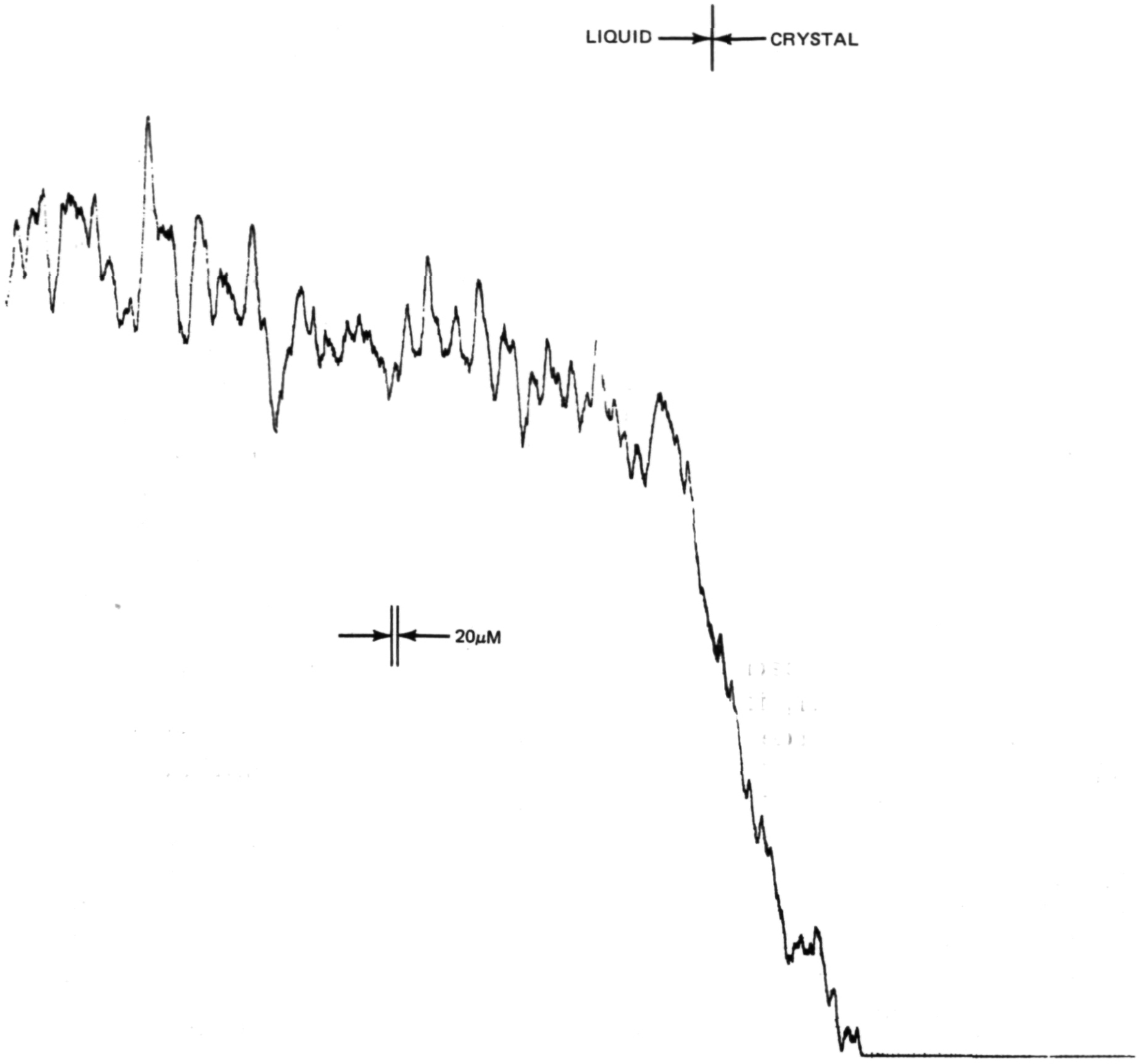

Figure 10. Microdensitometer trace from frame 674-1, vertical test, flat position of interface [optical density (ordinate) is plotted against distance (abscissa)].

larger grain size, columnar morphology, and a smaller growth rate. The terrestrial experiments were performed with three different orientations of the gravitational vector.

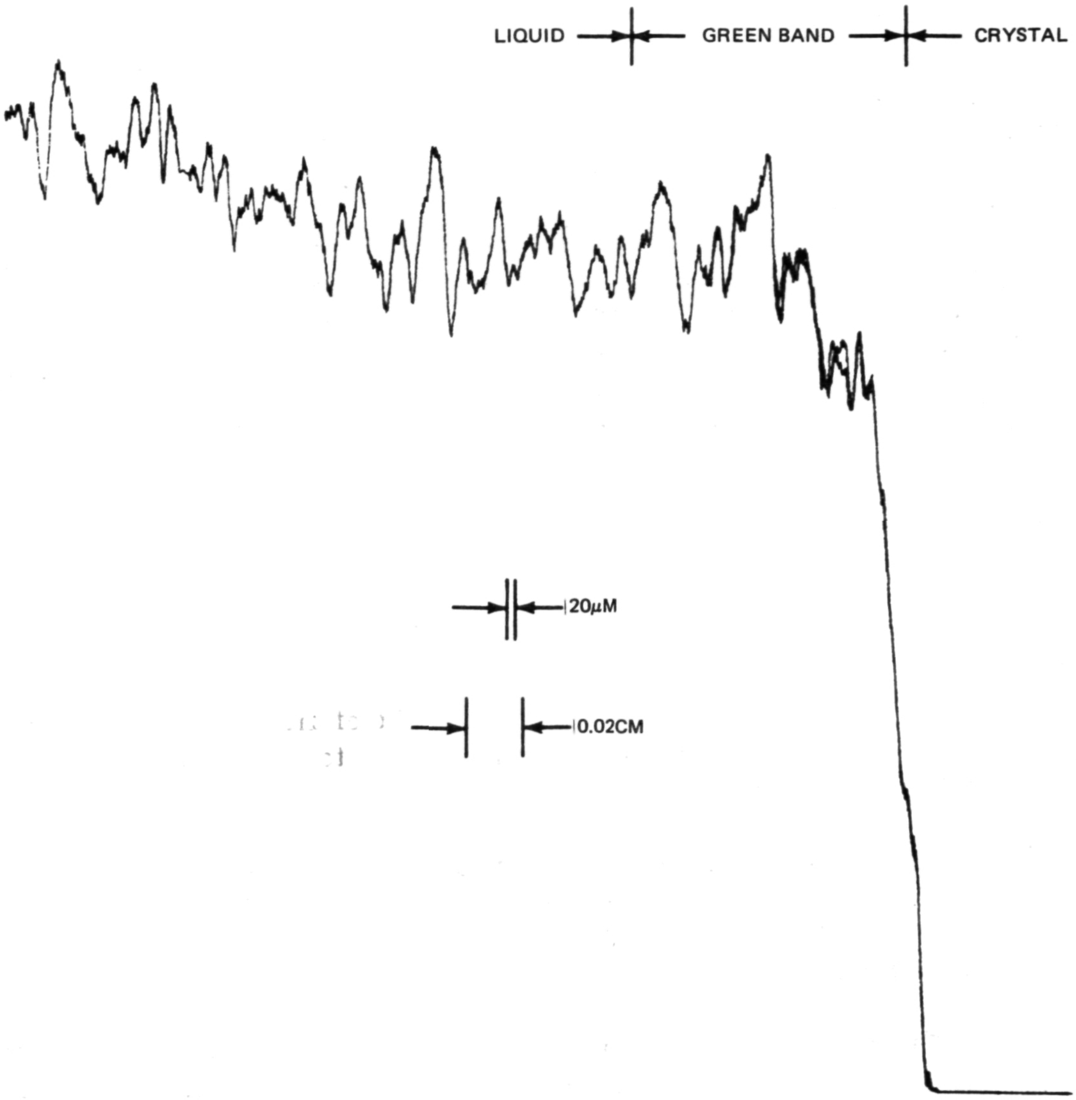

Figure 11. Microdensitometer trace from frame 674-1, vertical test grain boundary groove [optical density (ordinate) is plotted against distance (abscissa)].

It is believed that all of the possible experimental reasons that this might be a spurious observation were eliminated. The most obvious possibility was a different thermal history between GBS and flight; this was quickly eliminated.[1] The next possibility considered was an impurity effect, but the same cuvette, unopened, was used for the horizontal, vertical, flight, and January 28 tests so

---

[1] Latest telemetry data, provided by MSFC, show significantly different thermal histories (see the appendix).

that contamination can also be ruled out. The perturbation introduced by the bubble was shown to be minimal by comparison to the December 7 flight and January 29 tests. Bench tests to determine whether launch-induced fluid motion could lead to parasitic nucleation were negative; it was not possible to cause nucleation ahead of the interface even by violently shaking the cuvette assembly for 1 min before the bench test. Another possibility is that the solution was not adequately superheated before launch; this could result in the presence of numerous small ordered islands that would act as nuclei. The rocket was kept in a thermostatically controlled environment of 23.3 to 23.6°C overnight before launch, which is approximately 1.5°C above the liquid's temperature. Some ordered islands might have survived remelting, presumably because of the low superheating, might not have settled, and then acted as nuclei during cooling. Thus, the formation of parasitic equiaxed grains, observed ahead of the solid-liquid interface in the flight specimen, could be explained.

CONCLUSIONS

1. The darker green layer observed ahead of the solid-liquid interface is most likely the solute-enriched zone and appears to become wider in the flight specimen.

2. The irregular shape of the interface in the flight specimen, the smaller grain size, the equiaxed grain morphology, and the larger average macroscopic growth rate are attributed to parasitic nucleation ahead of the solid-liquid interface.

3. The formation of parasitic equiaxed grains ahead of the solid-liquid interface in the flight specimen may be attributed to ordered islands within the liquid, which survived remelting because of the low degree of superheating (approximately 1.5°C), and did not settle because of reduced gravity and acted as nuclei during cooling.

REFERENCES

1. Proc. Third Space Processing Symposium, Skylab Results, Vols. 1 and 2. National Aeronautics and Space Administration, George C. Marshall Space Flight Center, Alabama, June 1974.

2. Papazian, J. M. and Larson, D. J. Jr.: Research On Metal Solidification In Zero-G State. Grumman Aerospace Corporation, Report RE-505, July 1975.

3. Jackson, K. A.; Hunt, J. D.; Uhlman, D. R.; and Seward, T. P.: Trans. TMS-AIME 236, vol. 149, 1966.

4. Papazian, J. M.: Experiment Implementation and Requirements Plan for 74-37. Submitted to MSFC, July 1975.

APPENDIX

On March 5, 1976, we received revised telemetry data from MSFC. The new data contains revised values for the bottom thermistor readings; these are plotted in Figure A-1 along with the thermal data from GBS II of January 28, 1976. Note that the new telemetry data portray a flight thermal history that is radically different from any of the previous GBS tests. It is thought that this different thermal history may be, at least in part, responsible for the anomalous flight observations.

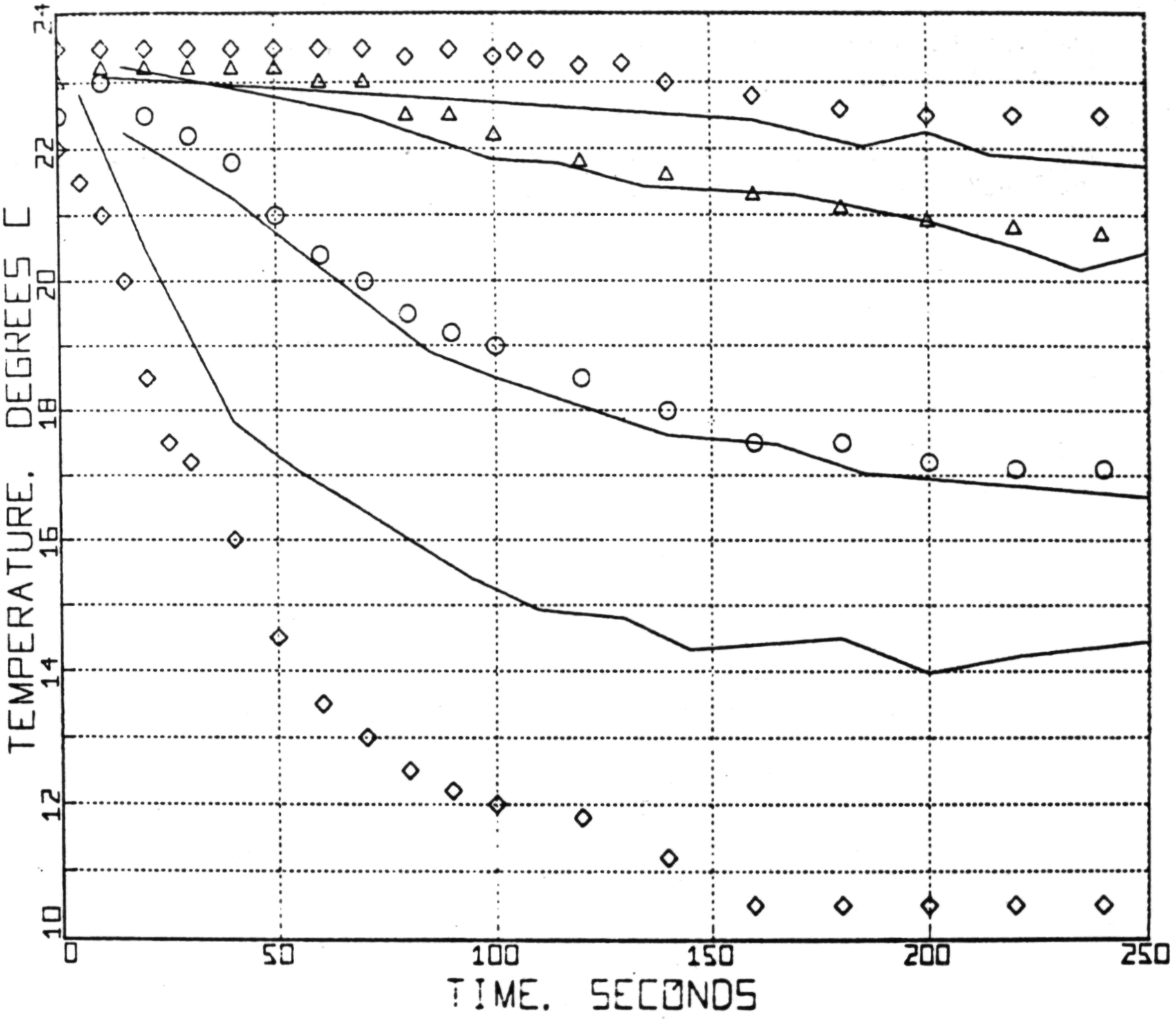

Figure A-1. Revised thermal history of the actual flight test (symbols).

CHAPTER IX

PREPARATION OF A SPECIAL ALLOY UNDER ZERO-GRAVITY FOR MAGNETIC HARD SUPERCONDUCTORS

Experiment 74-63

By

Werner Heye and Michael Klemm
Technical University
Clausthal, West Germany

ABSTRACT

The purpose of this experiment was the production of a second order or third order superconductor in the form of a mixture of a first order superconductor (lead) and a normal electrical material (silver). In this way, a PbAgBaO alloy was prepared by known powder metallurgical techniques. Avoiding different influences, such as considerable differences in densities of the components, the melting and solidification of this alloy was carried out under zero gravity. The alloy could be drawn to wires in the range of 50 μm diameter due to use of ductile metals. As a result of the BaO addition as a dispersion hardening element, the lead would be strain hardened so strong that an in situ deformation of the silver particles was reached. The small silver particles were finely dispersed with a grain size of $\leq 2\ \mu$m, while the original grain size was approximately 40 μm in the molten body. Smaller grain sizes could not be produced.

In spite of this grain size a transition was observed from the first order superconductor to a second order superconductor of the flight sample only. A splitting of the critical magnetic field H_c into a lower field H_{c1} and an upper field H_{c2} took place marking the superconducting behavior of this alloy.

BACKGROUND

The known second order superconductors are distinguished primarily by their almost undeformable state, e.g., intermetallic compounds such as Nb_3Sn. In search of superconductors ductile materials must be found where technical manufacturing will be interesting. By combining those metals, the production of a mixed state is possible and necessary. Within this state a first order superconductor must be combined with a normal conducting material. Table 1 is a summary of some alloys in a mixed state according to Kurz and Sahm.

TABLE 1. TABULAR SUMMARY OF SOME ALLOYS IN A MIXED STATE ACCORDING TO KURZ AND SAHM

SYSTEM MATRIX	SYSTEM 2. PHASE	TYP	ELEKTRISCHE EIGENSCHAFT MATRIX	ELEKTRISCHE EIGENSCHAFT 2. PHASE	BEOBACHTUNGEN UNTERSUCHTE EFFEKTE	LITERATUR
Sn	Zn	I	S	N	$T_c = T_c(\lambda)$: PROXIMITY EFFEKT	LUTES U. CLAYTON 1966
Cd	Sn	I	N	S	PROXIMITY EFFEKT	DOBROSAVLJEVIC ET AL., 1970
Cu	Pb	f	N	S	$H_c = H_c(\xi)$: PROXIMITY EFFEKT	LIVINGSTON, 1968
Pb	Cd	I	S	N	OBERFLÄCHEN-SUPRALEITUNG $H_{C3} > H_{C2}$	GOODFELLOW U. RHODES, 1970
In	In_2Bi	I	S	N		
Bi_2Tl	Bi	u	S	N		
Hg	Tl	*)	S	N		
Nb	Th	r	S	S	TYP I - II ÜBERGANG	CLINE ET AL., 1963
Pb	Bi		S	N		LEVY ET AL., 1966
Sb	Sb_2Tl		N	S		
In	Sn		S	S		
Pb	$AuPb_2$	I	S	S		
Pb	Sn	I	S	S		YUE ET AL., 1973

The essential supposition is that both phases exist parallel within dimensions at least equal to the mean free length of the path of electrons for cross direction of the electrical flux. This state contains thin fibers or small particles with diameters or thicknesses of approximately 100 Å.

Those materials can be divided into two categories. The first can be drawn down to wires and fibers with diameters in the range of 100 to 50 μm and 1000 to 100 Å, respectively, by conventional techniques. For the second, special methods are required because of their brittleness. As a result the first order superconductor changes to a second order superconductor because a magnetic field will penetrate the thin normal conducting areas uniformly and will also enter to some extent into the surrounding material. This field thereby stabilizes the superconducting state magnetically.

CHOICE OF SUITABLE METALS

When looking for proper materials the primary problem is to find metals with equal mechanical strength properties for the following deformation to wires and fibers, respectively. Taking superconducting lead (the best first order superconductor) and normal conducting silver (one of the best normal conducting materials) by the previously described method, the first order superconductor can be concluded to change into a second order superconductor (Fig. 1).

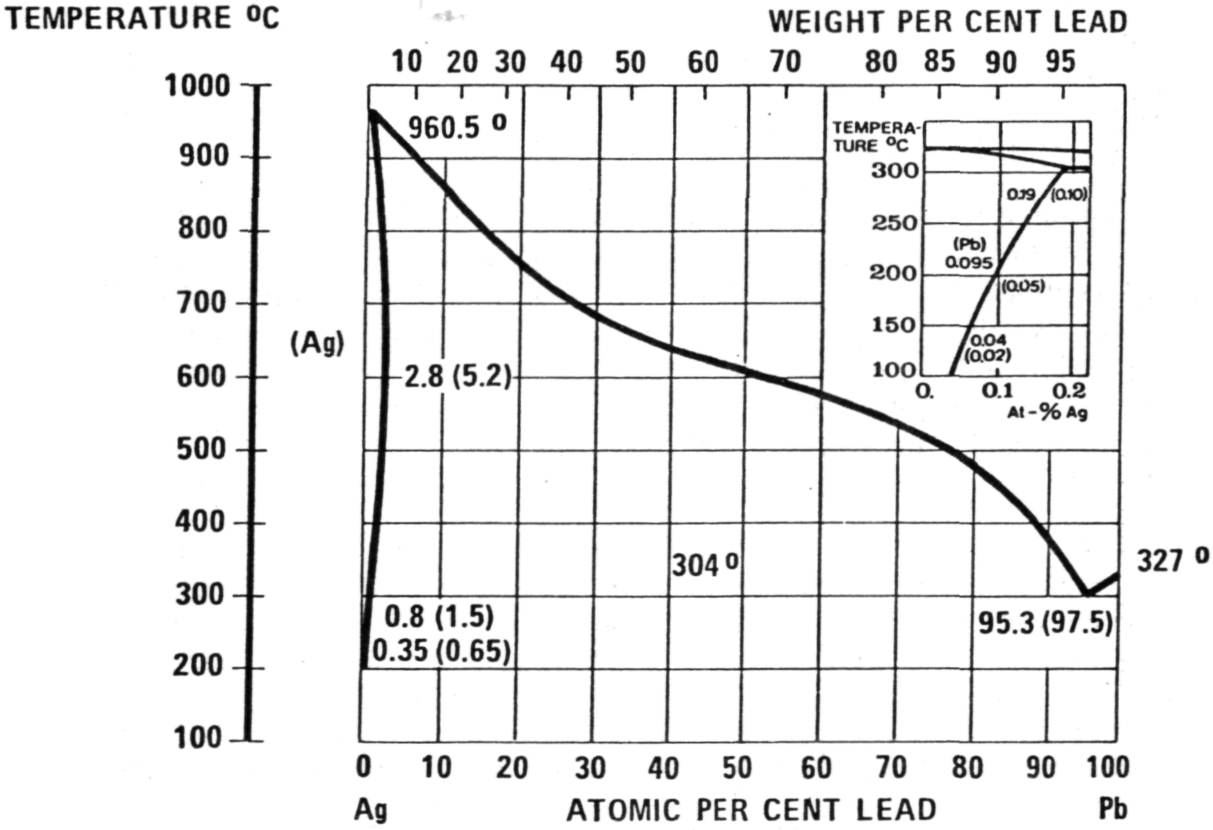

Figure 1. Constitution diagram of lead-silver according to Hansen.

However, in such an alloy (Pb-Ag), the differences of strength allow only deformation of the lead and not of the silver. Because lead has much smaller strength and strain hardening properties than silver, lead must be hardened by proper means without changing the electrical behavior significantly. For this purpose hardening by dispersion of a small amount of a large volume addition is considered to be the only possibility. In that case deformation of the silver may be achieved within the lead because the strength increases and apparently there is a remarkable strain hardening of the lead. This cold working of the lead can be explained by the mechanism of Orowan (Fig. 2).

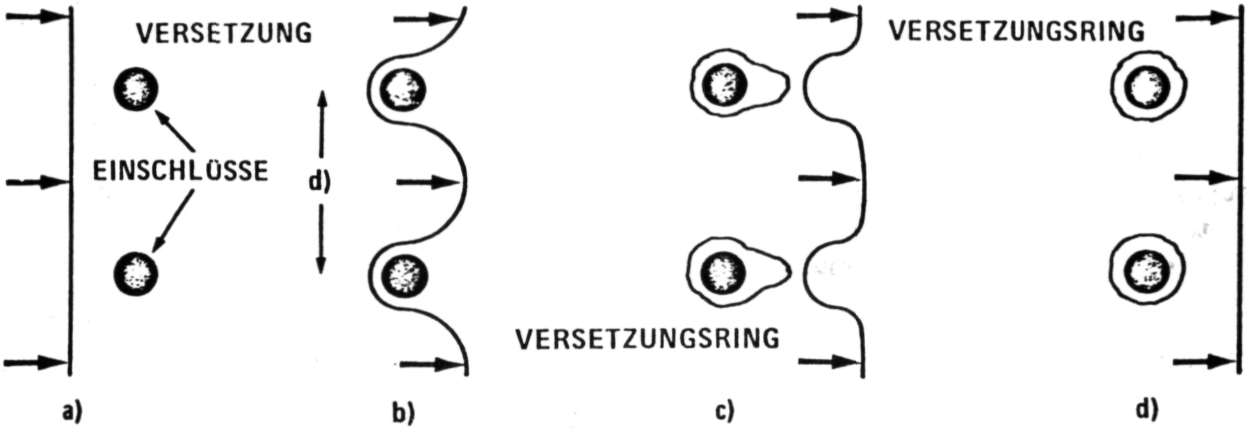

Figure 2. Strain hardening mechanism according to Orowan.

A proper addition for this alloy is BaO because the material is not soluble in lead or in silver, but has a large atom volume. In this manner we obtain a heterogenous alloy with three components for which the composition is: 89 vol. % lead, 10 vol. % silver, and 1 vol. % barium oxide.

PREPARATION OF A PbAgBaO ALLOY

This alloy shall be prepared by the known powder metallurgical method because of the considerable (2:1) difference of densities between Pb, Ag, and BaO. Therefore, it is not possible to produce the alloy without segregation by methods of metal melting under terrestrial gravity conditions. The BaO particles will not be uniformly and finely dispersed and will float to the upper regions of the molten sample. The remainder will be separated in the form of slag consisting of BaO and PbO. Even a very short solidification time cannot prevent segregation.

Preparing the alloy by powder metallurgy only does not lead to the success desired because the mechanical qualities become degraded by pores and cracks. This process is less deformable to wires in the requisite dimensions. For these reasons it was proposed to melt the alloy under zero gravity, reducing these problems to a negligible significance.

To prepare the alloy by powder metallurgy the Pb, Ag, and BaO powders are mixed in a ball mill, then compressed on a press at a pressure of 2000 kN. These ingots are sintered 2 h at 220°C under vacuum. The second compression takes place on an extrusion press at room temperature, where the slugs are deformed to rods with 13.1 mm diameter (Fig. 3).

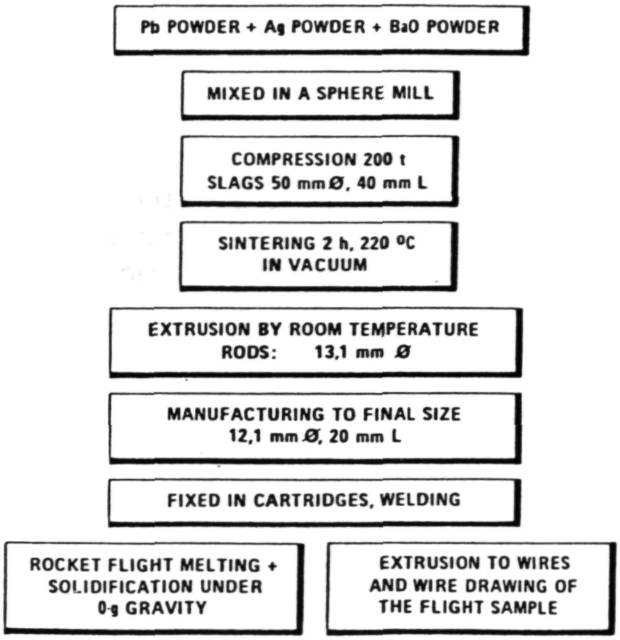

Figure 3. Preparing and manufacturing of the PbAgBaO alloy.

The rod material is sawed in plane parallel pieces to a length of 20 mm. These samples are then manufactured down to their final size with three small slots left in the surface to accommodate the thermal expansion. After a cleaning process the samples are placed in the NASA cartridges, and the bottom is fixed by point welding the cartridges (Fig. 4).

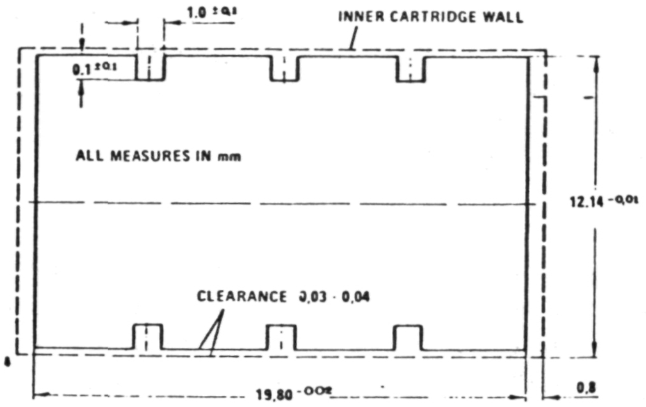

Figure 4. Sample and cartridge measurements according to Erno.

MELTING AND COOLING CONDITIONS, FLIGHT CONDITIONS

The composition of the compound is almost the eutectic composition; therefore, the basic possibility exists of reaching a directional eutectic solidification when the proper cooling rate or the gradient of cooling temperature can be adjusted. The primary advantage of such a solidification is that the silver particles can be precipitated as small parallel fibers. The desired fiber dimensions can be reached earlier than by normal solidification (Fig. 1). The following wire drawing process can be stopped at larger diameters of the wires because the deformed fibers occur earlier in the dimensions of the mean free path of length of electrons.

The rocket used for this experiment was the Black Brant VC, the flight profile of which is shown in Figure 5. The NASA furnace is shown in Figure 6.

To ensure the cartridge and the sample material are suitable for heating rates of 200°C/min and cooling rates of 600°C/min, two thermal tests have been performed to study the behavior of cartridge and sample material and the deformation of the cartridge by thermal expansion of the sample material (Fig. 7). The temperature profile of the cartridge during the thermal test was in accordance with the profile (Fig. 8).

The ideal schedule of the rocket flight corresponding to the conditions of NASA is presented in Figure 9. Accordingly, a process time of 260 s is possible without heating and cooling time. Results from the NASA thermal tests are presented in Figure 10. The process time is shortened because the heating and

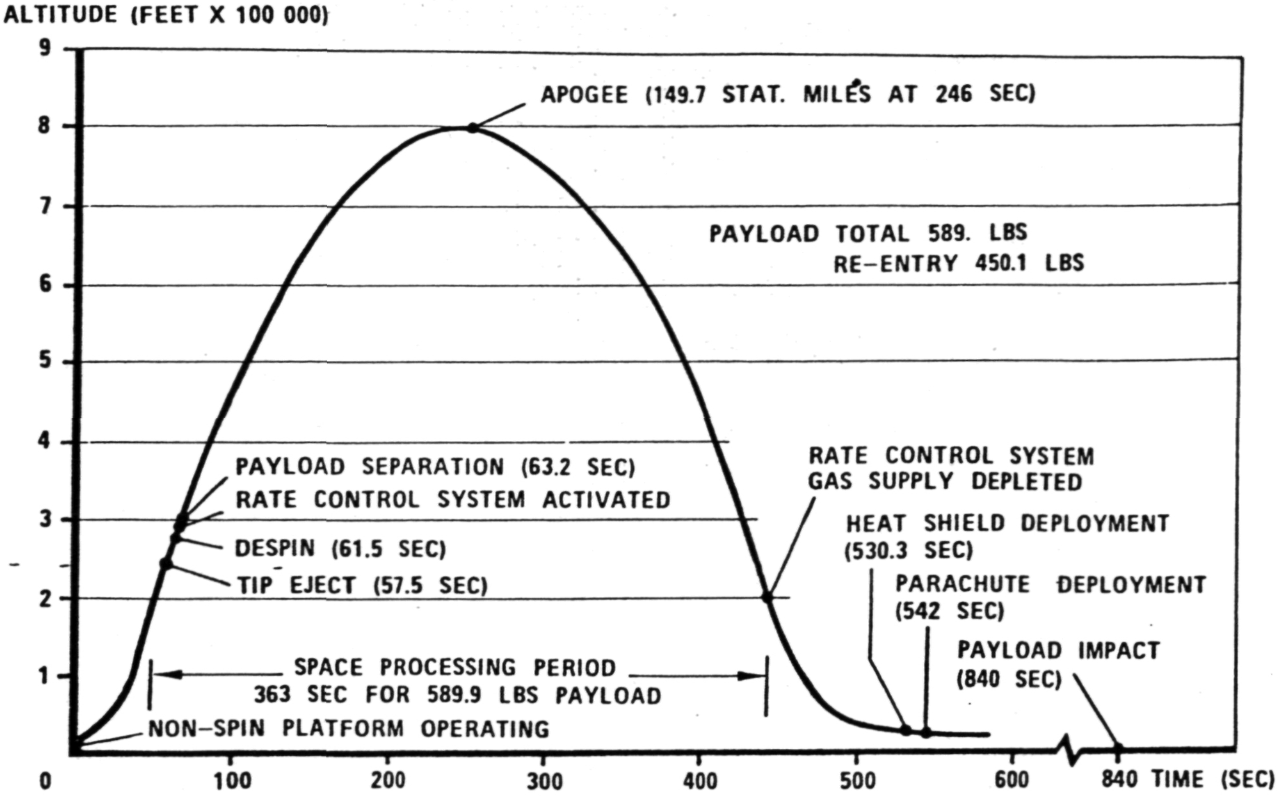

Figure 5. Black Brant sounding rocket flight profile.

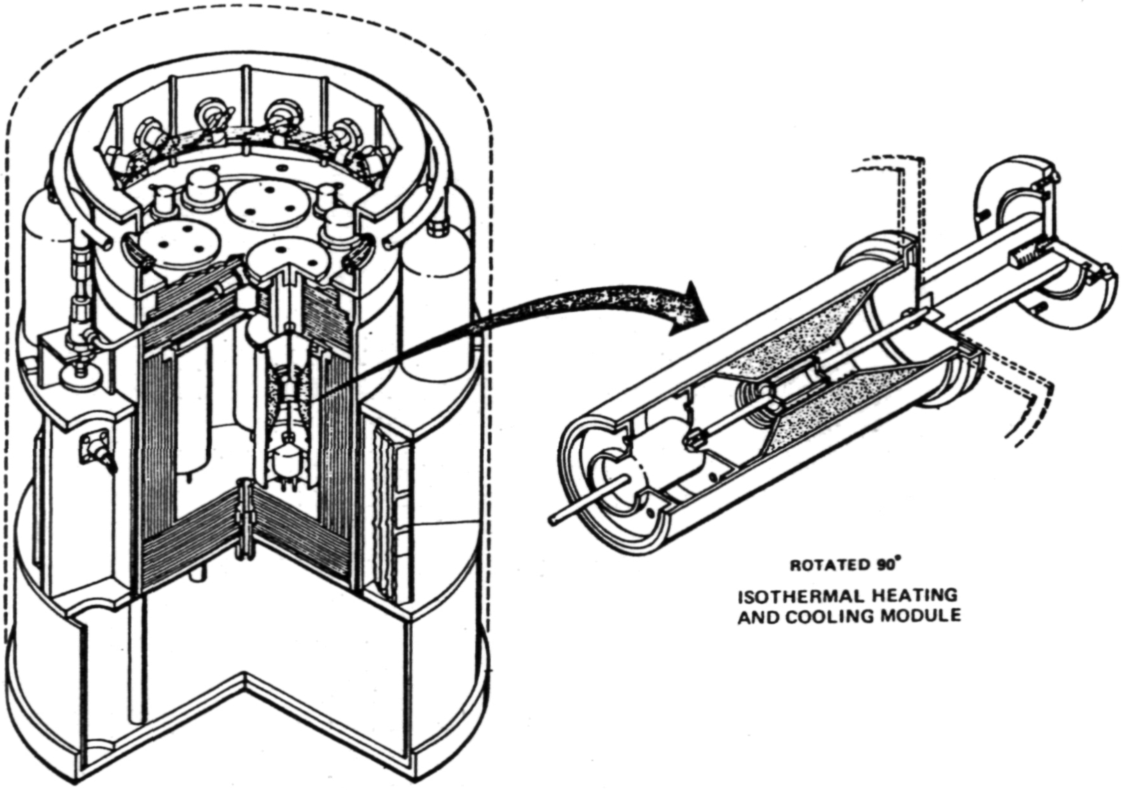

Figure 6. General purpose rocket furnace.

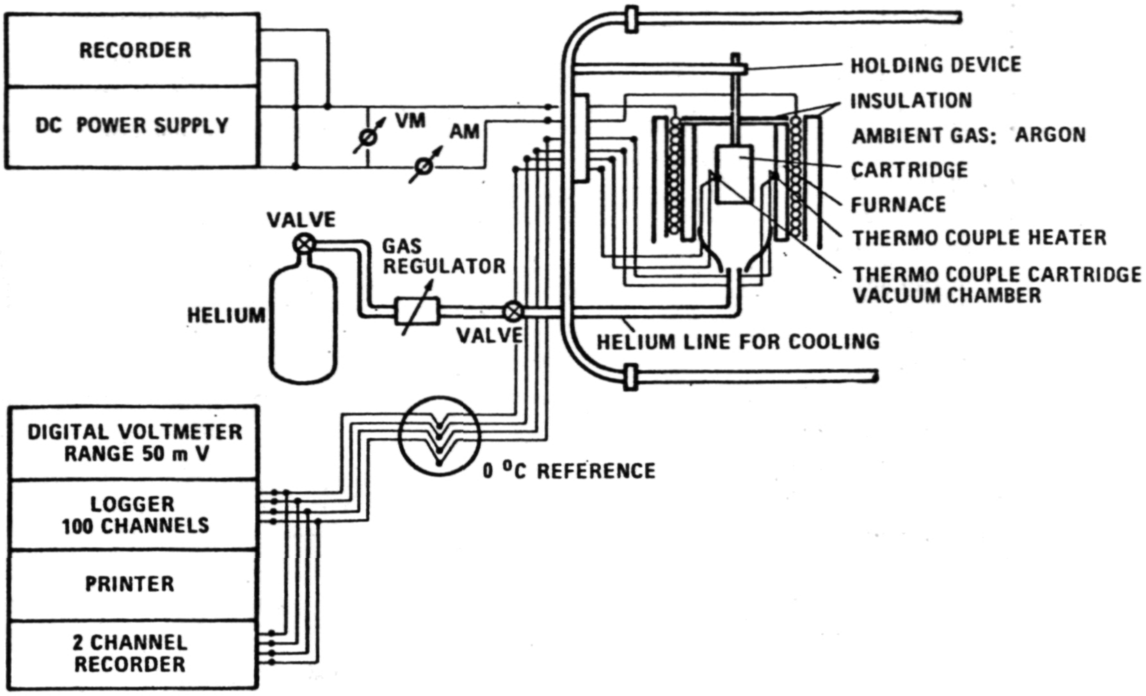

Figure 7. Facility for thermal test.

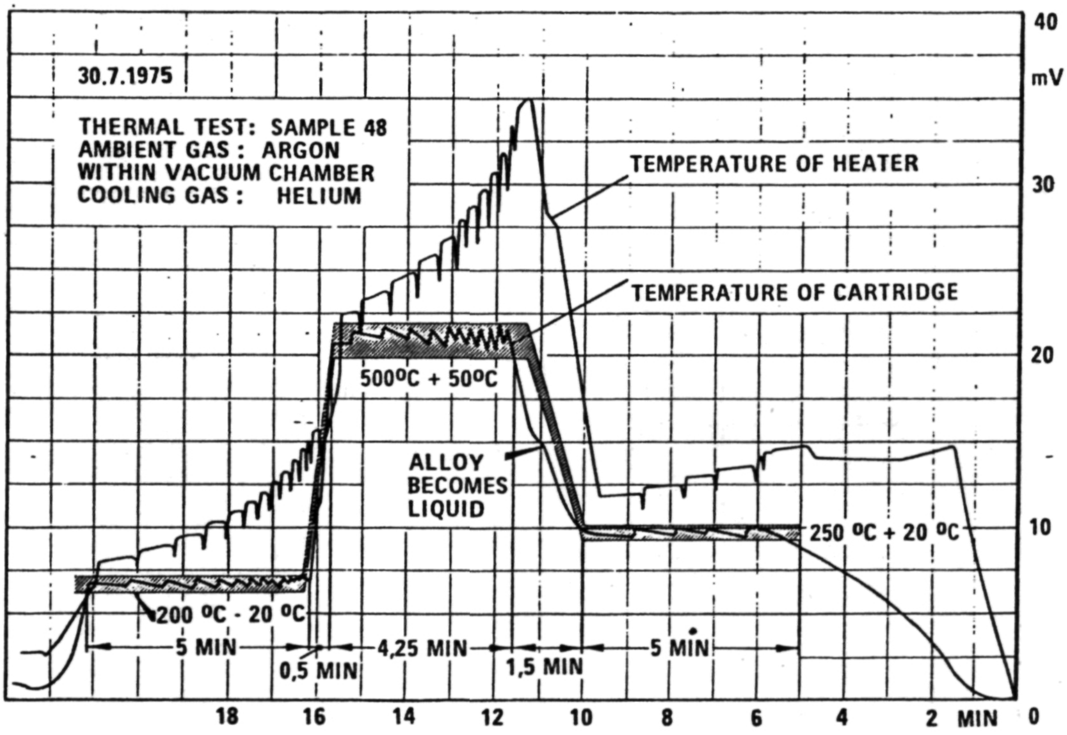

Figure 8. Temperature profile (ground test, Erno).

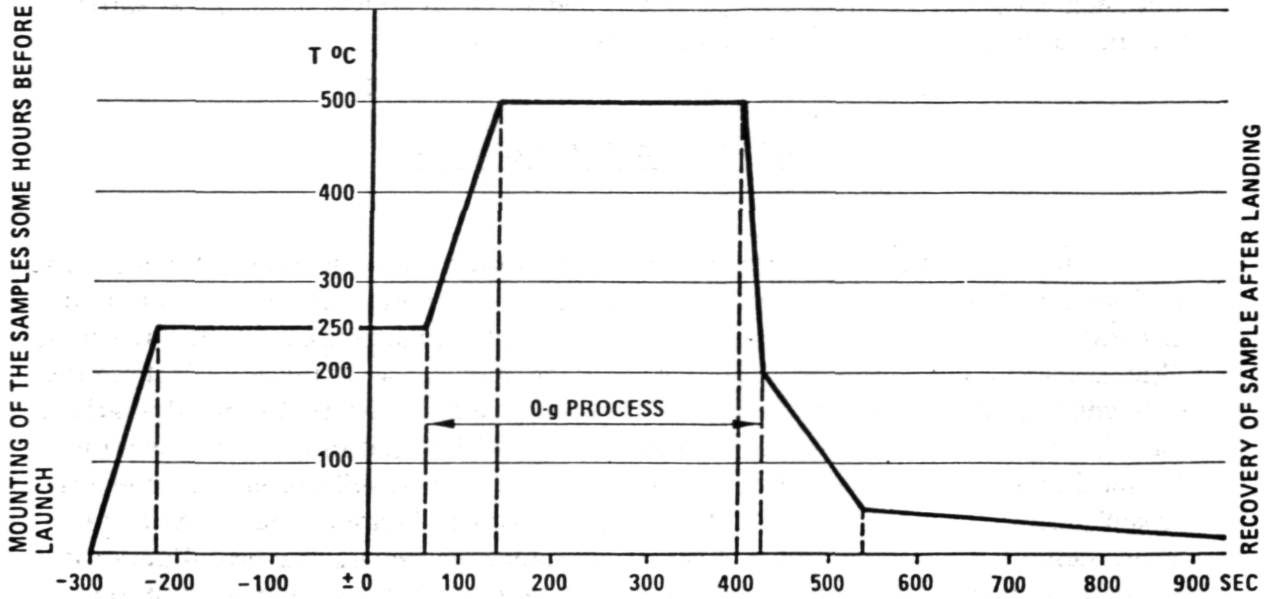

Figure 9. Operational plan (ideal) according to Erno.

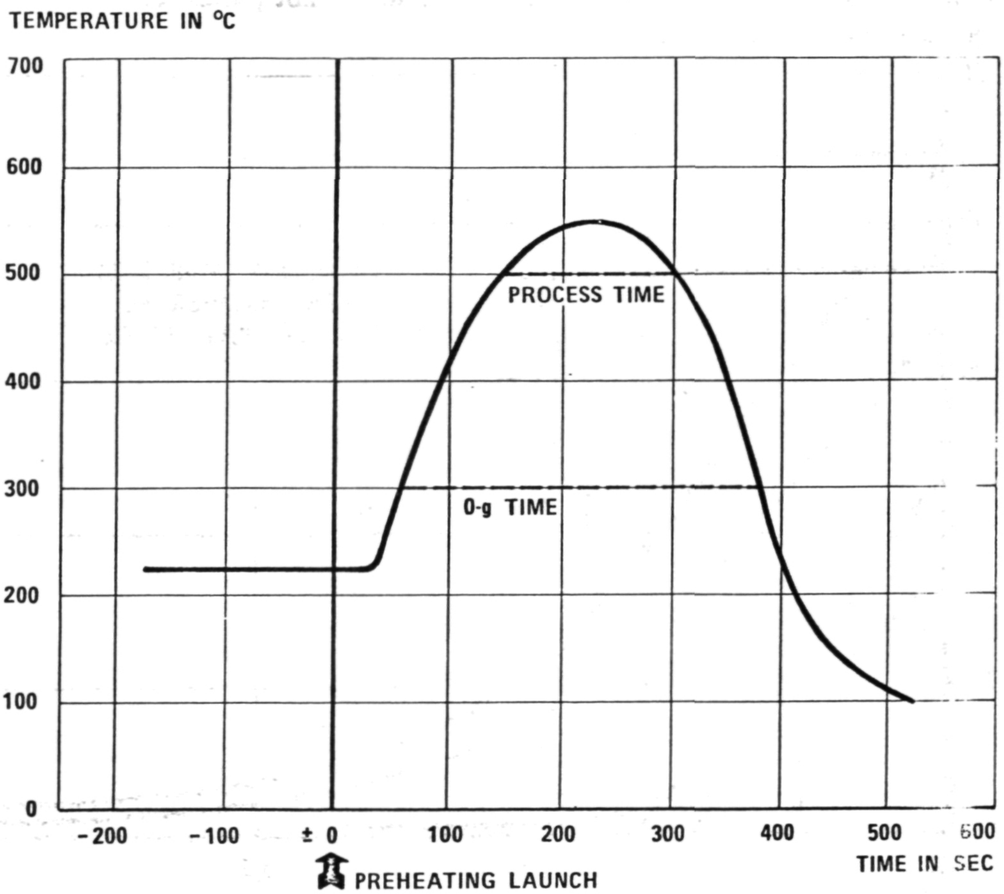

Figure 10. Temperature-time diagram of thermal tests (NASA).

1

cooling rates cannot be checked. Therefore, neither a directional eutectic nor a normal eutectic solidification can be expected because the time is too short for dissolving the silver in the lead.

DEFORMATION PROCESS

All samples, i.e. a sintered sample, a thermal test sample from NASA, and the flight sample, are deformed in the same manner. First, the samples are extruded from 12.1 mm diameter to the final diameters of 5 mm and 4 mm. This reduction by extrusion represents an optimum of deformation. Before the following drawing process the wires are enclosed in 1 mm or 2 mm thick silver tubes, avoiding a breakdown. The wires are cold rolled in presses down to 1 mm diameter, then cold drawn by means of dies in small steps to diameters of 900 μm, 180 μm, and 100 μm including the silver sheath. The wire of the flight sample could be drawn to 100 μm in diameter; hence, the true diameter of the alloy is 35 μm and the thickness of the sheath is in the range of 30 μm (Fig. 11). Only the sintered specimen cannot be reduced to those diameters because a codeformation of the silver particles is not possible.

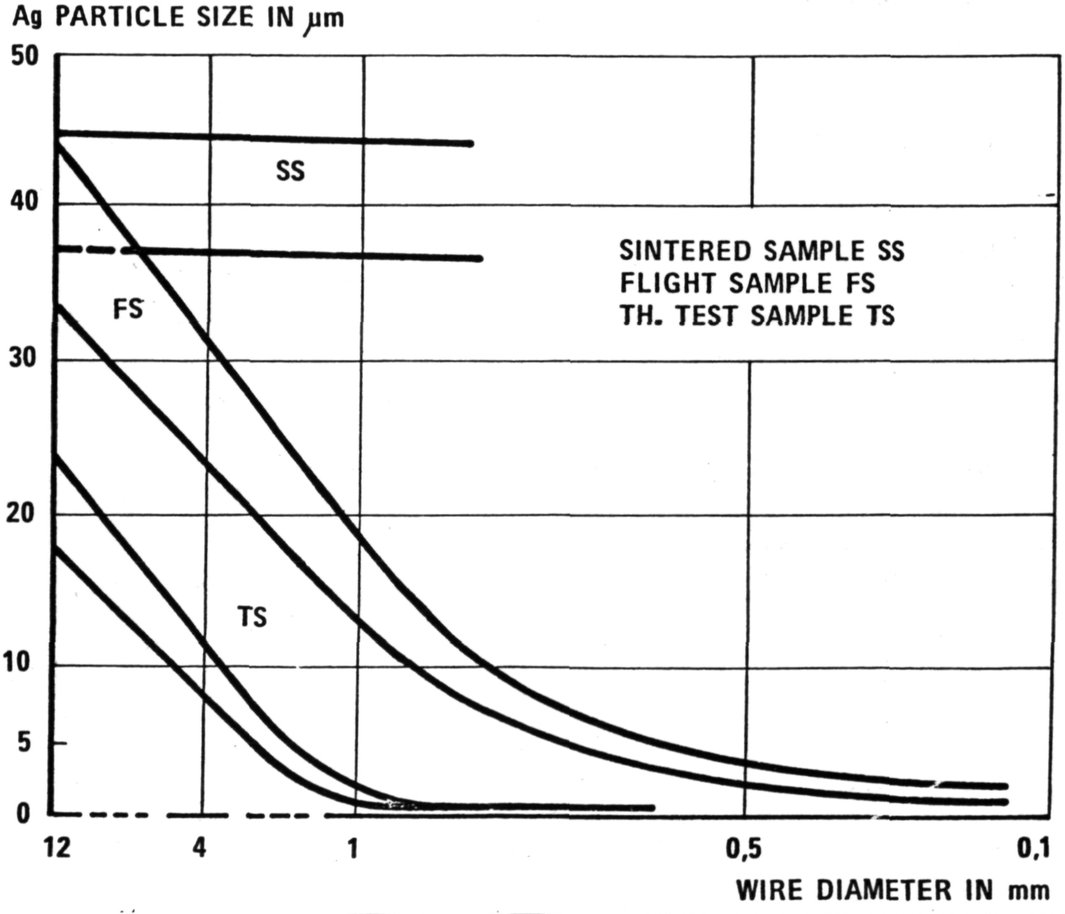

Figure 11. Particle size wire diameter diagram.

METALLOGRAPHIC ANALYSIS (RESULTS)

Microsection surfaces are prepared from the cylindrical samples before and after deformation. First the original state is investigated (cross section) because the distribution and grain size of the silver and BaO after sintering and melting are important in obtaining the desired deformation behavior.

The cross section of a sintered sample is shown in Figure 12(a). The BaO particles cannot be seen because of their fine dispersion and small size ($\leq 0.1\ \mu m$). The silver particles are visible; their grain size is approximately 50 μm. In Figure 12(b) the surface of the thermal test sample is presented. The melting process has been found to lead to a decrease of the grain size of the silver particles in the range of 30 μm. That means partial dissolving of the silver takes place, but the time is too short for a complete solution.

The grain size of the flight sample [Fig. 12(c)] is within the same range as the sintered specimen. The distribution of the silver particles is similar to the sample in Figure 12(c).

The longitudinal sections of the wires are especially interesting because of the changes of the silver during the deformation process. A visible extension of the silver is expected in the direction of deformation. Extension of the silver particles of the sintered sample cannot be obtained during extrusion [Fig. 13(a)].

Contrary to this behavior the other extruded specimens show an extension of the silver as expected. The thickness reduction of these particles is considerable, i.e. up to 50 percent [Figs. 13(b) and 13(c)]. During the subsequent rolling in presses and wire drawing, the thickness of the silver decreases to a final size of $\simeq 1\ \mu m$ [Figs. 14(a), 14(b), 15(a), and 15(b)].

A further deformation of the wires to 100 μm in diameter is possible without difficulty, but deformations to this extent cause extension of the silver. This behavior can be explained by the different strain hardening of the silver and the lead. The lead shows a remarkable strain hardening because of the BaO addition. This is normally sufficient to deform the silver (codeformation) in the compound, but the silver strain hardens during the extrusion and wire drawing also, until the strength of the metals is equal. Above this point the strength of the lead increases slower than that of silver. Then it is impossible to reach a codeformation of the two phases, because only the lead will be deformed. Therefore, the silver particles keep their grain size thickness by further deformation. The conclusion of this behavior is the fact that the process time is too short at the necessary temperature of 500°C (Figs. 9 and 10).

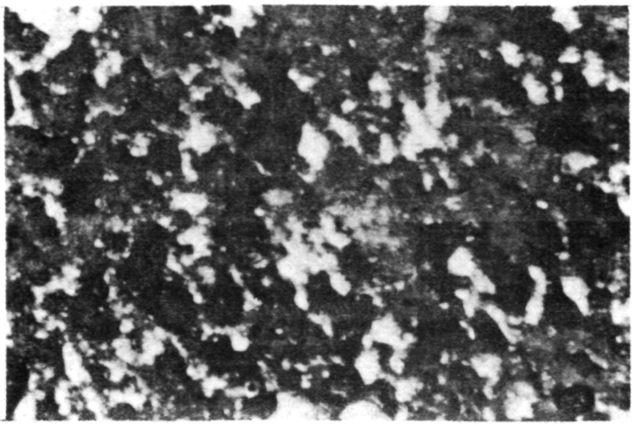

(a) Sintered sample.

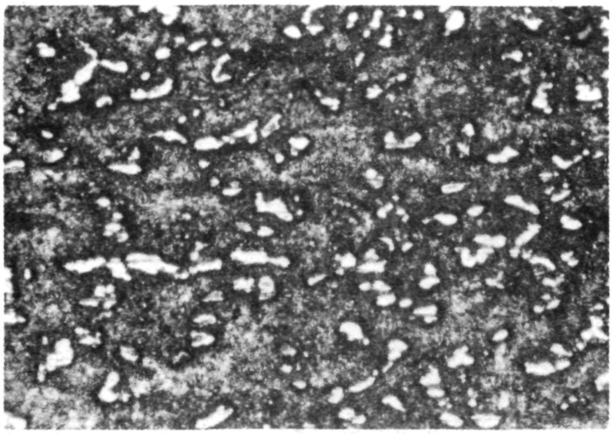

(b). Thermal test sample.

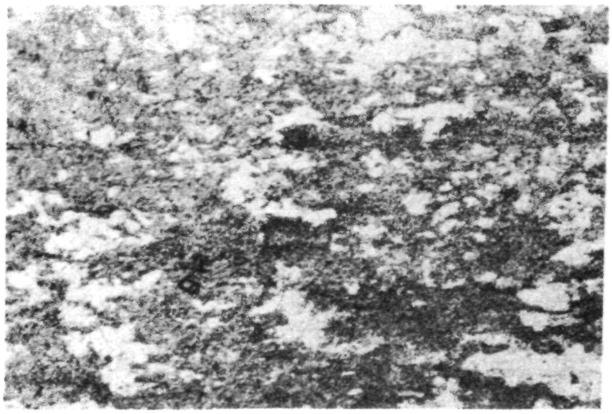

(c) Flight sample.

Figure 12. Cross sections of undeformed samples, 200X.

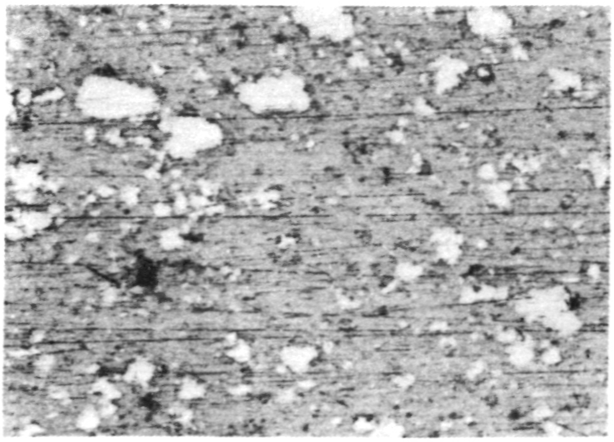

(a). Sintered sample, 4 mm ϕ, 200X.

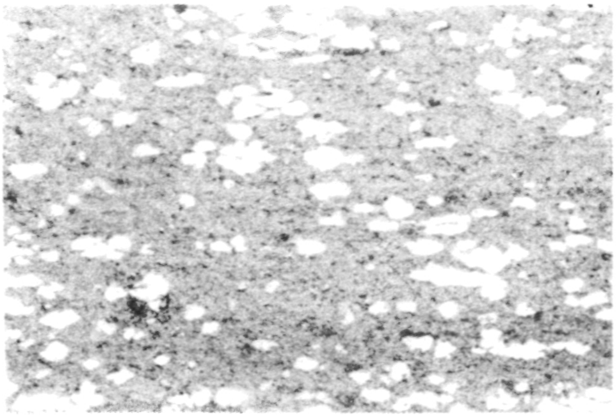

(b) Thermal test sample, 5 mm ϕ, 200X.

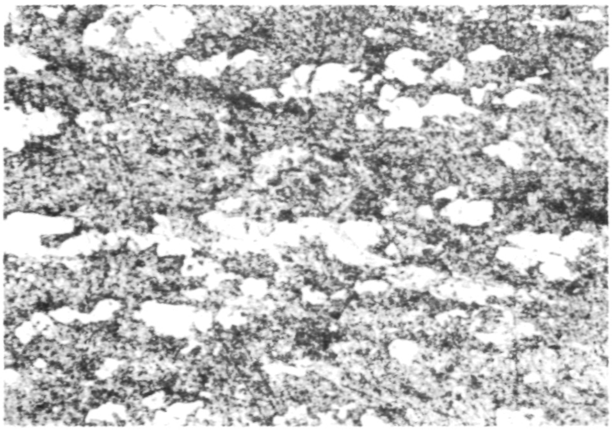

(c) Flight sample, 4 mm ϕ, 200X.

Figure 13. Longitudinal section of extruded samples.

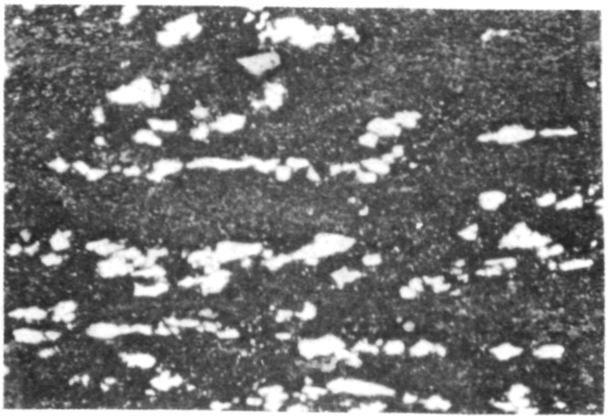

(a) Thermal test sample.

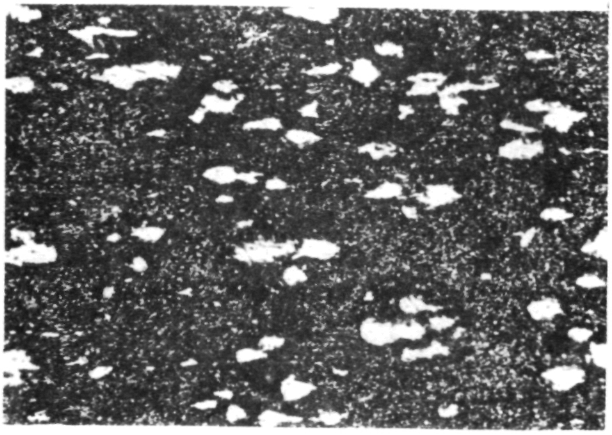

(b) Flight sample.

Figure 14. Longitudinal section of samples, 0.9 mm ϕ, 200X.

The silver cannot be completely dissolved in the lead; therefore the grain size is too large after solidification. When a normal eutectic or a directional eutectic solidification takes place, the grain size will be in the range of 3 to 1 μm. Then deformation of the precipitated silver to fibers in the desired dimensions of approximately 100 Å is possible without difficulty, because the strain hardening and cold working behavior of the metals used and the alloy, respectively, is now as expected.

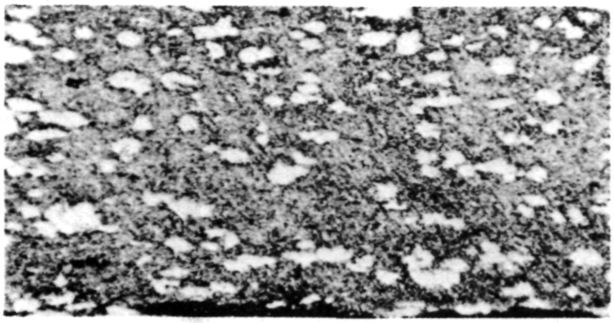

(a) Thermal test sample.

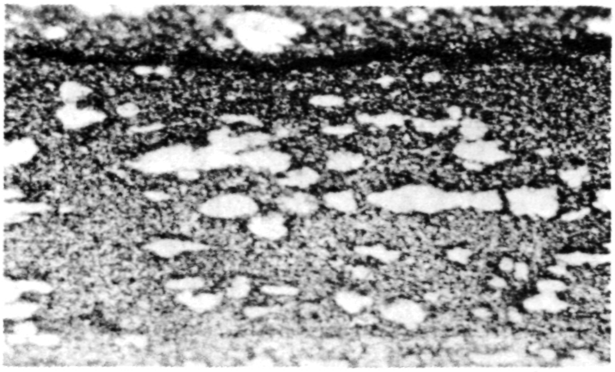

(b) Flight sample.

Figure 15. Longitudinal section of samples at 0.5 mm ϕ, 500X with no further silver particle extension taken place.

Besides the differences in strength of the two metals a normal or dynamical recovery of the lead phase can occur if the reduction is high enough. Then it is clear that the lead suffers a softening in strength, while the silver still has its larger strain hardening values. It is known that pure lead recrystallizes at room temperature in a very short time (dynamical recrystallization) after deformation. In this case the BaO addition inhibits the recrystallization of the lead so that only a recovery is possible.

These two cases, recovery and lower strain hardening, can not be distinguished clearly. To distinguish this behavior, further investigations are necessary and will be carried out in the future. A change of the amount of BaO will be dependent on these results.

SUPERCONDUCTING BEHAVIOR

Measurements of the superconductivity of the alloy wires of the thermal test sample (NASA) and of the flight sample were prepared. The diameters of these wires are in the range of 230 and 250 μm, while the grain size thickness of the silver particles is approximately 1 to 2 μm. After obtaining a large volume of the specimens, several wires are bundled into parallel pieces. This ensures measuring the complete volume of the samples instead of a single sample. The temperature at which measurements take place is 4.2 K or lower.

The result is shown in Figure 16. As can be seen in Figure 16, a splitting up of the critical magnetic field H_c into H_{c1} and H_{c2} is discovered. However, this behavior can be obtained from the flight sample only. The thermal test specimen shows only a very small inclination to pass into the mixed state, i.e. a transition from type I to type II is hardly recognized.

The different behavior of superconductivity of these samples is difficult to explain because the dimensions of the silver particles are almost the same in both specimens. Therefore, whether the melting process under zero gravity is important for this effect must be determined. Excluding any convection in the molten flight sample while in zero gravity, it is possible that diffusion only dissolved the silver in the lead. Then, a large number of very small particles are in the matrix after solidification, which are not visible by means of light microscopic examinations. However, these finely dispersed particles are instrumental in obtaining the desired effect in this sample.

In this case many areas clearly exist in the wires of the flight sample which are near the limit of the dimensions of the silver particles where a formation of a mixed state is possible. These areas lead to remarkable transition from a first order superconductor to a second order superconductor (Fig. 16), along with the larger grain size of the silver particles not being in the dimensions that are necessary.

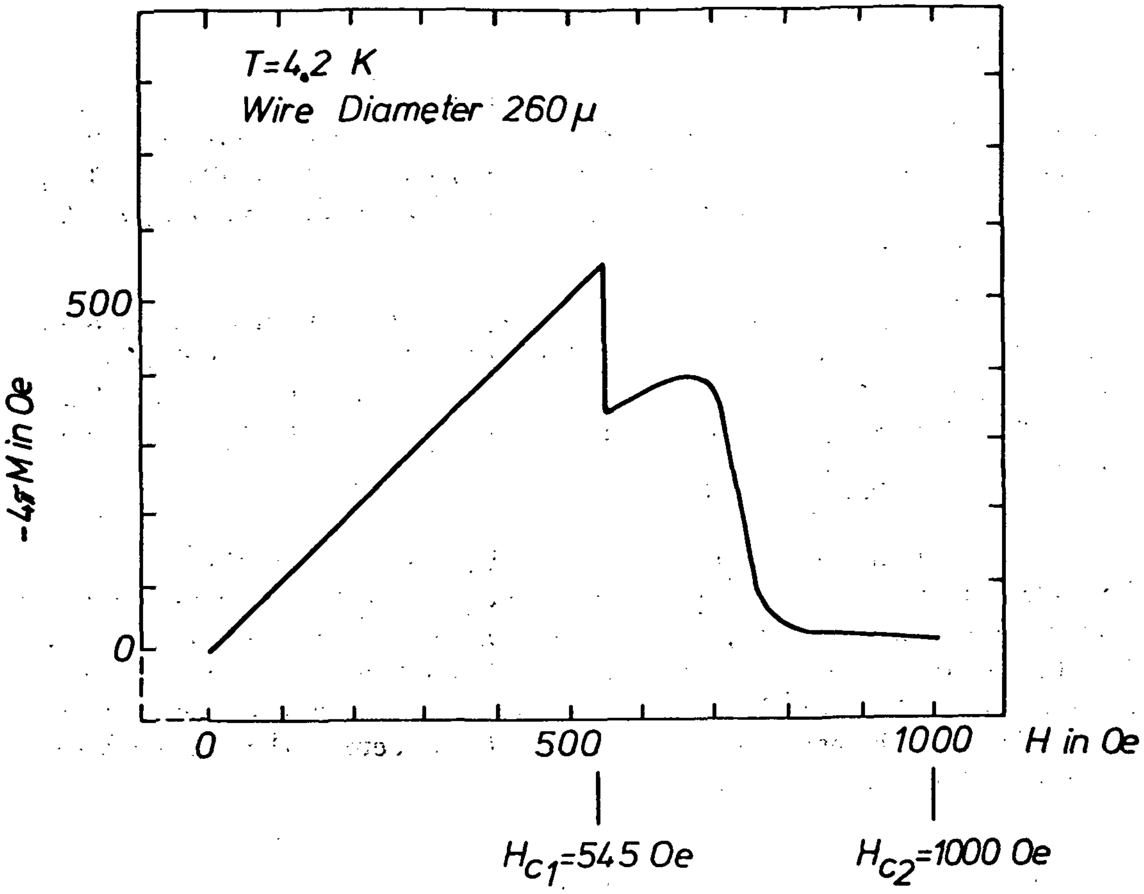

NOTE: TRANSITION OF TYPE I TO TYPE II SUPERCONDUCTOR BY H_{c1} = 545 Oe.

Figure 16. Superconducting behavior of a flight sample wire at 4.2 K.

In spite of this fact a large change in the superconducting behavior is obtained which is opposite that of pure lead and the thermal test sample.

CONCLUSIONS

The investigations of the PbAgBaO alloy lead to the following results:

1. An in situ deformation of the silver particles in a matrix of lead can be reached by a small amount of a BaO addition if molten material is used. By deforming sintered samples only, no codeformation of the silver phase is possible.

2. The strain hardening of the lead phase increases in such a large range during the deformation (rolling in presses and wire drawing) that the silver particles can be reduced to 90 percent in area (length/thickness = 10). At high reductions a softening in strength or recovery of the lead stops further deformation of the silver.

3. A remarkable effect in the superconducting behavior can be obtained by the flight sample only. A transition of a first order superconductor to a second order superconductor in the form of a mixed state takes place. This effect is expressed by a splitting of the critical magnetic field H_c of the lead phase into a lower field H_{c1} and an upper field H_{c2}.

4. To obtain a better superconducting behavior of this alloy, it is necessary to start at smaller dimensions of the silver particles before the deformation begins. Reaching an optimum of process time and/or an eutectic solidification, the silver particles can be precipitated as small fibers. The following wire drawing process can be stopped earlier at larger diameters of the wires because the deformed fibers of the silver occur earlier in the dimensions of the mean free path of length of electrons.

SUMMARY

The preparation and treatments of a PbAgBaO alloy are described, especially the deformation behavior by extrusion and the subsequent wire drawing. The dispersed silver particles can be shown to be deformable in lead by a small amount of BaO, but only in molten bodies. During the deformation a strain hardening of the lead occurs, reaching a large reduction of the silver until a 90 percent reduction in area is achieved. A further deformation of the silver is not possible because a recovery or softening in the lead phase strength takes place while the silver particles continue their strain hardening.

The measurements of the superconductivity show a remarkable effect expressed by the transition of a first order superconductor in a second order superconductor in the form of a mixed state. This result can be obtained only by the flight sample.

The grain size of the silver in the molten body is too large because the melting time under zero gravity is too short. Therefore, the desired dimensions of the silver particles cannot be reached during the deformation process.

In spite of this fact a high deformation of silver in lead is considered possible by a small addition of BaO. As a result a change in the superconducting behavior of the lead phase could be achieved.

BIBLIOGRAPHY

Ashby, M.: The Hardening of Metals by Nondeforming Particles. Z. Metallkunde, vol. 55, 1964, p. 5.

Berlingcourt, T. G. and Hake, R. R.: Superconductivity at High Magnetic Fields. Phys. Rev., vol. 131, 1963, p. 140.

Buckel, W.: Supraleitung. Physik Verlag, Weinheim W.-Germany, 1972.

Das Gupta, A.; Mordike, B., and Frommeyer, G.: Pinning of FluOxids in a Typ II Superconducting PbNaHg Alloy with Silver Particles. Z. Metallkunde, vol. 66, 1975, p. 319.

Haasen, P.: Physik und Metallkunde harter Supraleiter. Z. Metallkunde, vol. 66, 1975, p. 701.

Haasen, P.: Mechanismen der Härtung von Supraleitern. Z. Metallkunde, vol. 60, 1969, p. 149.

Hansen, M.: Constitution of Binary Alloys. McGraw Hill Book Comp. Inc., New York, 1958.

Hillmann, H.: Technologie der harten Supraleiter. Z. Metallkunde, vol. 60, 1969, p. 157.

Hoffman, W.: Blei und Bleilegierungen. Springer Verlag, Berlin, 1962.

Kittel, Ch.: Fertkörperphysik. R. Oldenbourg Verlag, München-Wien, 1968.

Kurz, W. and Sahm, P. R.: Gerichtet ertsarrte eutektisch Werkstoffe. Springer Verlag, Berlin, 1975.

Liesner, Ch. and Wassermann, G.: Verformungsverhalten und mech. Eigenschaften von Verbundwerkstoffen aus Kupfer mit α -Korund. Z. Metallkunde, vol. 60, 1969, p. 827.

Livingston, J. D.: Magnetization of Superconducting Cu-Pb Alloys. J. App. Phys., vol. 39, 1968, p. 3836.

Matthias, B. T., Geballe, T. H., and Compton, V. B.: Superconductivity. Rev. of Mod. Phys., vol. 35, 1963, p. 1.

Mordike, B.: On the Production of Superconducting Alloys Based on Copper. Z. Metallkunde, vol. 65, 1974, p. 319.

Orowan, E.: Symposium of Internal Stresses, Inst. of Met., 1948, p. 451.

Petermann, J.: Ausscheidungen und Flußverankerung in einer supraleitenden PbNa-Legierung. Z. Metallkunde, vol. 61, 1970, p. 724.

Wahl, H. P. and Wassermann, G.: Anomalien der Eigenschaften dünner Drahte aus Eisen-Silber-Legierungen. Z. Metallkunde, vol. 61, 1970, p. 326.

Wassermann, G.: Deformation Mechanism and Properties of Two Phase Composite Wires. Z. Metallkunde, vol. 64, 1973, p. 844.

Private communication with Prof. Heiden Universität Münster, Germany, 1976.

APPENDIX A

ABBREVIATIONS AND ACRONYMS

NASA	National Aeronautics and Space Administration
MSFC	NASA-George C. Marshall Space Flight Center
WSMR	White Sands Missile Range
SPAR	Space Processing Applications Rocket
GPRF	General Purpose Rocket (Furnish)
TCU	Temperature Control Unit
GBT	Ground-Based Test
ASTP	Apollo-Soyuz Test Project
at. %	Atomic percent
GSFC	NASA-Goddard Space Flight Center
g	Gravity (980 cm/sec^2)
wt %	Weight percent
ORSA	Ogive Recovery System Assembly
RCS	Rate Control System
low-g	Period of time during which accelerations are not greater than 1×10^{-4} g.
BBVC	Black Brant VC (Launch Vehicle)

*U.S. GOVERNMENT PRINTING OFFICE: 1976 - 735-004/14

NATIONAL AERONAUTICS AND SPACE ADMINISTRATION
WASHINGTON, D.C. 20546

OFFICIAL BUSINESS
PENALTY FOR PRIVATE USE $300

SPECIAL FOURTH-CLASS RATE
BOOK

POSTAGE AND FEES PAID
NATIONAL AERONAUTICS AND
SPACE ADMINISTRATION
451

U.S.MAIL

POSTMASTER : If Undeliverable (Section 158 Postal Manual) Do Not Return

---

> *"The aeronautical and space activities of the United States shall be conducted so as to contribute . . . to the expansion of human knowledge of phenomena in the atmosphere and space. The Administration shall provide for the widest practicable and appropriate dissemination of information concerning its activities and the results thereof."*
>
> —NATIONAL AERONAUTICS AND SPACE ACT OF 1958

NASA SCIENTIFIC AND TECHNICAL PUBLICATIONS

TECHNICAL REPORTS: Scientific and technical information considered important, complete, and a lasting contribution to existing knowledge.

TECHNICAL NOTES: Information less broad in scope but nevertheless of importance as a contribution to existing knowledge.

TECHNICAL MEMORANDUMS: Information receiving limited distribution because of preliminary data, security classification, or other reasons. Also includes conference proceedings with either limited or unlimited distribution.

CONTRACTOR REPORTS: Scientific and technical information generated under a NASA contract or grant and considered an important contribution to existing knowledge.

TECHNICAL TRANSLATIONS: Information published in a foreign language considered to merit NASA distribution in English.

SPECIAL PUBLICATIONS: Information derived from or of value to NASA activities. Publications include final reports of major projects, monographs, data compilations, handbooks, sourcebooks, and special bibliographies.

TECHNOLOGY UTILIZATION PUBLICATIONS: Information on technology used by NASA that may be of particular interest in commercial and other non-aerospace applications. Publications include Tech Briefs, Technology Utilization Reports and Technology Surveys.

Details on the availability of these publications may be obtained from:

SCIENTIFIC AND TECHNICAL INFORMATION OFFICE

NATIONAL AERONAUTICS AND SPACE ADMINISTRATION

Washington, D.C. 20546